# Combining magnetic tweezers and single-molecule fluorescence microscopy to probe transcription-coupled DNA supercoiling

Stephen John Cross

PhD Thesis

University of York
Department of Biology

September 2013

**Abstract**

Previous studies have shown that translocation of an actively transcribing RNA polymerase leads to local increases or decreases in DNA torsion (twin-supercoiled domain [1]), which cannot be resolved *in vivo* due to interactions of the template DNA, nascent RNA and polymerase with the crowded cellular environment. Local changes in DNA supercoiling are biologically relevant as they have been shown to regulate transcription initiation at promoters located downstream. Current *in vitro* single-molecule approaches are not able to directly probe transcription-coupled DNA supercoiling due to an inability to simultaneously monitor changes in torsional stress and localise individual transcribing RNA polymerase(s) on the DNA. Described here is a novel optical microscope, which utilises a combination of magnetic tweezers, bright-field illumination and wide-field epifluorescence imaging to permit the visualisation of fluorescently tagged polymerases transcribing in real-time on a torsionally constrained DNA template. With this unique geometry, transcription as a function of applied torsion can be probed directly *in vitro*. Unlike standard magnetic tweezers configurations this system extends tethers horizontally relative to the microscope slide surface, which allows individual enzymes to be directly viewed via attached fluorophores. The magnetic tweezers allow both the relative extension and linking number of the DNA tether to be manipulated, thus enabling transcription to be studied under conditions of constant DNA extension and defined torsional stress.

**List of contents**

**List of figures**

**List of tables**

**List of equations**

**List of accompanying material**

Custom Maple scripts:

- Biot-Savart_force_model.mw
- Biot-Savart_off-axis_force_model.mw

Custom MATLAB scripts (grouped by parent function):

- chooseFilter.m
- equationFit.m
  - efCalcResidual.m
- imageSplitter.m
  - isAlignImages.m
  - isCalibrateImageSplitter.m
  - isTrimImages.m
- monteCarloDiffusion.m
  - mcdCPCConversion.m
  - mcdCalculateMSD.m
  - mcdCellCurvature.m
  - mcdCellRotation.m
  - mcdComparePositions.m
  - mcdCompareTriMono.m
  - mcdCompareTriTri.m
  - mcdConstStepDiff.m
  - mcdCreateLocalTable.m
  - mcdDiffuseBtuB.m
  - mcdDiffusionCore.m
  - mcdHemisphereConversion.m
  - mcdMeshBug.m
  - mcdMeshFind.m
  - mcdMinOmpFDist.m
  - mcdMinTriDistance.m
  - mcdPlotDiffusion.m
  - mcdPopulateMembrane.m
  - mcdPositionBtuB.m
  - mcdRandomStart.m

- mcdRestrictedMovement.m
- mcdSettings.m
- mcdSignGeneration.m
- mcdStoreMonteCarloData.m

measureMag.m

measurePhotocleavage.m

measureTFSIntensity.m

- mtiAverageImages.m
- mtiSelectParticles.m

modelDisp.m

- mdSimulateCamera.m

multiTracker.m

- mtAnalyseTrackedParticles.m
- mtCheckFilesFirst.m
- mtDriftCorrect.m
- mtImRegisterFit.m
- mtLineDraw.m
- mtLoadParameters.m
- mtMakeMovie.m
- mtParticleTracking.m
- mtPeakFollow.m
- mtSelectParticles.m
- mtSequenceAnalysis.m
- mtTrackerDetectionSettings.m

numberImageStack.m

particleSizeDistribution.m

- psdFitFRETGauss.m
- psdGaussFit.m
- psdMeasureRadialProfile.m
- psdMultiOriginGaussEquation.m
- psdSelectParticles.m

**Acknowledgements**

Firstly I would like to thank my supervisor, Dr Christoph Baumann, for giving me the opportunity to delve into the world of biophysics. Without his support and guidance over the past four years this PhD would not have been possible. In addition, thanks goes to my TAP members, Dr James Moir and Dr Roland Kröger, whose objective input has kept me focussed on the project's ambitions. I'd also like to thank everyone from the Baumann lab group, past and present, who have either contributed to the project or just provided motivation and support. Of special mention are Urban Seger, Tom Storr and Sara De Ornellas, who made me feel at home during the start of my PhD. Similarly, thanks to those who have contributed time, samples or data; in particular, Diana Quinn, Gassan Suliman, Rebecca Milner, Jim Pullen, Laura Griffin and Tom Williamson. Thanks also to Professor Colin Kleanthous, his lab group and other LoLa members for all their help with the colicin work. Additionally, for his ideas and support in designing the microfabricated tethering substrates, I'd like to thank Dr Steven Johnson.

Throughout the project, technical advice and assistance has been kindly provided by many people, but in particular I'd like to thank Mark Bentley for building custom components used in the magnetic tweezers microscope, Meg Stark for help with electron microscopy and to Jonathan Cremer for assistance in using the clean-room. Thanks must also go to Steve Howarth, Trevor Illingworth, Dr Peter O'Toole and Professor Mark Leake.

Over my five years spent on L1, I've had some great times and met some wonderful characters. Their splendid banter and company has certainly helped during times when science has not been kind. I'd also like to thank Katie Grayson, who provided much scientific advice, especially in the early days of my PhD. A special mention needs to go to my expert team of proof-readers: Peter Cross ("Dad"!), Gemma Fisher, Andrew Cross, Laura Griffin, Sara De Ornellas and Dr Christoph Baumann. They have provided invaluable feedback and I can't express how much I appreciate their efforts.

I would like to thank my family, who have always been there when I fancied a chat/rant and are still my first port of call when I do something stupid (such as getting locked out my room…twice!). Finally, a massive thank you to Gemma Fisher, whose kindness and persistence has been my motivation whilst writing this thesis; I hope I can repay you in four years when you're going through the same thing.

**Author's declaration**

I declare that the contents of this thesis, submitted for the degree of PhD, are entirely the result of my own work except where explicitly stated. This work has not previously been submitted at The University of York or any other institution.

Stephen John Cross

# Introduction

## Chapter 1

## 1.1 Background to transcription-mediated DNA supercoiling

A direct consequence of any enzymatic activity which separates the two strands of the DNA double helix is a local change in substrate torsion [1–3]. This arises through compaction of the helix downstream of the separation event, leading to template overwinding. Correspondingly, there is a reduction in helical turn density occurring upstream, resulting in template underwinding in this region. For enzymatic motors moving along the DNA whilst maintaining this bubble, the effect is compounded, resulting in a continuous increase in the torsional change [1,4]. First identified by Liu and Wang for transcription by RNA polymerase (RNAP), the simultaneous formation of over- and under-wound regions of DNA by enzymatic activity was termed the "twin supercoiled domain model" (Figure 1-1) [1].

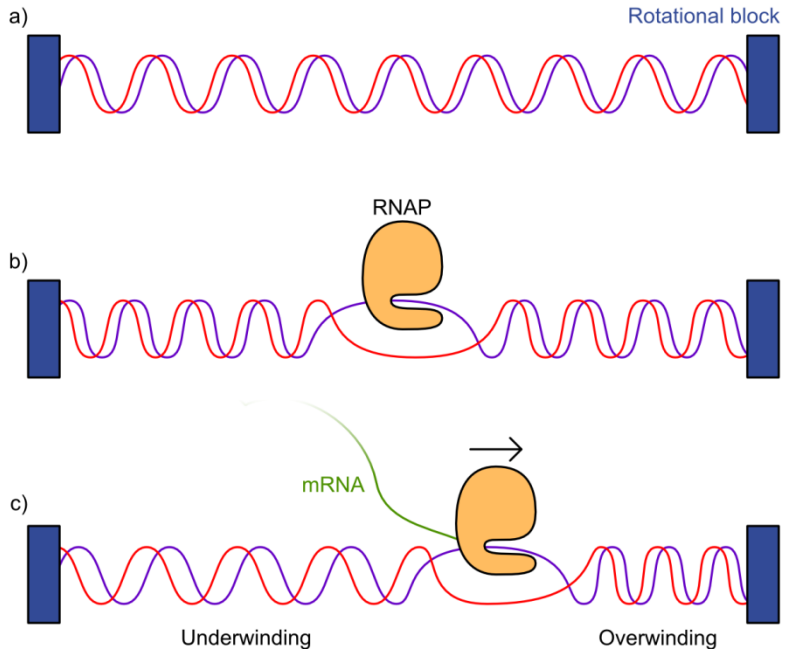


**Figure 1-1 – The twin supercoiled domain model**
For a rotationally-constrained system the process of separating the DNA double helix, such as during transcription, results in an increase in DNA torsion downstream of the polymerase and underwinding upstream. This is known as the twin supercoiled domain model and was first proposed by Liu and Wang [1]. For the rotationally-constrained template (a), initial separation of the strands results in overwinding both upstream and downstream to accommodate the strand-separated region (b). Movement of the separated region along the template causes the decrease in linear winding density upstream (underwinding) and compaction of winding downstream (overwinding), which characterises the twin supercoiled domain model (c).

In topologically unconstrained systems, resolution of this energetically unfavourable increase in torsion would manifest as rotation of the DNA template, enzyme complex or both [1,5]. The picture in the crowded cellular environment is not this simple however; rotational constraints arising from sources such as linkages to cellular machinery and high hydrodynamic drag serve as topological blocks [1,4,6–8]. This has led to the evolution of the

topoisomerase class of enzymes, which are tasked with *in vivo* torsional control of DNA. In bacteria, DNA gyrase creates negative supercoils and topoisomerase I relaxes them, whereas in eukaryotes, both functions are performed by topoisomerase I [1,9].

### 1.1.1 Transcriptional origins for DNA supercoiling *in vivo*

As the enzymatic machine responsible for encoding the sequence information stored in DNA as messenger RNA (mRNA), RNA polymerase (RNAP) subjects the DNA template to the same torsional stresses just described. As previously stated, restrictions on DNA and transcription complex rotation prevent relaxation of this increased torsion. Correspondingly, if the polymerase processivity exceeds the capacity for counter-rotation, the resulting increase in torsional stress can manifest in the duplex supercoiling characteristic of the aforementioned twin supercoiled domain model (Figure 1-1) [1].

One of the most notable causes for the observed twin supercoiled domains is hydrodynamic drag. To understand the origin and effect of hydrodynamic drag on the accumulation of torsional stress *in vivo* it is best to consider the idealised system described by Levinthal and Crane [10]. Although proposed for DNA replication, rather than transcription, the fundamental principles remain valid. For this system, the B-form DNA double helix is visualised as a cylinder wound about its axis. In response to the enzymatic action of the polymerase, this helical structure is forced to revolve about this same axis, with an energy required to overcome viscous drag being given by Equation 1-1 [10].

$$E = \frac{16\pi^3 n^2 \eta p r^2}{T}$$

**Equation 1-1 – Rotation of DNA against viscous drag**
The energy ($E$) required for rotation of an idealised DNA molecule against the effect of viscous drag [10]. This is a function of the number of helical turns ($n$), viscosity coefficient for the medium ($\eta$), helical pitch ($p$), helical radius (r) and the time taken for replication ($T$).

When calculated for biologically relevant parameters, such as those defined in the reported work, the energy required to overcome hydrodynamic drag is determined to be negligible; approximately 1000-fold less than is necessary for formation of phosphate bonds [10]. Accordingly, it could be expected that any unfavourable increases in torsional stress would simply and easily diffuse off the DNA molecule. In reality however, such free rotation is not observed *in vivo*; a paradox overcome by considering the DNA, not as a helix wound

round a straight axis, but as a tangled structure bound by proteins necessary for efficient cellular packaging [8]. This situation was also realised by Levinthal and Crane, who demonstrated a significant reduction in the capacity for rotation when helical and rotational axes are not coincident [10]. As a result of this, they hypothesised that DNA rotation would be dominated by rotational motion along coincident axes; known as the speedometer cable (or plumber's snake) analogy [10].

Krebs and Dunaway showed how linear DNA templates longer than approximately 18 kbp can alone also be sufficient to maintain significant levels of supercoiling *in vitro* [7]. Elucidation of this mechanism was achieved through analysis of the transcriptional efficiency from the topologically sensitive rRNA promoter as a function of distance to the end of the linear DNA template. This work was based on the fundamental assumption that any increases in torsion would be more readily reduced through diffusion at positions closer to the template ends, thus reducing efficiency of the promoter [7]. Interestingly, such behaviour appears to contradict the prediction of Levinthal and Crane that DNA rotation is energetically favourable when mediated via plumber's snake, rather than crankshaft, motion [10]. This disagreement was addressed by Nelson, who demonstrated how naturally-occurring bends in the DNA polymer could effectively "spin-lock" the template on length scales smaller than 1 kbp [8]. These results highlight how under certain conditions it may be possible to observe supercoiling *in vitro*, where many of the torsional restrictions encountered *in vivo* are absent. In particular, this arises when the velocity of the polymerase, and thus the rate at which torsion increases, is greater than the rate at which this excess torsion is capable of diffusing off the molecule [8].

Supplementary to the inhibition of DNA rotation described previously, localised torsional increases can manifest through anchoring of the transcribing polymerase with intra-cellular components. For example, it has long been known that simultaneous transcription and translation occurs in prokaryotic systems where there is no nucleus to provide segregation of DNA and ribosomes [11]. The most logical application of this is that the increased hydrodynamic drag of a transcription complex linked to the ribosome will experience reduced rotational capacity. Furthermore, for production of a membrane-bound protein, Liu and Wang hypothesised reduced RNAP rotation, not just due to the extra drag from simultaneous transcription and translation, but also from the subsequent incorporation of the nascent protein into the cellular membrane [1]. Conversely, in the case of eukaryotic

systems, additional restrictions can simply be incurred through the relatively large polymerase holoenzyme volume; yielding viscous drag coefficients in the intracellular milieu large enough to significantly hinder complex rotation [8].

It has further been hypothesised that such restriction on transcription complex rotation may have evolved from the intrinsic advantage that nascent mRNA chains do not become twisted round the template DNA [12]. One proposed method by which RNAP may achieve this is the formation of an apical loop at the transcription site, thus acting to locally steady the transcription complex [12]. Similarly, the "drag anchor" hypothesis proposes that the mRNA itself may act to minimise rotation of the transcriptional machinery about the template. This was demonstrated by Tsao *et al.*, who measured rapid accumulation of positive supercoiling in the pC15 DNA template within 1 minute [4]. At this point, average mRNA transcripts shorter than 6 kb had been synthesised, indicating a minimum transcript length necessary for torsional constraint. Confirmation of the role of mRNA was achieved via an observed inhibition of supercoiling upon addition of the mRNA nuclease enzyme, RNase A [4]. More recently, these observations have been repeated for *in vivo* transcription of plasmids pLUC5 (162 nt transcript length) and pLUC9 (3020 nt transcript length) by T7 RNAP [13]. With increasing time following IPTG-induction of T7 RNAP, increasing levels of hypernegatively supercoiled DNA (DNA exhibiting negative supercoiling significantly greater than normal [14]) were observed. Predictably, shorter transcripts required longer for hypernegativity to accumulate: 40 minutes for 67% supercoiling from pLUC5 compared to 10 minutes for 90% supercoiling from pLUC9 [13].

### 1.1.2 The effect of simultaneous transcription by multiple complexes

Simultaneous transcription by multiple elongation complexes was first observed *in vivo* for ribosomal precursor RNA genes in eukaryotes; a phenomenon no better demonstrated than with the electron micrograph images of Miller and Beatty (Figure 1-2) [15,16]. While the imaged sample was extracted from the newt, *Triturus viridescens*, this has since been observed for bacterial *E. coli*., where the nascent RNA chains are, in addition, capable of supporting multiple translating ribosomes [11,16]. As transcription complexes translocate along the gene, the nascent RNA chains are extended; a feature which can be observed as the characteristic wedge shape in Figure 1-2.

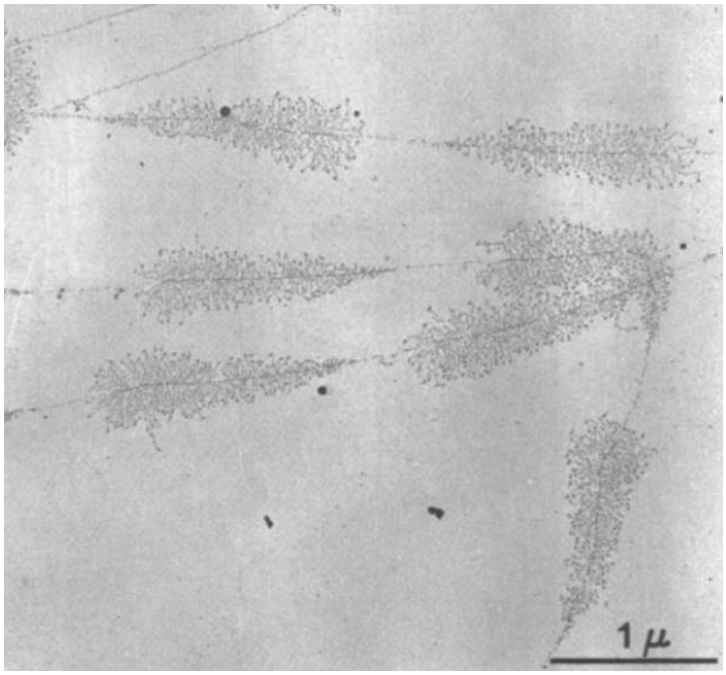


**Figure 1-2 – Multiple transcribing polymerases on a single DNA tether**
Transcription of ribosomal precursor RNA genes as viewed using an electron micrograph shows tens to hundreds of nascent molecules being produced simultaneously [16]. Distance from the gene promoter can be observed in terms of the nascent chain length, which gives rise to the characteristic wedge shape. Image taken from [16].

With the strong relationship between transcription and template supercoiling, these high polymerase densities will almost undoubtedly have an effect on processivity. Potential effects include increased initiation rates resulting from translocation-induced negative supercoiling [17,3,18,19] (see Section 1.1.3 for more detail) or cooperativity between adjacent polymerases. The latter case is exemplified by the work of Epshtein and Nudler, who demonstrated how a trailing elongation complex could restart a stalled complex [20] or the work of Epshtein *et al.*, who showed inter-RNAP assistance dissociating DNA-bound roadblocks [21]. Both reported works were conducted using *E. coli* RNAP [20,21]; however, a similar effect was hypothesised by Ferrari *et al.* for T7 RNAP [22]. The authors observed an increase in frequency of multi-round transcription at higher polymerase concentrations, leading to the conclusion that complexes may stall at the termination sequence, but were successfully dissociated through cooperative interactions [22].

### 1.1.3 Biological roles for DNA supercoiling

*In vivo,* elevated levels of DNA torsion are relaxed through the combined actions of the topoisomerase enzymes. In bacterial organisms these enzymes fall into two classes: DNA gyrase, a type II topoisomerase which introduces negative supercoils, and topoisomerase I, which relaxes negative supercoiling. Similarly, in eukaryotic systems activities are

performed by type I topoisomerases (topoisomerase I and III) and type II topoisomerases (topoisomerase IIα and IIβ); the latter class being capable of relaxing both positive and negative supercoils [23].

In spite of the aforementioned evolved ability to remove the excess supercoiling incurred through twin supercoiled domain action, elevated levels of template torsion have been shown to be vital for transcription [17,3,18,19]. An example of this is how negative supercoiling leads to an associated energy change in the Watson-Crick base-pairing, favouring DNA melting and assisting initiation [3,18]. For transcription of a negatively supercoiled DNA template containing the immunoglobulin heavy chain gene, this has been observed as a direct increase in RNA production in relation to a decreasing superhelical density (described in Section 1.2). Interestingly, this trend continues to a threshold value of $\sigma = -0.07$, beyond which transcription by RNA polymerase II was shown to decrease slightly [19]. In the same series of experiments, Parvin and Sharp observed diminished RNA production upon addition of the torsionally regulating topoisomerase I enzyme, further demonstrating the necessity for a negatively supercoiled DNA template [19]. This is, however, only a general relationship; in the case of the gene encoding DNA gyrase, the enzyme responsible for introduction of negative supercoils, Menzel and Gellert observed improved transcriptional activity on increasingly relaxed templates [24]. While uncommon, such a relationship is logical since up-regulation of DNA gyrase is preferential under conditions of minimal supercoiling, thus acting as a topological feedback system [24].

Experiments measuring end-to-end template extension as a function of applied superhelical density (Section 1.2) demonstrate the propensity of DNA to form plectonemes; structures extruding perpendicular to the normal DNA helical axis, thus reducing the observed end-to-end template extension (Figure 1-3) [25]. This response has implications for single-molecule experiments implementing controlled DNA topology where, given an applied force of known magnitude, the intrinsic template superhelical density can potentially be elucidated. Furthermore, these results demonstrate the ability to negatively supercoil DNA and not observe an appreciable change in end-to-end extension. Such a trait is particularly useful when studying the effect of template topology across biologically-relevant forces and superhelical densities using single-molecule fluorescence techniques to localise actively translocating polymerases. In such situations, supercoiling-mediated DNA

condensation would have severe consequences, preventing accurate localisation of enzymes along the template.

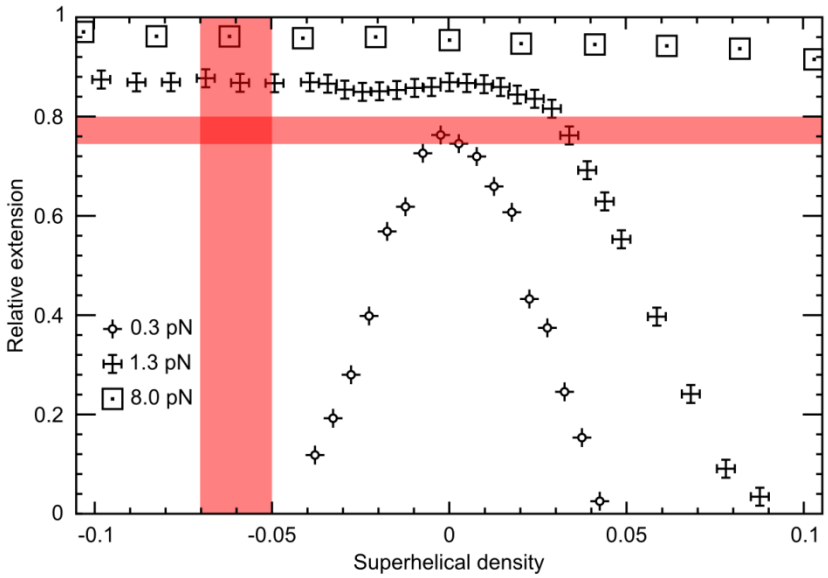


**Figure 1-3 – DNA compaction as a result of applied torsion**
With increasing superhelical density (see Section 1.2) the end-to-end extension of the molecule decreases due to the formation of plectonemes and supercoils. At higher applied forces (see legend on figure), the ability to condense the DNA decreases and reductions in end-to-end length are only observed for positive supercoiling. The biologically-relevant torsion regime of $\sigma$ = -0.05 to -0.07 has been highlighted in red [23]. Similarly, a force region sufficient to prevent DNA compaction, but low enough to prevent over-extension has also been highlighted. Figure redrawn from Strick et al. for data collected using *in vitro* magnetic tweezers equipment [25].

### 1.1.4 Rationale for torsional constraint of DNA tethers *in vitro*

It is of no doubt that supercoiling can accumulate *in vitro* simply through naturally occurring bends in the template DNA and due to the anchoring effect of the nascent mRNA transcript [7,8,4,13]. Nonetheless, it is common for single-molecule experiments to be conducted blind with respect to levels of template supercoiling [26–28]. Generally, the assumption is that at high stretching forces the torsion becomes relaxed [29]; however, for a parameter possessing such a marked influence over enzymatic activity, it is preferable that a method of quantifying and controlling template topology is employed. In particular, DNA compaction in response to applied torsion and stretching force (Section 1.1.3) offers a characterisable system that can be used to measure the intrinsic template topology. Once this has been established, torsional modifications can be applied and their effect on enzymatic activity monitored.

Realisation of topological tether control for *in vitro* study of transcription on the single-molecule level necessitates the combination of two well-established approaches:

reproducible formation and manipulation of individual DNA tethers and single-molecule fluorescence microscopy. Standard techniques for achieving the former are outlined in Section 1.4 along with analysis of their suitability and limitations with regards to torsional control and compatibility with single molecule fluorescence microscopy.

## 1.2 Torsional properties of double-stranded DNA

Since double-strand DNA (dsDNA) is comprised of two inter-wound strands, it has physical properties which can be described mathematically through the concept of linking number. Linking number (Lk) applies to two or more independent strands that are torsionally constrained with respect to each other; this can either be through a closed loop, or through an inability for the strands to rotate. Each time one strand passes completely around the other, the linking number increases by a value of one (Figure 1-4).

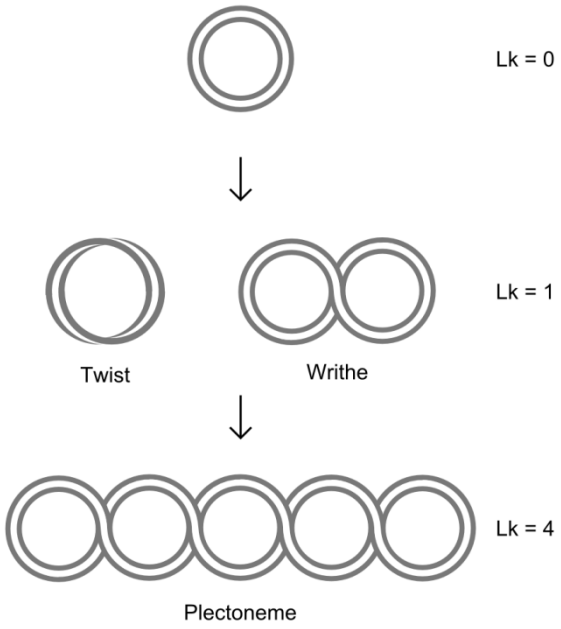


**Figure 1-4 – Linking number manifesting as twist and writhe**
For two or more torsionally constrained strands, linking number (Lk) defines the number of complete passes one strand makes around the other. Increases in linking number can manifest as twist (Tw), the numbers of turns in the helix, and writhe (Wr), where one strand passes over the other. Stages of torsional increase are not drawn to scale.

When the linking number results in the system being in the most energetically favourable state, the system is said to be relaxed. This value, $Lk_0$, does not have to be zero; for example, dsDNA has a linking number of approximately 0.1 turns/bp (10.4 bp/turn) [30] in its relaxed state. Increases in linking number manifest in two possible ways, twist (Tw) and writhe (Wr) [8,31] (Figure 1-4), with the relationship between linking number, twist and

writhe shown in Equation 1-2. At high levels of writhe, plectonemic structures can form, which in the case of DNA protrude perpendicularly from the normal helical axis of the molecule.

$$Lk = Tw + Wr$$

**Equation 1-2 – Linking number of a torsionally-constrained polymer**
Linking number (Lk) is a function of twist (Tw) and writhe (Wr). Twist and writhe both increase by a value of one when one of the linked strands passes completely around the other in that particular manner.

Any deviation in linking number from the relaxed state is described by another quantity, the superhelical density, σ, defined in Equation 1-3. The superhelical density is a measure of the number of turns added to, or removed from, the molecule compared to the relaxed state. With this metric, a reduction in the number of turns yields a negative superhelical density and the molecule is said to be under-wound. Similarly, an increase in turns gives a positive superhelical density; a state referred to as over-wound. *In vivo* DNA has a negative superhelical density (σ = -0.05 to -0.07) [25], which is known to assist initiation of the transcription complex [3,32].

$$\sigma = \frac{Lk - Lk_0}{Lk_0} = \frac{\Delta Lk}{Lk_0}$$

**Equation 1-3 – Superhelical density of a torsionally-constrained polymer**
Superhelical density (σ) is the number of turns added to, or removed from, a pair of linked strands compared to their relaxed state. This is defined as the difference between the current linking number (Lk) and the relaxed-state linking number ($Lk_0$). Negative supercoiling arises for $\sigma < 0$ and positive supercoiling for $\sigma > 0$.

## 1.3 The mechanism of transcription by T7 RNA polymerase

### 1.3.1 Initiation

RNAP induced duplex melting is highly sequence specific due to interactions between the specificity and recognition loops and bases flanking the promoter region. This melting creates a transcription bubble across which the template and non-template DNA strands separate. The template strand is fed through the polymerase, with the +1 and +2 nucleotides (relative to the origin of RNA synthesis) positioned precisely in the catalytically active site. Ribonucleoside triphosphates (NTPs) that diffuse into the active site are base-paired with the corresponding nucleotides in the template strand to form an RNA-DNA heteroduplex [33].

Whereas DNA polymerase (DNAP) requires a short RNA or DNA primer to provide a stable foundation from which to initiate DNA synthesis, RNAP is capable of incorporating new nucleotides *de novo*. For T7 RNAP, this is reliant on a guanine residue at position +1 (or in two cases, at +2) [34]. Watson-Crick base pairing alone is energetically insufficient to retain the initiating nucleotides in place, therefore interactions between the N-7 (and possibly O-6) atom of the guanine base and the polymerase provide a stabilizing effect [34].

### 1.3.2 Abortive synthesis

Before entering the processive elongation phase of transcription, the RNAP enters a phase of abortive synthesis, during which oligonucleotides are generated [35]. DNA footprinting shows that the enzyme remains complexed to the upstream portion of the promoter at position -21, whilst extending downstream with heteroduplex formation [36]. Dissociation of the polymerase from the promoter occurs at a nascent RNA length of approximately 8 nucleotides [36,37], a process known as *promoter clearance*, signifying the start of the elongation phase. Generally, 50% of all oligonucleotides produced in abortive synthesis are dinucleotides, irrespective of NTP concentration [35]. However, it is possible to get products up to 8bp long [35], contradicting crystallographic data on the T7 RNAP initiating complex, which indicates a maximum oligonucleotide transcript capacity of 3 bp in the enzyme active site, where the products gather before dissociation [38].

DNA *scrunching* is the favoured mechanism by which so many base-pairs can fit into a volume, which would at first glance appear too small. In this model, the polymerase is conformationally unaltered and the heteroduplex scrunches up inside [33]. Accumulated stress from this compressed DNA eventually forces the polymerase into an active state [39]. The capacity of the active site was evaluated through crystal studies performed by Cheetham *et al*. and indicated a maximum of 6-9 bp could be accommodated [33]. Other potential models addressing this spatial paradox are “inchworming”, in which the polymerase extends along the DNA template and alternatively, sliding of the polymerase along the template. These however, are considered unlikely candidates in light of both the crystallographic data [33] and single-molecule studies utilising FRET, whereby the distance between DNA and *E. coli* RNAP-immobilised fluorophores was monitored during transcription initiation [40]. Similarly, Skinner *et al.* used an optical tweezers arrangement to probe stability of the pre-initiation complex under varying levels of applied tension.

Observed destabilisation of the complex indicated a reduction in ability to accumulate the necessary scrunched DNA [41].

Following synthesis of each abortive product, the DNA remains complexed to the enzyme and the oligonucleotide dissociates from the DNA template and is ejected [35]. The rate of full run-off transcription (transcription where the elongation complex encounters the end of the template before a termination sequence) for a promoter relative to the other promoters in that genome is the promoter strength [42]. It has been shown that class III promoters are stronger than class II by a factor of 2-3, with 68%-75% of class III promoters entering run-off transcription, compared to 16%-36% [43]. However, there is a large strength distribution in the class II promoters, with some having strengths closer to that of class III [43].

### 1.3.3 Elongation

Eventually, the initiation complex progresses from abortive synthesis to create a more stable elongation complex [37]. This is accompanied by a conformational change in the enzyme, most notably in the location and orientation of the N-domain [44,45]. The conformational change involves a rotation of 220° and translation of 30Å by 6 α-helices and the intercalating hairpin into the promoter region of the initiation complex [46]. This promoter displacement severs the promoter-enzyme interactions and facilitates promoter clearance [44]. In addition to this change, residues 160-190 move by 70 Å to the opposite side of the enzyme, where they form a tunnel through which the nascent RNA exits [44].

During elongation, the number of RNA nucleotides in the heteroduplex was calculated by Huang and Sousa to be 7-8 [47], a value also predicted by Temiakov *et al.* [48]. This agrees with fluorescence characterization data from Liu and Martin, which indicates that the transcription bubble is 9 bp long [49].

It has been postulated that translocation arises in the form of a Brownian "flashing" ratchet, which operates in two steps [50,51]. In this model, NTP diffuses into the active site and is condensed onto the nascent RNA strand in a step assumed to be irreversible. Following this, the RNAP unbinds from the DNA and is free to relocate under the influence of thermal motion to place the 3' RNA terminus in position for further NTP incorporation. This provides the net downstream motion of translocation [50].

### 1.3.4 Termination

Transcription termination generally occurs at one of two classes of termination sequence [52]. At class I termination sites, often referred to as stem-loop termination sites, termination occurs during incorporation of a guanine residue, following a stem and loop structure and 6 uracil residues (Figure 1-5) [53]. Incorporation of the uracil sequence has been demonstrated to cause transcription pausing, thus may allow time for the stem-loop structure to form. It is believed that this structure interferes with the protein-RNA interactions, resulting in termination. However, influence on termination is not isolated to the termination site; Macdonald *et al.* demonstrated that the upstream sequence has a significant influence on termination efficiency [54].


**Figure 1-5 – Structure of the class I terminator, TΦ**
Class I termination site, TΦ, for T7 RNAP, which forms in nascent RNA strand. The stem and loop structure is clearly visible, ending with a sequence of 6 uracil residues (red) and terminating at a guanine residue (blue). Image adapted from [53].

Class II termination sites contain the nucleotide sequence, 5'-ATCTGTT-3', in the non-template DNA strand. Termination generally occurs 6-8 bp after this, providing the sequence is followed by incorporation of a run of uridine residues [52,55]. In the absence of the uridine repeat, a paused transcription state is more probable [52]. This termination sequence was initially isolated in human prepro-parathyroid hormone (PTH) and was shown to terminate T7 RNAP transcription by Mead *et al.* [56]. It is possible that class II termination accompanies a conformational change opposite to that undergone during the transition from the initiation to elongation complex [52]. This theory was given weight by Ma *et al.* who restricted intramolecular domain motion by substituting cysteine residues at Lys179 and Met750 to generate a disulphide *conformational lock*, which prevented termination [57].

## 1.4 Tools for studying torsional stress effects *in vitro*

Several well established single-molecule techniques exist which have the capability to extend individual DNA tethers; however, each has at least one significant problem that makes it unsuitable for torsional constraint of DNA whilst allowing transcription to be followed using fluorescently labelled enzymes. These methods are outlined here along with the associated advantages and disadvantages.

### 1.4.1 Laminar flow devices

Probably the simplest method for extending individual DNA tethers is through the application of hydrodynamic drag. Here, DNA is tethered to the interior surface of a microfluidic channel and exposed to a fluid flow; the hydrodynamic force from which extends the tether parallel to the flow direction [58–60]. This technique benefits from an ease of fabrication and wealth of published examples, with entire journals dedicated to the construction of microfluidic devices. In particular, the development of PDMS-based systems in the mid-1990s has facilitated complex channel configurations [61], which can be used to expose the sample to multiple different reagents without the need for direct interaction with the device [61].

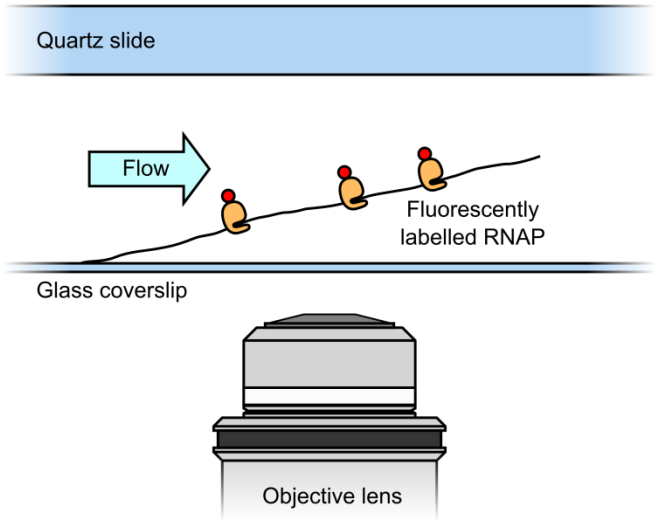


**Figure 1-6 – DNA extension using hydrodynamic drag**
The tether is attached at one end to the channel surface through antibody-ligand binding and is pulled straight via the drag it experiences from the fluid flow. This method allows high numerical aperture fluorescence microscopy of the sample, but is unable to exert torsional constraint on the DNA molecule.

Having the DNA tethered directly to the channel surface yields advantages, such as compatibility with the high numerical aperture Total Internal Reflection Fluorescence

(TIRF) microscopy technique (described in detail in Section 2.7.5) [59,60]. Implementation of this requires fluorophores to be within 100 nm of the channel surface to be sufficiently inside the evanescent field region (Section 2.7.5). Unfortunately, this approach is incompatible with torsional control of tethers, thus it is unsuitable for the desired application. Laminar flow extension has, however, been implemented for characterisation and optimisation of tethering and transcription assays (Section 5.2).

### 1.4.2 Optical tweezers and spanners

Extension of individual DNA molecules can also be achieved with an optical tweezers setup [62,63]. Here, force is transferred to the molecule by a pair of optically trapped dielectric microspheres, one either end of the tether (Figure 1-7) [64,65]. Attachment of the DNA molecule to the microspheres is achieved using unique antibody-ligand binding; for example, a digoxigenin-anti-digoxigenin linkage at one end of the tether and a biotin-streptavidin linkage at the other.

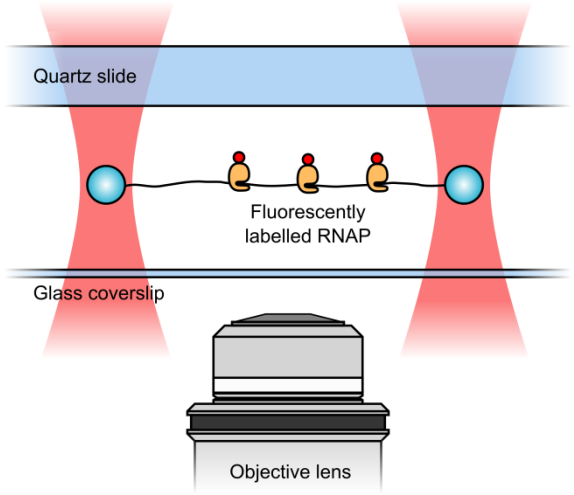


**Figure 1-7 – Extension of DNA using optical tweezers**
A single DNA molecule is tethered between two optically trapped microspheres. Since the microspheres experience a force directed towards the focal point of the trapping laser, a single DNA tether held between them can be extended. This technique is compatible with high numerical aperture fluorescence microscopy; however, application of torque is achieved through use of laser polarisation.

Optical tweezers are compatible with high numerical aperture microscopy techniques, such as TIRF microscopy (Section 2.7.5). Indeed, the standard configuration has the trapping lasers coupled into the sample via the objective lens, so inclusion of high numerical aperture oil-immersion optics represent not just a design improvement, but a necessity.

Coupling with such high precision microscopy permits spatial resolutions on the sub-nanometre scale; however, this precision is ultimately determined by factors such as laser stability, since fluctuations in the trapping laser result in noise, which can interfere with force measurements. In addition to this, optical tweezers are susceptible to localised sample heating, which can be especially deleterious when probing biological mechanics, due to the temperature dependency of enzymatic reactions, or on large time-scales (longer than a few seconds) where thermal expansion becomes significant [65].

$$F = -kx$$

**Equation 1-4 – Simple Hookean spring**
The equation of motion for a dielectric particle held in an optical trap, undergoing displacements with an amplitude less than 150 nm. This is a simple Hookean spring, where force (F) is linearly inversely proportional to the displacement (x). The trap stiffness is given by the spring constant (k).

Force acting on the trapped microsphere is linearly proportional to displacement from the centre of the trap for displacements less than 150 nm. Within this range of motion, the force response behaves like a simple Hookean spring and can be described by the relation shown in Equation 1-4. Since excessive particle displacement results in a loss of trap stability, force increases are obtained by increasing the trap stiffness, which in turn is achieved through an increase in the trap optical gradient or laser intensity [65,66]. The force range available in a standard configuration exceeds 100 pN [67,65], but with a lower limit of 0.1 pN imposed by the necessity to have a sufficiently high trap stiffness to ensure stability of the trapped particle [65]. It is also possible to apply torque to the beads through the implementation of a variety of methods, most of which require polarisation of the trapping laser or formation of a helical waveform [68,67,69]. Such an approach is further complicated by the convention to couple the laser into the sample through the objective lens [68,69], thus making torsional control about an axis parallel to the focal plane difficult. While this is necessary for the intended experiment, realisation of this method of torsional control is unnecessarily complex, since bead rotation can be more easily achieved using a magnetic tweezers assembly.

### 1.4.3 "Vertical" magnetic tweezers

In a magnetic tweezers assay, a superparamagnetic microsphere tethered through a single polymer, such as DNA, to a stationary surface is manipulated using force acting on it from an externally applied magnetic field. The origin of this force is described in detail in

Section 1.4.5; however, it is suffice to say at this point that the force experienced by the microsphere is proportional to its distance from the magnet field source and that alignment of the microsphere to this applied field permits rotational control. Such control is a feature not easily possible with the other techniques discussed in Sections 1.4.1 and 1.4.2 and is one of the key advantages of a magnetic tweezers system; however, this is reliant on the tether being restricted such that it cannot undergo free rotation relative to the microsphere. In the case of dsDNA this requires the molecule to be attached to both the stationary surface and microsphere through both strands. Consequently, it is not possible to torsionally constrain ssDNA, since the molecule can pivot around any number of backbone bonds. Although tethering of dsDNA through both strands is not covered here, a full method has been reported by Seol and Neuman [70].

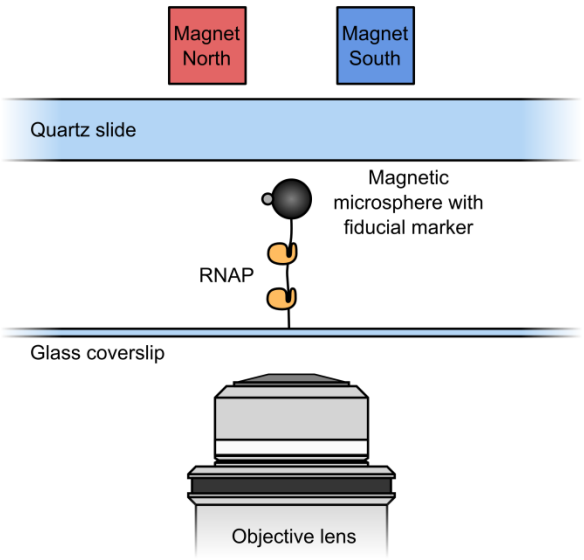


**Figure 1-8 – Magnetic tweezers in the "vertical" configuration**
The tethered molecule is attached at one end to the microfluidic channel surface and at the other to a superparamagnetic microsphere. In this configuration the microsphere is pulled away from the channel surface towards the region of highest flux density of an externally applied magnetic field, thus extending the tether by an amount determined by the magnitude of the force. Alignment of the microsphere to the applied field permits torsional control of both the microsphere itself and any torsionally constrained tether (such as DNA, bound to the microsphere through both strands).

The standard magnetic tweezers set-up is such that the microsphere is pulled directly away from the tethering surface in a configuration referred to here as the "vertical" system. Unlike the methods described in Sections 1.4.1 and 1.4.2, observation is along the axis of the DNA tether (Figure 1-8) and as such, direct observation of bound proteins is not possible. Instead, information on the system being probed is elucidated through monitoring of the magnetic microsphere position. Tether extension is inferred through

comparison of the interference pattern generated by the microsphere to calibrated reference images [71] and rotation is evaluated through observation of a fiducial marker attached to the side of the microsphere [5,72] (Figure 1-8). While this may be sufficient for experiments where action of the enzyme being investigated results in topological changes in the substrate, it is not possible to easily determine inter-enzyme spacing or rates of movement along the substrate.

### 1.4.4 "Horizontal" magnetic tweezers

Although the majority of magnetic tweezer systems adopt the vertical configuration described in Section 1.4.3 there are a few examples of systems designed to be run horizontally. These systems utilise the same basic principle as for vertical magnetic tweezers, whereby a single tether is extended between a stationary surface and a superparamagnetic microsphere moving in response to an applied magnetic field. However, unlike the vertical configuration, the tether is extended in the focal plane of the objective lens. This affords the notable advantage of permitting both real-time observation of enzyme motion along the tethering substrate, as with laminar flow extension (Section 1.4.1) and optical tweezers (Section 1.4.2), whilst maintaining the capacity of vertical magnetic tweezers for torsional control of the tether (Section 1.4.3). As highlighted by Neuman *et al.* in their review of single-molecule micromanipulation techniques, despite suffering from a lower resolution than optical tweezers (0.1 - 5 nm for optical tweezers compared to 2 – 10 nm for magnetic tweezers), magnetic tweezers benefit from a significantly larger applicable force range (0.1 – 100 pN for optical tweezers compared to 0.001 – 10000 pN for magnetic tweezers) [73].

#### 1.4.4.1 Existing horizontal magnetic tweezer approaches

Currently, no standard configuration for a horizontal magnetic tweezers microscope exists, with relatively few systems having thus far been published. Scrutiny of those approaches which have been reported highlights common compromises. One of the earliest examples was reported by Danilowicz et al., who formed DNA tethers between superparamagnetic microspheres (2.8 μm diameter) and the antibody-functionalised surface of a cylindrical capillary (330 μm diameter) [74]. This assembly was placed inside a square microcell (600 μm cross-section), which permitted fluidic sample delivery and buffer exchange. Force was applied using a stack of five permanent magnets (each 6.4 x 6.4 x 2.5 $mm^3$)

placed to one side of the microcell and the corresponding superparamagnetic microsphere response observed using a 10x objective lens (NA = 0.25) placed underneath the sample (Figure 1-9a). Although not explicitly stated, the low resolving power of the optics indicates a long working distance and was likely a compromise designed to permit both a large observable region and close proximity of the magnet stack and sample. While this allowed forces up to 30 pN to be measured simultaneously for dozens of tethers, the low magnification of the microscope corresponded to a severe limitation for applications other than that reported.

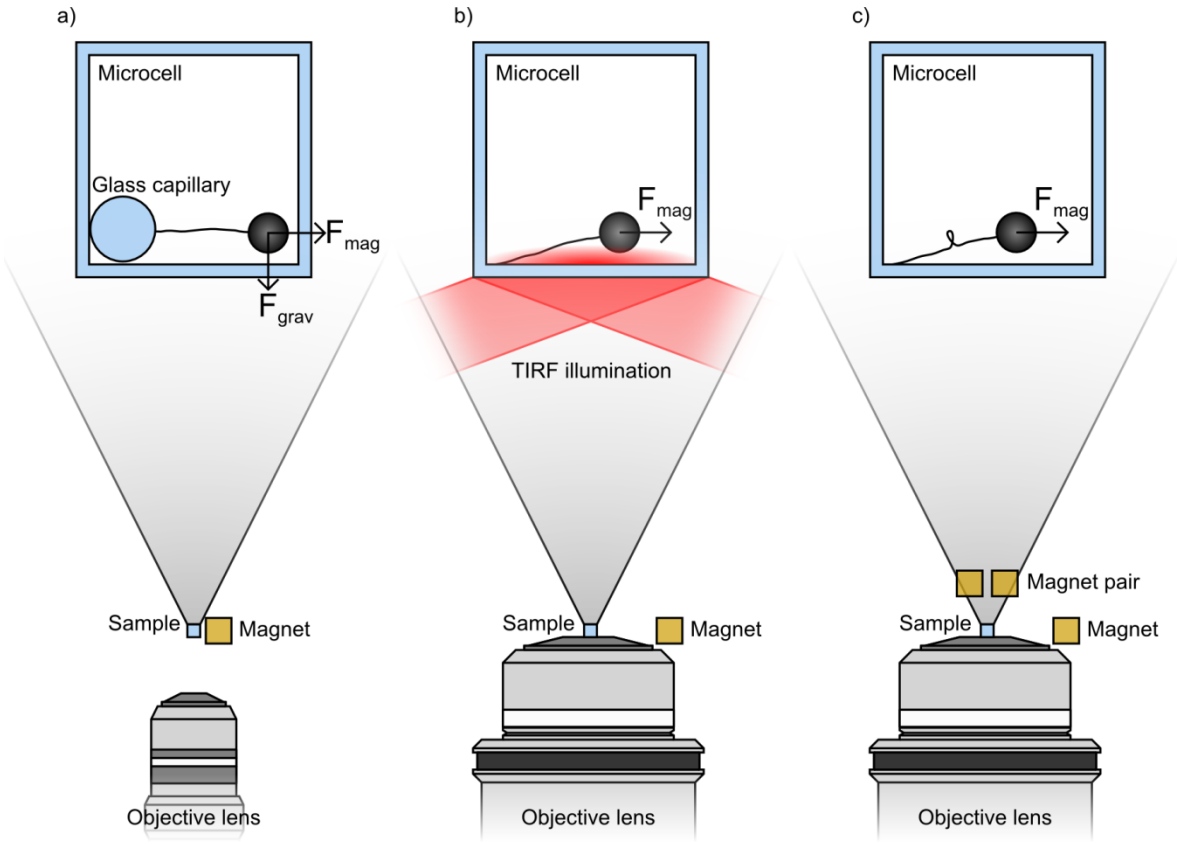


**Figure 1-9 – Example configurations for a horizontal magnetic tweezers microscope**
a) Tethers immobilised on an antibody-functionalised glass capillary inner surface and extended horizontally using a stack of permanent magnets [74]. Use of a low-magnification objective lens allows close proximity between the magnets and sample, thus higher force application. b) Evolution of the design shown in pane a) with attachment of the tether to the lower microcell surface, prompting compatibility with TIRF illumination [75] in addition to epifluorescence [76]. Use of oil-immersion objective lenses tends to restrict application of force to the low piconewton range. c) Combination of vertical and horizontal magnet configurations allows initial coiling of DNA followed by lateral extension [77]. As with the TIRF implementation, this system precludes observation of truly horizontal tethers.

The Danilowicz *et al.* compromise of low magnification in favour of high force application was reversed in a similar design reported by Graham *et al.* [76]. In this system tethers were formed directly onto the microcell surface (1 mm cross-section; VitroCells; VitroCom, New Jersey, USA) and imaged from below using a 60x magnification oil-immersion

objective lens (NA = 1.25; PlanApo; Olympus, Melville, New York, USA) and epifluorescence illumination. The superparamagnetic microsphere (M-280; Invitrogen, California, USA) was manipulated using a stack of four cubic NdFeB magnets (12.7 mm cross-section) held perpendicular to the objective lens optical axis on the end of a micromanipulator. With this configuration, forces up to 3 pN were tested; higher force application may have been possible, but was not stated. Nonetheless, a relatively low force limit is a likely consequence of spatial restrictions imposed by the oil-immersion objective lens.

Through use of an EMCCD camera (iXon; Andor Technology plc., Belfast, Northern Ireland), Graham *et al.* were able to observe dsDNA-binding by the proteins Fis, HU and NHP6A with a high signal to noise ratio [76]; however, epifluorescence illumination ultimately limits the contrast possible through significant bulk fluorescence excitation. This can be addressed via implementation of Total Internal Reflection Fluorescence (TIRF) microscopy (described in Section 2.7.5) as demonstrated by Schwarz *et al.* [75] (Figure 1-9b). Fundamentally, the microscope configuration is near-identical to that reported by Graham *et al.*, but with tethers formed from the lower surface, permitting TIRF illumination. This is only a partial solution however, since the finite microsphere diameter will result in non-horizontal tether inclination and limit the amount of DNA within the fluorescence excitation region. For typical 1 µm diameter microspheres, only one fifth of the tether will be within the 100 nm evanescent field. While the exponential field decay will likely result in observation beyond this range, a significant variation in fluorescence will be evident. This would make molecular tracking and stoichiometry determination difficult. Similar to the epifluorescence system, this method also suffers from limited force generation, with the highest reported value being 1.5 pN when using a single cubic permanent magnet (5 x 5 x 1 $mm^3$; Q-05-05-01-HN; Supermagnete, Gottmadingen, Germany).

Horizontal tethers in a magnetic tweezers system have also been demonstrated through DNA attachment to the edge of functionalised microscope slides and coverslips [78–80]. While this addresses the aforementioned problem of out-of-focus regions of the tether, issues relating to the uneven tethering substrate edges are introduced. Even at minimal coverslip thicknesses of approximately 80 µm, there will still be significant optical distortion from defocussed regions of the substrate. Such effects can be seen in the

supplementary information of Zhang, *et al.* [80], where the full extent of a 7249 bp tether is obscured by diffraction of the tethering substrate (in this case, a microscope slide). For the purpose of inferring enzymatic action purely through microsphere motion, as with the vertical magnetic tweezers system, these distortions shouldn't pose a significant problem; however, they are much more serious when fluorescently labelled enzymes are to be observed binding to the DNA.

A permanent magnet tweezer system has also been reported by van Loenhout *et al.* [77]. They used a standard vertical configuration to initially twist DNA, but with a second magnet to pull the coiled tether horizontally (Figure 1-9c). This has been used in conjunction with the fluorescent dye Cy3 to view plectoneme formation in DNA. While demonstrated using epifluorescence, such a configuration is not too dissimilar to that described by Schwarz *et al.* [75], unlocking the potential for implementation of TIRF microscopy. As with the methods of Graham *et al.* and Schwarz *et al.*, lateral forces appear to be restricted, with magnitudes no greater than 3.2 pN reported.

An alternative approach to realisation of a horizontal magnetic tweezers configuration is to use electromagnets; an early example of which was the implementation by Haber and Wirtz, which used large electromagnetic coils (8 cm in diameter) placed either side of the sample to generate a relatively uniform magnetic field [81] (Figure 1-10). While this configuration was reported to yield field gradients of 100 T/m, corresponding to forces of ~15 pN (using M280 superparamagnetic microspheres; Invitrogen, California, USA), it was contingent on a coil to coil spacing of 15 mm. Such a configuration was not possible with the water-immersion objective used, thus necessitating a larger spacing and limiting reported forces to ~1.7 pN. Furthermore, resistive heating of the coils required implementation of an active water-cooling system; a problem characteristic of electromagnets [65,81]. The relatively low field generation, compared to permanent magnets, and the necessity for complex infrastructure makes the basic implementation of electromagnets unattractive.

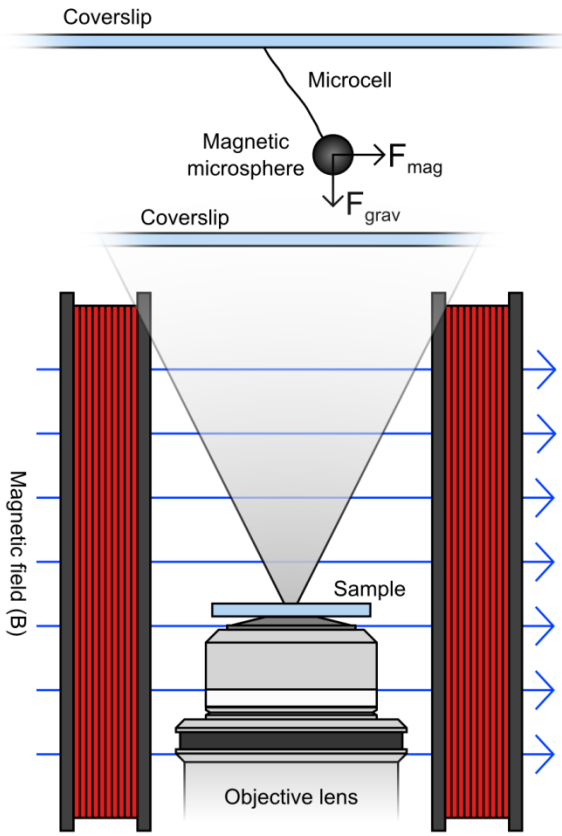


**Figure 1-10 – Early configuration of electromagnetic tweezers**
Lateral force application in a horizontal magnetic tweezers microscope using electromagnetic coils either side of the sample [81]. Such an approach allows for easy computational control of field gradients; however it suffers from excessive heat, generated by resistive heating of the coils, and a relatively low field compared to permanent magnets.

Through implementation of micro-fabricated electromagnets, Chiou *et al.* were able to achieve three-dimensional control of magnetic substrates [82]. Demonstrating an evolution of the configuration of Haber and Wirtz [81], this configuration was reported to benefit from reduced heat generation and produce applied forces exceeding 20 pN when acting on 2.8 µm diameter superparamagnetic M280 microspheres. Furthermore, through placement of the electromagnets above the sample, the approach was compatible with high numerical aperture microscopy and epifluorescence illumination [82]. Arguably, such a system may justify the initial outlay of resources if complex sample manipulation is required. However, the technology represents a higher order of magnetic tweezers construction, requiring clean-room component fabrication using expensive equipment, somewhat minimising the advantage over the optical spanner described in Section 1.4.2. Notably, neither electromagnetic tweezer configuration discussed used DNA substrates tethered to vertical surfaces, thus resulting in non-horizontal extension of the tether.

### 1.4.5 Fundamentals of a magnetic tweezers microscope

Magnetic tweezers utilise the force experienced by a superparamagnetic microsphere in response to application of an external magnetic field in order to extend individual polymer tethers (Figure 1-8). These microspheres are comprised of $Fe_2O_3$ nanoparticles [83], each encompassing a single magnetic domain, embedded in a polystyrene sphere (Figure 1-11). In the absence of an externally applied magnetic field the magnetic domains adopt random orientations and the microsphere has no net magnetisation (Figure 1-11a). As the magnitude of the externally applied field increases, the magnetisation begins to align with the field, thus resulting in a net magnetisation of the microsphere itself (Figure 1-11b). This effect increases up to the point where all the domains are perfectly aligned with the external field and the microsphere magnetisation reaches saturation (Figure 1-11c).

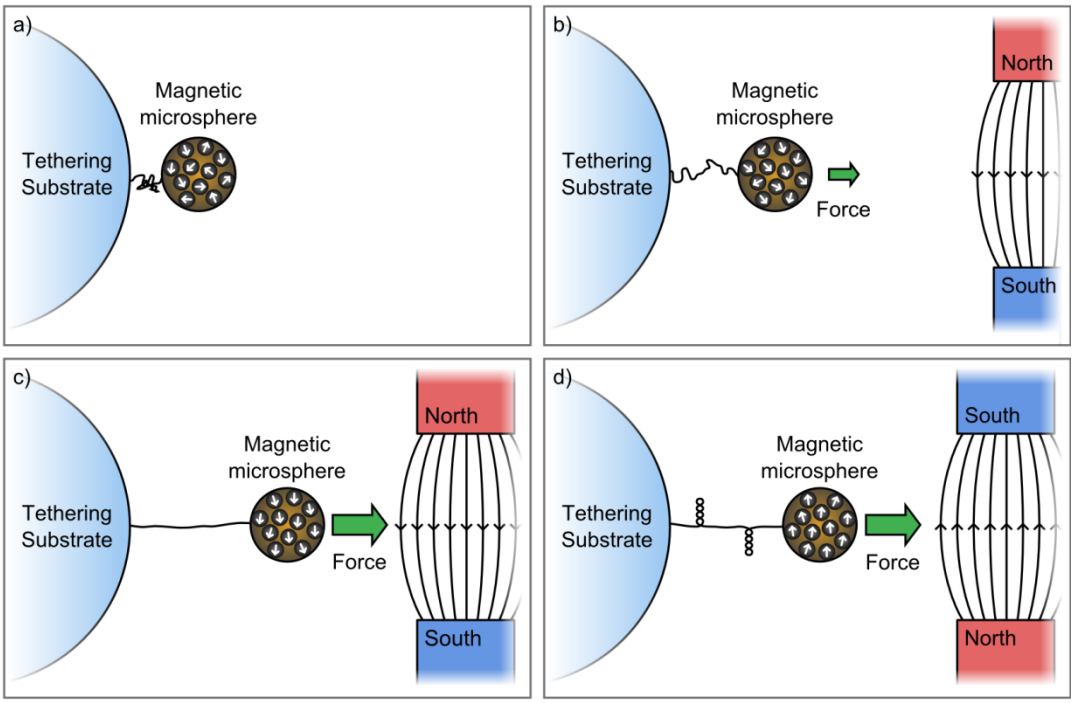


**Figure 1-11 – Magnetisation of superparamagnetic microspheres**
Individual magnetic domains (white arrows) within the superparamagnetic microsphere align in response to application of an external magnetic field (*B*). a) In the absence of an external field the domains adopt random orientations and the microsphere has no net magnetisation. b) Upon the presence of a slight magnetic field the domains begin to align and the microsphere gains a net magnetisation. This causes the microsphere to be attracted towards the region of highest magnetic flux density. c) As the magnets move closer to the microsphere the domains align further until they reach a saturation point and the microsphere magnetisation can increase no further. d) The presence of some fixed domains gives the microsphere a preferred magnetisation direction, which it will align with the external field. Rotation of the field will be mirrored by corresponding rotation of the microsphere, thus yielding the ability to control the torsion of the tethering molecule (assuming it is unable to rotate independently of the microsphere).

Importantly, in reality not all domain magnetisations are free to rotate and thus the microsphere has an intrinsic preferred magnetisation direction; as a result, the microsphere will rotate to align this preferred direction with the external field (Figure 1-11d). This

alignment to the external field yields one of the key benefits of a magnetic tweezers setup; namely, the ability to manipulate microsphere rotation, and as an extension of this, the torsion of any polymers attached in such a way that they are unable to achieve rotation independent of the microsphere.

## 1.5 Aims and objectives

The primary aim of this work is to probe the effect of transcription-coupled DNA supercoiling at the single-molecule level. Such work has substantial biological relevance, since RNAP is an enzyme present across all domains of life, from the single subunit polymerase of the bacteriophage T7 virus to complex, multi-subunit polymerases found in eukaryotes. Intrinsic to the mechanism of transcription is a local change in substrate DNA torsion, described by the twin supercoiled domain model. This localised torsional change has been shown to rapidly accumulate due to a range of interactions and rotational restrictions present *in vivo* and as such is recognised as playing an important genetic regulatory role. Despite this, experiments conducted *in vitro*, where the aforementioned rotational restrictions occur to a lesser degree, are often conducted without detailed understanding of the topological state of the substrate DNA.

Several methods to manipulate individual DNA molecule extension whilst permitting simultaneous single-molecule fluorescence observation have been reported. Despite this, there is no easily-applicable, standardised approach for applying quantifiable template torsion. The emerging trend is to adapt the established technique of magnetic tweezers, in which DNA is extended orthogonally from the tethering substrate, to permit extension within the observable plane of the microscope. However, limitations in the relatively few published techniques arise from the need to strike a balance between three main factors: maximum achievable force, optical spatial resolution and the capacity to generate truly horizontal tethers. Compromise between force and resolution is necessary since short sample-to-magnet separations are required for high force application, yet such positioning is generally precluded by the large objective lenses used for high numerical aperture microscopy. Similarly, high spatial resolution and horizontal tethers have thus far been mutually exclusive, with inclined extension from the lower sample surface used in conjunction with total internal reflection fluorescence (TIRF) microscopy.

Evidently, there is a need for an easily implementable approach to facilitate single-molecule fluorescence experiments to be conducted on torsionally-constrained and characterisable DNA tethers. This can be realised through implementation of design alterations to the previously reported horizontal magnetic tweezer configurations. Firstly, use of thin microfluidic cells (< 10 μm) in which experiments are conducted limits bulk fluorescence excitation, thus facilitating use of epi-fluorescence illumination, as opposed to spatially-restricted approaches like TIRF. As a result, tethers can be extended horizontally in the centre of the sample chamber, rather than attached to the lower surface and extended at an angle. Secondly, use of a long-working distance objective lens to permit reduced sample to magnet separations increases the applicable force range dramatically. Finally, use of nanoscale-diameter fluorescent probes (TransFluoSpheres; Invitrogen, Carlsbad, California, USA), rather than individual fluorophores, reduces the deleterious effects of sample photobleaching. Additionally, the relatively large quantity of fluorophore present in a single TransFluoSphere further facilitates implementation of epi-illumination, where reductions in signal-to-noise ratio relative to TIRF are inevitable.

To achieve implementation of a novel horizontal magnetic tweezers microscope and investigate transcription-coupled DNA supercoiling requires realisation of the following experimental objectives:

- Produce fluorescently-labelled RNAP and demonstrate enzymatic activity through bulk transcription assays (Chapter 2).
- Prepare DNA substrates compatible with micromanipulation; requirements for which are unique functionalisation at either end and also functionalisation of termini in both single-strands if torsional control is necessary (Chapter 2).
- Demonstrate the ability to form multiple stable transcription complexes on DNA substrates (Chapter 3).
- Design and construction of a horizontal magnetic tweezers microscope capable of simultaneous single-molecule fluorescence detection and precise control of DNA extension and torsion. Specifically, this necessitates opto-mechanical design, development of a particle tracking system for force calibration, and development of a suitable tethering substrate (Chapter 4).
- Characterise force transduction in the magnetic tweezers microscope through both application of equipartition analysis to observed tethered microsphere motion and measurement of DNA extension as a function of applied force (Chapter 4).

- Characterise optical components of the magnetic tweezers microscope; in particular, mechanical noise in bright-field images, optical magnification and sensitivity of fluorescence detection (Chapter 4).
- Develop a microfluidic system compatible with TIRF microscopy, thus facilitating implementation of single-molecule transcription assays on flow-extended DNA tethers and high signal-to-noise fluorescence imaging (Chapter 5).
- Optimise conditions for single-molecule transcription assays using TIRF microscopy; in particular, minimising the fluorophore concentration to reduce fluorescence background and limit photocleavage of DNA tethers (Chapter 5).

# Materials and methods

## Chapter 2

Throughout the thesis, error in measurement has been reported as standard error, along with the number of measurements taken (n), unless stated otherwise.

## 2.1 Buffers and reagents

**Table 2-1 – Standard buffers used in the described experiments**
All mixtures are for the 1x concentration; usage in experimental conditions may require higher concentrations as stated in the text.

| **Buffer or reagent** | **Components** |
|---|---|
| AFM buffer | 4 mM HEPES, 10 mM NaCl, 2 mM $MgCl_2$. Adjusted to pH 7.4. |
| Agarose gel loading buffer | 10 mM Tris-HCl, 50 mM EDTA, 0.025% bromophenol blue, 60% glycerol. Adjusted to pH 7.6. |
| BSA coat | 10 mM Tris, 172 mM NaCl, 1 mM EDTA, 15 µM acetylated BSA. Adjusted to pH 8.0. |
| Dialysis buffer for protein purification and biotinylation | 5 ml 1 M $NaH_2PO_4$, 35 ml 1 M $Na_2HPO_4$, 60 ml 5 M NaCl, 2 ml 0.5 M EDTA, 1 ml 1 M DTT and 897 ml ultra-pure water (18.2 MΩ•cm; Purelab Ultra; Elga, Marlow, UK). Adjusted to pH 7.7. |
| Elution buffer for protein preparation | 5 ml 1 M $NaH_2PO_4$, 35 ml 1 M $Na_2HPO_4$, 60 ml 5 M NaCl, 500 ml 1 M imidazole, 365 µl 13.7 M β-mercaptoethanol (added immediately prior to use) and 400 ml ultra-pure water. Adjusted to pH 7.7. |
| Equilibration buffer for avidin column | 200 mM NaCl, 10 mM Tris, 1 mM EDTA, 1 mM DTT and made to 50 ml with ultrapure water. |
| Lysogeny broth (LB) | 10 g 1% tryptone, 5 g yeast extract, 10 g NaCl and made to 1 L using ultra-pure water and adjusted to pH 7.5. |
| Lysis buffer for protein purification | 5 ml 1 M $NaH_2PO_4$, 35 ml 1 M $Na_2HPO_4$, 60 ml 5 M NaCl, 10 ml 1 M imidazole, 10 mg bacitracin (added immediately prior to use), 16 mg benzamidine (added immediately prior to use) and 890 ml ultra-pure water. This was adjusted to pH 7.7. |
| Qiagen elution buffer (EB) | 50 mM Tris-HCl (pH 8.1-8.2), 1.4 M NaCl. |

| | |
|---|---|
| SDS PAGE loading buffer | 50 mM Tris-HCl (pH 6.8), 100 mM DTT, 2% (w/v) SDS, 0.1% (w/v) bromophenol blue and 10% (w/v) glycerol. |
| SDS PAGE running buffer | 25 mM Tris, 264 mM glycine and 0.1% (w/v) SDS. |
| SDS PAGE stain | 0.25 g Coomassie Brilliant Blue R250 in 90 ml 1:1 methanol:ultra-pure water and 10 ml glacial acetic acid. Solution filtered through Whatman No. 1 filter (GE Healthcare, Little Chalfont, UK). |
| Protein storage buffer | 5 ml 1 M $NaH_2PO_4$, 35 ml 1 M $Na_2HPO_4$, 60 ml 5 M NaCl, 2 ml 0.5 M EDTA, 1 ml 1 M DTT and 897 ml ultra-pure water. Adjusted to pH 7.7. |
| T7 RNAP transcription buffer | 40 mM Tris-HCl, 10 mM NaCl, 6 mM $MgCl_2$. Adjusted to pH 7.7. |
| TAE electrophoresis buffer | 20 mM acetic acid, 40 mM Tris, 1 mM EDTA. Adjusted to pH 8.0. |
| TBE electrophoresis buffer | 90 mM Tris base, 90 mM boric acid and 2 mM EDTA, made up using ultra-pure water. |
| Tethering buffer (TetBu+) | 10 mM Tris, 172 mM NaCl, 1 mM EDTA, 1.5 μM acetylated BSA. Adjusted to pH 8.0. |
| Transcription stop buffer | 100 μl formaldehyde, 5 mM EDTA, bromophenol blue. |
| Tris-EDTA buffer (TE) | 10 mM Tris, 1 mM EDTA in ultrapure water. Adjusted to pH 8.0. |
| Wash buffer for protein purification | 5 ml 1 M $NaH_2PO_4$, 35 ml $Na_2HPO_4$, 60 ml 5 M NaCl, 50 ml 1 M imidazole, 365 μl 13.7 M β-mercaptoethanol (added immediately prior to use) and 850 ml ultra-pure water. Adjusted to pH 7.7. |

## 2.2 Primers

Primers used in all experiments are included in Table 2-2. They were all purchased from MWG Eurofins and are written in the 5'-3' orientation.

**Table 2-2 – List of primers used in the described experiments**
Each primer sequence is listed along with the intended sequence and key features, such as restriction sites introduced.

| **Primer name** | **Primer sequence** | **Key features** |
|---|---|---|
| CGB31 | CCCCAAGCTTCATCTTGTCA GATGAGACTACCCCTCTGAA | Anneals to bacteriophage T7 DNA. Introduces restriction site for HindIII. |
| phi13_600rev | GCGGATCCTTCTGGATGTTC GTCTGCCTCATG | Anneals to bacteriophage T7 DNA. Introduces restriction site for BamHI. |
| SJC01 | CCCCGTCGACCATCTTGTCA GATGAGACTACCCCTCTGAA | Anneals to pUC-Φ600 DNA. Introduces SalI |
| SJC02 | GGGGCCATGGCCTGAGCGCC AGATATAGCGATAGG | Anneals to pUC-Φ600 DNA. Introduces NcoI |

## 2.3 Preparation of DNA templates and end-labelling

### 2.3.1 Production of the pUC-Φ600 DNA template

A key component of pSJC-Φ13, the DNA template for transcription studies (Section 2.3.5), is pUC-Φ600 (Figure 2-1). Preparation of pUC-Φ600 was carried out by Ann-Josée Noël. The 3933 bp long pUC-Φ600 plasmid is a hybrid of pUC-19 and the Φ13 T7 RNAP promoter region of T7 DNA (Yorkshire Biosciences Ltd., York, UK).

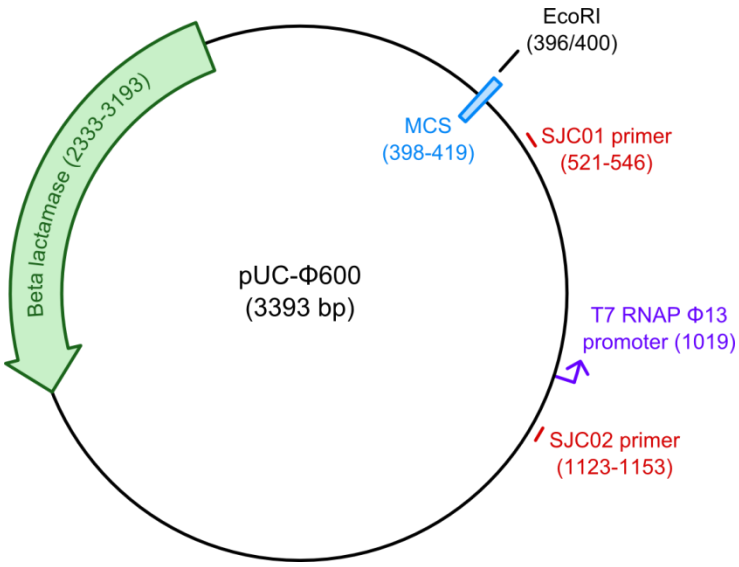


**Figure 2-1 – Plasmid map for pUC-Φ600 showing key locations**
Highlighted is the EcoRI restriction site within the multiple cloning site (MCS), the annealing locations for primers SJC01 and SJC02 used for PCR preparation of PCR pUC-Φ600, the T7 RNAP Φ13 promoter and the beta lactamase gene, responsible for ampicillin resistance. The full plasmid length is 3393 bp.

The Φ13 promoter region of T7 DNA was PCR amplified using the forward primer CGB31 and reverse primer phi13_600rev (see Section 2.6.2 for PCR protocol and Section 2.2 for primer sequences) to yield a product with HindIII and BamHI endonuclease restriction sites at either end, which have counterparts in plasmid pUC-19. Sequencing was used to verify the integrity of the PCR product. Both the PCR product and pUC-19 were digested with HindIII (New England Biolabs, Massachusetts, USA) and BamHI (New England Biolabs, Massachusetts, USA) and mixed to allow annealing of "sticky ends". T4 DNA ligase (New England Biolabs, Massachusetts, USA) was used to ligate nicks in the sugar-phosphate backbone. The full pUC-Φ600 sequence is included in Appendix D-I.

New stocks of pUC-Φ600 were prepared by amplifying in DH5α *E. coli* cells with 100 μg/ml ampicillin selection (see Section 2.6.1 for protocol). Three colonies were grown

and each subsequently divided in half for plasmid purification. The integrity of all six new stocks was verified using a 1% agarose gel stained with SybrSafe (Invitrogen, Carlsbad, California, USA) (Figure 2-2), onto which 2 µl of each plasmid was loaded, with all the samples diluted using 2 µl loading buffer (Yorkshire Biosciences Ltd., York, UK). For reference, 10µl of Q-Step 4 DNA ladder (Yorkshire Biosciences Ltd., York, UK) was also loaded. Through comparison of the sample band intensities on the gel with those of the ladder using ImageJ [84–88], plasmid concentrations of approximately 511 nM ± 18 nM (n = 6) were determined.

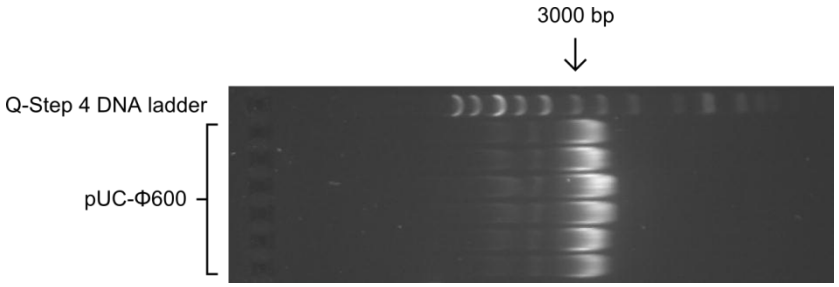


**Figure 2-2 – Verification of pUC-Φ600 production using a 1% agarose gel**
Three colonies from transformation of the plasmid into DH5α E. coli cells were grown, with each sample divided in two for purification, thus yielding the six samples on the gel. An average sample concentration was measured to be 511 ± 18 nM (n = 6). The bands are quite broad, which is due to the presence of various levels of superhelical density in the sample, with more twisted samples occupying a smaller volume and thus exhibiting improved motility through the gel.

### 2.3.2 Linearisation of pUC-Φ600 with EcoRI for bulk transcription assays

When conducting bulk transcription assays to confirm the correct DNA sequence for the Φ13 T7 RNAP promoter (see Section 2.3.8) or activity of produced T7 RNAP (see Sections 2.4.1 and 2.4.1.2) EcoRI-digested pUC-Φ600 is used as a positive control. This linearised plasmid yields RNA products 602 bases in length, which are easy to visualise on 6% urea acrylamide gels. To linearise pUC-Φ600 the reaction mixture is: 15µl 50 nM pUC-Φ600 (18.75 nM final concentration), 4 µl Buffer H (Promega, Wisconsin, USA), 0.2 µl acetylated BSA (B8894; Sigma-Aldrich, Missouri, USA) and 1 µl 12 U/µl EcoRI endonuclease (Promega, Wisconsin, USA), made up to a 40 µl final volume with 19.8 µl of ultra-pure water. Depending on the stock DNA concentration the volumes of DNA and water can be varied accordingly. The mixture is incubated at 37°C overnight and quenched via the addition of 4µl 0.5 M EDTA.

### 2.3.3 Production of the PCR pUC-Φ600 DNA template

Transcription assay verification of RNA polymerase activity (Section 2.4.1.3) requires a short DNA template (<1000 bp). A 100-fold dilution of plasmid pUC-Φ600 (production described in Section 2.3.1) in EB (Section 2.1) is amplified via PCR using primers SJC01 and SJC02 (see Section 2.6.2 for PCR protocol and Section 2.2 for primer sequences) to yield an amplified sequence of 652 bp. This product is purified using a QIAquick PCR purification spin column (Qiagen, Netherlands) and sample homogeneity demonstrated using a 1% agarose gel stained with SybrSafe (Invitrogen, Carlsbad, California, USA) (Figure 2-3) onto which 10 µl of Q-Step 4 DNA ladder (Yorkshire Biosciences Ltd., York, UK), 5 µl PCR pUC-Φ600 and 1 µl pUC-Φ600 were loaded. The PCR pUC-Φ600 sample was diluted using 2 µl loading buffer (Yorkshire Biosciences Ltd., York, UK) and 3 µl ultra-pure water (18.2 MΩ•cm; Purelab Ultra; Elga, Marlow, UK) and the pUC-Φ600 reference sample was diluted using 2 µl loading buffer and 2 µl water. Analysis of the gel using ImageJ [84–88] yielded a PCR pUC-Φ600 concentration of 179 nM. The full PCR pUC-Φ600 sequence is included in Appendix D-II

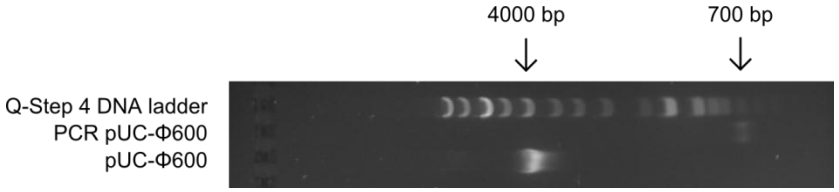


**Figure 2-3 – Verification of PCR pUC-Φ600 production using a 1% agarose gel**
A sample of the template pUC-Φ600 is also run to show a degraded sample had not been used. The estimated DNA lengths for two key bands on the ladder have been highlighted. Both samples run at the expected relative locations of 3000-4000 bp for pUC-Φ600 and 500-600 bp for PCR pUC-Φ600. Analysis of the PCR pUC-Φ600 band intensity yields an approximate sample concentration of 179 nM.

### 2.3.4 Production of the pSR-550 DNA template

The second key component of pSJC-Φ13 is the plasmid pSR-550. This 12,460 bp plasmid was provided by Marjan van der Woude and was chosen for its lack of T7 RNAP termination sequences.

Prior to production of pSJC-Φ13, new stocks of pSR-550 were prepared using DH5α *E. coli* cells with 100 µg/ml ampicillin selection (see Section 2.6.1 for protocol). As was the case with pUC-Φ600, three colonies from the transformed cells were grown and each subsequently divided in half for purification. A 1% agarose (in TAE buffer) gel stained with SybrSafe (Invitrogen, Carlsbad, California, USA) (Figure 2-5) was used to

demonstrate plasmid production. Each sample on the gel contained 2 µl of DNA and 2 µl loading buffer (Yorkshire Biosciences Ltd., York, UK). For reference, 10µl of Q-Step 4 DNA ladder (Yorkshire Biosciences Ltd., York, UK) was also loaded. Through comparison of the sample band intensities on the gel with those of the ladder using ImageJ [84–88], plasmid concentrations of approximately 24 ± 2 nM (n = 6) were determined. The full pSR-550 sequence is included in Appendix D-III.

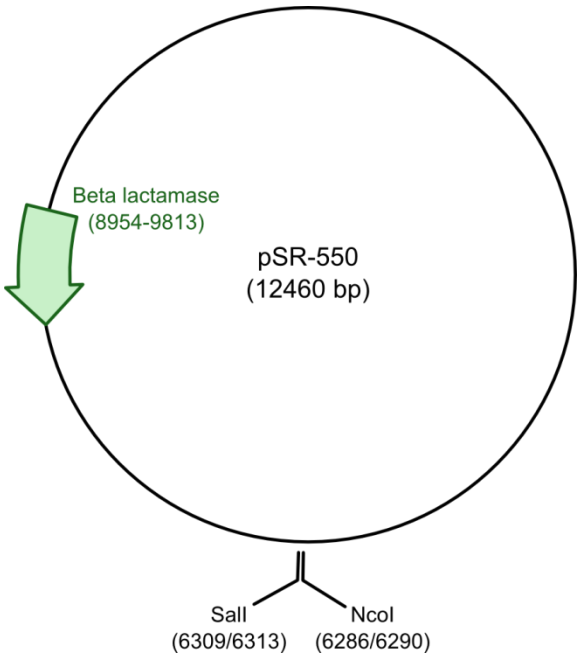


**Figure 2-4 – Plasmid map for pSR-550 showing key locations**
Restriction sites SalI and NcoI cut the DNA 23 bp apart to allow insertion of the PCR pUC-Φ600 fragment. The beta lactamase gene is responsible for ampicillin resistance.

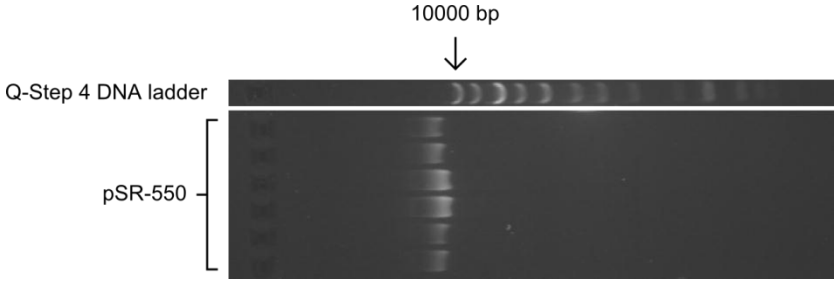


**Figure 2-5 – Agarose gel electrophoresis of new pSR-550 stocks**
Demonstrating the quality and production of cloned pUC-Φ600 and pSR-550 DNA stocks. There is some variation in the sample concentrations; however, all samples show a single bright band thus indicating good plasmid quantities. An average sample concentration was measured to be 24 ± 2 nM (n = 6). The gel has been digitally cut to remove irrelevant bands.

### 2.3.5 Production of the pSJC-Φ13 DNA template

Plasmid pSJC-Φ13 was prepared using the T7 RNAP Φ13 promoter region of the pUC-Φ600 plasmid (production described in Section 2.3.1) and the majority of the pSR-

550 plasmid (12,460 bp; provided by Marjan van der Woude, Department of Biology, University of York), chosen for its lack of T7 RNAP termination sequences. A map of the pSJC-Φ13 sequence is shown in Figure 2-6. BLASTn analysis of the proposed sequence showed it to contain just one promoter and no termination sequences for T7 RNAP. An overview of pSJC-Φ13 production is given in Figure 2-7.

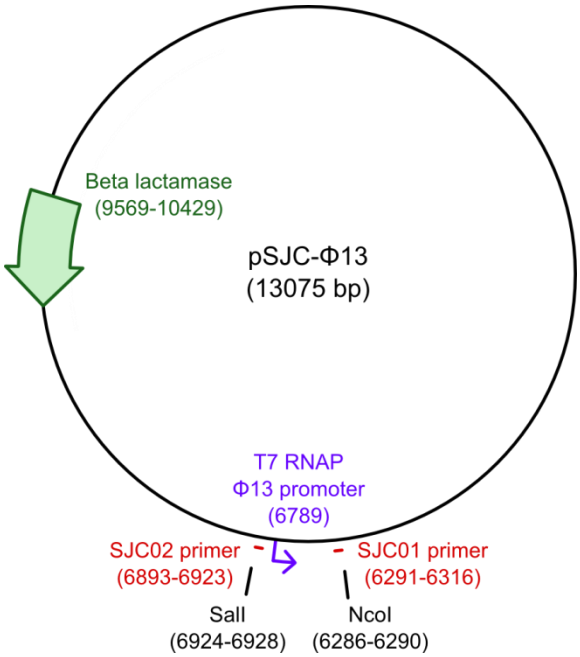


**Figure 2-6 – Map of the pSJC-Φ13 DNA sequence with key regions highlighted**
The NcoI and SalI restriction sites are remnants from ligation of the two precursor sequences; these were introduced to the pUC-Φ600 PCR product via the primers SJC01 and SJC02. Complimentary sequences to both primers are present in pSJC-Φ13, which is useful for verification of the successful ligation of both pSR-550 and pUC-Φ600. A single T7 RNAP promoter is present in the produced plasmid. The beta lactamase gene is responsible for ampicillin resistance.

The 652 bp sequence containing the T7 RNAP Φ13 promoter was extracted from pUC-φ600 via PCR using primers SJC01 and SJC02 (Figure 2-7b) (Section 2.3.2). These primers introduce restriction sites SalI and NcoI at either end of the amplified sequence (Figure 2-7b); they were chosen due to digestion leaving 3'-overhang "sticky ends" and for the presence of counterpart restriction sites in pSR-550.

Both PCR pUC-Φ600 and pSR-500 need to be digested at NcoI and SalI restriction sites for later ligation. First, the two samples were digested with NcoI using the following protocols. For PCR pUC-Φ600 the reaction mixture was: 30 µl 179 nM DNA (150 nM final concentration), 1.2 µl 10 U/µl NcoI (New England Biolabs, Massachusetts, USA), 3.6 µl NEB Buffer 3 (New England Biolabs, Massachusetts, USA), 1.2 µl ultra-pure water. The reaction mixture was incubated at 37 °C overnight, with digestion subsequently

quenched by addition of 2 µl 0.5 M EDTA. Similarly, the pSR-550 reaction was: 50 µl 24 nM DNA (20 nM final concentration), 2 µl 10 U/µl NcoI (New England Biolabs, Massachusetts, USA), 6 µl NEB Buffer 3 (New England Biolabs, Massachusetts, USA), 2 µl ultra-pure water (18.2 MΩ•cm; Purelab Ultra; Elga, Marlow, UK). The reaction mixture was incubated at 37 °C overnight, with digestion subsequently quenched by addition of 2 µl 0.5 M EDTA.

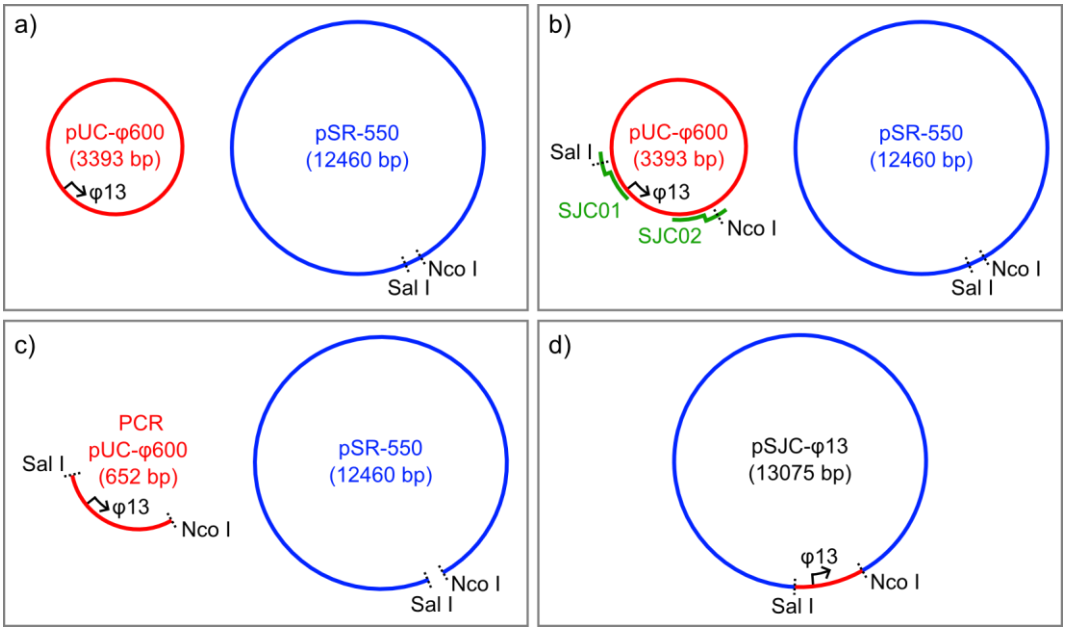


**Figure 2-7 – Production of the pSJC-Φ13 DNA template for transcription studies**
a) The two starting plasmids are pUC-Φ600 and pSR-550. b) Using PCR, the T7 RNAP Φ13 promoter region is amplified out of pUC-Φ600 and SalI and NcoI endonuclease sites introduced using the primers. c) Digestion of the pUC-Φ600 PCR product and pSR-550 with SalI and NcoI endonucleases to produce fragments with sticky ends. d) Ligation of the two fragments with T4 DNA ligase completes production of pSJC-Φ13.

A QIAquick spin column (Qiagen, Netherlands) was used to purify the samples and the eluent was run on a SybrSafe (Invitrogen, Carlsbad, California, USA) stained 1% agarose (in TAE buffer) gel (Figure 2-8). As well as the digested DNA in both purified and unpurified forms, reference samples of pSR-550 and pUC-Φ600 were run. For the digested samples, 2 µl of DNA was diluted with 2 µl of loading buffer and 1 µl of ultra-pure water, while the undigested samples had 1 µl of DNA, 2 µl of loading buffer and 2 µl of water. A 10 µl aliquot of Q-Step 4 DNA ladder was run for comparison of DNA concentrations and sample lengths. The concentration of the NcoI-digested and purified PCR pUC-Φ600 was measured to be 73 nM and similarly 18 nM for pSR-550, both based on comparison with the DNA ladder using ImageJ analysis [84–88]. Upon digestion of circular DNA, supercoiling in the molecule can be relaxed; this leads to the observed

reduction in motility, since supercoiled DNA tends to be more compact, thus it experiences less resistance as it passes through the gel. Correspondingly, linearised samples tend to have more well-defined bands on an agarose gel, since they do not have the variation in linking number of their circular equivalents [89].

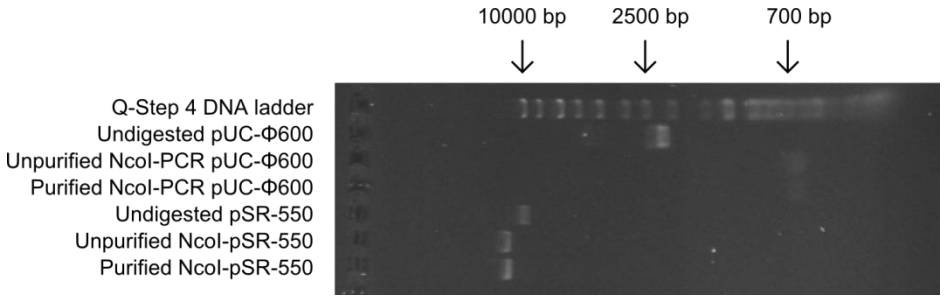


**Figure 2-8 – Analysis of NcoI-digestion of PCR pUC-Φ600 and pSR-550**
The results of NcoI-digestion of PCR pUC-Φ600 and pSR-550 prior to and following purification with a QIAquick spin column as well as undigested samples of pUC-Φ600 and pSR-550 for reference. Key bands on the DNA ladder have been highlighted. While the digested PCR samples have low fluorescence intensities, this is due to their short length (652 bp) rather than a low concentration. Digestion of pSR-550 has resulted in a slight shift in the band location, which is due to differences in motility between circular and linearised DNA. From band fluorescence intensity analysis, the purified and NcoI-digested PCR pUC-Φ600 and pSR-550 concentrations are calculated to be 73 nM and 18 nM, respectively.

Following NcoI digestion, PCR pUC-φ600 and pSR-550 were digested at the SalI (Figure 2-7c) using the following protocol: 50 µl DNA (73 nM for PCR pUC-Φ600 and 18 nM for pSR-550; final concentrations of 60 nM and 15 nM, respectively), 2 µl 20 U/µl SalI (New England Biolabs, Massachusetts, USA), 6 µl NEB Buffer 3 (New England Biolabs, Massachusetts, USA), 0.6 µl 20 mg/ml acetylated BSA (B8894; Sigma-Aldrich, Missouri, USA) and 1.4 µl ultra-pure water. The reaction mixture was incubated at 37 °C overnight, with digestion subsequently quenched by addition of 2 µl 0.5 M EDTA. Digested DNA was purified using QIAquick spin columns (Qiagen, Netherlands), which should also remove the 23 bp fragment from the pSR-550 mixture, since the columns are only rated for purification of DNA between 100 bp and 10000 bp long. The samples were analysed on a 1% agarose gel stained with SybrSafe (Figure 2-9) for length homogeneity, where each sample contained 2 µl DNA, 2µl loading buffer and 1 µl of ultra-pure water. A 5 µl aliquot of Q-Step 4 DNA ladder was also run as a reference. Concentrations of PCR pUC-Φ600 and pSR-500 were calculated using ImageJ analysis [84–88] of sample and ladder bands to be 55 nM and 5 nM, respectively.

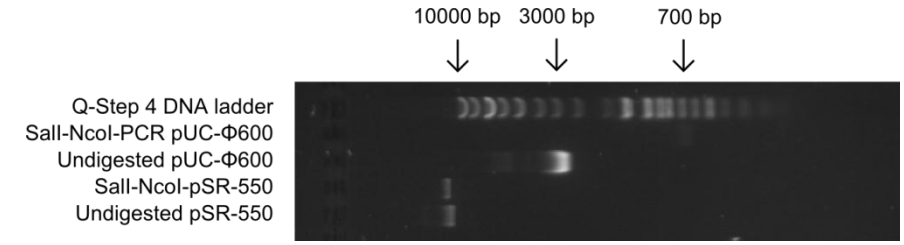


**Figure 2-9 – Analysis of SalI-digestion of PCR pUC-Φ600 and pSR-550**
A 1% agarose gel demonstrating successful digestion of both PCR pUC-Φ600 and pSR-550 with NcoI and SalI. Although faint, the digested and purified PCR pUC-Φ600 sample exhibits a single, well defined band. This is the same case for the pSR-550 sample, which shows a slight, but expected, reduction in motility. As a comparison of sample concentration, an undigested stock of pUC-Φ600 was also run. Both digested samples run near the expected ladder bands corresponding to molecule lengths of 10000 bp and 700 bp. Band fluorescence intensity analysis yields sample concentrations of 55 nM for SalI-NcoI-PCR pUC-Φ600 and 5 nM for SalI-NcoI-pSR-550.

Equimolar quantities of the products were incubated together with T4 DNA ligase, which allows complimentary DNA "sticky ends" to anneal and for T4 DNA ligase to repair the nicks in the sugar-phosphate backbone (Figure 2-7d). Ligation was performed as follows: 2 µl 55 nM SalI-NcoI-PCR pUC-Φ600 (5.5 nM final concentration), 7 µl 5 nM SalI-NcoI-pSR-550 (1.75 nM final concentration), 2 µl 10x T4 DNA ligase buffer (New England Biolabs, Massachusetts, USA), 1 µl 400 U/µl T4 DNA ligase (New England Biolabs, Massachusetts, USA) and 8 µl ultra-pure water. A negative control for ligation used SalI-NcoI-pSR-550, since this should be unable to undergo religation as SalI and NcoI restriction leaves sticky ends with different sequences. The negative control sample was 7µl 5 nM SalI-NcoI-pSR-550 (1.75 nM final concentration), 2 µl 10x T4 DNA ligase buffer, 1 µl 400 U/µl T4 DNA ligase and 10 µl ultra-pure water. Ligation mixtures were incubated at room temperature for 2 hours.

Following ligation, the pSJC-Φ13 plasmid was transformed into DH5α *E. coli* cells with 100 µg/ml ampicillin-resistance selection and 5 µl of the target plasmid (see Section 2.6.1for protocol). Two additional transformations using 1 µl 511 nM (26 nM final concentration) undigested pUC-Φ600 and 5 µl of the ligation negative control acted as positive and negative controls, respectively. For pSJC-Φ13, a pair of colonies was grown-up separately to ensure a high yield of plasmid. To verify successful production of pSJC-Φ13 the produced plasmid was run on a 1% agarose gel stained with SybrSafe (Invitrogen, Carlsbad, California, USA) (Figure 2-10). A sample of undigested pSR-550 was also run as for reference. Each sample contained 2 µl DNA and 2 µl loading buffer. An aliquot of 10 µl Q-Step 4 DNA ladder was also run as a reference for plasmid length. The produced pSJC-Φ13 plasmid concentration was measured through comparison with

the DNA ladder using ImageJ [84–88] to be 17 nM. The full pSJC-Φ13 sequence is included in Appendix D-IV.

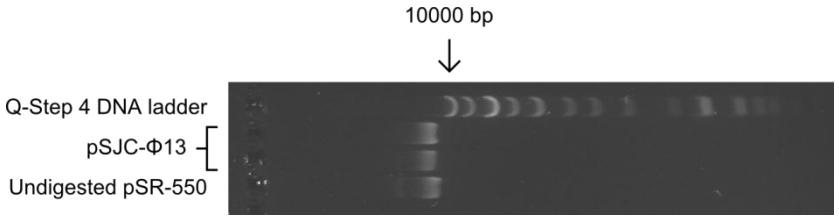


**Figure 2-10 – Agarose gel electrophoresis analysis of pSJC-Φ13 production**
1% agarose gel showing ligated pUC-Φ600 and pSR-550 (pSJC-Φ13) produced through molecular cloning. The samples are compared to undigested pSR-550, against which they exhibit slightly reduced motility. This is expected since pSJC-Φ13 is 615 bp longer than pSR-550. The pSJC-Φ13 concentration was elucidated through comparison with the DNA ladder to be 17 nM.

### 2.3.6 Linearisation of pSJC-Φ13 with SalI for AFM studies

For use with AFM, the ligated pSJC-Φ13 plasmid was linearised with SalI, which digests the DNA approximately 140 bp upstream of the T7 RNAP Φ13 promoter. The reaction used the following protocol: 20 µl 17 nM pSJC-Φ13 (8.5 nM final concentration), 1 µl 10 U/µl SalI (Promega, Wisconsin, USA), 4 µl 10x Buffer D (Promega, Wisconsin, USA), 0.4 µl 20 mg/ml acetylated BSA and 14.6 µl ultra-pure water (18.2 MΩ•cm; Purelab Ultra; Elga, Marlow, UK). The reaction mixture was incubated at 37 °C for 3 hours, with digestion subsequently quenched by addition of 4 µl 0.5 M EDTA. Purification of the DNA was performed using a QIAquick spin column (Qiagen, Netherlands).

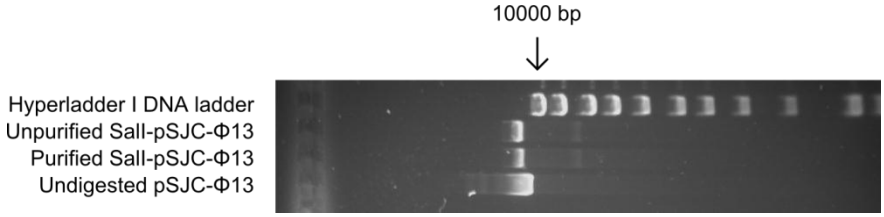


**Figure 2-11 – Demonstration of successful linearisation of pSJC-Φ13 with SalI**
Shown is the digested sample prior to and following purification with a QIAquick spin column (Qiagen, Netherlands). There is a slight decrease in DNA after purification, which can be attributed to the spin column being rated for samples up to 10000 bp; approximately 3000 bp less than the sample loaded. Comparison of purified sample band to the ladder yields an approximate concentration of 3.0 nM.

Electrophoresis of the linearised DNA sample with a 1% agarose gel (in TAE buffer) stained with SybrSafe (Invitrogen, Carlsbad, California, USA) (Figure 2-11) was used to verify successful digestion. Each sample contained 2 µl DNA, 2 µl loading buffer (Yorkshire Biosciences Ltd., York, UK) and 1 µl ultra-pure water (18.2 MΩ•cm; Purelab Ultra; Elga, Marlow, UK). For reference, 5 µl of Hyperladder I DNA ladder was also run

on the gel (BioLine, London). Comparison of the purified SalI-pSJC-Φ13 to the ladder using ImageJ [84–88] yielded a concentration of 3 nM.

### 2.3.7 Linearisation of pSJC-Φ13 with NcoI for transcription assay analysis

To demonstrate the successful incorporation of the T7 RNAP Φ13 promoter sequence into the final pJSC-Φ13 plasmid a bulk transcription assay was run. Bulk transcription assays to verify promoter integrity are most effective with short transcripts, thus facilitating high RNA production. Therefore, pSJC-Φ13 was digested with NcoI, which should yield ~500 bp transcripts (Figure 2-6). Digestion was performed using the following protocol: 20 µl 6.5 nM pSJC-Φ13 (4.3 nM final concentration), 1 µl NcoI enzyme (New England Biolabs, Massachusetts, USA), 3 µl 10x NEB Buffer 3 (New England Biolabs, Massachusetts, USA) and 6 µl ultra-pure water (18.2 MΩ•cm; Purelab Ultra; Elga, Marlow, UK). The reaction mixture was incubated at 37 °C overnight, with digestion quenched through addition of 4 µl 0.5 M EDTA. A QIAquick spin column was used to purify the sample DNA from enzymatic reagents.

The quality of digestion was evaluated by electrophoresis using a 1% agarose (in TAE buffer) gel stained with SybrSafe (Invitrogen, Carlsbad, California, USA) (Figure 2-12). Each sample contained 2 µl DNA, 2 µl loading buffer (Yorkshire Biosciences Ltd., York, UK) and 1 µl of ultra-pure water (18.2 MΩ•cm; Purelab Ultra; Elga, Marlow, UK). For verification of the sample lengths, 5 µl of Hyperladder I DNA ladder (BioLine, London) was also run. Comparison of the purified SalI-pSJC-Φ13 to the ladder using ImageJ [84–88] yielded a concentration of 1.6 nM.

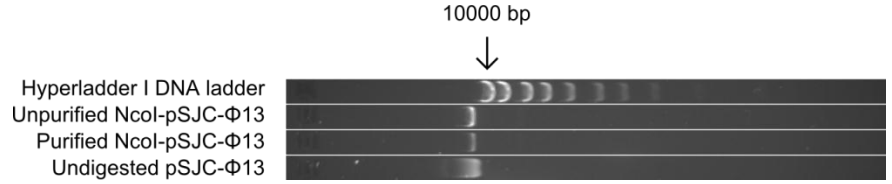


**Figure 2-12 – Analysis of NcoI-digestion of pSJC-Φ13**
1% agarose gel of pSJC-Φ13 digested with NcoI to produce a single, linearised DNA template for use in bulk transcription assay verification of the T7 RNAP Φ13 promoter. The slight loss of concentration following purification is due to incomplete elution from the spin column and arises because the DNA is longer than recommended. Comparison of purified sample band to the ladder yields an approximate concentration of 1.6 nM

### 2.3.8 Verification of the pSJC-Φ13 DNA sequence

Inclusion of pSR-550 in the final plasmid was verified by gel electrophoresis (see Figure 2-10, Section 2.3.5). Since 95% of the plasmid's length is contributed by pSR-550, the running of both pSJC-Φ13 and pSR-550 bands at approximately the same location on the gel can only be accounted for by the presence of this component. These bands have a lower motility than the largest band on the ladder, which is expected.

#### 2.3.8.1 AFM measurement of contour length

Homogeneity of the produced DNA was demonstrated through AFM analysis of contour length measurement; such an analysis is intended to highlight sample degradation, the presence of ligation precursors and successful digestion (Section 2.3.6). AFM is a scanning probe microscopy technique, discussed in detail in Section 3.1, which can be used to topographically image biological samples deposited onto the atomically-flat substrate, mica. Assuming a rise per base-pair of 0.34 nm [90], the expected contour length for the 13,075 bp pSJC-Φ13 DNA molecule is 4.45 µm.

A complete description of sample preparation and imaging using AFM is provided in Section 3.2.2; however, to briefly summarise, SalI-digested pSJC-Φ13 was diluted in AFM buffer to approximately 60 pM (784 nM base-pair concentration) and deposited on a freshly-cleaved mica surface. This was imaged using a diCaliber AFM (Veeco Instruments Inc., New York, USA) and self-mounted silicon tapping mode tips (OMCL-AC160TS-E, Olympus Corporation, Tokyo, Japan) following the vendor-recommended protocol. Using this approach, multiple images were obtained for typical scan settings of: 10 µm x 10 µm scan area, 1 Hz scan rate and 1024 px x 1024 px scan resolution (Figure 2-13) or 5 µm x 5 µm scan area, 2 Hz scan rate and 512 px x 512 px scan resolution. Contour length measurements for each DNA molecule were performed in ImageJ [84] by tracing the molecule profiles with segmented lines and recording the calibrated length. To reduce the likelihood of mis-measurement, any molecules with intersections were omitted, since it is not possible to determine the correct path of the backbone. Additionally, molecules shorter than approximately 1 µm were discarded as degradation of only a few full size molecules can lead to a high concentration of these very short strands.

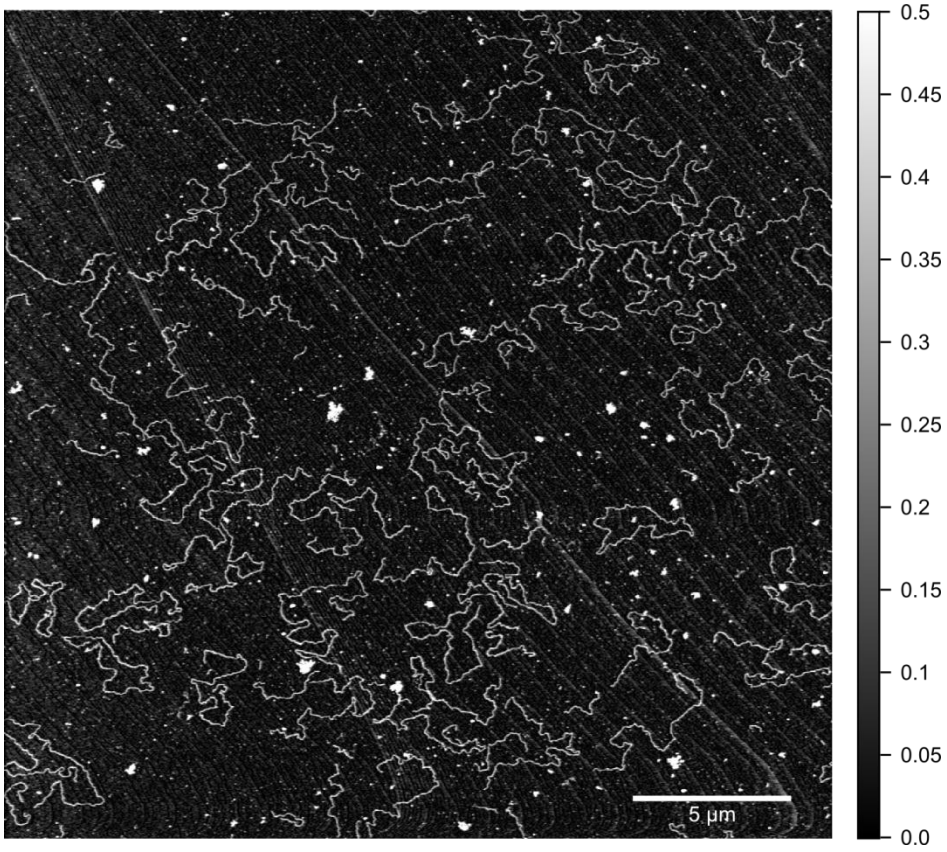


**Figure 2-13 – Example AFM image of the SalI-linearised pSJC-Φ13 plasmid**
The self-avoidance demonstrated by the molecules indicates equilibrating deposition conditions, thus making accurate contour length measurements easier. Any molecules which indicated intersection were omitted to improve the accuracy of measurement. Image was levelled using the revolve arc function in Gwyddion.

Across 31 sample images, 314 molecules were measured, the contour lengths for which are shown in the histogram in Figure 2-14. Of all the measured lengths, 163 contour lengths (53% of total) fall within the range 4 µm to 4.5 µm and yield an average length of 4.20 µm ± 0.01 µm (n = 163); this demonstrates good sample homogeneity. Molecules falling outside the 0.5 µm range were excluded as it is assumed they correspond to incomplete lengths. There is strong agreement between the measured average contour length and predicted length of 4.45 µm; the slight shortfall in measured length (5%) has also been observed elsewhere, where it was attributed to dehydration of the DNA and an inability to resolve small bends in the molecule when tracing the backbone [91,92].

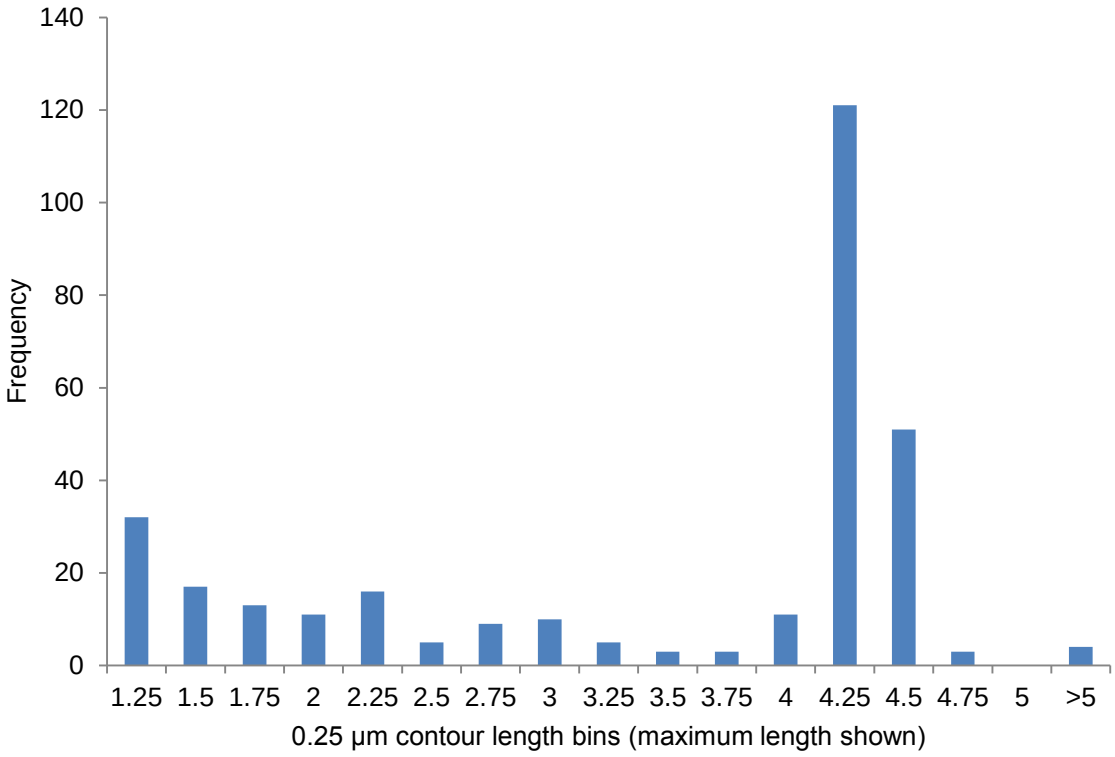


**Figure 2-14 – Histogram of measured contour lengths for SalI-linearised pSJC-Φ13**
AFM measurement of 314 molecules yielded a clear cluster of lengths in the range 4 µm to 4.5 µm corresponding to 53% of all measured molecules, yielding an average of 4.20 ± 0.01 µm (n = 163), which agrees with the predicted value of 4.45 µm. Slight under-measurement of contour length is expected and has been attributed elsewhere to molecule dehydration and an inability to resolve small bends in the DNA [91].

#### 2.3.8.2 Bulk transcription assay to demonstrate T7 RNAP promoter integrity

The presence of PCR pUC-Φ600 in the final plasmid was verified through repetition of the PCR amplification with primers SJC01 and SJC02. The sequence complimentary to these primers is incorporated into pSJC-Φ13 (Figure 2-6), so a 652 bp product following PCR is indicative of successful incorporation. This product was shown to be present by running a sample on a 1% agarose (in TAE buffer) gel stained with SybrSafe (Invitrogen, Carlsbad, California, USA) (Figure 2-15), where each sample contained 2 µl sample DNA, 2 µl 2x loading buffer (Yorkshire Biosciences Ltd., York, UK) and 1 µl ultra-pure water (18.2 MΩ•cm; Purelab Ultra; Elga, Marlow, UK). A 5µl aliquot of the DNA ladder, Hyperladder I (BioLine, London) was run for verification of the produced DNA length.

Verification of Φ13 promoter integrity in the final pSJC-Φ13 sequence was achieved through analysis of the RNA products from a bulk transcription assay using T7 RNAP. For this assay, a sample of pSJC-Φ13 was digested with endonuclease NcoI (see Section 2.3.7), which recognises a single restriction site approximately 500 bp downstream of the

Φ13 promoter. Therefore, assuming the products from abortive and non-runoff transcription to be negligible, the produced RNA should fit into a single, well-defined population, 500 bases long.

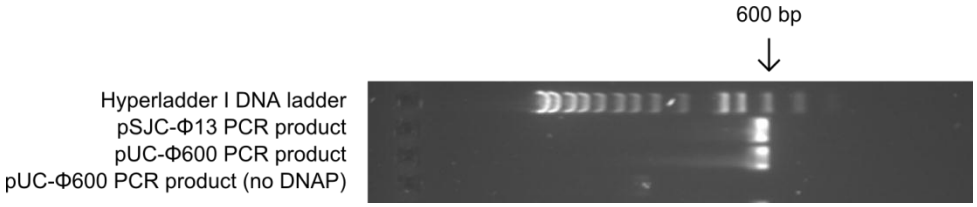


**Figure 2-15 – Analysis of pSJC-Φ13 PCR product**
A 1% agarose gel of products from the PCR of pSJC-Φ13 with primers SJC01 and SJC02. The presence of a band at ~600 bp can only be explained by inclusion of PCR pUC-Φ600 in the pSJC-Φ13 sequence.

Five samples were prepared for the transcription assay using the method described in Section 2.6.3. As a positive control for transcription, 3.5 µl 5 nM EcoRI-digested pUC-Φ600 (see Section 2.3.2) was incubated with 0.7 µl 18µM T7 RNAP (Promega, Wisconsin, USA). The NcoI-digested pSJC-Φ13being tested in the assay was mixed as 3.5 µl 3 nM NcoI-pSJC-Φ13 (see Section 2.3.7) and 0.7 µl 18 µM T7 RNAP (Promega, Wisconsin, USA). To verify any bands observed weren't due to the reagents, rather than transcription, a negative control with RNAP replaced with 0.7 µl ultra-pure water was used. The final two samples contained DNA only, since the DNA will also be stained by the ~1 µg/ml ethidium bromide and so it is important to determine where on the gel it runs. These samples contained 3.5 µl 3 nM NcoI-pSJC-Φ13 and 3.5 µl 5 nM EcoRI-pUC-Φ600, respectively.

Gel analysis was conducted as described in Section 2.6.3, with 8 µl of each sample loaded following incubation at 80°C for 5 minutes with the transcription stop buffer. For transcript length reference, a 5 µl aliquot of low-range RiboRuler (Thermo Fisher Scientific, Massachusetts, USA) was also run. The ladder was preheated at 70°C for 10 minutes prior to use.

Successful transcription was confirmed by the presence of a band on a 6% urea acrylamide gel (Figure 2-16) with a length of ~500 bases, as expected. Comparison of the two bands in the transcriptionally-active pSJC-Φ13 lane to the single band in the pSJC-Φ13 only lane shows that the smaller band, running barely beyond the wells is due to the DNA template. This is similar to the result for the transcription positive control (pUC-Φ600 DNA), where

the smaller band running at ~1000 bases can be attributed to the template. Furthermore, the lack of a second band in the third sample lane (pSJC-Φ13 without RNAP) indicates the production of RNA is catalysed by RNAP, as expected.

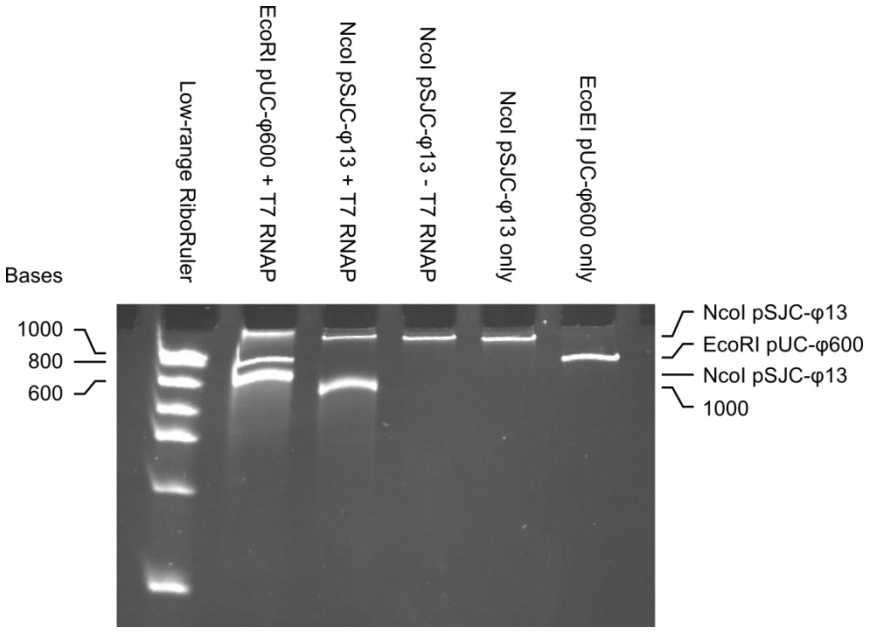


**Figure 2-16 – Bulk transcription assay verification of pSJC-Φ13**
RNA products from the bulk transcription assay demonstrate the presence and activity of the T7 RNAP Φ13 promoter in the produced plasmid, pSJC-Φ13. Both the positive control and pSJC-Φ13 sample exhibit bands, which cannot be accounted for by the DNA template, which indicates transcription was successful. The EcoRI pUC-Φ600 sample has an RNA band slightly larger than 600 bases and the NcoI pSJC-Φ13 sample has the expected band corresponding to a transcript of 500-600 bases.

### 2.3.9 Single-strand functionalisation of DNA with digoxigenin and biotin

Experiments concerned with testing and demonstrating the application of force to single DNA tethers, but not controlling torque, require DNA labelled at either end with functionalisations, such as biotin (bound by streptavidin) and digoxigenin (bound by anti-digoxigenin). Incorporation of labelled nucleotides is achieved with the terminal transferase (TdT) enzyme in a process known as 3'-end-tailing. Following incorporation of 5-10 labelled nucleotides, ddTTP is added to the reaction, since this is recognised and incorporated by the TdT, but does not permit further nucleotide incorporation due to absence of the 3'-hydroxyl group.

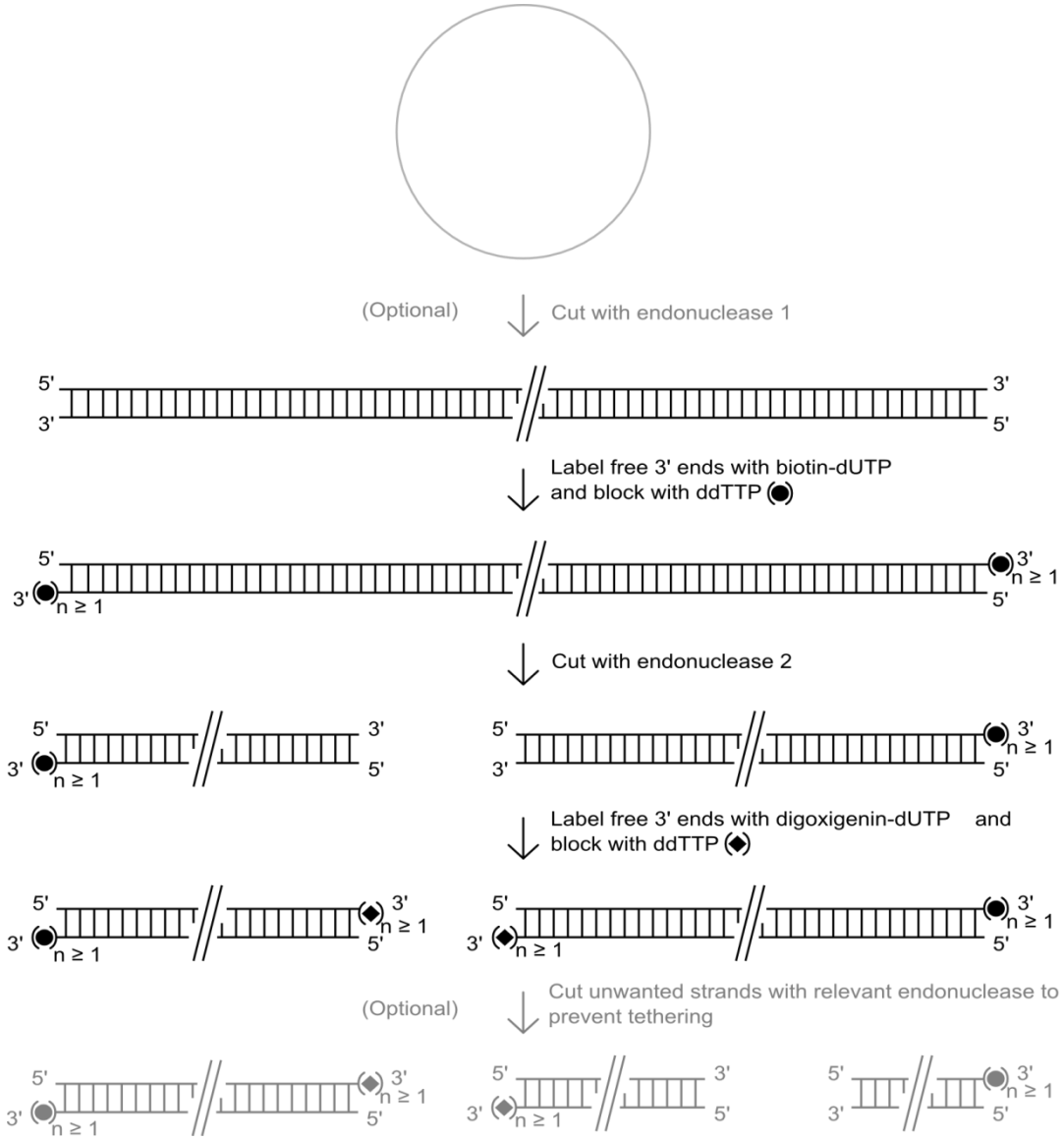


**Figure 2-17 – Generalised method for labelling of dsDNA**
Labels are introduced at each 3'-end with either biotin or digoxigenin, thus permitting the application of force through attachment to spatially-controlled substrates. Circular plasmids are linearised with endonuclease 1 (optional); then labelled at both exposed ends with dig-dUTP and blocked from further extension with ddTTP. Digestion with endonuclease 2 exposes two fresh 3'-ends, which are labelled in the same manner using biotin-dUTP. Restriction with endonuclease 3 is optional and prevents the shorter, unwanted template forming tethers. Adapted from [64].

The key properties of end-labelled DNA will vary depending upon the intended ufor example, verification and troubleshooting of tether formation (Section 5.4) requires a high DNA concentration; whereas, for experiments following transcription in real-time, homogeneity of tethers is vital. To put this in the context of labelling T7 DNA, high concentration stocks can be produced through digestion of template approximately at the mid-point (restriction site StuI), thus yielding molecules of similar lengths, but with opposite promoter alignment. Conversely, for templates where concentration is less important than homogeneity and length, digestion can be performed closer to one end, with

the shorter template disabled through an additional digestion step. Described is the protocol for labelling of T7 DNA; however, this can be easily modified to work for other templates, such as pSJC-Φ13 with appropriate restriction enzyme selection. Furthermore, description of the optional first and third digestions are not included here, since they are unnecessary for the example provided and follow near-identical protocols to the reaction discussed in Section 2.3.9.2.

#### 2.3.9.1 End-labelling DNA with biotin-dUTP

Labelling of T7 DNA 3'-end was achieved through the following protocol: 45 µl 19 nM T7 DNA (Yorkshire Biosciences Ltd., York, UK), 7 µl 10x NEB Buffer 4 (New England Biolabs, Massachusetts, USA), 7 µl 2.5 mM $CoCl_2$ (New England Biolabs, Massachusetts, USA), 10 µl 0.25 mM biotin-11-dUTP (Yorkshire Biosciences Ltd., York, UK) and 1 µl terminal transferase (TdT) (New England Biolabs, Massachusetts, USA); this was incubated at 37 °C for 1 hour. Further elongation of the 3'-end was prevented by addition of 2 µl 10 mM ddTTP, which was incubated with the end-labelled DNA at 37 °C for a further 2 hours. Finally, the TdT is heat-inactivated at 75 °C for 20 minutes. End-labelling is performed in NEB Buffer 4, rather than the TdT buffer provided by the enzyme manufacturer since both buffers are near identical (both containing 50 mM potassium acetate, 20 mM Tris-acetate, 10 mM magnesium acetate, but with an additional 1 mM of DTT in NEB Buffer 4) and buffer exchange to NEB Buffer 4 for the subsequent digestion will be necessary irrespectively.

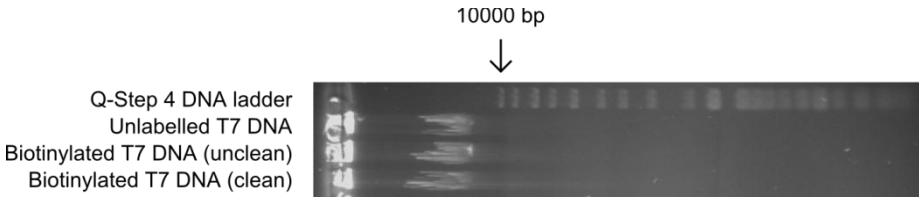


**Figure 2-18 – Biotinylated and purified T7 DNA analysed using a 1% agarose gel**
There does not appear to be an appreciable difference in sample concentration throughout the biotinylated and purification procedure. The observed smudging of bands results from overloading of the wells; this is indication of a high-concentration sample.

The labelled DNA was purified from the reaction components using a NucAway spin column (Invitrogen, Carlsbad, California, USA), which was equilibrated with 65µl NEB Buffer 4, 65 µl 2.5 mM $CoCl_2$ and 520 µl of ultra-pure water (18.2 MΩ•cm; Purelab Ultra; Elga, Marlow, UK). Samples from before and after purification were run on a 1% agarose

(in TAE buffer) gel stained with 2 mM ethidium bromide to verify successful purification. Each sample contained 1 µl DNA mixture, 2 µl loading buffer (Yorkshire Biosciences Ltd., York, UK) and 2 µl of ultra-pure water. A 5µl aliquot of Q-Step 4 DNA ladder (Yorkshire Biosciences Ltd., York, UK) was also used for length comparison. Concentration estimation through comparison to the gel was not possible since the closest band on the ladder was nearly 4-fold shorter than the biotinylated sample. Instead, a concentration of 12 nM was estimated in accordance with the labelling reaction dilution.

#### 2.3.9.2 Digestion of biotin-functionalised DNA

Depending on the preparation route being taken, the biotinylated T7 DNA can either be digested to produce two templates of similar length, or to produce a single, long template. Described here is the former, which uses the StuI enzyme. The reaction mixture for digestion of biotinylated T7 DNA was as follows: 40 µl 12 nM biotinylated T7 DNA (Section 2.3.9.1), 5 µl NEB Buffer 4 (New England Biolabs, Massachusetts, USA), 5x TE buffer and 2 µl StuI endonuclease (New England Biolabs, Massachusetts, USA). This mixture was incubated at 37 °C overnight, followed by addition of 2 µl 0.5 M EDTA to quench the reaction. Since the digestion-reaction components should not affect the ability to functionalise the freshly-exposed 3'-ends with dig-dUTP, the sample was not purified. Based on the sample dilution in the aforementioned reaction, the concentration of StuI-biotin T7 DNA is predicted to be approximately 9 nM. Verification of sample purity was performed in parallel with the final digoxigenin and biotin-labelled DNA (Figure 2-19, Section 2.3.9.3).

An alternative route taken to generate a 36 kbp substrate for force characterisation of the magnetic tweezers microscope used the enzyme SfiI (New England Biolabs, Massachusetts, USA). This was implemented in a similar manner to the StuI restriction, using the vendor-recommended conditions.

#### 2.3.9.3 End-labelling biotinylated DNA with digoxigenin-dUTP (dig-dUTP)

Irrespective of the previous digestion step, the previously biotinylated T7 DNA was functionalised at the freshly-exposed 3'-ends with digoxigenin-dUTP (dig-dUTP). The reaction mixture was as follows: 35µl 9 nM StuI-biotin T7 DNA (Section 2.3.9.2), 7 µl 10x TdT buffer (New England Biolabs, Massachusetts, USA), 7µl 2.5 mM $CoCl_2$, 10 µl

0.25 mM dig-11-dUTP (Roche Applied Science, Penzberg, Germany), 1 µl TdT (New England Biolabs, Massachusetts, USA) and 10 µl of ultra-pure water. This was incubated at 37 °C for 1 hour, followed by addition of 2 µl ddTTP to block further elongation; requiring an additional 2 hour incubation at the same temperature. Purification of the sample was achieved using a NucAway spin column (Invitrogen, Carlsbad, California, USA) hydrated with 650 µl and used in accordance with the manufacturer-supplied protocol.

Samples were run on a 1% agarose gel containing SybrSafe (Invitrogen, Carlsbad, California, USA) to verify successful purification (Figure 2-19). Each sample contained 1 µl sample DNA, 2 µl loading buffer (Yorkshire Biosciences Ltd., York, UK) and 2 µl ultra-pure water (18.2 MΩ•cm; Purelab Ultra; Elga, Marlow, UK). A 5 µl aliquot of Q-Step 4 DNA ladder was also run for comparison of sample concentrations and lengths. The concentration of the purified dig-StuI-biotin T7 DNA was measured using Nanodrop (ND-1000; Thermo Fisher Scientific, Massachusetts, USA), yielding a value of 6.4 nM.

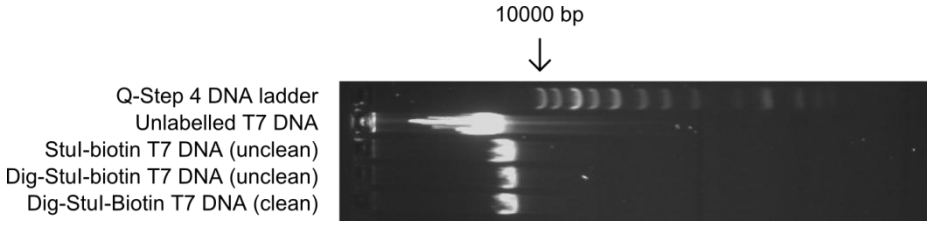


**Figure 2-19 – Analysis of dig-StuI-biotin T7 DNA using a 1% agarose gel**
There is no appreciable change in concentration between the three labelled samples, indicating purification did not retain significant quantities of DNA. A slight increase in concentration during purification can be attributed to elution in a smaller volume than initially input. As with Figure 2-18, smudging of the unlabelled T7 DNA band is due to overloading of the gel.

## 2.4 Protein preparation

### 2.4.1 Biotinylated wild-type T7 RNA polymerase

Despite having a much less complex composition, the single-subunit T7 RNA polymerase (RNAP) retains all the key functions of its multi-subunit eukaryotic and bacterial counterparts [33]. Such characteristics make it an ideal system for early studies on the effect of torsion on transcription rates using the magnetic tweezers microscope (Chapter 4). To enable fluorescence visualisation of the polymerase in real-time it is covalently conjugated with biotin, allowing the binding of streptavidin-functionalised fluorophores such as TransFluoSpheres (TFS; Invitrogen, Carlsbad, California, USA) or Q-Dots (Invitrogen,

Carlsbad, California, USA). This approach used mutants lacking seven surface cysteines [93]; however, previous attempts conducted by Rebecca Milner have proven unsuccessful at yielding transcriptionally active unlabelled mutants. As a result, the technique described here uses wild-type T7 RNAP (henceforth referred to simply as RNAP), which has seven surface-accessible cysteine residues (Figure 2-20).

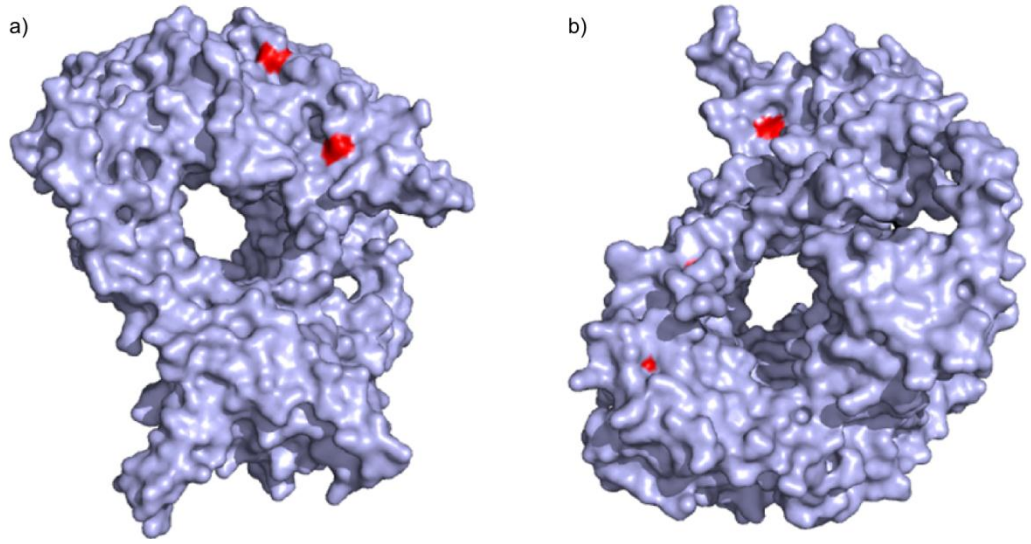


**Figure 2-20 – Surface accessible cysteine residues of WT T7 RNAP**
Surface representations of opposing faces of wild-type T7 RNAP, with accessible cysteine residues highlighted in red. The enzyme has seven such residues, which can be labelled via the thiol group with biotin-maleimide. Model rendered using PyMol (Version 1.5.0.4 Schrödinger, LLC.).

#### 2.4.1.1 Overexpression and purification of wild-type T7 RNAP

Production of wild-type T7 RNAP is performed using a previously-established protocol [64], whereby plasmid pDL21 is used to transform BL21* (DE3) cells. pDL21 encodes the enzyme with a pair of $His_6$ tags on the N-terminal separated by a single Met residue [94], thus enabling nickel-affinity purification. Antibiotic selection through ampicillin resistance is provided by presence of the beta-lactamase (bla) gene in pDL21. The pDL21 plasmid was provided by R.K. Durbin.

Transformation of BL21 Star (DE3) cells was achieved following the initial stages of the protocol described in Section 2.6.1 (first two paragraphs) using 1 µl of 47.3 ng/µl pDL21 plasmid and 50 µl of cells. The transformed cells were spread onto LB agar plates containing 200 µg/ml of ampicillin and the plates incubated overnight at 37 °C. Assuming successful cell growth, single colonies were transferred to 10 ml volumes of LB and incubated at 37 °C with shaking (200 rpm). A single overnight culture was then used to

inoculate a 500 ml volume of LB, which was incubated at 37 °C with shaking (120 rpm) over the course of 315 minutes, with optical density at 600 nm ($OD_{600}$) measurements taken at regular intervals (Figure 2-21) to monitor progress. After incubation for 130 minutes, expression of WT T7 RNAP was induced through addition of 120 mg of IPTG (Melford, Ipswich, UK), which binds to the lac repressor, causing it to dissociate from the lac operator and allowing transcription from the lac promoter. Once at an $OD_{600}$ of 3.392 (185 minutes since induction) the culture was split in half and the cells pelleted by centrifugation at 6000 xg for 15 minutes at 4 °C (JLA-16.250 rotor; Avanti J-26XP centrifuge; Beckman-Coulter, Pasadena, California, USA), then the supernatant was removed and the pellets stored at -20 °C until required.

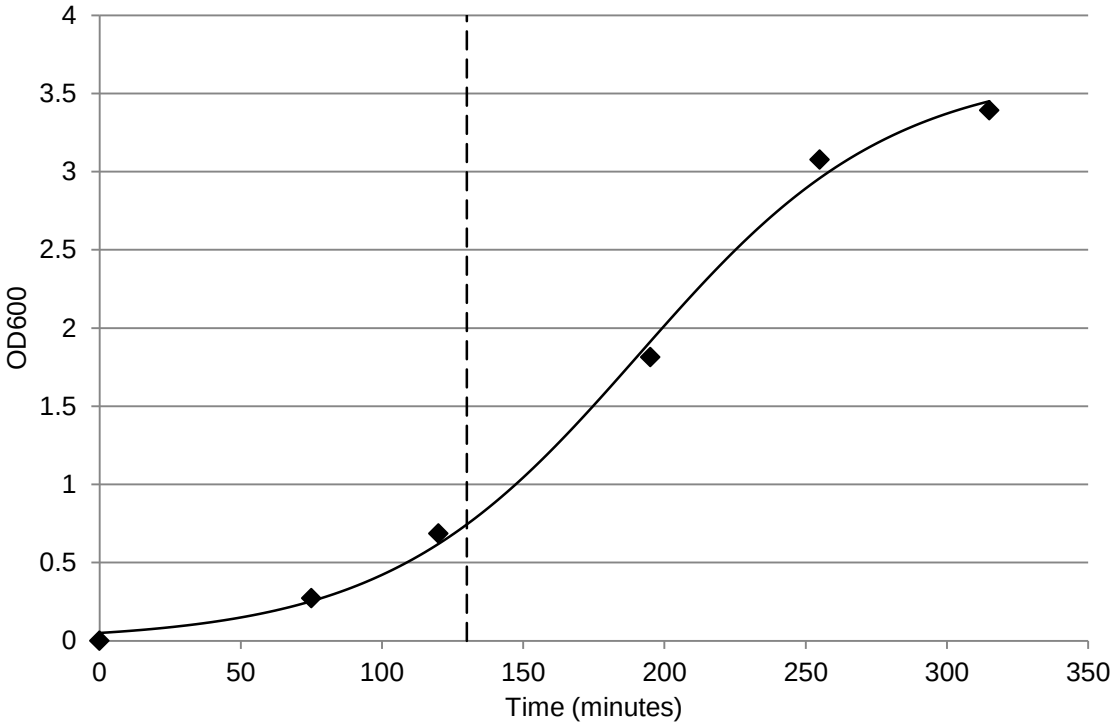


**Figure 2-21 – Growth curve for cells expressing WT T7 RNAP**
Optical density as a function of time corresponding to growth of BL21* (DE3) cells containing the pDL21 plasmid encoding N-terminal His-tagged wild-type T7 RNAP. Expression of the enzyme is induced by addition of IPTG (dashed line) after 130 minutes of incubation at 37 °C and growth allowed to progress for a further 185 minutes. The growth curve has been fit with a sigmoidal logistic function [95] (Equation 2-1; $a$ = 3.6646, $k$ = 0.022407, $x_c$ = 191.0634) using the MATLAB fminsearch function and custom script, *equationFit.m* (Accompanying Material)

$$y = \frac{a}{1 + exp\big(-k(x - x_c)\big)}$$

**Equation 2-1 – Sigmoidal logistic function for fitting the bacterial growth curve**
The magnitude of the function ($y$) is determined at each time point ($x$) by the amplitude ($a$), the point of inflexion ($x_c$) and the scale parameter ($k$) [95].

Continuation of RNAP purification required resuspension of the cell pellets in a total of 35 ml lysis buffer (see Section 2.1 for composition) using continuous motion with a plastic pipette. Immediately prior to lysis, 350 µl 100 mM PMSF was added to the cell mixture and the tube sonicated using the manufacturer-recommended protocol (Sonicator 3000; Misonix, New York, USA); sonication used 6 cycles of 15 second bursts (126 W power, ~8 µm amplitude) at 30 second intervals. A 5 µg/ml quantity of DNaseI was added and the mixture incubated on ice for 20 minutes.

Purification of RNAP used a $Ni^{2+}$-chelating HiTrap column (Q FF 1 ml; GE Healthcare, Little Chalfont, UK), which was washed using a peristaltic pump with a 0.45 µm filter (Millex; Merck Millipore, Massachusetts, USA) between the pump and column to prevent blockage from particulate matter. To regenerate the HiTrap column, 5 ml of the following were added sequentially: ultra-pure water (18.2 MΩ•cm; Purelab Ultra; Elga, Marlow, UK), 50 mM EDTA, ultra-pure water, 100 mM $NH_4$-acetate (pH 4.0), ultra-pure water, 100 mM $NiSO_4$ (diluted in ultra-pure water) and finally ultra-pure water. Prior to addition onto the column, lysate was removed from the lysed cell mixture by centrifugation at 20,000 rpm for 30 minutes at 4 °C (JA-12.50 rotor; Avanti J-26XP centrifuge; Beckman-Coulter, Pasadena, California, USA).

The HiTrap column was connected to the FPLC (Biologic DuoFlow; Bio-Rad Laboratories, California, USA) and flushed with 10 ml of wash buffer (see Section 2.1 for composition) at a rate of 1 ml/min and pressure of 9-11 psi. Next, the sample was loaded at the same rate, whilst monitoring the optical density at 280 nm, with a maximum value of 0.2282 observed. Column flow-through from this step was collected for subsequent comparison to eluted fractions. Following sample loading, the column was flushed with wash buffer until the measured $OD_{280}$ reached ~0.03, corresponding to imidazole absorption. His-tagged WT T7 RNAP is finally eluted from the $Ni^{2+}$-chelating HiTrap column by imidazole displacement; imidazole is increased from 59 mM (98% wash buffer, 2% elution buffer) to 500 mM (0% wash buffer, 100% elution buffer). Eluent is collected in forty 1 ml fractions for subsequent analysis by SDS PAGE.

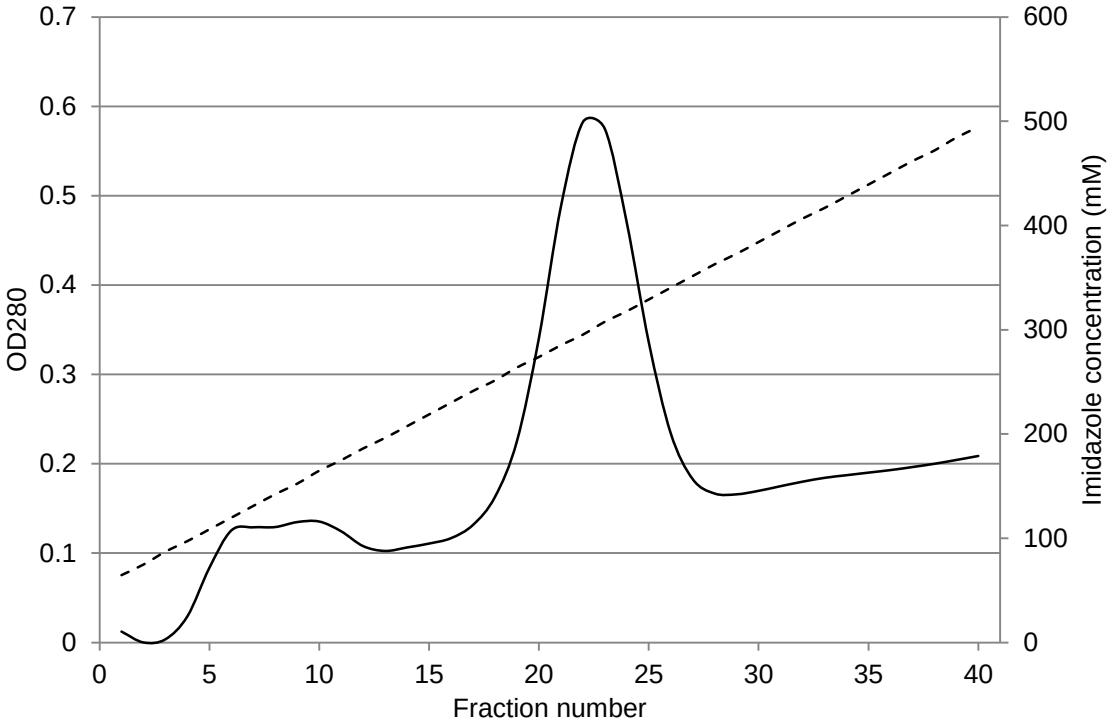


**Figure 2-22 – Elution of WT T7 RNAP from HiTrap column**
FPLC measurement of optical density (solid line) during elution of His-tagged wild-type T7 RNAP from a HiTrap column upon addition of an imidazole gradient (59 mM to 500 mM; dashed line. Elution of His-tagged protein appears to occur for fractions 16 to 28, which correspond to an imidazole concentration of 230 mM to 360 mM.

Optical density readings from the FPLC indicated protein elution in fractions 16 through 28 (Figure 2-22). Each gel sample contained 15 µl of eluent and 5 µl 4x loading buffer (see Section 2.1 for composition). In addition to the eluted fractions, an aliquot of HiTrap column flow-through from sample loading and the cell lysate were run. For comparison of band sizes, 10 µl of PageRuler (Thermo Fisher Scientific, Massachusetts, USA) was also run. Samples were pre-heated at 95 °C for 5 minutes, then a 14µl aliquot of each sample was loaded across two gels and gels run for 90 minutes at a constant voltage of 150 V. Gels were stained in Coomassie Blue (see Section 2.1 for composition) for 30 minutes; then destained overnight in water (Figure 2-23).

The band present at ~100 kDa in the SDS PAGE gels (Figure 2-23) indicates elution of His-tagged T7 RNAP ($M_r$ = ~98 kDa [96]) and occurs for HiTrap column imidazole concentrations in the range 230 mM to 350 mM; this agrees with the optical density observation for protein elution in this range (Figure 2-22). It is likely that the smaller band at ~30 kDa corresponds to the His-tagged N-terminal region of the protein, which can be cleaved at the protease site present in this region. This occurs due to a protease present in bacteria, OmpT [97]. Fractions 18 to 28 were pooled and first dialysed against dialysis buffer

(see Section 2.1 for composition) using 12-14 kDa molecular weight cut-off dialysis tubing overnight at 4 °C, followed by dialysis in storage buffer under the same conditions. Storage buffer contains 50% glycerol, which allows the protein to be stored at -20 °C without degradation due to the formation of ice crystals. Dialysis into glycerol is accompanied by an approximate three-fold decrease in volume.

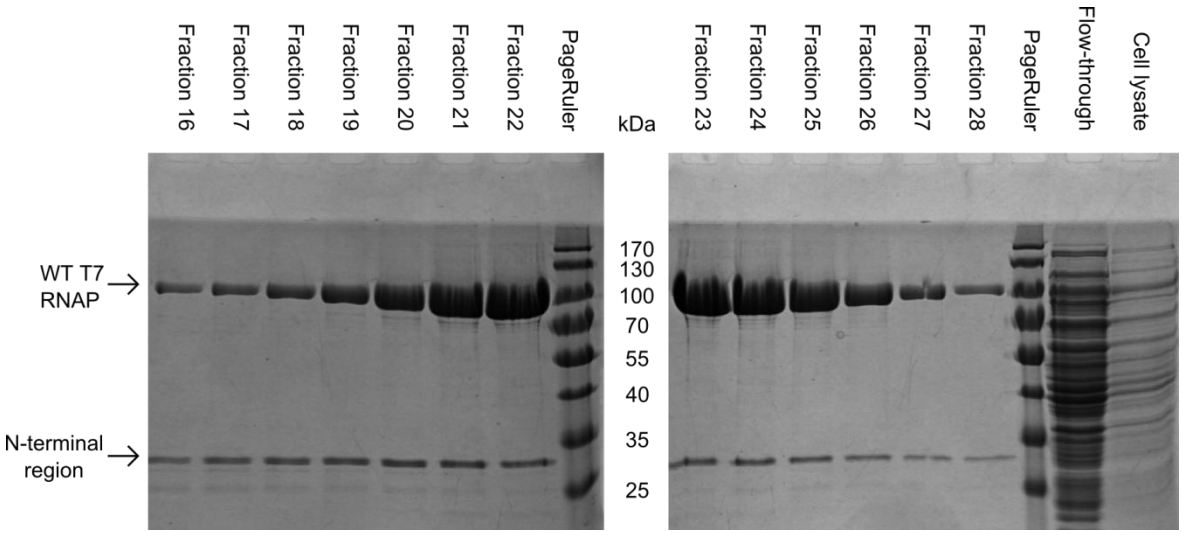


**Figure 2-23 – Analysis of fractions eluted from FPLC**
SDS PAGE gel of fractions 16 through 28, eluted from the HiTrap under an imidazole concentration ranging from 230 mM to 350 mM. The strong single band at ~100 kDa corroborates the optical density measurements from the FPLC that protein elution was centred on an imidazole concentration of 295 mM.

### 2.4.1.2 Biotinylation of wild-type T7 RNAP

To facilitate conjugation of T7 RNAP with commercially-purchased streptavidin-functionalised TransFluoSpheres (TFS; Invitrogen, Carlsbad, California, USA) or Q-Dots (Invitrogen, Carlsbad, California, USA) the enzyme must be biotinylated. A covalent linkage is formed between the enzyme and biotin via reaction of the maleimide group in biotin-maleimide with the thiol of surface-accessible cysteine residues.

Following production as described in Section 2.4.1.1, the protein is suspended in dialysis buffer (Section 2.1) containing dithiothreitol (DTT); however, the thiol in this molecule is incompatible with the labelling method used due to its reactivity with maleimide. Resultantly, the RNAP is transferred to an identical buffer containing TCEP as the reducing agent. Buffer exchange is achieved in a step-wise manner, starting with dialysis against buffer containing 1 mM DTT, then 1 mM TCEP and finally 0.2 mM TCEP. A volume of 700 µl 18 µM RNAP was placed in 12-14 kDa molecular weight cut-off dialysis

tubing. Each dialysis step was performed twice, against 1 litre of fresh buffer and for a minimum of 12 hours per step. Following dialysis, 2100 µl of protein was recovered and measured with a Nanodrop (ND-1000; Thermo Fisher Scientific, Massachusetts, USA) to have a concentration of 4.47 µM. The protein concentration was increased using a 30,000 MW cut-off VivaSpin 20 (Sartorius Stedim Biotech GmbH, Göttingen, Germany) spun for 3 minutes at 8000 xg, which left 750 µl protein (from a starting volume of 1600 µl) that was measured using a Nanodrop to have a concentration of 11.5 µM. This represents a 2.5-fold increase in concentration (flow-through concentration was measured to be 0.34 µM).

Biotinylation was performed in two steps, with 0.8 µl 100 mM biotin maleimide (dissolved in DMSO) added to 700 µl 11.5 µM WT-T7 RNAP in two 0.4 µl aliquots. Following each biotin maleimide addition the sample was mixed via inversion on a vertically-inclined turntable for 15 minutes at room temperature. Labelled protein was dialysed against 1 mM DTT in dialysis buffer to remove excess biotin-maleimide. Purification of labelled protein used an avidin affinity column (Soft Link; Promega, Wisconsin, USA), inside which biotin binds resin-immobilised avidin, to be subsequently eluted upon addition of an excess of free biotin. The column was used in accordance with the vendor-supplied protocol using an equilibration buffer containing the maximum recommended salt concentration to aid protein stability: 200 mM NaCl, 10 mM Tris, 1 mM EDTA, 1 mM DTT and made to 50 ml with ultrapure water (18.2 MΩ•cm; Purelab Ultra; Elga, Marlow, UK). Briefly, the avidin is initially denatured with 10% acetic acid to release any bound biotin; then allowed to refold in sodium phosphate buffer (one part $NaH_2PO_4$ to two parts $Na_2HPO_4$ at pH 7). Biotinylated RNAP was diluted four-fold in equilibration buffer and added in 500 µl stages to the avidin column, with 10 minute incubations between each. Bound protein was eluted by addition of 10 ml 5 mM free biotin, with the eluted protein collected in ten 1 ml fractions.

Presence of biotinylated RNAP was confirmed using denaturing SDS PAGE analysis (10% SDS gels), in which all ten fractions were run in addition to the column flow-through from sample loading and wash steps. Each sample contained 15 µl of protein mixture and 4 µl of 4x loading buffer (see Section 2.1 for composition) and a 10 µl aliquot of PageRuler (Thermo Fisher Scientific, Massachusetts, USA) per gel was run for size reference. Gels were run at a constant voltage of 150 V for 90 minutes at room temperature, before

staining in Coomassie Blue (see Section 2.1 for composition**)** for 30 minutes and destaining overnight in water (Figure 2-24).

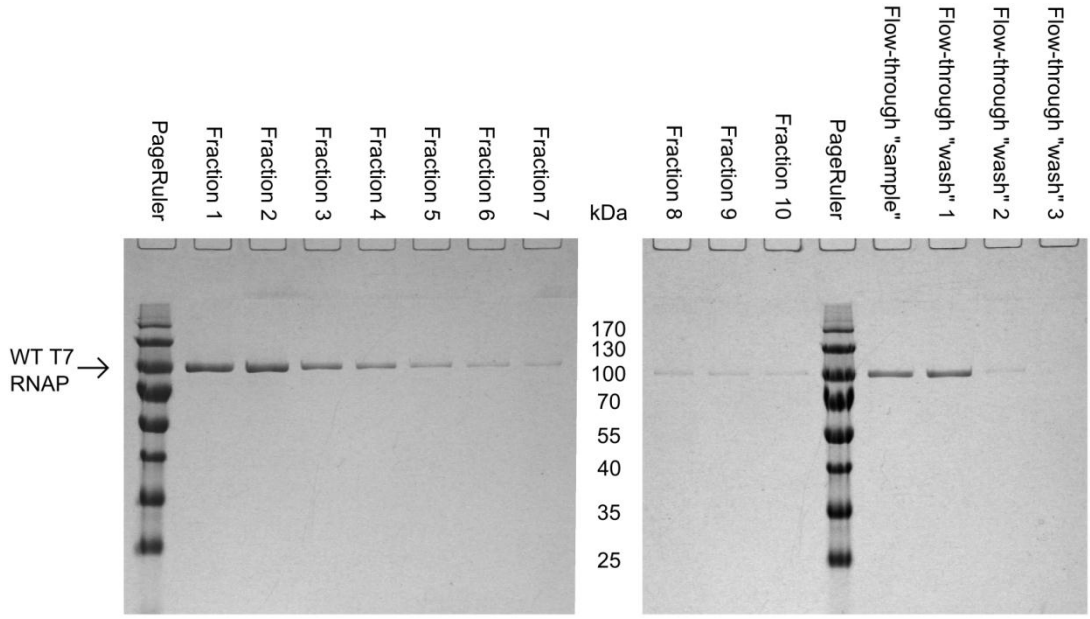


**Figure 2-24 – WT T7 RNAP elution from the avidin affinity column**
Purified biotinylated wild-type T7 RNAP, eluted from SoftLink avidin affinity column, analysed on two 10% SDS PAGE gels. The presence of a band in the sample-loading flow-through and first wash step is due to both unlabelled protein and biotinylated protein, which did not bind to the column. Significant reduction of eluted protein in subsequent wash steps indicates immobilisation of RNAP in the column. Elution of biotinylated RNAP commenced upon addition of a free biotin excess, as expected, with the majority of protein eluting in the first three 1 ml fractions.

Following SDS PAGE verification of successful biotinylation, fractions 1 to 3 were combined and dialysed against dialysis buffer (1 mM DTT) to remove any free biotin. The concentration of the dialysed fractions was measured to be approximately 300 nM using a Nanodrop.

#### 2.4.1.3 Verification of biotinylated wild-type T7 RNAP transcriptional activity

Transcriptional activity of the biotinylated RNAP was demonstrated using a bulk transcription assay (see Section 2.6.3 for general method). In addition to biotinylated RNAP at final concentrations of 10 nM, 50 nM and 100 nM, unlabelled RNAP from different steps in the labelling process were tested. A positive control of commercially-purchased T7 RNAP (Promega, Wisconsin, USA) at a final protein concentration of 770 nM, and negative controls, one with no RNAP and one with just DNA, were used for comparison of activity. In addition to RNAP, each sample contained the following: 1.4 µl 69.4 nM pUC-Φ600 PCR product DNA (see Section 2.3.3), 1.4 µl 5x T7 RNAP transcription buffer, 0.7 µl 100 mM DTT (Melford, Ipswich, UK), 0.4 µl RNasin

(Promega, Wisconsin, USA), 0.3 µl 25 mM rNTPs (each species at 25 mM) and made to a final volume of 7 µl with ultra-pure water (18.2 MΩ•cm; Purelab Ultra; Elga, Marlow, UK). The DNA-only negative control contained 1.4 µl pUC-Φ600 PCR product DNA and 5.6 µl of ultra-pure water. Samples were incubated at 37 °C for 2.5 hours, followed by addition of 7 µl of 2x transcription stop buffer and further incubation at 70 °C for 5 minutes. Electrophoresis used a 6% urea acrylamide gel (pre-run at 100 V constant current for 1 hour), onto which 10 µl of each sample was loaded, along with 10 µl of low-range RiboRuler (Fermentas, Burlington, Canada) pre-heated at 80 °C for 5 minutes. The gel was run at 100 V constant current for 90 minutes, then stained in ~1 µg/ml ethidium bromide for 20 minutes, followed by a 20 minute destain in ultra-pure water.

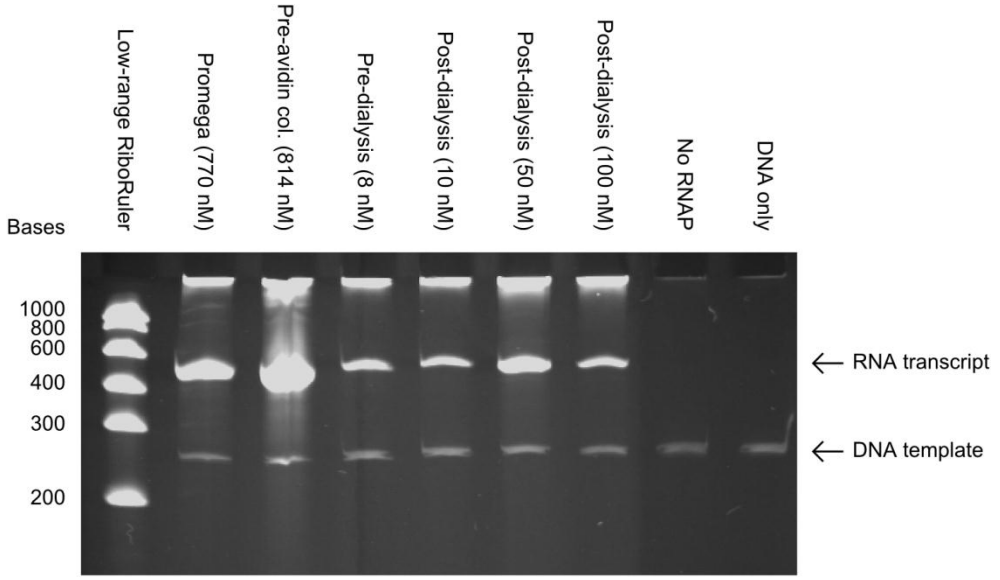


**Figure 2-25 – Bulk transcription assay with biotinylated WT T7 RNAP**
Demonstration of transcriptional activity for the biotinylated wild-type T7 RNAP using a bulk transcription assay run on a 6% urea acrylamide gel. Comparison of the first six sample lanes shows a band at approximately 510 bases corresponding to the expected RNA product. The highest production rate is observed for pre-avidin column RNAP, which also has the highest protein concentration. Importantly, the biotinylated enzyme shows good activity, comparable to the commercially-available Promega RNAP, but at a much lower protein concentration. The negative controls verify that the presumed RNA band cannot be explained due to protein or the DNA template.

Analysis of the transcription assay products (Figure 2-25) demonstrate that all samples containing a full transcription mixture exhibit a single RNA band of the expected length (510 bases), proving transcription has occurred. It appears that the biotinylated RNAP has a better transcriptional activity than the commercially bought enzyme. There appears to be negligible difference in RNA production between the three biotinylated samples (10 nM, 50 nM and 100 nM). The two negative controls show the lower, darker band is due to the template DNA and that the RNA band cannot be attributed to the assay components.

### 2.4.2 Digoxigenin-BSA for surface immobilisation of DNA tethers

For efficient functionalisation of surfaces within microfluidic devices, the target molecule can be coupled to bovine serum albumin (BSA), which exhibits useful surface passivation properties. Using the same technique as employed by Schlehuber *et al.*, BSA can be coupled through the N-terminal amino group to a digoxigenin-hydroxysuccinimide ester (dig-NHS; Roche Applied Science, Penzberg, Germany) in a reaction containing a ten-fold excess of dig-NHS to BSA [98].

Dig-BSA is prepared using the following reaction: 25 µl 120 mM dig-NHS diluted in DMSO and 1 ml 0.3 mM ultrapure BSA (P2489; Invitrogen, Carlsbad, California, USA) diluted in of 5% (W/V) $NaHCO_3$ (pH 8.1) incubated for an hour with continuous stirring at room temperature. Subsequently, a 1 ml volume of the conjugated dig-BSA was purified via a pair of dialysis steps against 1 litre of 1x TE buffer at 4 °C, over the course of two days. Following dialysis, 1.3 ml of protein was recovered, with a concentration of 26 µM measured using a UV biospectrophotometer and the Beer-Lambert law ($\lambda$ = 280 nm, $\varepsilon_{280}$ = 43824 $M^{-1}cm^{-1}$).

### 2.4.3 Effect of fluorophore on RNAP processivity

Fluorophore labelling of the polymerase raises the possibility for a drag-mediated effects on processivity. This could be especially significant when using fluorophores such as 40 nm diameter TransFluoSpheres or 15-20 nm diameter Q-Dots, both of which are larger than the approximate T7 RNAP diameter of 6 nm [27]. To evaluate this effect the drag force acting on the fluorophore as it passes through the buffer can be estimated. According to Skinner *et al.*, forces less than 3 pN acting against the motion of T7 RNAP result in negligible changes in processivity [26].

$$F_d = 6\pi\eta R v$$

**Equation 2-2 – Stokes law for calculating drag force on a sphere in laminar flow**
Drag force ($F_d$) acting on a sphere passing through a liquid under laminar flow conditions is a function of the medium dynamic viscosity ($\eta$), sphere radius ($R$) and sphere velocity ($v$).

Assuming a spherical fluorophore and laminar flow conditions, characterised by a very small particle passing through a viscous medium, the drag force ($F_d$) acting on the fluorophore can be estimated using Equation 2-2. The elongation rate of T7 RNAP has been reported as 43 nt/s, which corresponds to a velocity of 14.62 nm/s using a rise per

base-pair of 0.34 nm [90]. Taking the dynamic viscosity ($\eta$) to be 1.002 x$10^{-3}$ Nm/s this yields forces of 5.5 x$10^{-6}$ pN and 2.4 x$10^{-6}$ pN for TransFluoSpheres and Q-Dots, respectively. Both calculated forces are several orders of magnitude lower than the reported 3 pN limit for deleterious effects on T7 RNAP processivity. In terms of hydrodynamic drag, the presence of RNAP-conjugated fluorophores has a negligible effect.

## 2.5 Preparation and characterisation of other materials

### 2.5.1 Functionalisation of 9 µm diameter microspheres with anti-digoxigenin

Horizontal DNA tethers in the magnetic tweezers microscope are achieved via attachment of DNA between anti-digoxigenin functionalised 9 µm latex microspheres and streptavidin-functionalised superparamagnetic microspheres (M280; Life Technologies, Carlsbad, California, USA). Functionalisation of the latex microspheres (MS) is done using a method based on that from Baumann and Cross [64]. Both Protein A/G and antibody concentrations are equivalent to those from the paper, despite the stocks employed here having approximately a quarter the net MS surface area, due to their larger radius (9 µm compared to 2 µm in the paper). Resultantly, the proteins have a four-fold excess compared to those recommended. Had this appeared to detrimentally affect functionalisation, the concentrations would have been decreased.

Prior to and following each incubation step, MS are repeatedly washed using a vortex (30 seconds at 1200 RPM), centrifuge (2 minutes at 750 xg) and resuspend (remove and replace the same volume of buffer) cycle, which should remove any unbound protein. The Protein A/G functionalisation steps are conducted in BSA-passivated microcentrifuge tubes. To prepare these, 1.5 ml tubes are incubated at room temperature for 2 hours on a vertically-inclined turntable with a 1 ml solution of PBS and 10 mg/ml acetylated BSA (B8894; Sigma-Aldrich, Missouri, USA). Following passivation, the tubes are washed with ultra-pure water (18.2 MΩ•cm; Purelab Ultra; Elga, Marlow, UK) and stored at 4 °C until required.

A stock of 4% (w/v) sulphate-aldehyde functionalised MS (A37307, Invitrogen, Carlsbad, California, USA) were washed and resuspended in 25 mM MES buffer (pH 6.0) to a final concentration of 2% (w/v) in which, Protein A/G (Purified Recomb® Protein A/G from E.

coli, Pierce) was added to a final concentration of 0.42 mg/ml. This mixture was incubated overnight at room temperature on a vertically-inclined turntable to ensure continuous mixing and thus preventing sedimentation of MS. Following incubation, the Protein A/G-coated MS (PAG-MS) were pelleted (2 minutes, 750 xg), resuspended to a final concentration of 2% (w/v) in glycine to quench the labelling reaction and incubated at room temperature on the turntable for 40 minutes. The PAG-MS are then repeatedly washed in PBS with 2 mg/ml acetylated BSA and resuspended to a final concentration of 2% (w/v) in a PBS mixture with 2 mg/ml acetylated BSA and 0.01% (w/v) sodium azide. This mixture is stored at 4 °C until required.

To attach anti-digoxigenin antibody to the PAG-MS, the MS solution was washed multiple times, and resuspended, in TetBu+ buffer (TE buffer, 172 mM NaCl, 0.1 mg/ml acetylated BSA) to a final concentration of 2% (w/v). The washed PAG-MS mixture was incubated with anti-digoxigenin at a final concentration of 160 µg/ml at room temperature for 1 hour. To ensure the PAG-MS remained suspended in the labelling mixture, the tube was occasionally agitated by hand. Excess antibody was removed from the mixture containing Protein A/G and anti-digoxigenin functionalised MS (PAG-AD-MS) by repeated washing steps in TetBu+, with final PAG-AD-MS resuspension to a concentration of 2% (w/v). These stocks were initially stored at 4 °C until required; however, poor performance with DNA tethering indicated anti-digoxigenin functionalisation needed to be conducted immediately prior to use.

### 2.5.2 Microsphere size distributions

In addition to the Protein A/G functionalised 9 µm diameter microspheres described in Section 2.5.1, two types of superparamagnetic microsphere are also used in the discussed work. These superparamagnetic microspheres are used to manipulate tethered DNA, with their motion controlled via an applied magnetic field. Since the characteristics of this response depend strongly upon the physical properties of the microspheres, a precise knowledge of particle size distributions for each stock is paramount. The two stocks of superparamagnetic microsphere are MyOne (Invitrogen, Carlsbad, California, USA), which have a vendor-specified diameter of 1.05 µm (CV <5%) and M280 (Invitrogen, Carlsbad, California, USA), which have a vendor-specified diameter of 2.8 µm (CV <3%).

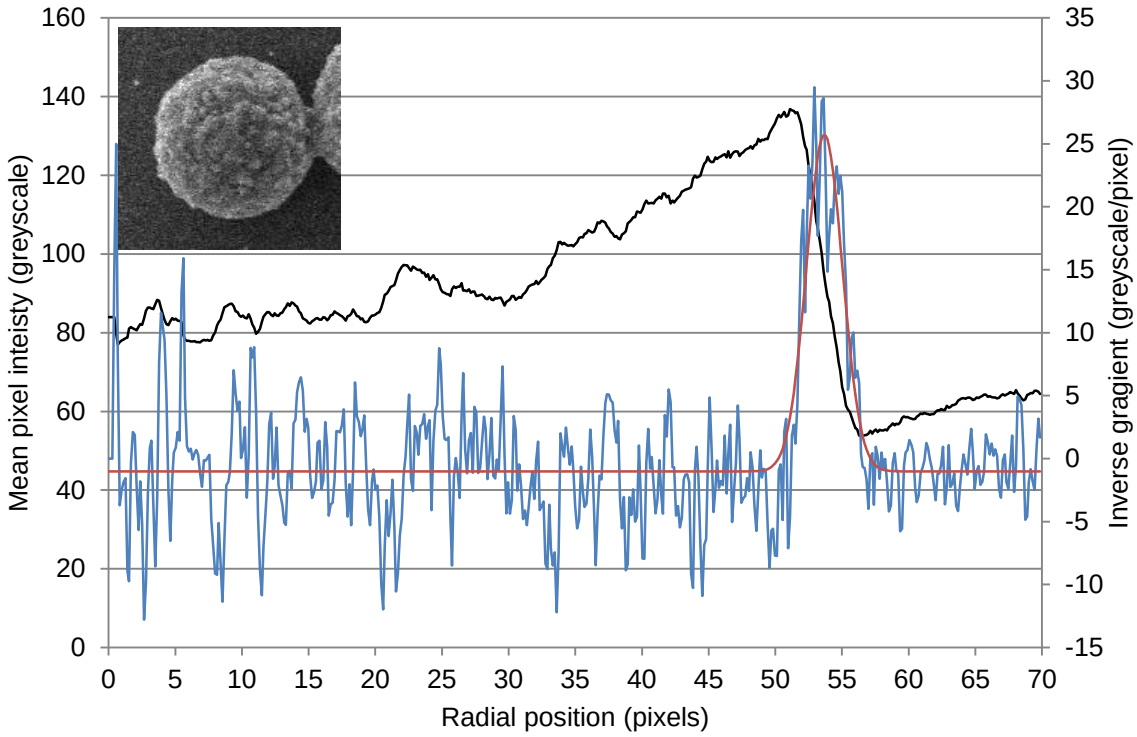


**Figure 2-26 – Measurement of microsphere diameter using mean radial intensity profile**
Example data used to determine the radius of a 2.8 µm diameter superparamagnetic microsphere. A mean radial intensity profile (black line; primary vertical axis) calculated from 300 constituent lines and differentiated (blue line; secondary vertical axis). This differentiated profile was fit with a standard Gaussian curve (red line; secondary vertical axis) and the centre of the peak taken to correspond to the microsphere edge. (inset) SEM image of measured microsphere.

A series of SEM (JSM 6490; JEOL, Tokyo, Japan) images were collected by Meg Stark (Technology Facility, University of York) for both stocks of superparamagnetic as well as 9 µm microspheres. Stocks were diluted to appropriate concentrations in deionized water (18.2 MΩ•cm; Purelab Ultra; Elga, Marlow, UK) and a few microliters deposited on an ethanol-cleaned silicon wafer and allowed to dry. This was subsequently sputtered with ~7 nm of gold/palladium to provide contrast in the microscope. The SEM was calibrated using a metal replica of a cross-grating with 2160 lines/mm. For each magnification, a set of 50 grid measurements were taken (10 lines per measurement) using ImageJ and a mean value calculated. Particle size distributions were measured using a custom MATLAB script (function *particleSizeDist.m*; Accompanying Material), which requires the user to specify the centre location and radius of each particle using an integrated graphical user interface (GUI). Linear pixel intensity profiles are measured radially from each centre point (black line; Figure 2-26), then averaged and differentiated with respect to radial position (blue line; Figure 2-26). A Gaussian curve is fit to each differentiated profile (red line; Figure 2-26) and the peak centre taken to correspond with the microsphere edge.

Averaging profiles around the microsphere should compensate for slight inaccuracies in centre identification, resulting in a slight broadening of the Gaussian profile.

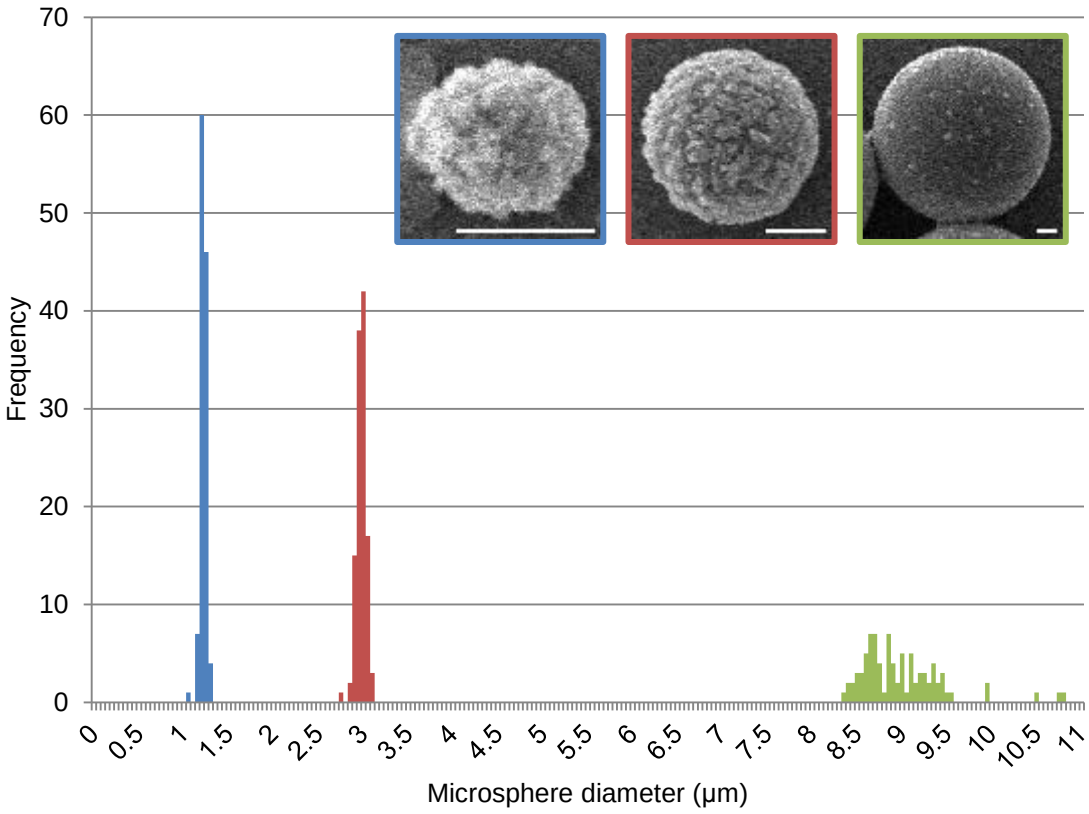


**Figure 2-27 – Measured microsphere particle diameter distributions**
Well defined size distributions are observed for both superparamagnetic microsphere stocks, but not for the larger, 9 µm microsphere. MyOne microspheres (blue distribution) have a vendor-specified diameter of 1.05 µm (CV <5%), but were measured at 1.192 ± 0.003 µm (n = 118). Conversely, the M280 microspheres (red distribution) were measured at 2.947 ± 0.005 µm (n = 130), which is within the expected 3% range. The 9 µm microspheres (green distribution) have a very large size distribution, but were measured to have a mean diameter of 9.23 ± 0.09 µm (n = 94), which is close to the expected value. (inset) Example SEM images of each size of microsphere (MyOne, M280 and 9 µm; left to right). Image border colour corresponds to data shown. Scale bar on each image is 1 µm.

Both MyOne and M280 microspheres exhibit well defined distributions (Figure 2-27) with mean values at 1.192 ± 0.003 µm (n = 118) and 2.947 ± 0.005 µm (n = 130), respectively, while the 9 µm microspheres yielded a much larger distribution centred on 9.23 ± 0.09 µm (n = 94). In the case of the two larger microsphere stocks the measured and expected diameters fell within an acceptable range; however, the MyOne microspheres were measured to be ~13% larger than expected. This is discrepancy is significantly greater than the 5% range specified by the vendor, but is in close agreement with the observed diameter of 1.17 µm predicted by Lipfert *et al.* [99]. It should be noted that Lipfert *et al.* simply used bead diameter as a fitting parameter and that no direct size measurements were made [99].

For the purpose of force prediction in the horizontal magnetic tweezers microscope (Section 4.2), the measured microsphere diameters shall be used.

### 2.5.3 Cubic NdFeB magnet remanence

Force application in a magnetic tweezers system is strongly dependent upon the properties of the magnets employed. This force response is characterised in particular by the remanence ($B_r$), which is the magnetisation remaining in the magnets in the absence of an externally applied field. The cubic gold-plated NdFeB magnets (W-05-N50-G; Supermagnete, Gottmadingen, Germany) used in the magnetic tweezers microscope have a manufacture-specified remanence of $B_r$ = 1.40 – 1.46 T; however, a value of 1.24 ± 0.08 T has been measured elsewhere [99].

Verification of remanence in the available magnet stock was performed using the method of Lipfert *et al.*, whereby a standard Hall probe (WT-3A; Bostech Ltd., York, UK) is used to measure the flux density ($B_x$) at the magnet pole [99]. This value is subsequently converted to remanence with Equation 2-3. A series of 48 measurements was made, with 4 measurements at each magnet pole for 6 individual magnets. Magnets were rotated 90° about an axis parallel to the magnetisation direction following each measurement. The finite size of the Hall probe precluded precise measurement of remanence through ambiguity in the magnet-to-probe separation ($x$); however, assuming readings to be greatest at the core of the probe, as was consistent with measured flux densities, a separation of 0.5 ± 0.1 mm was deduced.

$$B_r = \pi B_x \left[ \arctan\left( \frac{l^2}{2x\sqrt{4x^2 + 2l^2}} \right) - \arctan\left( \frac{l^2}{2(l+x)\sqrt{4(l+x)^2 + 2l^2}} \right) \right]^{-1}$$

**Equation 2-3 – Magnetic remanence from a single cubic magnet**
Remanence is a function of the magnetic flux density ($B_x$) at a distance ($x$) from the magnet pole surface. In this configuration, the x-axis is parallel with the magnetisation axis of the magnet. Each magnet has equal edges of length, $l$.

Across the 48 measurements an average flux density ($B_x$) of 449 ± 6.4 mT was measured. Calculation of remanence from this value requires evaluation of the Hall probe to magnet distance ($x$); in the absence of vendor-supplied technical data for the probe this was estimated to be 0.5 ± 0.1 mm, which takes into account the finite size of the probe. Substitution of $B_x$ and $x$ into Equation 2-3 yields a remanence ($B_r$) of 1.26 ± 0.05 T, where

the stated accuracy corresponds to evaluation of $B_r$ at the extremes of $x$. A measured remanence slightly less than stated by the manufacturer is consistent with a value of 1.24 ± 0.08 T observed by Lipfert *et al.* for an equivalent magnet stock [99].

## 2.6 Methods used during preparation of materials

### 2.6.1 Bacterial transformation and cell culture

Plasmid DNA was produced in DH5α bacterial strain cells. This used a previously-established transformation protocol, frequently used in the lab. For each transformation, 50 µl of competent cells (previously prepared using the Hanahan Method [100] and stored at -80°C) are thawed on ice and transferred to a chilled 2 ml microcentrifuge tube. An aliquot of the plasmid (20 – 100 ng) is added to the cells to a final concentration of 20-100 ng/ml, and then the sample is gently flick-mixed and left to incubate on ice for 20 minutes. The competent cells are transformed using a heat-shock step in which the tube is placed on a preheated heating block at 42°C for 45 seconds, then incubated on ice for a further 2 minutes. Next, 450 µl of pre-warmed, sterile LB medium is added to the sample, followed by incubation for 1 hour at 37°C with shaking (200 rpm).

LB-agar plates, pre-prepared with the relevant antibiotic selection, are used to culture colonies of the transformed bacteria. 100 µl of transformed cells are evenly distributed onto the plates using a flame-sterilised glass bar and allowed to be absorbed by the LB-agar. The plates are incubated overnight at 37°C with the LB-agar side up, which prevent condensation forming on the lid and transferring cells between colonies. Following overnight incubation, individual colonies are transferred to 10 ml of autoclave-sterilised LB using a flame-sterilised metal loop and incubated overnight at 37°C.

Overnight cultures are centrifuged at 5000 xg for 10 minutes at 4°C to form a cell pellet. The expressed DNA is then extracted from this cell pellet using a QIAprep Spin Miniprep Kit (Qiagen, Netherlands) and the recommended protocol. Gel electrophoresis with a 1% agarose gel is used to verify the presence of the target plasmid. Generally, DNA samples for electrophoresis comprise 1 µl DNA, 2 µl loading buffer (Yorkshire Biosciences Ltd., York, UK) and 2 µl ultra-pure water (18.2 MΩ•cm; Purelab Ultra; Elga, Marlow, UK).

### 2.6.2 Standard PCR protocol

PCR reactions were conducted using the following reagents unless otherwise stated: 5 µl 10x buffer for KOD Hot Start DNA Polymerase (Novagen, Germany), 5 µl 2 mM dNTPs (Novagen, Germany), 4 µl 25 mM $MgSO_4$ (Novagen, Germany), 1.5 µl 10 µM forward primer, 1.5 µl 10 µM reverse primer, 1 µl 1 U/µl KOD Hot Start DNA Polymerase (Novagen, Germany). Approximately 50 ng of DNA and ultra-pure water (18.2 MΩ•cm; Purelab Ultra; Elga, Marlow, UK) were added to make a final reaction volume of 50 µl, where the ratio varied depending on stock DNA concentration. Reactions were performed in a thermal cycler (Px2, Thermo Fisher Scientific, Massachusetts, USA) using the settings shown in Table 2-3.

**Table 2-3 – Settings for standard PCR reactions**
The stages shaded in grey were cycled 25 times. Following completion of all steps, samples were held at a constant temperature of 4 ºC.

| **Temperature** | **Time** |
|---|---|
| 94 °C | 120 seconds |
| 94 °C | 15 seconds |
| 62 °C | 30 seconds |
| 72 °C | 60 seconds |
| 72 °C | 300 seconds |
| 4 °C | Hold |

### 2.6.3 Bulk transcription assays using T7 RNA polymerase

For the purpose of verifying T7 RNAP promoter sequences are intact (see Section 2.3.8) or demonstrating the production of active T7 RNAP (see Sections 2.4.1 and 2.4.1.2) bulk transcription assays are used. A standard bulk transcription assay sample contains the following: 1.4 µl 5x T7 RNAP transcription buffer (200 mM Tris-HCl, 50 mM NaCl, 30 mM $MgCl_2$), 0.4 µl 40 U/µl RNasin (Promega, Wisconsin, USA), 0.7 µl 100 mM DTT and 0.3 µl 25 mM rNTPs (each rNTP at 25 mM in stock). The DNA template and RNAP are added at experiment-specific concentrations and the entire mixture made up to a final volume of 7 µl with ultra-pure water (18.2 MΩ•cm; Purelab Ultra; Elga, Marlow, UK). Samples are incubated at 37 °C for 2 hours. Transcription is stopped through addition of

7 µl 2x transcription stop buffer (see Section 2.1 for composition) and heating at 70 °C for 5 minutes, which quenches enzymatic activity and denatures secondary structure in the RNA transcripts.

Transcriptional activity is determined by running the samples on a 6% urea acrylamide gel, which is later stained with the intercalating fluorescent dye ethidium bromide (~1 µg/ml). Any RNA present, indicative of successful transcription, shows up as a bright band on the gel. The 6% urea acrylamide gels are prepared by heating a mixture of 2.63 g urea, 1.25 ml 5x TBE (90 mM Tris base, 90 mM boric acid and 2 mM EDTA, made up using ultra-pure water) and 1.325 ml ultra-pure water until the urea has dissolved. At this point, a further 1.045 ml of ultra-pure water is added and the mixture allowed to cool. When approaching ambient temperature 0.94 ml 40% acrylamide/bis-acrylamide (19:1 ratio; Sigma-Aldrich, Missouri, USA), 30 µl 10% ammonium persulphate (APS, 98% minimum; Sigma-Aldrich, Missouri, USA) and 7.5 µl Tetramethylethylenediamine (TEMED, 99%; Sigma-Aldrich, Missouri, USA) are added, which cause polymerisation to begin. Quickly, the gel mixture is transferred to the gel casting unit, with the well-forming comb inserted immediately after gel, then allowed to cool for 20 minutes. Prior to use, gels are run at 100 V for 1 hour to remove contaminants. The gel is run for 2 hours at 100 V constant voltage mode, then stained in 1 µg/ml ethidium bromide for 20 minutes before being destained in water for a further 20 minutes and imaged under UV illumination.

## 2.7 Single-molecule fluorescence techniques

### 2.7.1 Reduced oxygen and oxygen scavenger systems

Formation of reactive oxygen species (ROS) in single-molecule fluorescence experiments is a persistent concern, especially for tethered-DNA setups where these molecules catalyse single-strand nicks in the DNA backbone [101–103]. ROS are generated by excitation of fluorophores, such as the DNA-intercalating dye YOYO-1, and ultimately lead to double-strand template breakage; an outcome, which has clear deleterious implications for experimental lifetime. Minimisation of ROS formation, and the accompanying increase in tether stability, can be achieved using oxygen scavenger systems. Characterisation of such systems is described in detail in Section 5.4.1; however, included here is a summary of the standard technique using the glucose oxygen scavenger [104].

Buffer for the scavenger system depends on the experiment being conducted, but is always either degassed under vacuum with stirring for at least 15 minutes to remove oxygen, or bubbled with $N_2$, which replaces $O_2$ [102,105,106]. Immediately following removal of oxygen, the following components are combined (example final volume of 1 ml): 960 µl degassed buffer, 20 µl 1 M DTT (Melford, Ipswich, UK), 10 µl 300 mg/ml glucose (Fisher Scientific, Waltham, Massachusetts, USA), 5µl 10 mg/ml glucose oxidase (Sigma-Aldrich, St. Louis, Missouri, USA) and 5 µl 2 mg/ml catalase (Sigma-Aldrich, St. Louis, Missouri, USA). The oxygen scavenger mixture is stored on ice (or at 4 °C) in a 1 ml syringe and capped with a needle to minimise the surface area exposed to air. This must be prepared fresh on the day of use.

### 2.7.2 Preparation of substrates for single-molecule experiments

For single-molecule experiments, where biomolecules may be directly attached to sample surfaces, it is imperative that substrates are chemically clean. In the case of two commonly used substrates, glass coverslips and quartz slides, detergent and potassium hydroxide cleaning protocols were implemented, respectively. Glass coverslips (22 mm x 64 mm, No. 1; Menzel-Gläser, Braunschweig, Germany) and quartz slides (75 mm x 25 mm x 1 mm; UQG Optics Ltd., Cambridge, UK) are sonicated (U300 H; Scientific Laboratory Supplies, Hessle, UK) at 50 °C in a 2% (v/v) Neutracon solution (Decon Laboratories Ltd., Hove, UK) for 10 minutes, followed by immediate and thorough rinsing with deionised water. Following this, coverslips and slides are blown dry with compressed filtered air.

### 2.7.3 Preparation of samples for horizontal magnetic tweezers microscopy

One of the ultimate goals of the horizontal magnetic tweezers (HMT) microscope is the ability to visualise fluorescently-labelled RNAP transcribing along horizontally-extended DNA tethers. While this can be achieved through tethering directly to the channel surface (as utilised elsewhere and summarised in Section 1.4.4.1), the finite volume of the superparamagnetic microsphere prevents realisation of a truly horizontal tether. To overcome this, the sample preparation technique described here utilises functionalised 9 µm diameter latex microspheres (PAG-AD-MS; Section 2.5.1), which act in both a mechanical role, separating the slide and coverslip, and as the vertical tethering substrate (Figure 2-29). Preparation of samples in this manner is based on a pair of established

protocols; one for functionalization of microspheres and the other for preparation of samples, using microspheres as the mechanical support between coverslip and slide.

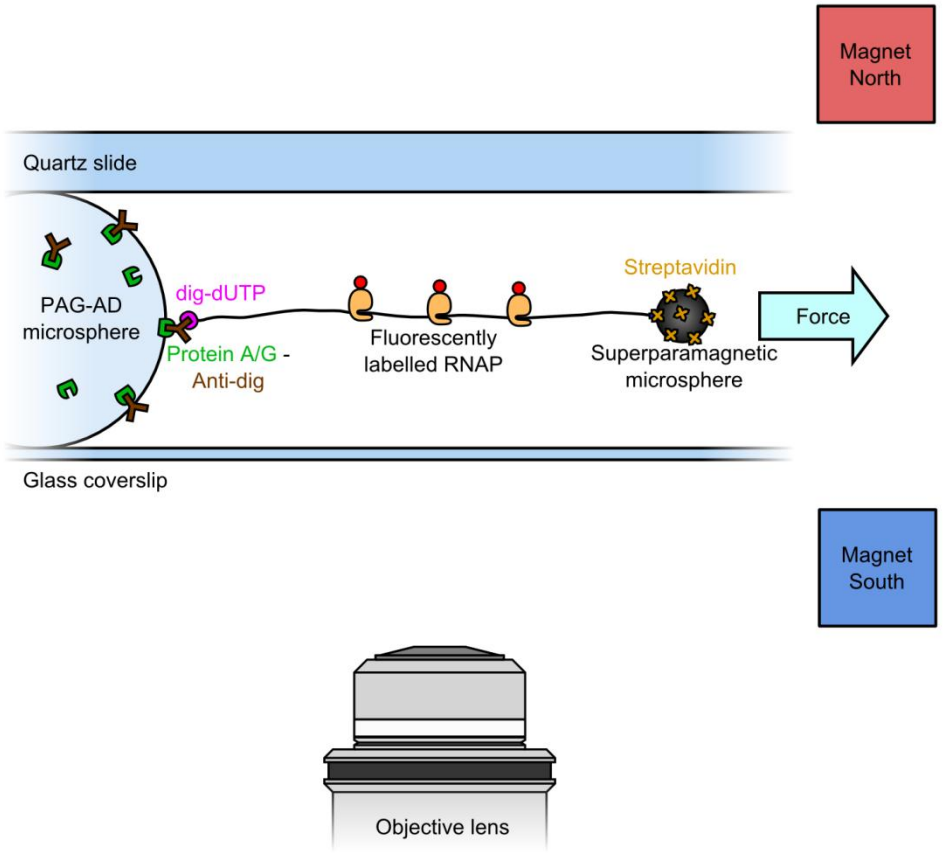


**Figure 2-28 – Schematic diagram of DNA tethering for horizontal magnetic tweezers**
Typical configuration of a horizontal magnetic tweezers sample, with a single DNA tether attached at one end to the 9 µm diameter protein AG/anti-digoxigenin functionalised microsphere (PAG-AD-MS) and at the other to the streptavidin-functionalised superparamagnetic microsphere. The tether is extended horizontally using the force exerted on the superparamagnetic microsphere by a pair of permanent magnets. Fluorescently-labelled RNAP is observed from below using a long working-distance objective lens and wide-field epifluorescence illumination.

Pre-functionalised PAG-MS are labelled with the full anti-digoxigenin antibody immediately prior to the experiment, as described in Section 2.5.1. Simultaneously, commercially purchased streptavidin-functionalised superparamagnetic microspheres (MyOne or M280; both from Life Technologies, Carlsbad, California, USA) are labelled with biotin and digoxigenin end-labelled DNA (Sections 2.3.9). A 50 µl volume of the 10 mg/ml superparamagnetic microspheres are washed three times via magnetic separation and supernatant exchange in TetBu+, followed by final resuspension in 28 µl TetBu+ along with 1 µl 2.8 nM end-labelled DNA (35 pM final concentration). This is incubated for 1 hour at room temperature on a vertically-inclined turntable. Following incubation, any unbound DNA is removed through a further three washes in the previously-described manner.

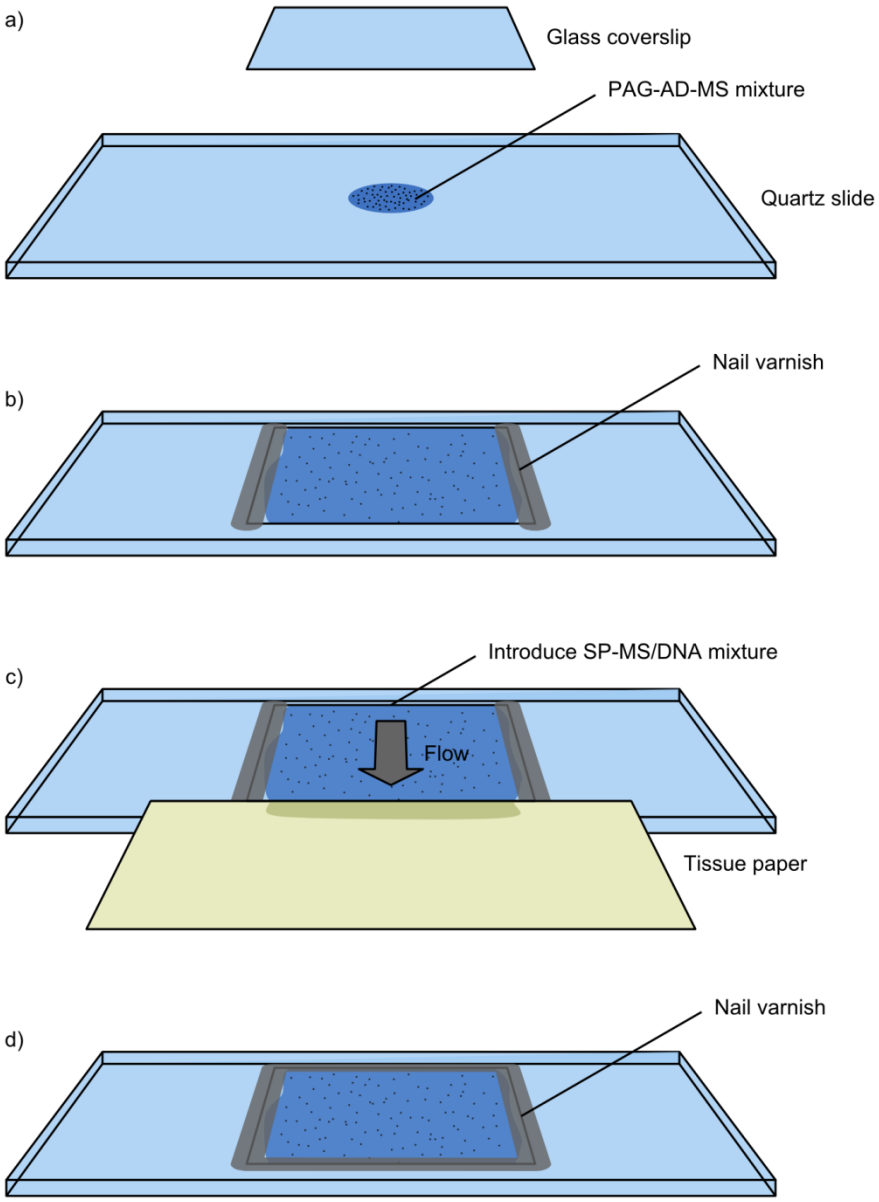


**Figure 2-29 – Sample preparation for the horizontal magnetic tweezers microscope**
a) A small volume (~10 µl) of PAG-AD-MS mixture is deposited on a chemically-cleaned quartz slide and trapped beneath a glass coverslip. b) Opposite edges of the channel are sealed with nail varnish to create a flow-cell. c) Superparamagnetic microsphere/DNA mixture (~30 µl) is introduced along one open end of the channel and drawn through using a piece of tissue paper applied to the opposite end. d) Following introduction of all reagents, the chamber is sealed along the remaining edges with nail varnish.

Sample preparation follows the steps shown in Figure 2-29, whereby approximately 10 µl of 2% (w/v) PAG-AD-MS mixture is deposited in a single drop onto a chemically clean (Section 2.7.2) quartz slide (UQG Optics Ltd., Cambridge, UK) and trapped beneath a coverslip (Menzel-Gläser, Braunschweig, Germany) (Figure 2-29a). The coverslip is sealed to the slide along two opposing edges with nail varnish to create a flow cell (Figure 2-29b). Small volumes of TetBu+ are deposited along the open edges of the channel after the varnish sets to prevent sample evaporation. Further samples, such as the

superparamagnetic microsphere/DNA mixture, are introduced along one open edge of the channel and drawn through using capillary action with a sheet of lens-cleaning tissue paper (Structure Probe Inc., West Chester, Pennsylvania, USA) (Figure 2-29c). Following incubation with all samples, the chamber is sealed along the open edges with nail varnish (Figure 2-29c).

### 2.7.4 Microfluidic surface-functionalisation for single-molecule DNA tethering

Functionalisation of substrates for immobilisation of individual DNA molecules is achieved with sequential incubations, which allow end-labelled DNA (see Section 2.3.9) to be specifically attached at one end. Introduction of reagents to microfluidic channels is performed in two ways, depending on the flow-rate limitations; syringe-introduction where rate-limitations are minimal and tissue-introduction where high flow-rates may result in sample dissociation. For syringe-introduction, the specified volume of mixture is applied to each inlet port and drawn through the channel network via application of negative pressure at the outlet port. Pressure is applied with a 2 ml syringe with a flexible plastic tubing gasket, to provide a seal. Conversely, for tissue-introduction, the mixture is drawn through the channel network by application of an optical tissue at the outlet port. During each incubation step, the inlet and outlet ports are sealed with adhesive tape (Lyreco, Telford, UK).

The following protocol describes functionalisation of the channel with digoxigenin-BSA (dig-BSA) and the whole anti-digoxigenin antibody for immobilisation of digoxigenin-end-labelled DNA; however, the principle is the same for alternative ligand-receptor pairs, such as biotin-streptavidin.

Channel functionalisation begins with non-specific immobilisation of dig-BSA (Section 2.4.2); four channel volumes of 7.5 nM (500 ng/ml) dig-BSA are syringe-introduced into the channel and incubated at room temperature for 45 minutes (Figure 2-30a). Following this, the channel is syringe-flushed with ten channel-volumes of TetBu+ (10 mM Tris, 172 mM NaCl, 1 mM EDTA, 1.5 μM acetylated BSA; corrected to pH 8.0) and any remaining exposed surface passivated through syringe-introduction of four channel-volumes of BSA-Coat (10 mM Tris, 172 mM NaCl, 1 mM EDTA, 15 μM acetylated BSA; corrected to pH 8.0) and incubation at room temperature for 1 hour (Figure 2-30b). Again,

the channel is syringe-flushed with ten channel volumes of buffer TetBu+ to remove the previous mixture.

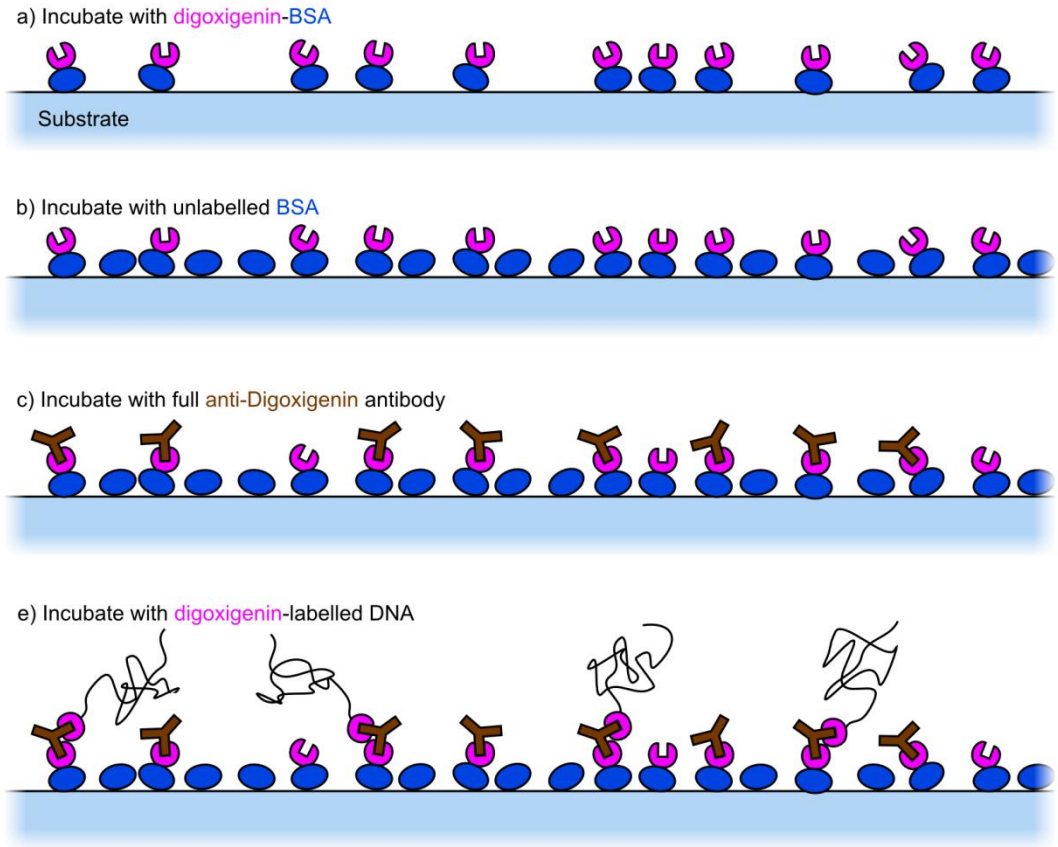


**Figure 2-30 – Surface functionalisation for DNA tethering in a microfluidic device**
a) Non-specific immobilisation of BSA-conjugated digoxigenin via the hydrophobic regions of the BSA surface. b) Passivation of exposed surfaces with BSA to prevent immobilisation of additional reagents. c) Incubation with the whole anti-digoxigenin antibody to functionalise surface-bound digoxigenin. d) Coupling of digoxigenin-end-labelled DNA to unoccupied binding sites on surface-immobilised anti-digoxigenin.

Further functionalisation of the channel surface requires syringe-introduction of a four channel-volume quantity of 17 nM (2.5 µg/ml) anti-digoxigenin whole antibody (polyclonal IgG antibody from sheep; AbD Serotech, now part of Bio-Rad Laboratories, California, USA) and incubation at room temperature for 15 minutes (Figure 2-30c). Next, the channel is syringe-flushed with ten channel-volumes of buffer TetBu+ and finally incubated with four channel-volumes of 0.5 nM digoxigenin-labelled DNA (Section 2.3.9) diluted in TetBu+ (Figure 2-30d). In an additional pair of steps, the channel can be tissue-flushed with ten channel-volumes of TetBu+; then incubated with additional components, such as DNA-binding proteins, tissue-introduced into the channel.

### 2.7.5 Total Internal Reflection Fluorescence (TIRF) microscopy

Bulk excitation of fluorophore in the magnetic tweezers microscope sample chamber leads to a relatively high background fluorescence. This makes identification of single fluorophore labels difficult when compared to a high signal-to-noise approach like Total Internal Reflection Fluorescence (TIRF) microscopy, where only a region 100 nm from the channel surface is fluorescently excited [107]. The obvious spatial restrictions imposed by such a system make it incompatible with a magnetic tweezers system (Chapter 4), where the superparamagnetic microsphere has a diameter of at least 1 μm. In spite of this, TIRF is ideally suited for demonstrating successful transcription by the fluorescently-labelled wild-type T7 RNAP (Section 2.4.1) on hydrodynamically-extended surface-tethered DNA (Section 5.4).

$$n_1 sin(\theta_1) = n_2 sin(\theta_2)$$

**Equation 2-4 – Snell's law for refraction of light**
Light is refracted at the interface between two media with differing indices of refraction. Parameters $n_1$ and $n_2$ are the indices of refraction for the incident and exiting material, respectively. Similarly, $\theta_1$ and $\theta_2$ are the angles of incidence and transmission for the two materials, measured relative to the interface normal.

$$\theta_C = sin^{-1}\left(\frac{n_2}{n_1}\right)$$

**Equation 2-5 – The critical angle for refraction of light at an interface**
Above the critical angle ($\theta_C$) light reflected from the interface is totally internally reflected. This is the special case for Snell's law (Equation 2-4), where $\theta_2 = 90°$.

With TIRF microscopy, a laser incident at the critical angle (Equation 2-5) on the slide-sample chamber interface is totally internally reflected in accordance with Snell's law (Equation 2-4); however, a component of the electric field still permeates a small distance into the sample chamber (Figure 2-31a). The intensity of this component decays exponentially and thus appreciable fluorophore excitation only occurs within approximately 100 nm of the interface. While the incident laser in a TIRF system can be coupled into the sample using either a sample-mounted prism or the objective lens, only the prism-coupled variant will be discussed here. For an equilateral quartz prism ($n_{quartz}$ = 1.463015 [108]) placed above a water-based sample ($n_{water}$ = 1.33738 [109]) and illuminated with a 488 nm laser, the critical angle is 66.1° (at a temperature of 20 °C). Taking the geometric considerations of an equilateral prism into account, this corresponds to an angle of incidence relative to the air-prism interface ($n_{air}$ = 1.000276 [110]) of 8.94°. To enable

refraction-free coupling of the laser to the quartz slide of the sample, refractive index-matching glycerol oil is used between the prism and quartz slide.

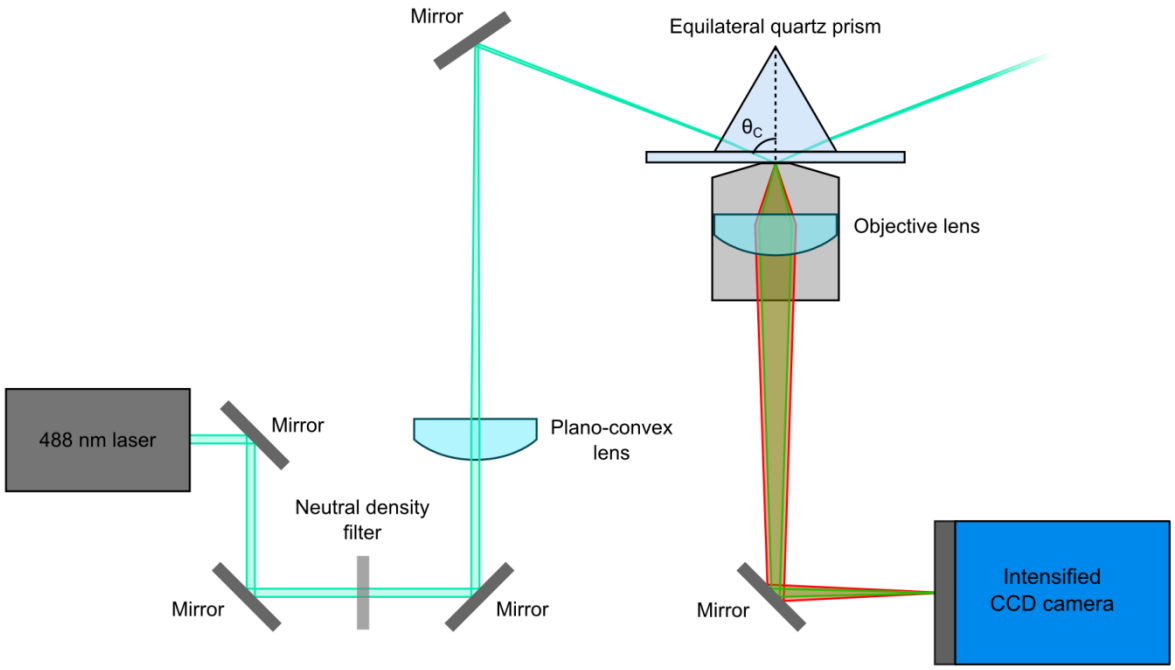


**Figure 2-31 – Optical configuration of the prism-coupled TIRF microscope**
The TIRF microscope is used for visualising transcription by fluorescently-labelled wild-type T7 RNAP on hydrodynamically-extended DNA tethers. The exciting laser (488 nm) is steered using two mirrors, attenuated with a neutral density filter and then finally focussed onto the slide-sample chamber interface at the critical angle, $\theta_C$. From here, the resulting evanescent field excites fluorophores up to 100 nm from the slide surface, with emission collected by the objective lens and directed towards the intensified CCD camera. In this setup the sample chamber is 30 µm high and is positioned on the underside of the quartz slide.

The existing TIRF microscope system (Figure 2-31) used for all experiments was designed and constructed by Urban Seger on an adapted inverted microscope (Zeiss IM35; Carl Zeiss AG, Jena, Germany). TIRF illumination is achieved with a 488 nm laser (other wavelengths can be implemented with minor modification) steered via a pair of mirrors and attenuated with a neutral density filter (optical density depending on application). Following this, the laser is focussed and reflected with a single mirror onto the incident face of the equilateral quartz prism. The refracted laser beam is coupled through to the sample, where it is totally internally reflected at the slide-sample chamber interface. Emission from fluorophores within the evanescent field region is detected with a 100x oil-immersion objective lens (Plan-Apochromat; W.D. = 0.17 mm, N.A. = 1.4; Carl Zeiss AG, Jena, Germany) positioned on the opposite side of the sample. Finally, the light collected by the objective lens is focussed to the intensified camera CCD chip (IC-300; Photon Technology International, New Jersey, USA).

# Atomic Force Microscopy (AFM) of transcription complexes

Chapter 3

## 3.1 Introduction

### 3.1.1 Background to the AFM system

Atomic force microscopy (AFM) is a scanning probe technique capable of both force spectroscopy and two-dimensional imaging; it was developed in the early 1980s as an adaptation of the Scanning Tunnelling Microscope (STM) [111]. The technique utilises the physical deflection encountered by a silicon cantilever as it is rastered across a sample in order to report topographical information. The high precision of AFM permits nanometre lateral and Angstrom vertical resolutions to be measured [65,112,111], thus lending the technique to, among other things, the study of single biomolecules.

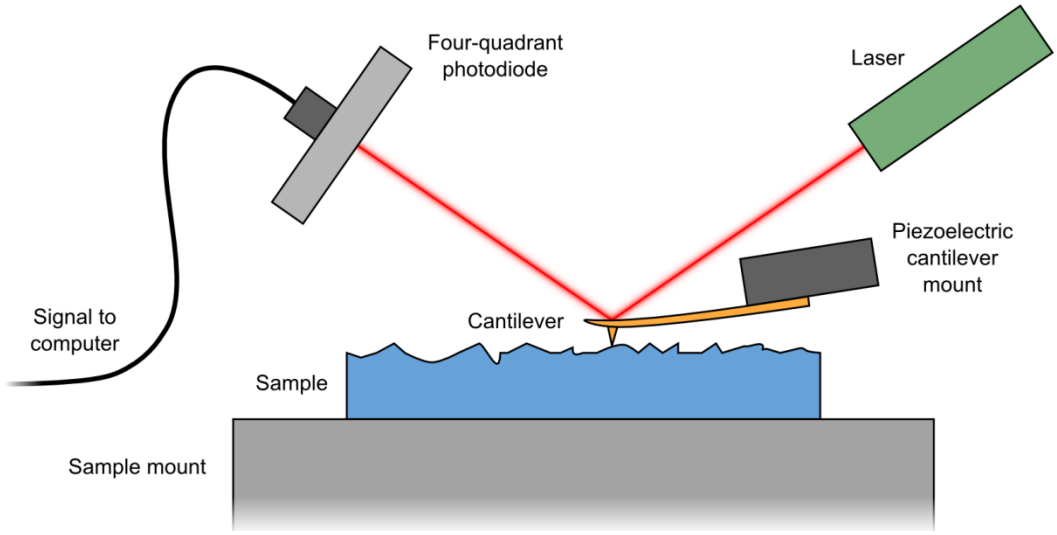


**Figure 3-1 – Schematic diagram of an Atomic Force Microscope (AFM)**
The sample is imaged by raster scanning a cantilever with an atomically sharp tip across the sample using a piezoelectric mount. As the cantilever is bent via interactions with the sample, the laser, incident on the upper face of the cantilever, is deflected across a four-quadrant photodiode. Computational analysis of the resulting signal allows the surface profile to be digitally reconstructed. An alternative AFM design has the sample, rather than the cantilever, attached to a piezoelectric material.

In AFM, an atomically sharp tip on the under-side of a flexible cantilever acts as the imaging probe by interacting with the sample surface in a variety of different ways, depending on the imaging mode being employed. This tip is either raster scanned across the sample via manipulation of a piezo-electric material onto which the cantilever is mounted or the tip is held stationary as the sample is moved in a similar manner. While the latter often yields higher resolution imaging, the former is to be considered only from here on due to the equipment used. As the tip is scanned over the sample it interacts with the sample surface and the cantilever undergoes twisting and bending; this movement is monitored via deflection of a laser incident upon the upper surface of the cantilever and

reflected onto a four-quadrant photodiode (Figure 3-1). Through computational analysis of the signal from the photodiode, a digital representation of the sample topography can be reconstructed.

There are three main techniques through which AFM can be used to extract topographical detail; contact mode (also known as "static" mode), non-contact mode and tapping mode (both also known as "dynamic" mode). In contact mode, the cantilever is raster scanned across the sample using a piezoelectric mount and deflection information from the laser builds up a topographical map of the surface [113]. Deflection of the cantilever in contact mode is the result of the repulsive (short-range) region of the Lennard-Jones potential (Figure 3-2), arising from Pauli repulsion [114–116]. An alternative method for contact mode operation utilises a feedback system through which the sample-tip separation is maintained at a constant value and the feedback system provides the information necessary to compile the surface profile image [114,117]. This mode provides high vertical resolution, but is often too damaging to biomolecular samples due to the relatively high lateral force load [113,114]. Therefore, a less destructive method for tip-sample interaction is required, which is achieved through operating the AFM in tapping mode.

In non-contact mode the cantilever is oscillated close to its resonant frequency and brought into close proximity with the sample. Interaction between the tip and sample is reported as a variation in the cantilever frequency, phase and amplitude of vibration [114,117], with closer interaction resulting in more significantly altered oscillations. The sample-tip spacing is larger than that for contact mode operation and results in interactions being dominated by the attractive region of the Lennard-Jones potential (Figure 3-2), thus corresponding primarily to Van der Waals and ionic interactions [113–116]. Since the average forces involved in non-contact mode operation are approximately a thousandth of those in contact mode ($10^{-9}$ N for contact mode and $10^{-12}$ N for non-contact mode) the sample is much less likely to be distorted and broken [114]. Despite this, damage does occur in tapping mode; the primary source of this being short-lived durations of high force (up to 200 pN) at the point of tip-sample contact [118,119].

Tapping mode is a compromise between contact and non-contact mode with the tip oscillated above the sample with a larger amplitude than in non-contact mode, thus causing it to come into contact with the surface at the bottom of each oscillation [114,113,117,120].

While the sample is still depressed by the tip, this technique avoids the lateral dragging forces which can disturb samples. Therefore, tapping mode operation is most ideal when samples are only weakly adsorbed onto the substrate [114,120].

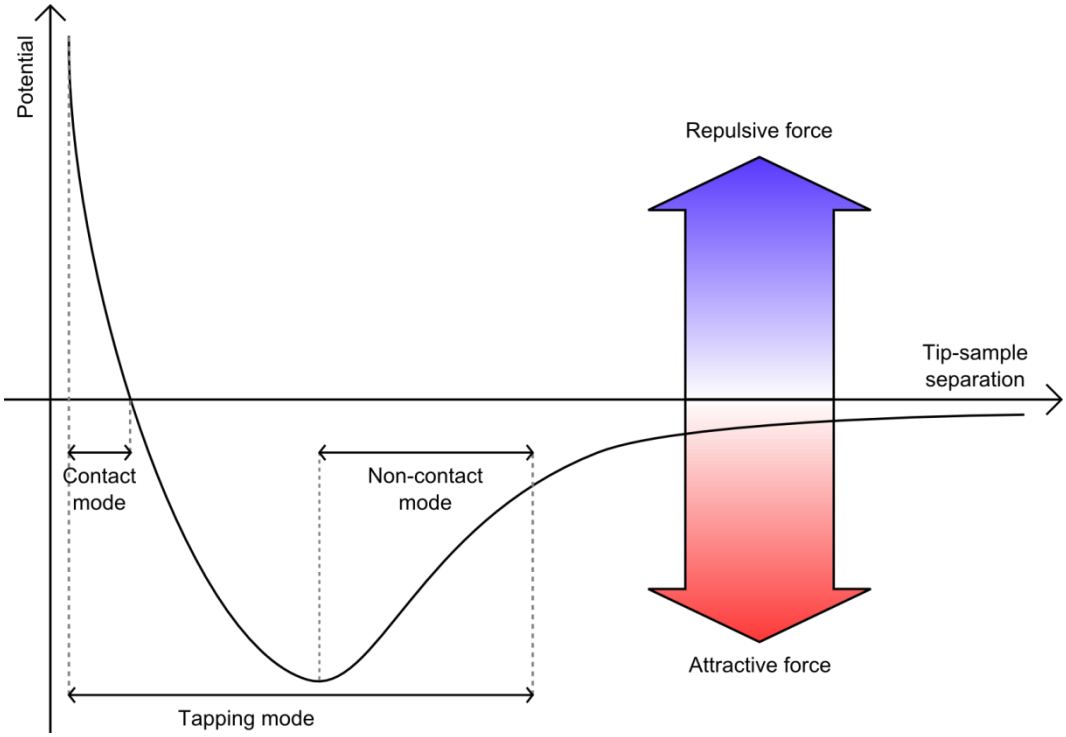


**Figure 3-2 – Representation of the Lennard-Jones potential**
This relationship describes the interaction between the AFM tip and sample. At large separations the potential is dominated by long-range, Van der Waals forces and ionic interactions that give rise to an attraction between the tip and sample; however, at much smaller separations this interaction is dominated by short-range nuclear force arising from Pauli repulsion. In this region, the tip experiences a force acting away from the sample. Different AFM modes make use of these various force regimes; contact mode taking advantage of the large repulsive force at short distances to deflect the tip and non-contact mode relying on the smaller force variation at large tip-sample separations to affect the oscillatory properties of a tip vibrated above the sample. A third system, tapping mode, spans both these regimes to take advantage of the larger, contact mode forces and the reduced sample damage of non-contact mode. Image adapted from [117].

### 3.1.2 Advantages and disadvantages of AFM

There are several advantages to the use of AFM for imaging compared to other high magnification microscopy techniques, such as Scanning Electron Microscopy (SEM) and Transmission Electron Microscopy (TEM). One key advantage is the ability to generate three-dimensional surface profiles [113], rather than the two-dimensional images obtained via both SEM and TEM. Additionally, AFM can be operated at ambient temperature and pressure and with the sample in either air or liquid without significant modifications to the experimental set up, thus permitting studies on living organisms at physiological conditions [113,121]. AFM also offers native imaging of non-conducting samples, which is not possible with its STM precursor or SEM [112,113]. Sputter metal deposition required to

make insulating samples conduct, as well as other sample preparations necessary for SEM and TEM, may also lead to sample distortion and degradation [113,122].

Despite the wealth of advantages, AFM is not without its drawbacks; in particular, traditional AFM systems acquire images relatively slowly. Image acquisition can take on the order of tens of minutes per frame [123,124]; however, modern systems typically operate on the 10 seconds to 5 minutes range. This leaves AFM susceptible to drift-based image distortion and precludes the visualisation of systems in real-time. However, advancements have been reported; in particular, the development of high-speed AFM imaging (HS-AFM), which is made possible with the use of higher resonant frequency cantilevers with lower spring constants than those found in standard AFM set-ups [125]. This technique has been demonstrated with reliable image acquisition times of 30 ms across 250 nm (100 pixels) scan ranges [125,123,124].

### 3.1.3 Immobilisation of biological samples for AFM

In order to probe topographical variations on the sub-nanometre scale, background fluctuations in height need to be kept at a minimum. Therefore, samples are prepared on atomically flat substrates, such as mica [126,127]. Mica is a naturally occurring mineral, which arises in a number of different compositions that generally follow the chemical composition shown in Equation 3-1. Irrespective of composition, all micas have layered atomic structures; basal cleavage of which yields atomically flat substrates, making it ideal for biological sample deposition [128].

$$X_2Y_{4-6}Z_8O_{20}(OH,F)_4$$

**Equation 3-1 – General chemical composition of mica**
In the specified formula, X is usually potassium, sodium or calcium; Y is usually aluminium, magnesium or iron; and Z is usually silicon or aluminium [128].

For the purpose of AFM, muscovite (ruby) mica is generally used, which has the chemical composition $KAl_2(Si_3Al)O_{10}(OH)_2$ and exhibits cleavage along the relatively weakly-bonded potassium plane [128–130]. This potassium layer is responsible for balancing the negative charge of the adjacent aluminosilicate layers; thus, upon cleavage along this plane, some of this negative charge is exposed due to potassium ion disruption [130].

Through appropriate choice of buffers, the negative charge of the partially-exposed aluminosilicate layer can be used to equilibrate DNA and proteins devoid of positive regions (Figure 3-3a); however, incorrect buffer concentrations can lead to the sample becoming kinetically trapped on the mica (Figure 3-3b). Kinetic trapping occurs when the substrate is made too adhesive to the sample, thus the sample becomes trapped in a two-dimensional projection of its three-dimensional solubilised form [91] (Figure 3-3b). Such conditions have been shown to occur following extensive washing of the mica with water, prior to deposition of DNA. This process is believed to displace the metal ions, typically held on the mica surface, which interact with the negatively-charged DNA backbone. Accordingly, addition of $MgCl_2$ to water-washed mica has been demonstrated to suppress this tendency to cause kinetic trapping, presumably through binding of $Mg^{2+}$ ions to the vacant binding sites [91].

Adhesion of DNA to the mica is usually achieved through the inclusion of magnesium salts, which readily dissociate in aqueous conditions to yield the $Mg^{2+}$ ion. This divalent species mediates a non-specific electrostatic interaction between the negatively charged mica surface and negative charge of the DNA backbone phosphate groups [131]. In early reports of DNA imaging using AFM, magnesium acetate, $Mg(CH_3COO)_2$, acted as the source of divalent magnesium ions [127,126]; however, more recently magnesium chloride, $MgCl_2$, has been adopted as an alternative [132,133,121].

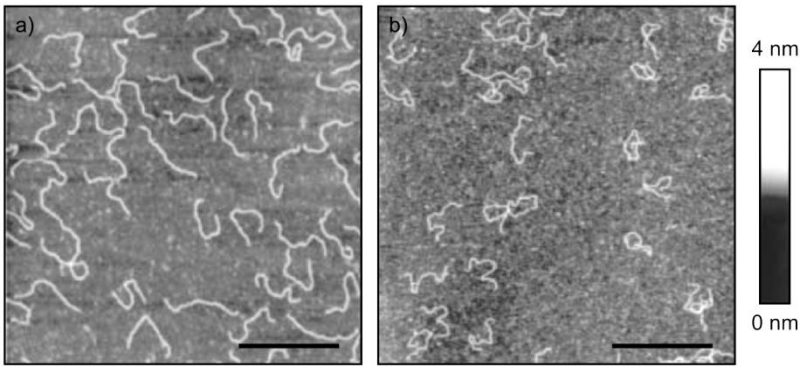


**Figure 3-3 – Examples equilibrated and kinetically trapped DNA imaged by AFM**
a) In equilibrating conditions the DNA is able to achieve a lowest-energy conformation on the mica and adopt a self-avoiding path. b) Conversely, in kinetic trapping conditions (in this case, $K^+$ ions have been exchanged with $H^+$ ions through a 12 hour water-soak step of the mica), the DNA is rapidly immobilised on the mica in a two-dimensional projection of its three-dimensional form in solution. Image adapted from [91].

The kinetically trapped scenario does not represent a meaningful state of the polymer, since it has not been allowed to adopt a lowest-energy conformation [91]. As such, for

accurate analysis it is important to be able to determine the nature of any DNA molecules observed through AFM. This can be achieved either through qualitative analysis of AFM images, where trapped molecules exhibit significantly more compact forms (Figure 3-3), or quantitatively, through comparison of DNA end-to-end and contour length measurements to theoretical predictions for trapped polymers. End-to-end length approximations for DNA both equilibrated in 2D on a planar surface and equilibrated in 3D in solution [134] have been described by Rivetti, *et al.* [91] (Equation 3-2 and Equation 3-3, respectively).

$$\langle R^2 \rangle_{2D} = 4PL_0 \left[ 1 - \frac{2P}{L_0} \left( 1 - e^{-L_0/2P} \right) \right]$$

**Equation 3-2 – End-to-end length of a DNA molecule equilibrated in 2D**
The end-to-end length is a function of the persistence length ($P$) and DNA contour length ($L_0$). This equation applies to DNA molecules equilibrated in 2D on a planar surface. When evaluated for dsDNA, persistence length is taken to be 53 nm.

$$\langle R^2 \rangle_{3D} = 2PL_0 \left[ 1 - \frac{P}{L_0} \left( 1 - e^{-L_0/2P} \right) \right]$$

**Equation 3-3 – End-to-end length of a DNA molecule equilibrated in 3D**
The end-to-end length is a function of the persistence length ($P$) and DNA contour length ($L_0$). This equation applies to DNA molecules equilibrated in 3D when they are free in solution. When evaluated for dsDNA, persistence length is taken to be 53 nm.

Under equilibrium deposition conditions, DNA observed on the mica is described by Equation 3-2; however, under kinetic trapping conditions, the DNA is described by a 2D projection of the 3D form (Equation 3-4). This can be further simplified as the DNA contour length approaches infinity (Equation 3-5); such conditions can be considered valid for the long template lengths used in the described work.

$$\langle R^2 \rangle_{proj} = \langle R_x^2 \rangle + \langle R_x^2 \rangle = \frac{2}{3} \langle R^2 \rangle_{3D}$$

**Equation 3-4 – End-to-end length of a kinetically-trapped DNA molecule**
Projection of the 3D form onto a 2D plane removes one spatial dimension; as such, the observed end-to-end length is two thirds that of the 3D form (Equation 3-3). The end-to-end length is a function of the persistence length ($P$) and DNA contour length ($L_0$). This equation applies to DNA molecules equilibrated in 3D when they are free in solution. When evaluated for dsDNA, persistence length is taken to be 53 nm.

$$\langle R^2 \rangle_{proj} = \frac{4PL_0}{3}$$

**Equation 3-5 – Kinetically trapped DNA end-to-end length**
Simplified form of Equation 3-4 for the limit where DNA length approaches infinity. The end-to-end length is a function of the persistence length ($P$) and DNA contour length ($L_0$).

Control over the transition between trapping and equilibration is achieved through variations in ionic conditions. Numerous published reports exist which look in great detail at the effect of salt concentrations on the ability to immobilise DNA and other biological samples on mica for subsequent imaging with AFM [91,133]. For immobilisation of transcription complexes, the generally accepted conditions are approximately 10 mM NaCl and 2 mM $MgCl_2$ [132,135].

### 3.1.4 Probing DNA-RNAP complexes with AFM

For the purpose of probing the interaction between transcribing RNA polymerases, AFM offers a method to gain a mechanistic insight which isn't possible with fluorescence based techniques. While AFM can typically only provide a static snap-shot of transcription, the spatial resolution is such that the proximity of adjacent RNAPs can be measured to a high degree of accuracy. This is thanks to the ability to identify individual enzymes without the need for reporter molecules or beads, as is the case with single-molecule transcription assays. With this information, the mechanism through which RNAPs interact, either directly through collision or at a distance mediated via modified DNA torsion, can be investigated. This method also offers the potential for verification of the transcriptional activity of the produced RNAP.

$$R_O = 2\sqrt{R_T R_S}$$

**Equation 3-6 – Observed sample radius in images acquired using AFM**
The observed sample radius ($R_0$) is a function of the tip radius of curvature ($R_T$) is significantly larger than the actual sample radius of curvature ($R_S$).

An important consideration when probing samples with feature sizes much smaller than the AFM tip radius of curvature is the apparent increase in feature size that occurs. This deleterious effect ultimately determines the spatial resolution for acquired images. It can be most easily envisaged for a tip with a known radius-of-curvature ($R_T$) imaging a cylindrical sample of known radius ($R_S$) positioned so its axis is perpendicular to the tip scan direction (Figure 3-4). Rather than measuring the correct sample radius, an enlarged radius will be observed ($R_O$) as the cantilever is deflected upwards significantly before the lowest part of the tip encounters the sample. The relationship between actual tip and sample radii and the observed sample radius is approximated by Equation 3-6, assuming the tip to be much larger than the sample [126].

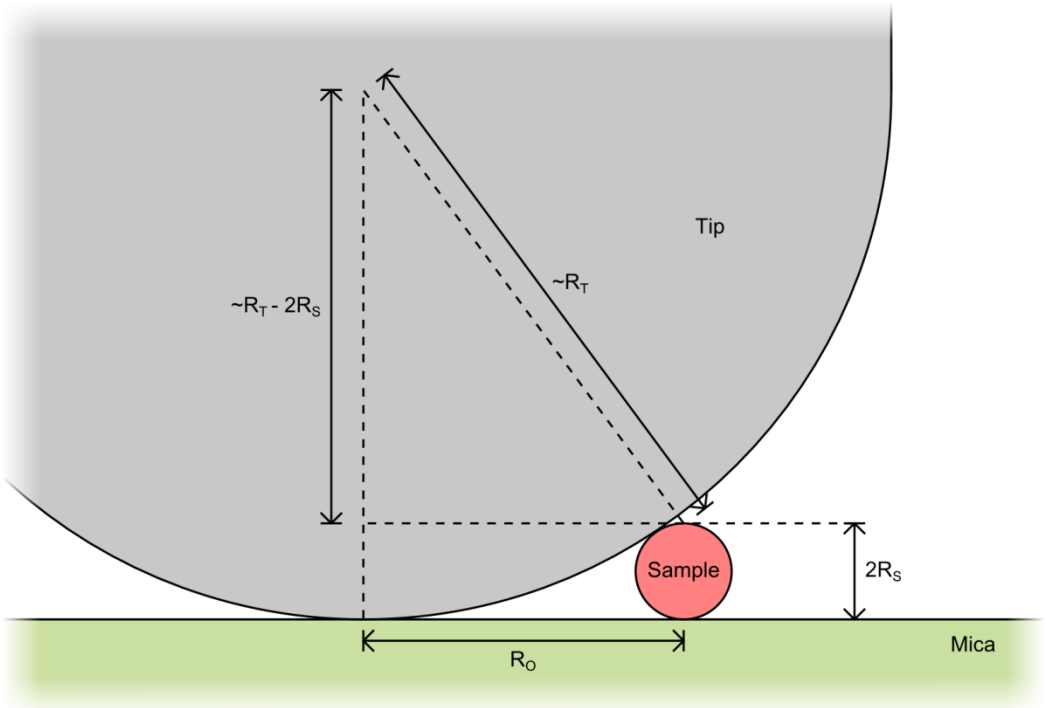


**Figure 3-4 – Schematic diagram showing the effect of tip curvature**
This approximation yields an observed sample radius ($R_O$) in AFM imaging where the sample radius of curvature ($R_S$) is much smaller than that of the tip ($R_T$). As the tip is scanned across the sample it will experience a vertical deflection significantly before the centre of the tip passes the sample, thus limiting spatial resolution in the acquired image. Improved spatial resolution is achieved through use of sharper tips. Figure adapted from Vesenka, *et al.* [126].

Typical images of DNA and DNA-RNAP complexes are collected using a tip-scanning diCaliber AFM (Veeco Instruments Inc., New York, USA) with antimony-doped silicon tapping mode tips (TESP-MT; Bruker Corporation, Billerica, Massachusetts, USA). These have vendor-supplied nominal and maximum tip radii of curvature of 8 nm and 12 nm, respectively. Assuming dsDNA adsorbed to mica retains the hydrated B-DNA radius of 1 nm [136] the predicted observed radius should be approximately 12.6 nm ($R_O$ = 10 nm).

## 3.2 Experimental design for imaging DNA-RNAP complexes

### 3.2.1 Evaluation of previously-demonstrated approaches

Deposition and binding of negatively charged biological samples onto mica is achieved through two key components in the AFM buffer; monovalent NaCl and divalent $MgCl_2$ salts. In solution, $MgCl_2$ dissociates to form divalent $Mg^{2+}$ and $Cl^{2-}$ ions, with the former mediating the interaction between the negatively charged mica surface and sample. The products of NaCl dissociation electrostatically-screen the sample during deposition, thus preventing premature adsorption of the sample to the substrate. Ideally, the sample is

equilibrated on the mica; however, under certain conditions the DNA can become kinetically trapped (Section 3.1.3).

Immobilisation of stalled transcription complexes has been addressed previously by various groups and is summarised in Table 3-1. Published examples detailing AFM studies of T7 RNAP transcription complexes are limited, so studies of *E. coli* RNAP have also been used. Despite the differences in each experiment, based on the biological problem being addressed, many of the fundamental parameters are largely similar. For each parameter, the published conditions are compared to those implemented in this work, as outlined in Section 3.2.2.

In the examples listed in Table 3-1, the template DNA has an average length of 964 ± 380 nm and is used at low nanomolar concentrations in the range 10-30 nM. To facilitate binding of one to two RNAPs per molecule, the enzyme is generally added at concentrations ranging from equimolar to three-fold excess. This highlights the first key difference between the published examples and the work being addressed here, where the intention is to observe multiple polymerases on a single DNA molecule. Accordingly, a longer (13,075 bp) template is used here at a lower molar concentration of 1.35 nM, which yields an equivalent base pair concentration: approximately 15 µM for the average example assay and 17.7 µM for the assay described. Similarly, to permit multiple simultaneous transcription events, an RNAP excess of approximately 70-fold was used.

Despite transcription conditions being dictated by the polymerase used, some variation between reported buffers is observed; for example, Limanskaya and Limanskii [137] use a four-fold excess of Tris-HCl over that used by Mukherjee [93]. The buffer implemented here is detailed in Section 3.2.2 and has been previously demonstrated to permit transcriptional activity of T7 RNAP (Section 2.4.1.3). There is little variation in transcription incubation conditions, since both T7 RNAP and *E. coli* RNAP exhibit optimal activity at a physiological temperature of 37 °C.

**Table 3-1 – Protocols for immobilisation of transcription complexes on mica**
Included are details of transcription mixtures used, incubation times and deposition conditions.

| Paper | DNA | RNAP | Transcription mixture | Incubation | Deposition mixture |
|---|---|---|---|---|---|
| Crampton et al. (2006) [132] | 20 nM (1150 bp) | 40 nM (E. coli $\sigma^{70}$ holoenzyme) | 20 mM Tris (pH 7.9), 50 mM KCl, 5 mM $MgCl_2$, 20 U RNasin, 1mM DTT, 100 μM rNTPs | 15 mins at 37°C | 10 to 20-fold dilution in 4 mM HEPES (pH 7.4), 10 mM NaCl, 2 mM $MgCl_2$ |
| Dame et al. (2002) [138] | 27 nM (1200 bp) | 47.5 nM (E. coli $\sigma^{70}$ holoenzyme) | 50 mM HEPES (pH 8.0) , 60 mM KCl, 15 mM NaCl, 1.5 mM $MgCl_2$, 12.5 ng/μl heparin, 1 mM ATP, 0.1 mM CTP | 10 mins at 24°C | 20-fold dilution in 2.5 mM HEPES (pH 8.0), 8 mM $MgCl_2$ |
| Guthold et al. (1999) [121] | 10 nM (1047 bp) | 30 nM (E. coli $\sigma^{70}$ holoenzyme) | 20 mM Tris or HEPES, 50 mM KCl, 5 mM $MgCl_2$, 1 mM β-ME (pH 7.0), 20 μM rNTPs | 10 mins at 37°C, then 10 mins at RT with rNTPs | 5 to 10-fold dilution in 4 mM HEPES, 1 mM KCl, 1 mM $MgCl_2$, pH 6.7-7.0 |
| Limanskaya and Limanskii (2008) [137] | 0.2 to 0.8 nM (1414 bp) | 1 to 100-fold excess over DNA (T7 RNAP) | 40 mM Tris (pH 7.9), 6 mM $MgCl_2$, 10 mM NaCl, 10 mM DTT, 2 mM spermidine, 200 μM rNTPs, 0.05% Tween 20, 40 U RNasin, | 4 mins at 37°C | 10 mM HEPES containing 2.5 mM $MgCl_2$ |
| Mukherjee et al. (2002) [93] | 10 nM (304 bp) | 10 nM (T7 RNAP) | 10 mM Tris-HCl (pH 8.0), 6 mM $MgCl_2$, 10 mM NaCl, 2 mM spermidine, 5 mM DTT, 500 μM GTP and ATP. | 15 mins at 37°C | 10-fold dilution in transcription buffer |
| Rivetti et al. (1999) [135] | 20 nM (1008 bp, 1054 bp and 1150 bp) | 20 nM (E. coli $\sigma^{70}$ holoenzyme) | 20 mM Tris-HCl (pH 7.9) , 50 mM KCl, 5 mM $MgCl_2$, 10 mM DTT, 5 or 15 mM $NiSO_4$ (when present) | 15 mins at 37°C | 10 to 20-fold dilution in 4 mM HEPES pH 7.4, 10 mM NaCl, 2 mM MgCl2 |
| Rivetti et al. (2003) [139] | 20 nM (350 bp) | 20 nM (E. coli $\sigma^{70}$ holoenzyme) | 20 mM Tris-HCl (pH 7.9) , 50 mM KCl, 5 mM $MgCl_2$, 1 mM DTT, 20 U RNasin, 100 μM rNTPs (excluding CTP) | 15 mins at 37°C, then 20 mins at room temperature with rNTPs | 10 to 20-fold dilution in 4 mM HEPES pH 7.4, 10 mM NaCl, 2 mM MgCl2 |

Deposition of samples is achieved using a large variety of buffer conditions. While final DNA concentrations are typically maintained around 1 to 2 nM, the buffer into which they are diluted may be based on either Tris or HEPES and contain a range of monovalent and divalent salt concentrations. Magnesium salt concentration is generally the key component, facilitating immobilisation of DNA onto the mica substrate, and has a concentration of 2 mM. Ancillary to this, the monovalent salt ranges from absence to 10 mM and has been provided as either NaCl or KCl. In the experiments described here, the buffer of Rivetti *et al.* [135] is implemented as it has previously been demonstrated to facilitate immobilisation of naked DNA on mica (Section 2.3.8.1).

### 3.2.2 Standard method for imaging DNA-RNAP complexes by AFM

Throughout the various assay preparations used, many parameters and approaches have been attempted in order to address the fundamental problem of poor immobilisation of transcription complexes to the mica substrate. Despite this, they all follow a similar fundamental protocol, which is slightly altered in each experiment according to the parameter being investigated. Described here is this standard technique used when preparing transcription assays and transferring them to the mica for AFM imaging. In subsequent sections, any deviations from this protocol are highlighted along with the reasoning and expected effect.

Transcription of the 13,075 bp pSJC-Φ13 template (see Section 2.3.5 for preparation) by T7 RNAP (Promega Corporation, Madison, Wisconsin, USA) is performed in a bulk assay, near identical to those used for verification of RNAP activity (Section 2.6.3). A typical mixture for such an assay is 1.3 µl 2.7 nM pSJC-φ13, 1.4 µl 1x T7 RNAP transcription buffer (40 mM Tris-HCl, 10 mM NaCl, 6 mM $MgCl_2$), 1 mM DTT, 1 mM rNTPs (1 mM per ribonucleotide species), 0.7 µl 90 nM T7 RNAP (diluted from 18 µM stock in 1x T7 RNAP transcription buffer) all made to a final volume of 7 µl with ultra-pure water (18.2 MΩ•cm; Purelab Ultra; Elga, Marlow, UK). This mixture is incubated at 37 °C for 15 minutes, in accordance with the methods of Crampton *et al.* [132] and Limanskaya and Limanskii [137] for similar systems. Early experiments used a NucAway spin column to perform the exchange between transcription and AFM buffers, as described in Section 3.3.1; however, later setups replaced this for simple 25-fold dilution of the transcription mixture in AFM buffer.

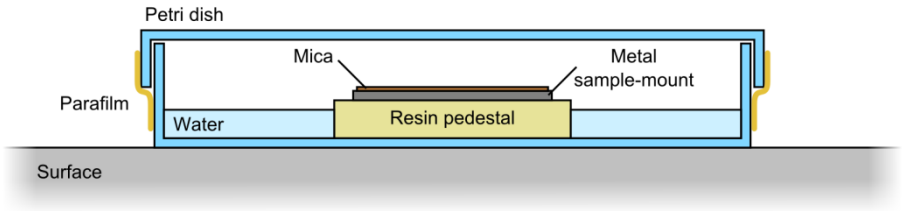


**Figure 3-5 – Schematic diagram showing incubation chamber for sample preparation**
Immediately following deposition of the transcription mixture onto the cleaved mica surface the sample is placed on a resin pedestal in a sealed incubation chamber. A small water reservoir helps maintain a hydrodynamic balance, preventing evaporation of the sample that could result in unwanted salt crystal deposition.

Commercially-available ruby mica (G250-1; Agar Scientific, Stansted, UK) is prepared onto 25 mm x 25 mm square metal plates, held in place in the AFM on the magnetic sample mount using a two-part epoxy resin (Rapid Bond; Wickes, Northampton, UK). AFM experiments are conducted following a protocol developed in-house by Gassan Suliman (unpublished data). In this approach, the mica surface is prepared using 2-3 cleaves with adhesive tape (Lyreco, Telford, UK), which should remove the uppermost layers, thus presenting an atomically flat and clean surface for imaging. Immediately afterwards, the DNA-RNAP mixture is deposited onto the mica and the sample placed in an incubation chamber comprised of a petri dish with a plastic pedestal surrounded by water (Figure 3-5). This chamber is sealed with Parafilm (Pechiney Plastic Packaging, Chicago, USA) for 5 minutes to allow the DNA-RNAP complexes to diffuse towards the mica surface and equilibrate. A small reservoir of water is present in the chamber to help maintain sample humidity, thus preventing sample evaporation, which may result in undesirable salt deposition.

Imaging in the diCaliber AFM (Veeco Instruments Inc., New York, USA) was performed using antimony-doped silicon tapping mode tips (TESP-MT; Bruker Corporation, Billerica, Massachusetts, USA) following the vendor-recommended protocol.

## 3.3 Approaches for formation of immobilised DNA-RNAP complexes on mica

### 3.3.1 Buffer exchange using a spin column

#### 3.3.1.1 Rationale for experimental approach

The efficiency of sample immobilisation for AFM is highly dependent on buffer conditions [91]; therefore, the less favourable conditions of the bulk transcription mixture

need to be minimised through dilution of the assay contents in a large volume of AFM buffer (4 mM HEPES pH 7.5, 10 mM NaCl, 2 mM $MgCl_2$). Depending on the concentration of DNA-RNAP complexes in the transcription assay, this can lead to a significant reduction in immobilised complex density on the mica substrate.

For the typical transcription assay mixture described in Section 3.2.2 the final salt concentrations are 10 mM NaCl and 6 mM $MgCl_2$. Although the monovalent salt concentration is identical between T7 RNAP transcription and AFM buffers, the divalent salt concentration is three-fold higher in the transcription mixture. A dilution of 5 µl transcription mixture in 45 µl AFM buffer still results in a magnesium ion ($Mg^{2+}$) concentration 20% higher than the optimised conditions. Published studies have shown that $Mg^{2+}$ plays an important role in modulating the mica surface charge, such that DNA is equilibrated, rather than kinetically trapped (Section 3.1.3). While $Mg^{2+}$ binding sites on the mica may become saturated at higher $MgCl_2$ concetrations, yielding no deleterious effects, it is optimal to limit the number of experimental variables. Therefore, to minimise the potential for problems and to maintain conditions as close as possible to those published, buffer exchange can be achieved using commercially available NucAway spin columns (Invitrogen, Carlsbad, California, USA).

#### 3.3.1.2 Method

NucAway spin columns were used in accordance with the vendor-supplied protocol, whereby the resin is rehydrated with 650 µl of AFM buffer (or the buffer for eventual sample elution), the column allowed to stand for 15 minutes; then spun for 2 minutes at 750 xg to remove excess fluid. In an additional step to those listed in the protocol, the column was washed three further times with 650 µl of AFM buffer (spun for 2 minutes at 750 xg) to ensure any loose material in the column, such as unhydrated resin, had been extracted. Following this, the transcription mixture was added and the column spun for a further 2 minutes at 750xg, with the sample present in the eluent.

#### 3.3.1.3 Results

Observed results with the NucAway column were varied, with large differences in the eluted sample volume casting doubt on the reliability of such an approach; however a reason for such variability could not be established. Despite performing multiple wash

steps prior to addition of transcription mixtures to the columns, small particles were often observed to be bound to the mica. A good example of this is shown for a typical transcription assay, stalled via addition of 3'-dATP, where the high particle background prevents analysis of legitimate RNAP-DNA colocalisation (Figure 3-6).

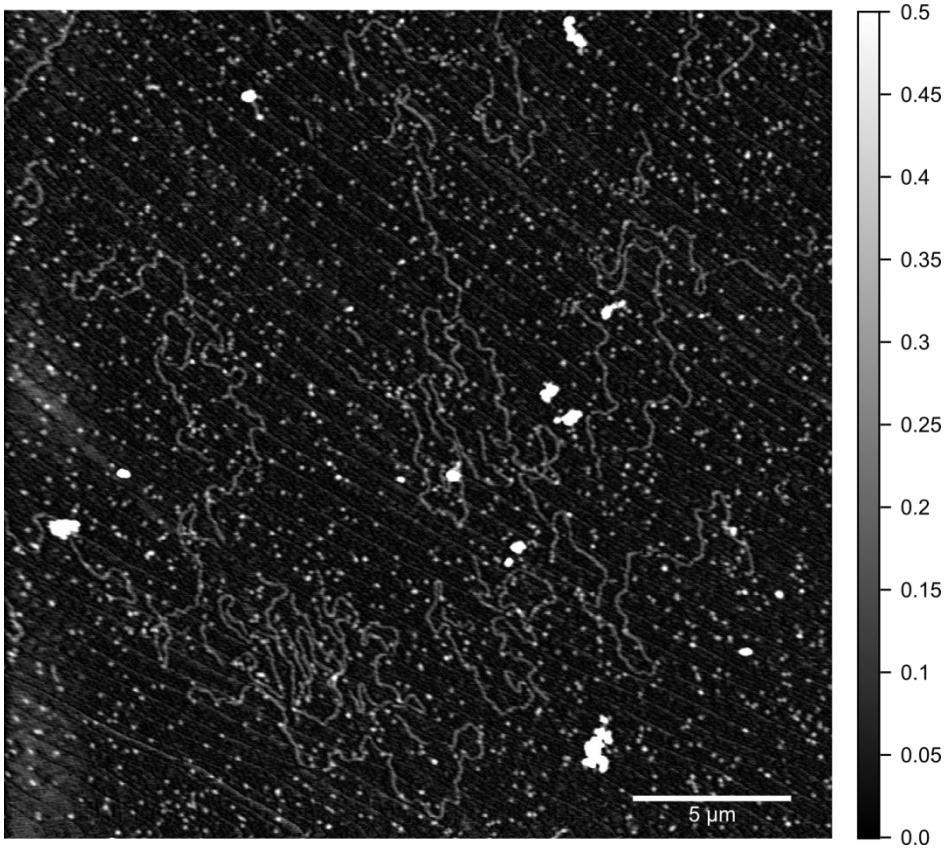


**Figure 3-6 – Purification of samples with a NucAway spin column**
Typical AFM image obtained for a T7 RNAP transcription assay deposited onto mica following clean-up using a NucAway spin column (pre-washed with AFM buffer three times prior to use). The high level of non-specific particle binding to the mica prevents accurate evaluation of cases where DNA and RNAP colocalisation arises due to the presence of a stalled transcription complex. Scale bar is 5 µm and gradient on right corresponds to vertical sample height (nm). Image was levelled using the revolve arc function in Gwyddion.

While the observed particles are likely components of the transcription assay, such as RNAP, they could also originate from the NucAway column. Furthermore, the quantity of protein-DNA complexes retained within the column could not be evaluated, which is also a potential problem for experimental reproducibility.

### 3.3.2 Stalling transcription complexes through nucleotide starvation

#### 3.3.2.1 Rationale for experimental approach

The ultimate goal of the AFM transcription assays is to observe complexes halted instantaneously, thus providing a snap-shot of transcription and yielding an insight into their spacing on the template. However, the results described in Section 3.3.1 have highlighted how working with such dynamic systems during the early stages of an experimental setup, where various buffer and reagent conditions need to be fine-tuned, adds an unnecessary layer of complexity. Therefore, it has proven preferable to initially work with artificially stalled complexes that can be reliably bound to the DNA substrate, thus demonstrating that elongation complexes are stable on DNA. Furthermore, the relatively long image acquisition times of AFM favour the use of stalled transcription complexes.

Although there are a few possible ways to reliably stall a transcription complex, nucleotide starvation is probably the most commonly used [140,141,47,138,121,139]. This involves the exclusion of one nucleotide from the reaction mixture, allowing the transcription machinery to progress so far, but then come to a halt when unable to incorporate the missing nucleotide. An important consideration for this experimental approach is the stability of stalled complexes, since the RNAP must remain bound to the template for the duration of deposition onto the mica. Stability of T7 RNAP initiation complexes have been shown to vary significantly based on template supercoiling; relaxed linear templates, such as those expected to be present in the *in vitro* transcription mix, yield lifetimes less than one minute; however, a marked improvement is observed when the template is supercoiled [142]. Conversely, stalled *E. coli* elongation complexes have been demonstrated to be stable for at least 5 days when stored at 4 °C and in the presence of acetylated BSA [140]. Such variability may be partially due to structural differences between the *E. coli* and T7 RNAP elongation complexes.

Selection of the most appropriate nucleotide to omit is generally determined by the maximum distance the complex can travel before stalling, ideally permitting the transcription complex to escape the abortive cycling phase of initiation in which it is generally much less stable [142]. As described in Section 1.3 the transition from abortive

cycling to elongation occurs around incorporation of the eighth or ninth nucleotide [37,46] as a result of the increased pressure from nascent RNA chain pushing on the RNAP active site [33]. For the pSJC-Φ13 template used in these assays the first 12 nucleotides incorporated at the T7 RNAP promoter (Φ13) are GGGAGAACAAUA; hence, through omission of rUTP the complex is unable to progress beyond the tenth position.

#### 3.3.2.2 Method

For this set of experimental conditions, bulk transcription assays were prepared as described in Section 3.2.2 but with rUTP replaced by an equivalent volume of ultra-pure water. Samples were transferred to AFM buffer using NucAway columns (Section 3.3.1); incubation and imaging was performed using the standard protocol.

#### 3.3.2.3 Results

When digested with restriction enzyme SalI, the T7 RNAP φ13 promoter lies 136 bp from the end of the pSJC-φ13. This corresponds to ~1% of the entire template length, thus if DNA does hold a successfully stalled transcription complex, a higher intensity dot is expected to be observed in AFM images at one end of the molecule. In the majority of instances such transcription complex immobilisation is not observed; however, this analysis is complicated by the presence of small particles immobilised onto the mica in addition to DNA (Figure 3-7). The origin of these is unknown, but they are likely to be individual RNAP enzymes. As a result, it is not possible to discern between chance colocalisation of RNAP and DNA and between stalled complexes.

With this high background immobilisation of RNAP, low frequency complex immobilisation permitting at most one stalled enzyme per DNA template is inappropriate. Instead, a more suitable approach would be one that enables multiple complexes to halt on a single template, potentially resulting in a significantly higher density of enzymes observed to be colocalised with the DNA than could be explained through chance positioning of the molecule. The technique implemented to achieve this is incorporation of the nucleotide-analogue, 3'-dATP, and is described in Section 3.3.3.

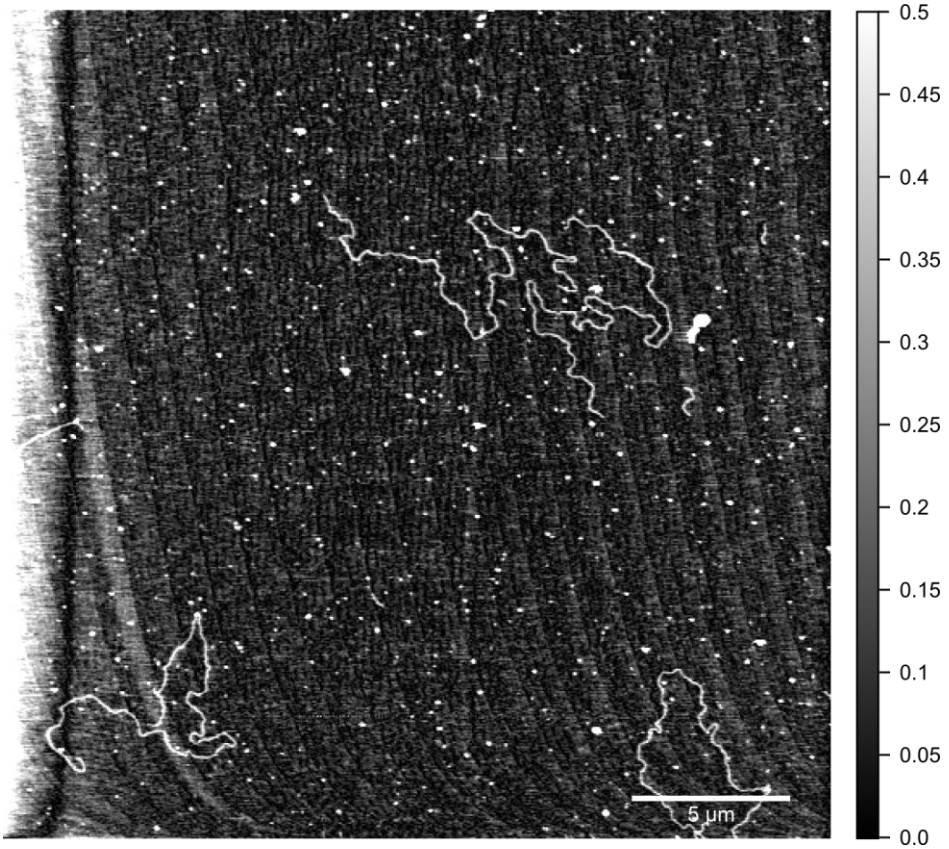


**Figure 3-7 – Stalling transcription complexes through nucleotide starvation**
Example AFM image of a T7 RNAP transcription mixture prepared with omission of UTP to encourage formation of stalled complexes. The single T7 RNAP promoter (φ13 promoter) contained within the DNA, SalI-digested pSJC-φ13, is located 136 bp from the template end; therefore, formation of stalled complexes is expected to be identifiable through the presence of a high intensity dot at one end of the DNA. Absence of this in all observed DNA molecules indicates either stalling was unsuccessful or occurred infrequently. Scale bar is 5 µm and gradient on right corresponds to vertical sample height (nm). Image was levelled using the revolve arc function in Gwyddion.

### 3.3.3 Stalling transcription complexes with 3'-dATP

#### 3.3.3.1 Rationale for the experimental approach

An alternative method to achieve artificially stalled transcription complexes is to supplement a small quantity of ATP with the analogue, 3'-dATP (alternatively called cordycepin) [93,143]. Unlike stalling induced through nucleotide starvation (Section 0), which results in complexes halting at the same location on each template, stalling induced through incorporation of 3'-dATP permits for multiple complexes to be present on a single template. Furthermore, assuming the ATP analogue is present at significantly lower concentrations than standard ATP, any potential issues with the transcription machinery being unable to escape the abortive cycling region of transcription are avoided.

This approach relies on the fact that incorporation of a nucleotide during transcription occurs at the hydroxyl group attached to the 3' ribose carbon of the nascent RNA chain.

Therefore, it is possible to stall the transcription complex through incorporation of 3'-dATP, in which the required hydroxyl group has been replaced with a single hydrogen (Figure 3-8). Due to the close similarity between ATP and its analogue, 3'-dATP is recognised and incorporated into the nascent RNA chain by RNA polymerase, but further elongation is not possible, thus causing the complex to stall [143].

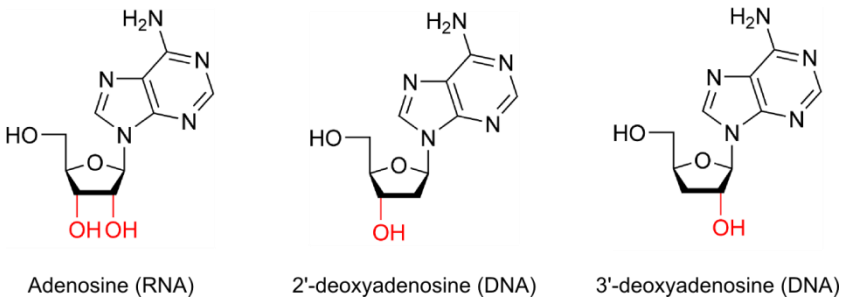


**Figure 3-8 – Chemical structures for the ribonucleotide ATP and two analogues**
The ribonucleotide variant has hydroxyl groups at positions 2' and 3' on the ribose, while in the DNA equivalent the 2'-hydroxyl is replaced by a single hydrogen atom. This difference is necessary for discrimination between the two closely related structures. However, in both DNA and RNA polymerisation, elongation of the nascent polynucleotide chain occurs at the 3'-hydroyl group; thus, due to structural similarity to ATP, 3'-dATP is recognised and incorporated by RNA polymerase, but prevents further elongation.

### 3.3.3.2 Method

Transcription complex stalling with 3'-dATP can be achieved in two ways. In the first, an approach referred to here as "stochastic stalling", a small proportion of ATP in the transcription mixture is replaced with the 3'-dATP form. Generally, such an assay contains one 3'-dATP to every 1000 standard ATP nucleotides; therefore, assuming there is no favourability for incorporation of one species over the other, this corresponds to a stalling event approximately once every 4000 incorporated nucleotides. Alternatively, a standard transcription assay is incubated at 37 °C to allow elongation complexes to form. Addition of an excess of 3'-dATP at a specified time should cause near-instantaneous stalling of all actively transcribing complexes. For a hypothetical case where all four nucleotides are evenly distributed in the DNA sequence and the polymerase is transcribing at a typical rate of 43 nt/s [26], addition of a 5-fold excess of 3'-dATP over unmodified ATP will stall all complexes in approximately a tenth of a second (assuming homogeneous distribution of all reagents). This technique shall hence be referred to as "instantaneous stalling".

#### 3.3.3.3 Results

The ability to determine if the transcription machinery has undergone stable stalling through addition of 3'-dATP relies on the successful deposition of DNA-RNAP complexes for imaging with AFM. Inclusion of 3'-dATP did not appear to yield clear evidence of stalled complexes when added to the basic transcription mixture; however, this doesn't necessarily indicate stalled complexes failed to form. Instead, it demonstrates the need for experimental refinement, for example through appropriate selection of mono- and divalent salts, the incorporation of additional components, such as spermidine (Section 3.3.4) or with modifications to make stalled complexes more visible.

### 3.3.4 Influencing DNA-RNAP complex immobilisation with spermidine

#### 3.3.4.1 Rationale for the experimental approach

An alternative route to DNA immobilisation on mica is to use the trivalent cation, spermidine (Figure 3-9) [144,145,131]. This polyamine is known to interact non-specifically with the negatively-charged DNA backbone and as such acts as a replacement for magnesium salts in the AFM buffer. Replacement of $Mg^{2+}$ is preferable for AFM experiments conducted at physiological ionic conditions, where the high monovalent salt concentration ([NaCl] > 100 mM) must be mirrored by high divalent salt levels to allow for adequate shielding of the DNA backbone. Since such high $Mg^{2+}$ concentrations are not physiologically relevant, spermidine becomes an attractive alternative. Relatively low concentrations of spermidine have been shown by Pastré *et al.* to permit DNA immobilisation in the presence of 200 mM NaCl without the deleterious effect of DNA condensation, as discussed below [133].

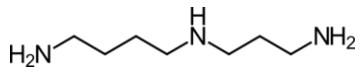


**Figure 3-9 – Structure of spermidine ($[C_7N_3H_{22}]^{3+}$)**
This molecule has an elongated form, which allows the molecule to bind along the DNA molecule. Such a structure reduces the negative impact on DNA persistence length as opposed to other trivalent cations, such as cobalt-hexamine.

One potential downfall of this approach is condensation of DNA due to the formation of intramolecular bonds mediated by spermidine [146–148]. Various published works have measured the compaction of DNA upon addition of varying spermidine concentrations. Chattoraj *et al.* showed with the use of electron microscopy that a mixture of 1 μM T7 DNA and 100 μM spermidine results in compaction of DNA to near-spherical (and

occasionally toroidal) structures, approximately 100 nm in diameter [146]. More qualitatively, Wilson and Bloomfield observe this compaction to occur suddenly when 89-90% of the negative phosphate charges on the DNA backbone have been neutralised [147]. Furthermore, the presence of spermidine was shown by Baumann *et al*. to have an effect on the measured persistence length for DNA. This value, which is accepted to be approximately 53 nm for dsDNA [149], decreased to 46.3 ± 6.5 nm in 100 μM spermidine and to 41.9 ± 4.7 nm in 25 μM spermidine [148]. Despite this, spermidine is a more attractive option than other trivalent cations, such as cobalt-hexamine ($Co(NH_3)_6^{3+}$), which have significantly smaller charge distributions and thus lead to greater modifications to the measured persistence length [148]. Cobalt-hexamine also interacts directly with DNA bases and the use of this for DNA immobilisation on mica is dissuaded by Pastré *et al.* [133].

For their study of DNA condensation, Zhang *et al.* used 2 ng/μl of λ-DNA (48,502 bp) diluted in 10 mM Tris-HCl (pH 7.5) and spermidine concentrations between 100 μM and 10 mM, representing a minimum 16-fold excess of spermidine over DNA backbone phosphates [145]. Under these conditions they saw flat structures, which exhibited condensation, but were not the spherical structures observed by Chattoraj *et al.* [146]. Similarly, Pastré *et al.* used 2 ng/μl pUC19 plasmid DNA (2686 bp) diluted in 10 mM Tris-HCl (pH 7.5) and a range of NaCl (10 - 800 mM) and spermidine (10 μM – 1 mM) concentrations. At ratios where DNA was immobilised, this resulted in condensed molecules spreading out upon deposition [131]. Such results can be explained both through interference of the negatively-charged mica surface [131,145] and through the dielectric properties of water, which Wilson and Bloomfield estimated to prevent DNA backbone phosphate neutralisation of more than 88%; hence the use of 50% methanol, which increases this value to 91%, in their light-scattering study of DNA condensation [147].

In a similar application to that intended here, Limanskaya and Limanskii used a small quantity of spermidine in a T7 RNAP transcription assay, which was subsequently prepared onto mica for AFM imaging [137]. Their transcription assay contained 40 mM Tris-HCl (pH 7.9), 6 mM $MgCl_2$, 10 mM NaCl, 10 mM DTT, 2 mM spermidine, 0.05 % Tween 20, 40 units of RNasin, 200 μM rNTPs, 20 units of RNAP and a 1414 bp DNA template containing a single T7 RNAP promoter (the A1 promoter) [137]. While the DNA concentration was varied between unspecified concentrations, the final concentration must be lower than the maximum stated stock concentration of 800 pM; at this concentration,

the spermidine is present at near 1000-fold excess. Prior to deposition, transcription was allowed to proceed for 60 minutes at room temperature. These conditions allowed equilibration of the RNAP-bound DNA [137].

#### 3.3.4.2 Method

The wide range of DNA phosphate to spermidine ratios summarised in Section 3.3.4.1 highlights how the numerous reaction conditions can be varied to achieve the same result. To investigate how spermidine concentration will affect the immobilisation efficiency of the transcription assay, spermidine to phosphate ratios of 60:1, 6:1 and 0.5:1 were tested. Transcription assay mixtures were based on the composition outlined in Section 3.2.2, with 1.3 nM pSJC-φ13, 1.4 µl 1x T7 RNAP transcription buffer, 0.7 µl 1 mM DTT, 0.3 µl 0.25 mM rNTPs (0.25 mM per ribonucleotide species), 10 µM, 100 µM or 1 mM spermidine (diluted in ultra-pure water), 1 nM T7 RNAP (Promega, Wisconsin, USA) and made to a final volume of 7 µl using 1x T7 RNAP transcription buffer. The lower than standard rNTP concentration is to permit 3'-dATP to be added at reasonable volumes. Following a 15 minute incubation at 37 °C, 1 µl of 10 mM 3'-dATP was added and the assay incubated for a further 10 minutes. Half the transcription assay reaction volume was diluted in 46 µl of AFM buffer and deposited straight onto the mica.

Since RNAP promoter binding utilises a different mechanism to the non-specific immobilisation on mica, it was postulated that an increase in RNAP concentration may favour one over the other and thus yield a relative improvement in colocalisation rates. To probe this, the final RNAP concentration in the transcription assay mixture was increased from 1 nM to 5 nM.

#### 3.3.4.3 Results

Representative images obtained from each of the samples described in Section 3.3.4.2 are shown in Figure 3-10. At relatively high spermidine concentrations (Figure 3-10a and b) there is evidence of DNA condensation, with the presence of structures similar to those reported by Zhang *et al.* [145]. Qualitatively, these are both visibly less well equilibrated and show structures which appear to fan out from a central, compacted region (Figure 3-10a). For lower spermidine concentrations (Figure 3-10c) the lack of spermidine appears to

inhibit the immobilisation of DNA. This is surprising, since 92% of the deposited sample is AFM buffer containing 2 mM $MgCl_2$ and implies low concentrations of spermidine may be involved in other functions, which prevent typical DNA immobilisation. The nature of these other functions is not presently apparent; however, it could simply be due to experimental variation. Verification that this is not an artefact due to experimental variation could be achieved through repetition using a range of spermidine concentrations from 0.2 mM to 0.02 mM. Should a thus-far unaccounted for interaction be occurring, the level of DNA immobilisation would be expected to decrease with lower spermidine concentrations.

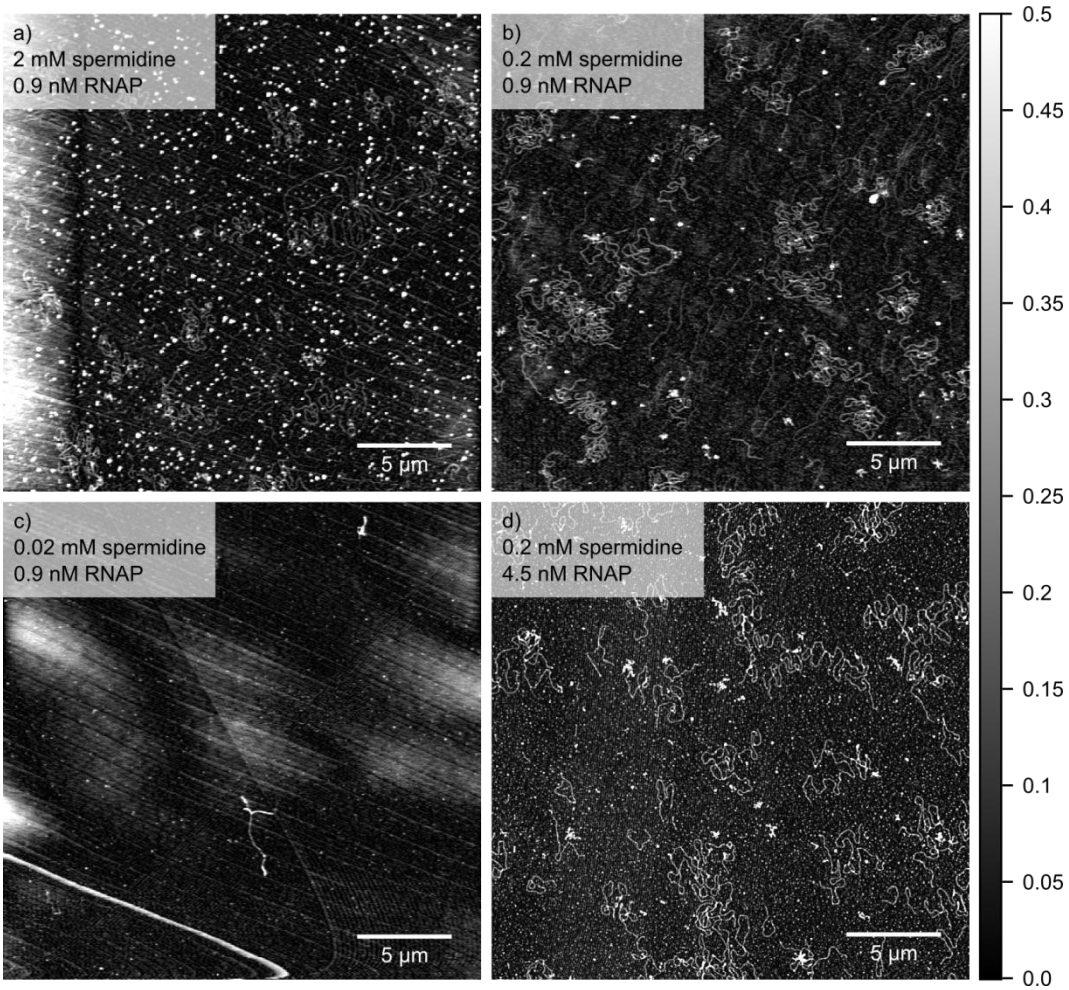


**Figure 3-10 – Immobilisation of transcription complexes on mica using spermidine**
The key components of each sample are stated in the figure and result in spermidine to DNA backbone phosphate ratios of 60:1 (a), 6:1 (b), 0.5:1 (c) and 0.5:1 in the presence of a five-fold increase in RNAP (d). At final concentrations of 2 mM and 0.2 mM, spermidine appears to result in similar condensed DNA structures as seen by Zhang *et al.* [145]; however, further reduction in concentration to 0.02 mM appears to prevent the immobilisation. Similarly, the presence of high spermidine concentrations results in undesirable increases in immobilisation of unbound RNAP; a problem which cannot be overcome by using higher RNAP concentrations to permit preferential binding to DNA relative to the mica. Scale bar in all panes is 5 µm and gradient on right corresponds to vertical sample height (nm). Image was levelled using the revolve arc function in Gwyddion.

In addition to enhanced DNA immobilisation, the rate of RNAP immobilisation also appears to have increased with the addition of spermidine. This poses a significant problem for identification of bound transcription complexes since instances of colocalisation between DNA and RNAP cannot be easily identified as chance occurrences. There is the potential for implementation of the statistical analysis described in Section 7.2.1.2; however, this wouldn't identify legitimate instances of colocalisation, which are vital for a meaningful investigation of inter-RNAP spacing on DNA.

To improve the frequency of transcription complex formation, a higher RNAP concentration was implemented; however, this resulted in the predictable increase in non-specific RNAP immobilisation on the mica.

The results obtained have led to the addition of spermidine being considered an unnecessary complication to the standard AFM imaging protocol; one that leads to an improvement in DNA immobilisation, but to a potentially deleterious level, where molecules are trapped rather than equilibrated. Similarly, the observed increase in non-specific RNAP immobilisation prevents accurate analysis of truly stalled transcription complexes. Such problems may explain the lack of published examples for spermidine being used in this manner.

### 3.3.5 Decreasing DNA template length

#### 3.3.5.1 Rationale for experimental approach

Numerous analogous examples of DNA-protein complex immobilisation on mica for AFM utilise template DNA lengths considerably less than the ~13,000 bp of pSJC-φ13 [132,138,121,137,93,135]; a fact which is highlighted in Table 3-1, where all DNA templates are shorter than 1500 bp. Such differences will not necessarily have an effect on immobilisation rates due to greater ionic sequestration, assuming the base-pair concentration is maintained constant between experiments; however, with longer tethers there is the potential for greater numbers of simultaneously transcribing polymerases. This gives rise to the potential for local variations in DNA torsion, occurring due to transcriptional separation of DNA base-pairs (Section 1.1.1) [1], manifesting as writhe and leading to the template adopting a condensed form. While the hypothesis is that the DNA-RNAP complex is capable of free rotation in *in vitro* experiments, where it is not

torsionally constrained, results from Nelson indicate that bends in the DNA backbone can significantly increase drag on the molecule [8]. Resultantly, the ability of the molecule to undergo rotation is hindered to such a degree that the capacity for relaxation of increased torsional states is much lower than predicted. In the case where DNA condensation is sufficiently high, equilibration of molecules may not be possible under standard AFM conditions.

Additionally, when considering templates with a single T7 RNAP promoter, shorter templates benefit from an increased number of promoters per mole of base-pairs. This can correspond to a greater number of stalled transcription complexes in an observable AFM region, thus facilitating improved experimental throughput.

To investigate the relationship between tether length and DNA immobilisation efficiency in the presence of stalled transcription complexes, the standard pSJC-φ13 template was substituted for the pUC-Φ600 PCR product of length 652 bp (see Section 2.3.3 for production). This agrees much more closely with the average template length from the examples included in Table 3-1 of 964 ± 380 bp.

#### 3.3.5.2 Method

The 652 bp pUC-Φ600 PCR product (henceforth referred to as PCR pUC-Φ600) was prepared as described in Section 2.3.3 and measured with a UV spectrophotometer (BioPhotometer; Eppendorf, Hamburg, Germany) to have a molecular concentration of 212 nM. This template was used in typical transcription assay conditions (Section 3.2.2), but with a final rNTP concentration of 100 µM, more closely mirroring the experiments detailed in Table 3-1. RNAPs were not artificially stalled with addition of 3'-dATP. Transcription mixtures were diluted 25-fold in standard AFM buffer. A final template concentration of 28 nM in AFM buffer was obtained, which is 20-fold higher than the standard pSJC-Φ13 concentration; however, the large difference in template lengths makes this an inappropriate metric. A better comparison can be achieved by looking at base-pair concentrations, which are 18.3 µM for PCR pUC-Φ600 and 17.7 µM for pSJC-Φ13. Therefore, for identical buffer conditions a similar surface immobilisation would be expected.

Following surprisingly low immobilisation of PCR pUC-Φ600 in the transcription assay a further investigation was conducted to identify the cause. Omission of all components from the assay except AFM buffer should indicate if the lack of immobilisation was due to the transcription assay or AFM buffer components. The sample was comprised of 0.45 µl PCR pUC-Φ600 and 99 µl standard AFM buffer, giving a final template concentration of 0.96 nM.

#### 3.3.5.3 Results

Counter to expectation, the conditions in the transcription assay yielded relatively low immobilisation of DNA (Figure 3-11). Considering the use of a near-identical base-pair DNA concentration to the standard pSJC- Φ13 concentration; under typical DNA deposition conditions (i.e. no transcription assay components), a much higher rate of surface immobilisation would be expected. Of the molecules that were immobilised there was no clear evidence of bound transcription complexes, which raises the possibility, hypothesised previously, that the presence of complexes on the DNA may be inhibiting binding to the mica. To probe this, immobilisation of a sample containing purely PCR pUC-Φ600 and AFM buffer was prepared; however, this showed similar rates of equilibration. Such a result leads to the conclusion that the observed low immobilisation is due to the AFM buffer, rather than the transcription assay.

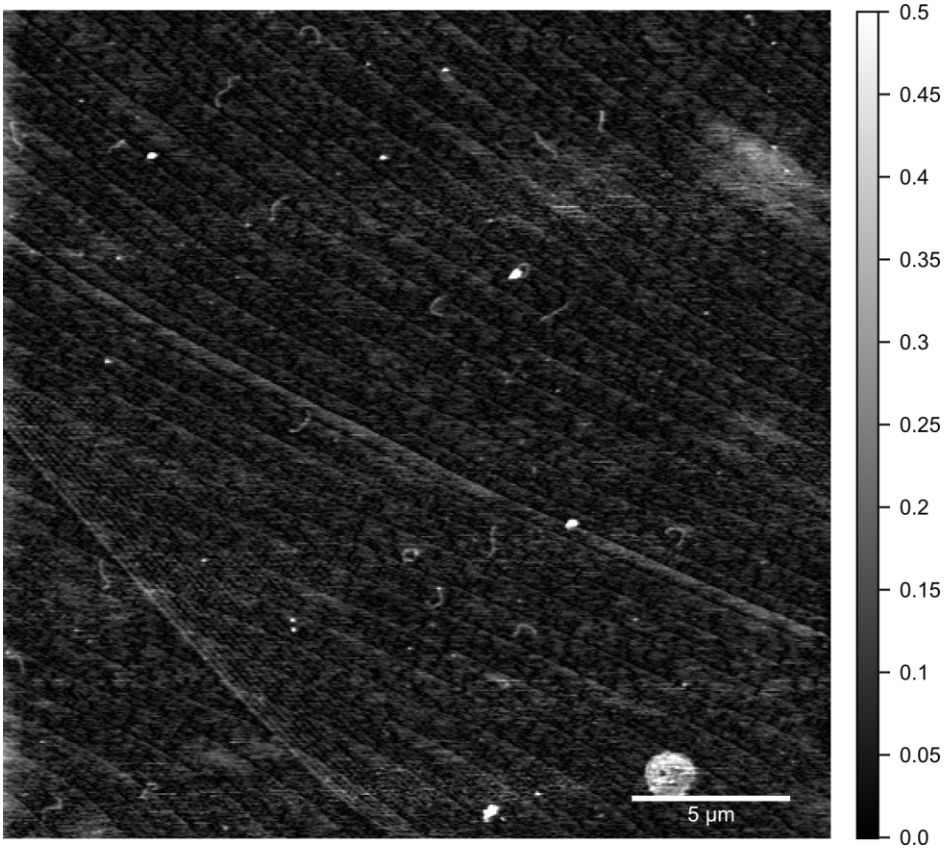


**Figure 3-11 – The effect of smaller DNA template lengths on immobilisation**
Probing deposition of standard transcription assay mixture, using PCR pUC-Φ600 (652 bp) as the template, deposited onto mica. Despite use of an equivalent DNA base-pair concentration to previously-successful samples with longer templates, there is a surprisingly low rate of sample immobilisation. The reason for such low immobilisation is unknown, but does not appear to be due to the binding of T7 RNAP, as demonstrated with a second sample containing only DNA and AFM buffer at equivalent concentrations. There was no clear evidence of transcription complexes formed on the molecules that were immobilised. Scale bar is 5 µm and gradient on right corresponds to vertical sample height (nm). Image was levelled using the revolve arc function in Gwyddion.

## 3.4 Evaluation of progress

Thus far it has not been possible to reliably identify transcription complexes bound to the DNA template. Primarily, this has been due to an inability to differentially immobilise DNA whilst preventing the deposition of unbound RNAP. This leads to acquired images potentially exhibiting DNA-RNAP complexes, but which cannot be distinguished from the multitude of instances where colocalisation arises purely by chance (Figure 3-6). Despite using both transcription assay and AFM buffer conditions similar to those used in near-equivalent published examples it has not been possible to resolve this issue. One likely cause is the nature of the experiments being conducted. Unlike elsewhere where template DNA is relatively short and, at most, a couple of polymerases are to be bound, the assays described here are designed to permit the observation of multiple binding events per template. The consequence of this is assays with much higher DNA to RNAP ratios, leading to the encountered issues.

This series of experiments was intended to complement the magnetic tweezers work, demonstrating the ability to observe multiple stalled transcription complexes on a single DNA tether. However, the static nature of any obtained data limits the overall benefit to the degree that while further modifications to the assay may yield sufficient improvements, the optimisation required to realise this has been deemed disproportionate to the perceived benefit.

# Horizontal magnetic tweezers microscope

Chapter 4

## 4.1 Design of a horizontal magnetic tweezers system

Described here is a basic outline of the horizontal magnetic tweezers system. While this summary does not contain specifics of magnet geometries or optical configurations, it does provide an appreciation of the fundamental system design and show how this has evolved from the existing microscopy technologies. This enables the key areas, which were targeted for analysis and development to be highlighted.

To briefly summarise the introductory chapter, the standard magnetic tweezers setup utilises a vertical configuration (Figure 1-8, Section 1.4.3), whereby superparamagnetic microsphere-attached samples are pulled away from their tethering substrate using magnets placed directly above the objective lens. Through comparison of the microsphere diffraction pattern to a pre-calibrated lookup table, positional information is acquired [71]. While such an approach has proven very successful in a wide range of DNA-protein interaction experiments, it is only possible to elucidate biological activity from the motion of the microsphere. As a result, work has increasingly turned to application of a side-pulling, or horizontal, magnetic tweezers system. Approaches thus far demonstrated in the literature have either adopted a surface-attachment technique, whereby the tether is bound at one end to the lower surface and pulled at an angle [75,77], or generate tethers to the side of a square capillary [74,76].

As described in detail later (Section 4.2.1), the force experienced by the microsphere in response to the magnetic field from the permanent magnets is strongly dependent on the spacing between the two magnets, with smaller separations yielding higher forces. Similarly, the inverse relation between force and microsphere to magnet-pair separation plays an important role; however, this distance is limited by the presence of the objective lens next to the sample. Furthermore, minimisation of this distance is also restricted in experiments where the magnet pair is to be rotated, as the magnets cannot pass beyond the leading edge of the sample. The resulting influence on sample thickness has been instrumental in dictating that the sample design permit sufficiently high forces to be accessible. Further reductions in thickness are possible beyond that demonstrated in Figure 4-1 by replacing the slide with a second coverslip.

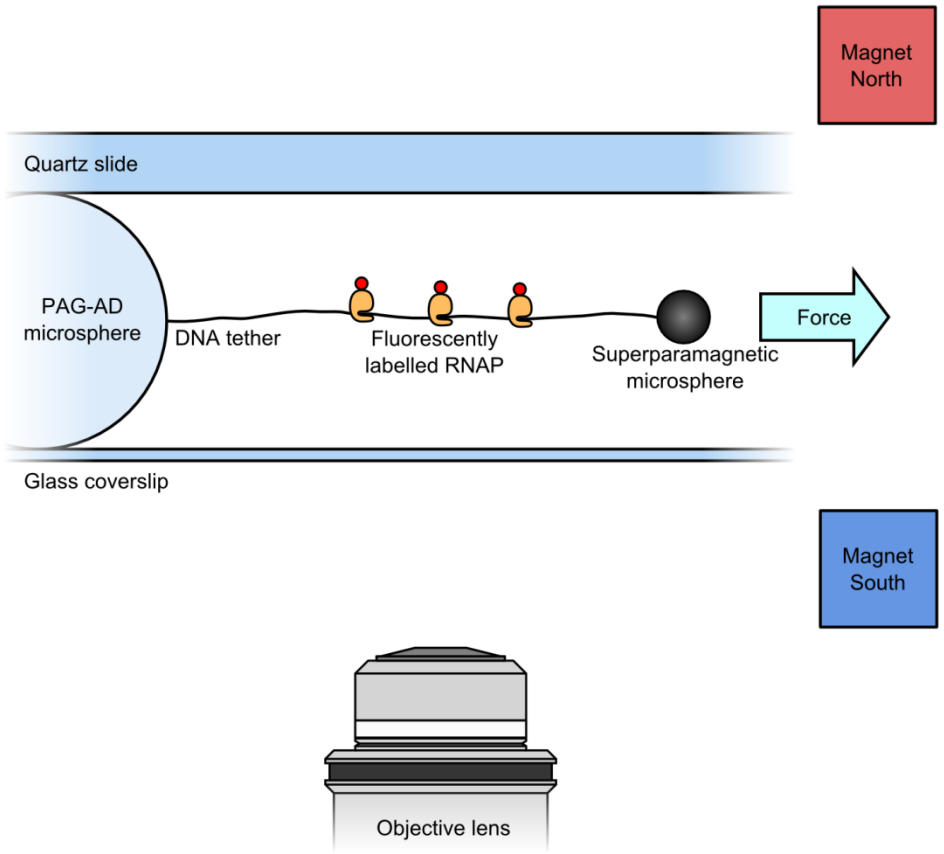


**Figure 4-1– Basic configuration of the horizontal magnetic tweezers microscope**
Rather than pull tethers at an angle from the surface, as is performed with equivalent systems, a vertical surface is used as the tethering substrate. Force is applied to the superparamagnetic microsphere with a pair of permanent magnets held either side of the sample. The optical system utilises a long working-distance objective lens to permit the magnet pair access to the entire sample, without the spatial restriction imposed by an oil-immersion lens.

Optically, the implementation described here is most favourably compatible with epifluorescence illumination. Using this, the TIRF limitations of fluorophore position within the sample chamber (described in Section 2.7.5) are removed, thus enabling implementation of truly horizontal tethers (Figure 4-1). In this approach the vertical tethering substrate is provided by a functionalised 9 µm diameter latex microsphere (PAG-AD-MS; Figure 4-1), which also serve a mechanical role in holding the quartz slide and coverslip apart at a fixed separation. Epi-illumination fails to offer the same signal to noise ratio as TIRF; however, background fluorescence from bulk excitation of fluorophores in this system is minimised through the use of atypically thin channels. Despite this, the limited focal depth of the long working-distance objective lenses used generally facilitates exclusion of surface-immobilised fluorophores from the acquired image.

## 4.2 Quantitative modelling of magnetic tweezers

Prior to design and construction of any scientific equipment it is vital to gain a complete understanding of the key physical factors and how their limitations will influence the final configuration. In the context of a magnetic tweezers system these key factors are the ability to generate large magnetic fields and the motion of the tethered superparamagnetic microsphere in response to both this field and thermally-induced forces.

### 4.2.1 Prediction of force acting on superparamagnetic microspheres

Accurate knowledge of the force exerted by the magnetic tweezers on superparamagnetic microspheres is vital for two fundamental reasons: first, to prevent conformational changes in the dsDNA template arising from over-extension of the tether, which occurs under relative extensions >1 [150,151] and can affect initiation [41] and elongation rates [152]; second, to minimise systematic error in measurements of transcription rate by precisely predicting the number of nucleotides per unit distance. The force experienced by the superparamagnetic microsphere in response to the applied magnetic field ($B$) can be predicted using Equation 4-1, where $m(B)$ is the induced microsphere magnetic moment. Net magnetic moment for the microsphere is obtained from knowledge of the magnetisation ($M$), which is defined as the magnetic moment density. Magnetisation can be estimated with the sigmoidal curve described by Equation 4-2 using values determined by Lipfert *et al.* for M280 ($M_{sat}$ = 14.0 A/m, $B_0$ = 15.5 mT [153]) and MyOne ($M_{sat}$ = 43 A/m, $B_0$ = 12 mT [99]) microspheres, where the saturation magnetisation ($M_{sat}$) and characteristic field ($B_0$) are properties of the microspheres.

$$F = -\vec{\nabla}U = \frac{1}{2}\vec{\nabla}\left(\vec{m}\left(\vec{B}\right)\cdot\vec{B}\right)$$

**Equation 4-1 – Force experienced by a magnetic material in an applied magnetic field**
General relation between force ($F$) and a the gradient of a potential ($U$), which can be applied to superparamagnetic materials as a function of the applied field strength ($B$) and field strength-dependent material parameter, magnetic moment ($m$) [99].

$$M(B) = M_{sat}\left(\coth(B/B_0) - \frac{1}{B/B_0}\right)$$

**Equation 4-2 – Sigmoidal curve describing microsphere magnetisation**
Magnetisation response ($M(B)$) of the superparamagnetic microspheres in an externally-applied magnetic field ($B$) is a function of the microsphere saturation magnetisation ($M_{sat}$) and the characteristic field ($B_0$).

### 4.2.2 Magnetic field modelling using Biot-Savart Law

For simple magnet geometries, the magnetic field experienced along trivial directions, such as that passing perpendicular to the long axis of the magnet pair (y-axis; Figure 4-2) can be calculated using the Biot-Savart law. With the Biot-Savart representation, magnets are considered to be comprised of infinitesimal current loops, each contributing a small magnetic component to the net magnetisation of the material. At the interface between two adjacent current loops the net current is zero; therefore, the net magnetisation can simply be described as a current passing along the surface of the magnet (Equation 4-3) [154].

$$\vec{B} = \frac{\mu_0}{4\pi}\int_C \frac{I\vec{dl} \times \vec{r}}{r^2}$$

**Equation 4-3 – Biot-Savart law for calculating magnetic field (B)**
The material to be modelled is described as the integral of infinitesimally small current elements (current, I; element length,$\vec{dl}$), a distance $\vec{r}$ from the coordinate origin. Inside the material these elements cancel out, so the current effectively passes across the surface.

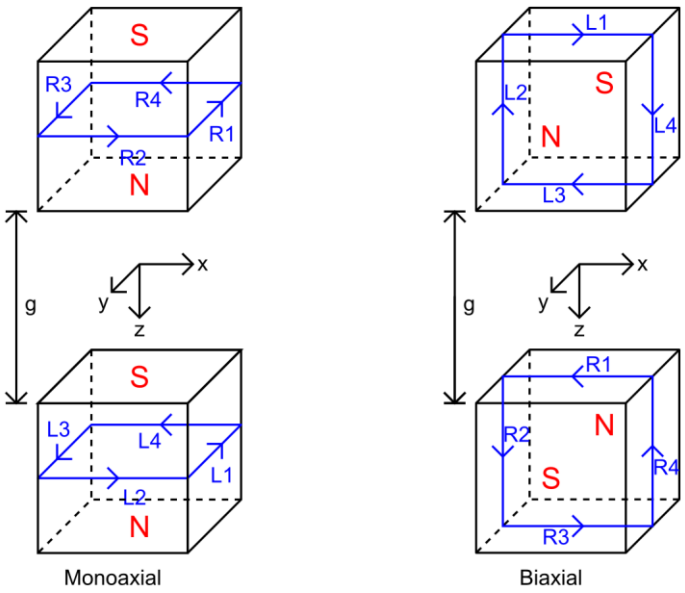


**Figure 4-2 – Geometries for Biot-Savart magnetic field modelling**
Schematic diagram showing key distances in the Biot-Savart prediction of the magnetic field originating from a pair of cubic permanent magnets with a spacing (*g*) and distance (*h*) from the point of measurement (POM) along the y-axis. The characteristics of the produced magnetic field depend strongly upon the magnet pair configuration; shown are two typical configurations, monoaxial and biaxial. Adapted from [99].

The magnetic field resulting from a pair of cubic permanent magnets will vary depending on their relative orientation. Here, two configurations have been evaluated for their suitability in offering both a high maximum field strength and sufficiently low field gradient as to enable precise control over the field magnitude as a function of distance from the magnets. These configurations are henceforth referred to as monoaxial, where

both magnet magnetisation directions are aligned along a single axis, and biaxial, where the axes are parallel, but in opposing directions (Figure 4-2). Of key importance is the distance (*h*) along the y-axis between the coordinate system origin and the point of measurement (POM; coincident with the centre point of the magnet pair).

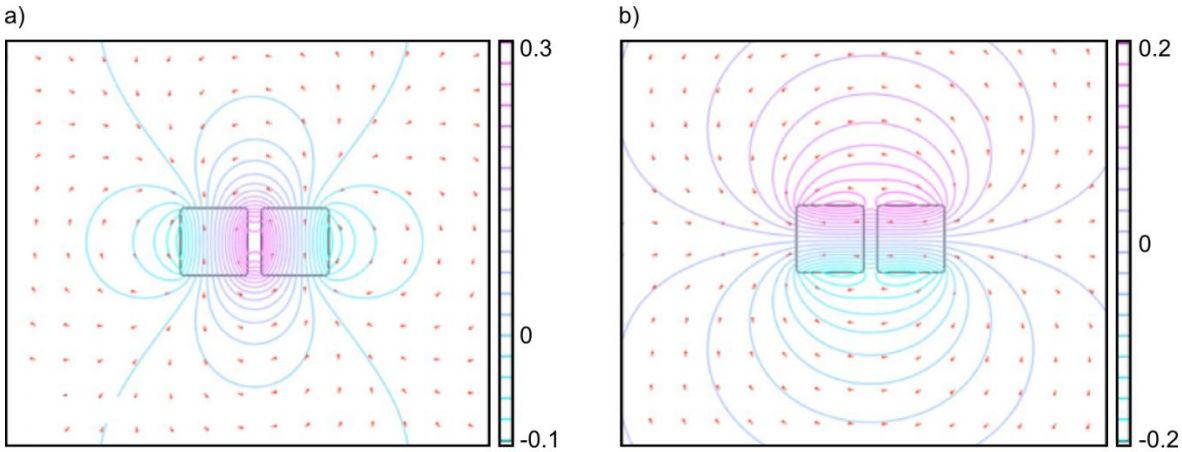


**Figure 4-3 – Magnetic field diagrams for two magnet configurations**
Field diagrams for the biaxial (a) and monoaxial (b) magnet configurations. Lines show the y-component of the magnetic vector potential, with magnitude corresponding to the colour scale to the right of each frame. The red arrows show the local direction of the magnetic field. Image taken from Lipfert *et al.*for identical magnet configuration [99].

Using the Biot-Savart implementation developed by Lipfert *et al.* for a similar magnetic tweezers setup, albeit in the vertical configuration, the magnetic field as a function of distance along the y-axis can be calculated with good experimental agreement [99]. With this approach, the z-component of the magnetic field ($B_z$), at a distance ($h$) along the y-axis is either given by Equation 4-4 for the monoaxial configuration or by Equation 4-5 for the biaxial configuration, as provided in the supplementary information of Lipfert *et al.* [99]. In both cases, the magnetic field is a function of the magnet separation ($g$), magnet edge-length ($L$) and magnetic remanence ($B_r$), where the latter is the magnetisation of a material in the absence of an externally-applied magnetic field. A full derivation of these equations from first principles is given in Appendix C-I.

$$B_z(0,h,0) = \frac{B_r}{4\pi}\int_{L2,L4,R2,R4}\frac{2L}{r^3}dzdy + \int_{L1,R1}\frac{2h+L}{r^3}dzdx + \int_{L3,R3}\frac{-2h+L}{r^3}dzdx$$

$$= \frac{B_r}{4\pi}\left[\int_{g/2}^{g/2+L}\int_{-L/2}^{L/2}\left(\frac{2L}{(z^2+(L/2)^2+(h-y)^2))^{3/2}}\right)dydz + \int_{g/2}^{g/2+L}\int_{-L/2}^{L/2}\left(\frac{2h+L}{(z^2+x^2+(h+L/2)^2))^{3/2}}\right)dxdz + \int_{g/2}^{g/2+L}\int_{-L/2}^{L/2}\left(\frac{-2h+L}{(z^2+x^2+(h-L/2)^2))^{3/2}}\right)dxdz\right]$$

**Equation 4-4 – Biot-Savart approach to modelling the monoaxial magnet configuration**
The monoaxial configuration is shown in Figure 4-2. The net magnetic field from the magnet pair is a function of the magnet residual magnetism ($B_r$), magnet edge length ($L$), magnet separation ($g$) and the distance between the microsphere and magnet pair centre ($h$).

$$B_z(0,h,0) = \frac{B_r}{4\pi}\int_{L2,R4}\frac{-2(h-y)}{r^3}dydx + \int_{L4,R2}\frac{2(h-y)}{r^3}dydx$$

$$= \frac{B_r}{4\pi}\left[\int_{-L/2}^{L/2}\int_{-L/2}^{L/2}\left(\frac{2(h-y)}{((g/2+L)^2+x^2+(h-y)^2)^{3/2}}\right)dxdy - \int_{-L/2}^{L/2}\int_{-L/2}^{L/2}\left(\frac{2(h-y)}{((g/2)^2+x^2+(h-y)^2)^{3/2}}\right)dxdz\right]$$

**Equation 4-5 – Biot-Savart approach to modelling the biaxial magnet configuration**
The biaxial configuration is shown in Figure 4-2. The net magnetic field is a function of the same parameters described for Equation 4-4; however, here, current segment pairs L1 and R1 along with L3 and R3 cancel out to simplify the equation.

Evaluation of the above two equations has been performed using Maple (*Biot-Savart_force_model.mw*; Accompanying Material) as a function of microsphere-magnet pair separation at two experimentally-relevant magnet separations for the 2.8 µm diameter M280 (Invitrogen, Carlsbad, California, USA) superparamagnetic microspheres. These magnet pair separations are 0.4 mm, representing the minimum gap when using a sample approximately two coverslips thick, and 2 mm, which represents the minimum gap for a slide and coverslip-based sample (Section 2.7.3). All simulations were performed using the vendor-supplied data for cubic gold-plated NdFeB magnets ($L$ = 5 mm; W-05-N50-G; Supermagnete, Gottmadingen, Germany), except magnetic remanence, which was measured to be 1.26 T (Section 2.5.3). The diameter of the M280 microspheres was actually taken to be 2.95 µm following the size characterisation described in Section 2.5.2.

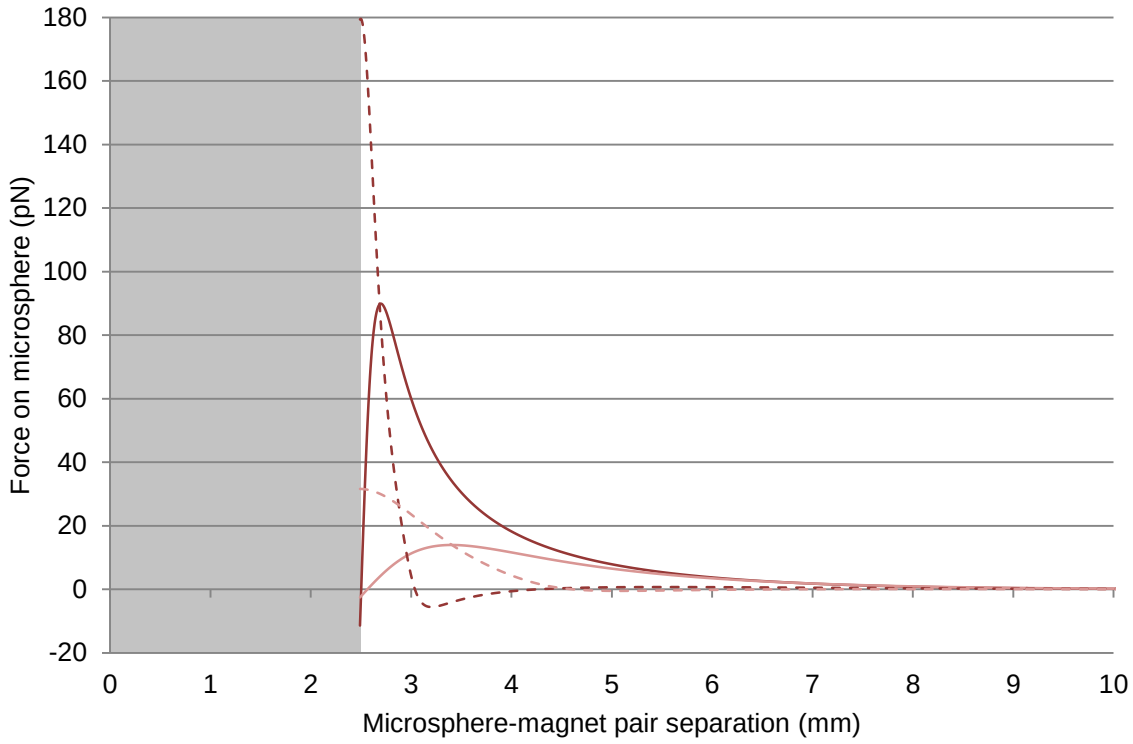


**Figure 4-4 – Predicted force with magnets in monoaxial and biaxial configurations**
Force acting on a superparamagnetic microsphere (M280) as a function of microsphere-magnet pair separation for two magnet-magnet separations; 0.4 mm (dark red lines), the minimum magnet gap for a coverslip-based sample, and 2 mm (light red lines), the minimum magnet gap for a slide-based sample. As expected, smaller magnet separations yield higher forces. Both separations have also been evaluated for the monoaxial (dashed lines) and biaxial (solid lines) magnet configurations. While monoaxial configurations provide higher absolute forces, the steeper curve gradient makes the configuration less suitable for a system requiring precise control over applied force.

Despite offering the greatest absolute forces, the monoaxial configuration suffers from a high field gradient compared to the biaxial equivalent (Figure 4-4); such behaviour is undesirable since it precludes precise control of the force acting on the microsphere. In addition to this, the highest force region of the monoaxial configuration occurs at the edge of the magnet pair; a position which produces observable levels of optical distortion due to partial obstruction of the objective lens. This occultation results from the finite magnet size (5 mm along an edge) and has led to omission of data for microsphere-to-magnet-pair separations smaller than 2.5 mm. Further spatial exclusion may be necessary depending on the objective lens used. Typical high numerical aperture oil-immersion objective lenses have physical radii of approximately 15 mm, thus preventing anything higher than negligible forces being experienced. Although such an effect has been avoided through implementation of a long working-distance objective (as described in Section 4.4.1), it is preferable to use a system which offers higher forces at larger microsphere to magnet pair separations. As a result, subsequent analyses focus solely on the biaxial magnet configuration.

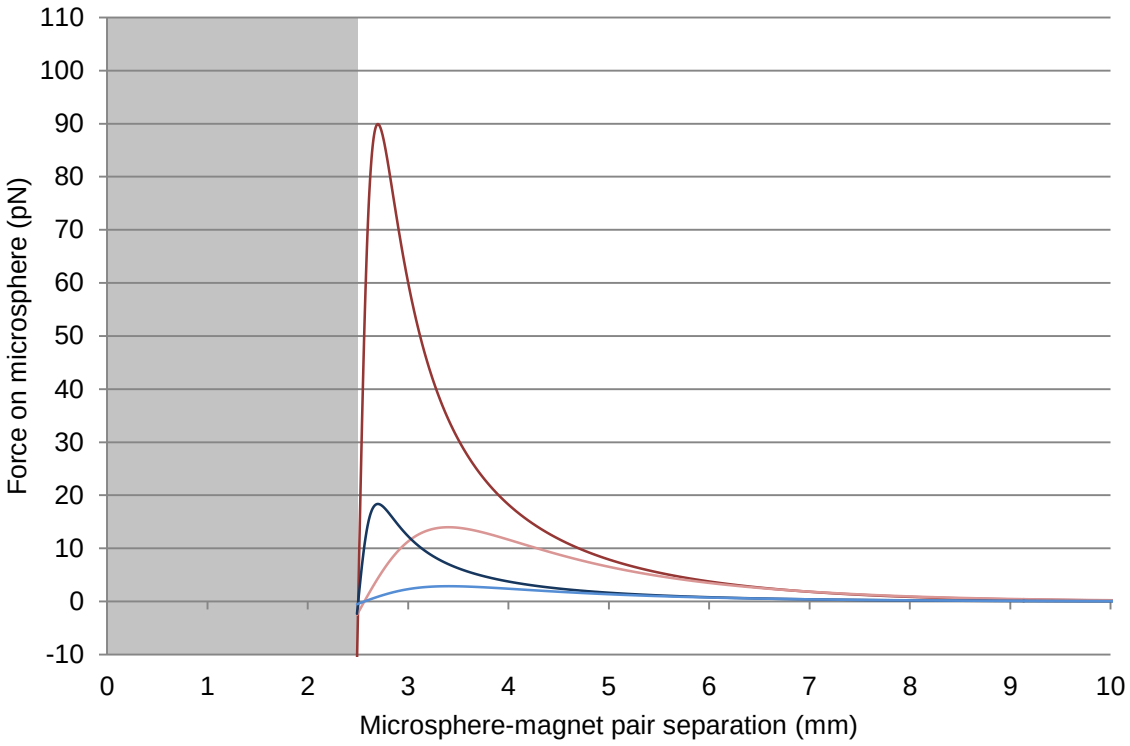


**Figure 4-5 – Predicted forces acting on M280 and MyOne microspheres**
Force acting on a superparamagnetic microsphere as a function of microsphere-magnet pair separation for both MyOne (1.19 µm diameter; blue lines) and M280 (2.95 µm diameter; red lines) microspheres at two relevant magnet-magnet separations; 0.4 mm (dark blue and red lines) and 2 mm (light blue and red lines), as described for Figure 4-4. M280 microspheres are capable of achieving significantly higher forces; however, their MyOne equivalents are still easily able to reach the 0.416 pN required for sufficient DNA tether extension to 77.5% contour length. Magnets are simulated in the biaxial configuration.

Results shown in Figure 4-5 demonstrate that the significantly larger M280 (2.95 µm diameter, 12% iron content, $M_{sat}$ = 14 kA/m [153], $B_0$ = 15.5 mT [153]) superparamagnetic microspheres experience greater forces than the smaller MyOne equivalent (1.19 µm diameter, 26% iron content, $M_{sat}$ = 43.3 kA/m [99], $B_0$ = 12 mT [99]) in spite of the higher iron density for MyOne microspheres. Both microsphere diameters were obtained through size distribution analysis and differ from the values specified by the vendor (Section 2.5.2). As detailed later in Section 4.3.2, the force required for sufficient extension of DNA tethers to permit transcription initiation by T7 RNAP is only 0.416 pN; a range easily accessible by both microspheres and at both relevant magnet-magnet spacings.

### 4.2.3 Modelling thermally-induced microsphere motion

When considering the percentage of tethers that may be interacting with the channel surface it is important to take into account thermally-induced motion of the microsphere. Such dynamic nature of the system represents an effective increase in the zone of interaction compared to the idealised model (Section 4.3.1), with microspheres in this

extended region experiencing transient contact with the channel surface. Quantification of the degree to which this will have an effect is achieved here using a model of tethered particle motion derived for magnetic tweezers in the vertical configuration by Velthuis *et al.* [155]. This model is applied in Section 4.3.2 as an extension to the idealised case outlined in Section 4.3.1.

Tethered particle motion in a harmonic trap can be described using the Langevin equation (Equation 4-6), where $x(t)$ is the position of the microsphere as a function of time and $\dot{x}$(t) and $\ddot{x}$ (t) are the microsphere velocity and acceleration respectively. Motion is also a function of the microsphere mass, *m*, the viscous drag coefficient, $\gamma$ (as defined in Equation 4-7), the trap stiffness (*k*) and the thermal force acting on the particle due to Brownian motion in the solution. Viscous drag is a function of the dynamic viscosity of the solution ($\eta$) and the microsphere radius (*R*) and can alternatively be written in terms of the bead diffusion constant (*D*) [156,155,71,157]. Since damping of motion due to friction occurs very rapidly, the inertial term (first term in Equation 4-6) can be considered negligible [155,71].

$$m\ddot{x}(t) + \gamma\dot{x}(t) + kx(t) = F_{Therm}$$

**Equation 4-6 – Langevin equation describing tethered particle motion**
Motion is dependent on four terms: first, the inertial term, which can be considered negligible for this analysis; second, the viscous friction force; third, the harmonic term and finally fourth, the random noise term arising from Brownian motion [155,158,157].

$$\gamma = 6\pi\eta R = \frac{k_B T}{D}$$

**Equation 4-7 – Viscous drag for a sphere passing through a liquid**
The viscous drag coefficient for the system is a function of the viscosity of the solution ($\eta$) and the microsphere radius (*R*). This can be written in terms of the microsphere diffusion constant, D [155,159].

The random thermal displacements arising from Brownian motion are assumed to occur with a discrete duration ($\Delta t$) and have a magnitude ($\delta x_{Langevin}$) extracted from a Gaussian distribution with a mean value of zero and variance of $2D\Delta t$ [160]. With this assumption, Equation 4-6 can be simplified to yield the displacement of the microsphere ($\Delta x$) during the time step ($\Delta t$) as shown in Equation 4-8, where the viscous drag coefficient has been expressed as shown in Equation 4-7 [155,160].

$$\Delta x(t) = -\frac{kx(t)}{6\pi\eta R}\Delta t + \delta x_{Langevin}\Delta t$$

**Equation 4-8 – Displacement of a tethered magnetic microsphere**
During the time step ($\Delta t$), the microsphere is subject to forces arising from the harmonic trap of the magnetic tweezers. Additional forces are due to fluid viscosity ($\eta$) and random thermal motion ($\delta x_{Langevin}$), which has displacement conforming to a Gaussian distribution.

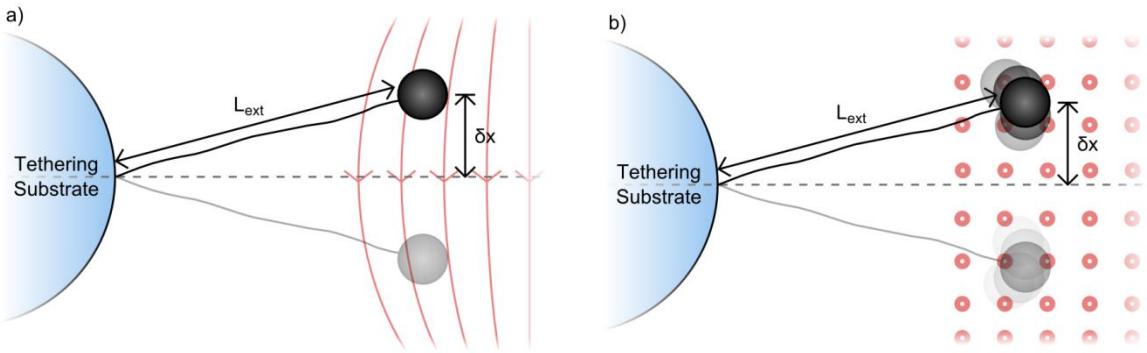


**Figure 4-6 – Superparamagnetic microsphere movement in an applied magnetic field**
Motion of a tethered superparamagnetic microsphere through an applied magnetic field, as viewed from above. a) Rotation of the microsphere is constrained along field lines (red lines), thus the trap stiffness is given by Equation 4-9. b) Microsphere rotation perpendicular to the magnetic field (red rings) is unconstrained, since movement is along lines of constant flux density; as such, motion is described by Equation 4-10. Image adapted from [155].

Stiffness of the magnetic tweezers trap is dependent on the direction of displacement relative to the magnetic field direction (Figure 4-6), with this difference arising due to a lack of magnetic microsphere rotational constraint perpendicular to the field, as described by te Velthuis *et al.* [155]. As a result of this, trap stiffness for microsphere motion perpendicular to the magnetic field becomes a function of microsphere radius in addition to tether extension, as can be seen in Equation 4-9 for motion parallel to the field and Equation 4-10 for motion perpendicular to it.

$$k_{\parallel} = \frac{F}{L_{ext}}$$

**Equation 4-9 – Trap stiffness for displacement parallel to the magnetic field**
Rotational constraint of the magnetic microsphere along this axis results in stiffness ($k_{\parallel}$) being a function of applied force ($F$) and tether extension ($L_{ext}$) alone.

$$k_{\perp} = \frac{F}{L_{ext} + R}$$

**Equation 4-10 – Trap stiffness for displacement perpendicular to the magnetic field**
Unlike motion parallel to the field, here the microsphere is free to rotate and as such, the microsphere radius ($R$) must be taken into consideration in addition to the applied force ($F$) and tether extension ($L_{ext}$).

$$\Delta x_{\parallel}(t) = -\left(\frac{F}{L_{ext}}\right)\left(\frac{x(t)}{6\pi\eta R}\right)\Delta t + \delta x_{Langevin}\Delta t$$

**Equation 4-11 – Microsphere displacement parallel to the magnetic field**
Displacement ($\Delta x_{\parallel}$) is a function of the applied force ($F$), tether extension ($L_{ext}$), lateral displacement ($x$), fluid viscosity ($\eta$), microsphere radius ($R$), time step ($\Delta t$) and random thermal motion ($\delta x_{Langevin}$), which has displacement conforming to a Gaussian distribution.

$$\Delta x_{\perp}(t) = -\left(\frac{F}{L_{ext}+R}\right)\left(\frac{x(t)}{6\pi\eta R}\right)\Delta t + \delta x_{Langevin}\Delta t$$

**Equation 4-12 –Microsphere displacement perpendicular to the magnetic field**
Displacement ($\Delta x_{\perp}$) is a function of the applied force ($F$), tether extension ($L_{ext}$), lateral displacement ($x$), fluid viscosity ($\eta$), microsphere radius ($R$), time step ($\Delta t$) and random thermal motion ($\delta x_{Langevin}$), which has displacement conforming to a Gaussian distribution.

Substitution of the two trap stiffnesses, given in the above two equations, yields the final equations for microsphere displacement ($\Delta x$) over a discrete time step ($\Delta t$) for motion parallel (Equation 4-11) and perpendicular (Equation 4-12) to the magnetic field direction. This additional term is most appreciable for the larger, M280 microspheres ($R$ = 1.475 μm), where it can change force measurements by approximately 18% when using the shorter, StuI-digested T7 DNA template (see Section 2.3.9.2). Since the hypothesised motion perpendicular to the field has not be experimentally-observed, all work described here uses the standard relationship (Equation 4-11).

## 4.3 Considerations for the horizontal magnetic tweezers system

In the standard "vertical" magnetic tweezers configuration, the magnetic microsphere is pulled away from the tether-immobilising surface into the bulk volume of the microfluidic chamber. Assuming the chamber is sufficiently taller than the combined tether length and microsphere diameter, interactions between the microsphere and the chamber surfaces can be neglected. Conversely, in the horizontal configuration outlined here, the tether is pulled along a narrow channel, barely three-fold wider than the microsphere diameter. As a result, interactions between the microsphere and channel surfaces form a real concern, since accurate analysis of microsphere motion is vital for determining the applied force. While a detailed explanation of force characterisation using microsphere motion is provided in Section 4.7, it is suffice to say here that unaccounted-for damping of motion would have a deleterious effect on the ability to precisely manipulate the DNA tether. The analyses described in this section are concerned with quantification of both lateral forces experienced in a horizontal magnetic tweezers configuration, which may increase the

probability of microsphere-surface interactions, and increase drag on the microsphere, which arises due to close proximity to the channel surface. It should be noted that this is merely a precautionary analysis; similar reported side-pulling geometries have observed no evidence for interactions between streptavidin-functionalised microspheres and a protein-functionalised surface [77]. Measurement of interactions would likely require application of high speed cameras or illumination onto a photodiode; thus facilitating observation of the complete microsphere motion (see Section 4.3.4 for an analysis of camera frame-rate limitations). Such measurements may be possible through analysis of variation in thermally-induced microsphere oscillations as a function of proximity to the channel surface. Alternatively, microsphere position in the channel could be elucidated through analysis of bright-field diffraction patterns (see Section 7.3.1.1).

### 4.3.1 Distribution of tethered magnetic microspheres across the channel

To establish an initial understanding of the potential interaction between the superparamagnetic microsphere and channel surface, a basic model can be envisaged. In this model, the magnetic microspheres are tethered to 9.23 µm diameter latex (PAG-AD) microspheres via a single double-stranded DNA molecule and are approximated as being pulled perfectly horizontally towards the magnet pair. At this scale, any tethers attached to the PAG-AD microsphere within the magnetic microsphere radius of the channel surface will undergo damping effects due to physical interaction (Figure 4-7). The vendor-specified diameter of the PAG-AD microspheres is 9 µm; however, the 9.23 µm value used here was measured via SEM analysis (Section 2.5.2). For consistency throughout this section, the areas adjacent to the channel surface in which microsphere-surface interactions are possible shall be referred to as "zones of interaction" (ZOI; shaded red in Figure 4-7).

Assuming homogeneous PAG-AD microsphere functionalisation, the percentage of tethers formed within the ZOI can be easily estimated since surface area is uniform across the channel. In the idealised situation described, where the tether is pulled perfectly horizontally along the channel and there is no thermally-induced vertical bead displacement, the percentage of tethers that will potentially interact with the surface is simply the percentage ratio of radii for the superparamagnetic and 9.23 µm diameter PAG-AD microspheres. Application of the ZOI analysis for both the 2.95 µm diameter M280

microspheres and 1.19 µm diameter MyOne microspheres yields values of 32% and 13% respectively.

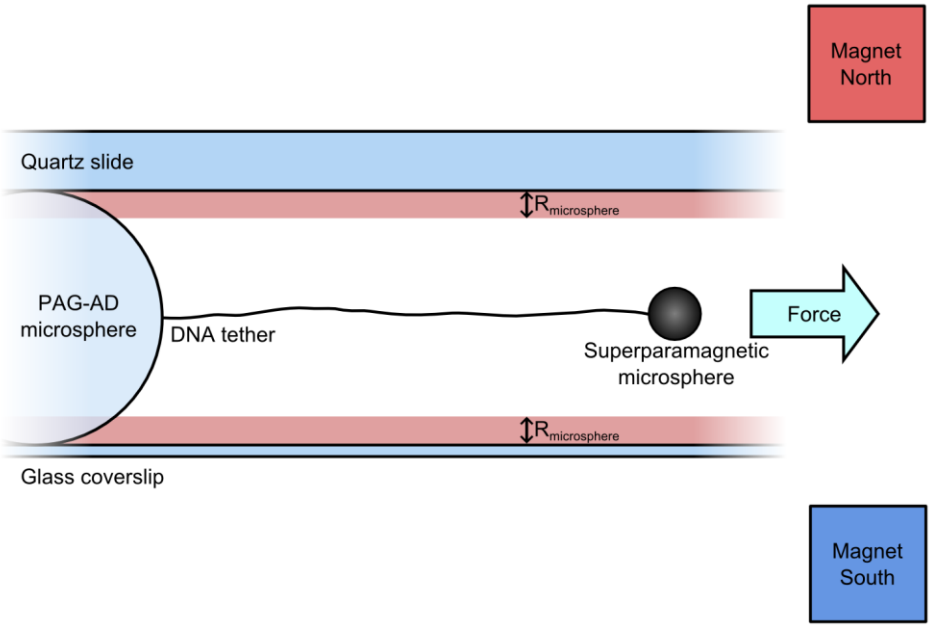


**Figure 4-7 – Cross-section of the HMT microscope tethering system**
For the most basic case with the tether pulled perfectly horizontally towards the magnet pair with negligible vertical displacement due to Brownian motion, the zones of interaction (ZOI) with the channel surface (shaded red) are equal to the radius of the superparamagnetic microspheres. In this situation, assuming homogeneous functionalisation of the PAG-AD microsphere, approximately 30% of tethers could experience an interaction with the channel surface.

### 4.3.2 The effect of thermally-induced microsphere motion

In the horizontal magnetic tweezers configuration, thermally-induced microsphere displacements will result in an increase in the ZOI, as defined for the idealised case in Section 4.3.1. This can be estimated through application of the model developed by Velthuis *et al.* [155] (see Section 4.2.3) for vertical microsphere motion (parallel to the magnetic field lines) and described by Equation 4-11. Displacement is estimated for a series of typical experimental setups, each using tethers with contour lengths of 6.79 µm, but extended through the application of force to two different types of superparamagnetic microsphere; 2.95 µm diameter, M280 (Invitrogen, Carlsbad, California, USA) and 1.19 µm diameter MyOne (Invitrogen, Carlsbad, California, USA) microspheres. While the former have a lower saturation magnetisation (14.0 kA/m [153]) compared to the MyOne microspheres (43.3 kA/m [99]), they experience a larger force due to their significantly greater volume. This potentially poses a problem for the M280 microspheres, since they will result in a wider ZOI, as described in Section 4.3.1). Therefore, it is important to

establish a compromise between the ability for high force generation and reducing the number of microspheres which may be in contact with the channel surface.

For this analysis, vertical microsphere displacements have been estimated for a range of relevant forces. These forces are the maximum force achievable with the experimental setup and the force required to extend to the tether to approximately 75-80% of its contour length, which is deemed the optimal range to extend DNA without causing overextension. The magnitude of these forces is, amongst other parameters, dependent on the distance between the two magnets, a parameter that has been maintained at 2 mm through all simulations. This represents the smallest distance possible through which a sample comprising a coverslip and slide, as described in Section 2.7.3, can freely pass. Maintaining this gap as small as possible is necessary since force acting on the microsphere decreases greatly with increasing magnet separation (Section 4.2). Applied force in this system is also dependent on the superparamagnetic microspheres used. For M280 microspheres the maximum achievable force in the horizontal magnetic tweezers is 14.0 pN and for the MyOne microspheres it is 2.9 pN. In both cases a relative tether extension of 77.5% occurs for an applied force of 0.416 pN.

In each case, the end-to-end tether extension as a function of the applied force is estimated using the worm-like chain (WLC) model, which is widely used to represent semi-flexible polymers, such as double-stranded DNA [149]. The WLC model (Equation 4-13) is dependent on the persistence length, a characteristic property of the molecule describing its bending stiffness. For contour lengths significantly greater than the persistence length the molecule can only be described through statistical means; however, shorter molecules can be considered as elastic rods.

$$F = \frac{k_B T}{P}\left[\frac{1}{4}\left(1 - \frac{x}{L_0}\right)^{-2} + \frac{x}{L_0} - \frac{1}{4}\right]$$

**Equation 4-13 – Worm-Like Chain (WLC) model for semi-flexible polymers**
The WLC model estimates the force required to extend a semi-flexible polymer to a given end-to-end length (x). This is a function of the polymer's contour length ($L_0$) and a characteristic stiffness property, the persistence length (P) [149].

For each system, a total of ten simulations were run (function: *modelDisp.m*; Accompanying Material), each across a time of 20 seconds, with a time step of 0.005 ms. Additional parameters, constant through all the simulations, were a temperature (*T*) of

293 K and fluid viscosity ($\eta$) of 0.001 kg/m$^2$. These parameters are all in agreement with those used by Velthuis *et al.* [155]. An example trace of vertical microsphere displacement as a function of time is included in Figure 4-8.

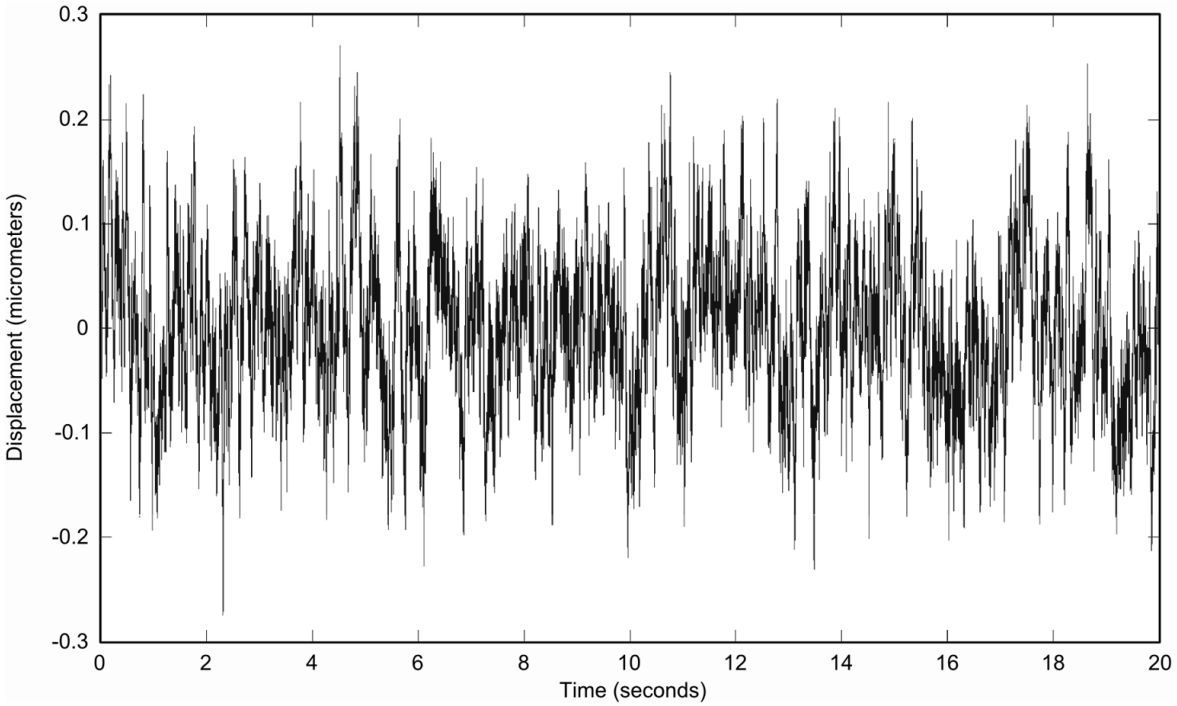


**Figure 4-8 – Simulating tethered particle motion in HMT microscope**
Displacement is simulated as a function of time for a tether extension of 6.37 µm under an applied force of 5 pN. Motion is centred on the attachment point, here at z = 0 µm, which acts as an equilibrium position. The simulation was run for 20 seconds, with an interval of 0.005 ms; these parameters are the same as those used in the analysis of thermally-influenced ZOI width.

Thermally-induced microsphere motion increases the width of the ZOI; these modified widths are calculated through summation of the static ZOI (Section 4.3.1) and the greatest observed thermal-displacement. The data in Table 4-1 demonstrates that when factoring in the effect of thermally-induced bead motion, the percentage of microspheres which may be in contact with the channel surface increases dramatically. For the larger M280 microspheres acted upon by a force of 0.416 pN, yielding a biologically relevant tether extension suitable for transcription initiation, the ZOI increases from 32% of the channel depth to as much as 48.8%. Similarly, the MyOne microsphere ZOI increases from 13% of the channel depth to up to 29.8%.

In practicality, the effect of this is likely to be less severe than an equivalent ZOI increase resulting from use of larger magnetic microspheres for a couple of reasons. First, contact occurring in this extended ZOI is likely to be transient, since the microsphere experiences a

restoring force towards the equilibrium (time-averaged) position. Second, the thermally-induced displacements conform to a Gaussian distribution, so the frequency with which the microsphere visits the furthest extent of the extended ZOI will be relatively low.

**Table 4-1 – Effect of thermal microsphere displacement on ZOI width**
Maximum vertical displacement experienced by a tethered superparamagnetic microsphere in a magnetic tweezers system. With increasing magnetic force ($F_m$), the maximum displacement ($\Delta z_{therm}$) of the bead decreases, as predicted by the equipartition theorem. The analysed forces (and resulting tether extensions; $L_{ext}$) correspond to the highest achievable forces for M280 and MyOne microspheres and to force required for a relative tether extension of 77.5%. For each example, the ZOI as a percentage of the entire channel width is provided.

| **Microsphere** | ***R*** **(μm)** | $L_{ext}$ **(μm)** | $F_m$ **(pN)** | $\Delta z_{therm}$ **(μm)** | **ZOI** |
|---|---|---|---|---|---|
| M280 | 1.475 | 5.26 (77.5%) | 0.416 | 0.778 | 48.8% |
| M280 | 1.475 | 6.54 (96.3%) | 14.0 | 0.181 | 35.9% |
| MyOne | 0.595 | 5.26 (77.5%) | 0.416 | 0.782 | 29.8% |
| MyOne | 0.595 | 6.23 (91.8%) | 2.9 | 0.382 | 21.2% |

### 4.3.3 The effect of gravity on the microsphere

A factor thus far neglected when considering the proportion of tethers possibly in contact with the channel surface is the effect of microsphere mass on the tether gradient. The gradient is a function of the magnetic force ($F_m$) acting horizontally and the gravitational force ($F_g$) pulling the microsphere vertically (Figure 4-9). Gravitational force is calculated using the relation, $F_g = mg$, where $m$ is the microsphere mass (obtained from the known microsphere density of $1.8 \times 10^3$ kgm$^{-3}$ and volume) and $g$ is acceleration due to gravity ($g = 9.81$ ms$^{-2}$). Such an approach assumes the tether itself has negligible mass and that gravity acts solely on the superparamagnetic microsphere.

Initially neglecting thermal influence, the effect of gravity on the ZOI can simply be characterised in terms of the change in microsphere height due to gravity ($\Delta z_{grav}$) and microsphere radius ($R$). For non-horizontal tethers, where the vertical decrease in height due to gravity is less than the radius of the superparamagnetic microsphere, there is no net change in the width of the ZOI (Equation 4-14). This arises because the observed decrease in the upper ZOI ($ZOI_{upper} = R + \Delta z_{grav}$) is exactly matched by an increase in the lower ZOI ($ZOI_{lower} = R - \Delta z_{grav}$); however, when the change in height exceeds the microsphere radius, the decreased upper ZOI can no longer compensate fully and the total ZOI width in the channel becomes the sum of the microsphere radius and change in height (Equation 4-15).

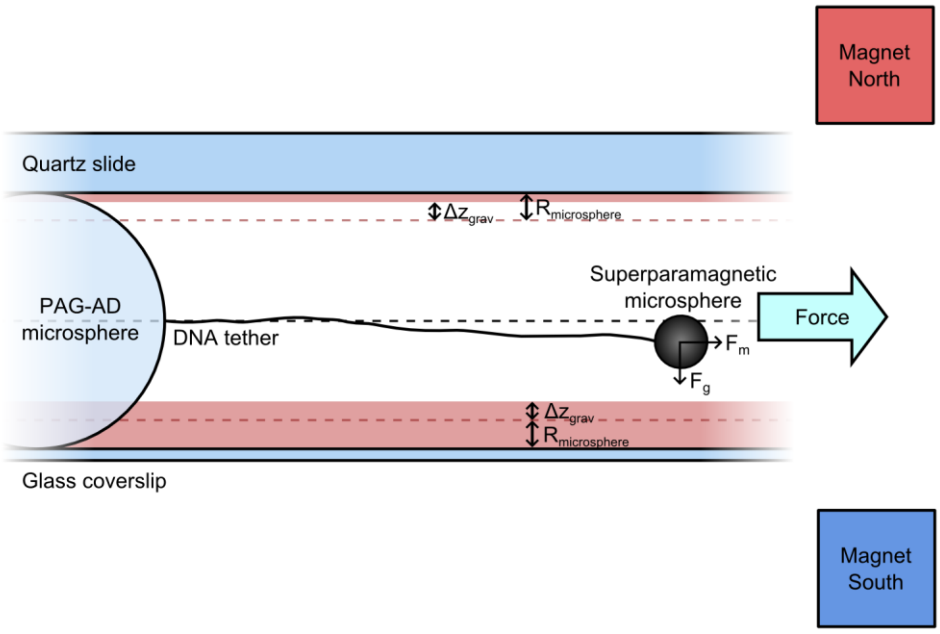


**Figure 4-9 – Effect of gravity on the zone of interaction (ZOI)**
Deviations in microsphere height from horizontal (black dashed line) result in a corresponding change in the ZOI (red regions) width from those shown in Figure 4-7 (red dashed lines). The degree of height change ($\Delta z_{grav}$) depends on the ratio between the magnetic ($F_m$) and gravitational ($F_g$) forces acting on the microsphere. For changes in microsphere vertical position due to gravity smaller than the microsphere radius ($R$), the increased lower ZOI is compensated by a reduced upper ZOI; however, when $\Delta z_{grav}$ exceeds $R$ this effect is insufficient and the total ZOI width increases.

$$ZOI = \frac{2R}{h}$$

**Equation 4-14 – Zone of interaction for $\Delta z_{grav} \leq R$**
Where the change in microsphere height due to gravity ($\Delta z_{grav}$) is less than the microsphere radius ($R$), the width of the ZOI is a function of just the radius and channel height ($h$).

$$ZOI = \frac{R + \Delta z_{grav}}{h}$$

**Equation 4-15 – Zone of interaction for $\Delta z_{grav} > R$**
Where the change in microsphere height due to gravity ($\Delta z_{grav}$) is greater than the microsphere radius ($R$), the width of the ZOI is a function of the radius, gravitationally-induced change in height and the channel height ($h$).

The magnitude of this effect has been evaluated for the same four representative cases investigated in Section 4.3.2, with the results shown in Table 4-2. For all but the low-force M280 case, the change in height due to gravity is negligible, generally leading to an off-horizontal angle less than 2.2° and resulting in no net increase in the ZOI. In contrast, gravitationally-induced change in microsphere height is sufficiently large for M280 tethers extended to 77.5%, where the extension force is relatively low, that the ZOI becomes enlarged, thus demonstrating the validity in considering the effect of gravity.

**Table 4-2 – Effect of gravity on the zone of interaction (ZOI)**
The gravitational force acting on the microsphere ($F_g$), and by extension the change in off-horizontal tether angle ($\theta$) and microsphere height ($\Delta z_{grav}$), is a function of the microsphere density ($\rho$; vendor-supplied), microsphere radius ($R$), tether extension ($L_{ext}$) and magnetic force acting on the microsphere ($F_m$). Only in the case of the M280 microspheres at low extension does gravity play a significant role. This assumes gravity to act solely on the superparamagnetic microsphere.

| **Microsphere** | $\rho$ (kg/m$^3$) | $R$ (µm) | $L_{ext}$ (µm) | $F_m$ (pN) | $F_g$ (pN) | $\theta$ (°) | $\Delta z_{grav}$ (µm) | **ZOI** |
|---|---|---|---|---|---|---|---|---|
| M280 | 1400 | 1.475 | 5.26 (77.5%) | 0.416 | 0.185 | 24.0 | 2.14 | 39.2% |
| M280 | 1400 | 1.475 | 6.54 (96.3%) | 14.0 | 0.185 | 0.76 | 0.09 | 32.0% |
| MyOne | 1800 | 0.595 | 5.26 (77.5%) | 0.416 | 0.016 | 2.20 | 0.20 | 11.7% |
| MyOne | 1800 | 0.595 | 6.23 (91.8%) | 2.9 | 0.016 | 0.32 | 0.03 | 13.0% |

Factoring in the thermal effects described in Section 4.3.2 effectively extends the range over which the microsphere height can change before the total ZOI is affected. This transition now occurs when the gravity-induced height change exceeds the sum of both the microsphere radius and range of thermal motion (Equation 4-16 below the threshold and Equation 4-17 above it).

$$ZOI_{total} = \frac{2(R + \Delta z_{therm})}{h}$$

**Equation 4-16 – Zone of interaction when considering thermal effects only**
This relationship is valid for the condition $\Delta z_{grav} \leq R + \Delta z_{therm}$, where $R$ is the microsphere radius, $\Delta z_{therm}$ is the range of thermal motion, $\Delta z_{grav}$ is the change in microsphere vertical position due to gravity and $h$ is the channel height.

$$ZOI_{total} = \frac{R + \Delta z_{therm} + \Delta z_{grav}}{h}$$

**Equation 4-17 – Zone of interaction when considering thermal and gravitational effects**
This relationship is valid for the condition $\Delta z_{grav} > R + \Delta z_{therm}$, where $R$ is the microsphere radius, $\Delta z_{therm}$ is the range of thermal motion, $\Delta z_{grav}$ is the change in microsphere vertical position due to gravity and $h$ is the channel height.

With the larger zones of interaction resulting from the inclusion of thermal motion shown in Table 4-3, the effect of gravity becomes even less significant. As a result, although gravity can lead to appreciable variations in microsphere height, for the conditions likely to be experienced in the described experiments it can be neglected.

**Table 4-3 – Zones of interaction when considering thermal effects and gravity**
In no situation is the microsphere sufficiently large to require inclusion in the calculation of ZOI (Equation 4-17). As a result, this table is identical to Table 4-1, barring inclusion of the change in height due to gravity ($\Delta z_{grav}$).

| Microsphere | $R$ (µm) | $L_{ext}$ (µm) | $F_m$ (pN) | $\Delta z_{therm}$ (µm) | $\Delta z_{grav}$ (µm) | ZOI |
|---|---|---|---|---|---|---|
| M280 | 1.475 | 5.26 (77.5%) | 0.416 | 0.778 | 2.14 | 48.8% |
| M280 | 1.475 | 6.54 (96.3%) | 14.0 | 0.181 | 0.09 | 35.9% |
| MyOne | 0.595 | 5.26 (77.5%) | 0.416 | 0.782 | 0.20 | 29.8% |
| MyOne | 0.595 | 6.23 (91.8%) | 2.9 | 0.382 | 0.03 | 21.2% |

### 4.3.4 Influence of camera characteristics on observed microsphere motion

As has been discussed in significant detail elsewhere [161], observed microsphere displacement is strongly susceptible to the deleterious effects of long camera integration time, low frame-rate and interlacing (the process of reading alternating pixel rows in adjacent frames). Of these, the most severe signal degradation occurs for long integration times and interlacing, which can result in blurred images, thus masking the true microsphere position at any given time. While a low frame-rate does not necessarily pose such immediate problems, an inability to collect meaningful amounts of data rapidly increases the potential for damaging levels of sample drift.

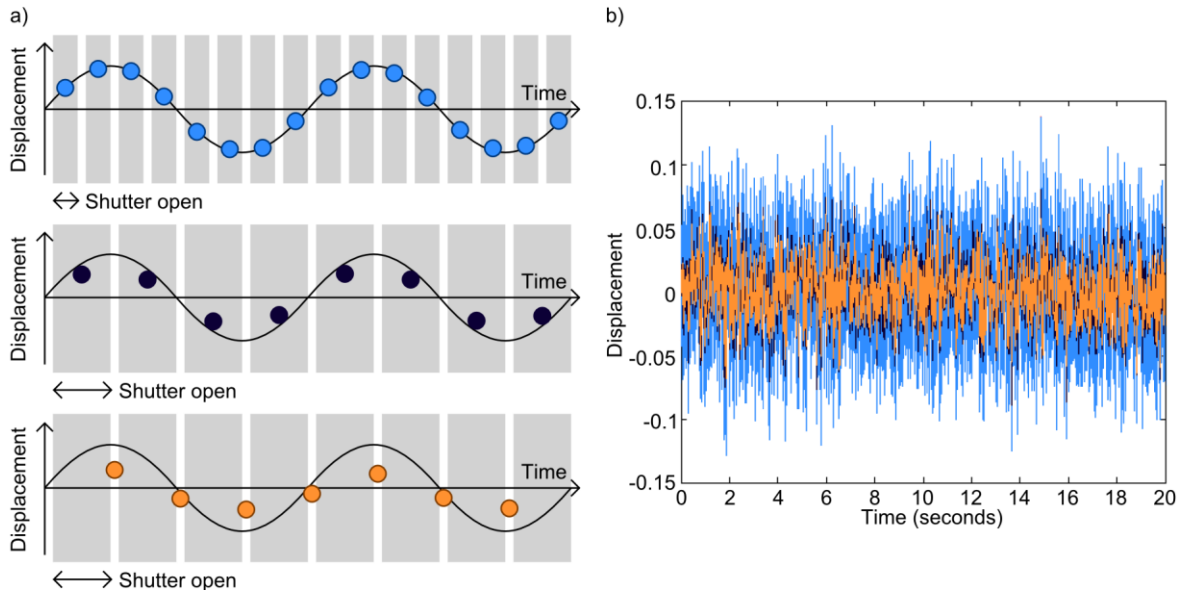


**Figure 4-10 – The result of camera integration effects on observed displacement**
a) For short integration times, significantly less than the relaxation time ($\tau_0$), all microsphere motion is captured in separate frames; however, as integration time increases, the effect of positional averaging across the duration the shutter is open results in a reduced measured variance in displacement. Interlacing of adjacent frames leads to further degradation of the signal. b) Simulated microsphere displacement sampled with an integration time of 5 µs without interlacing (light blue), 0.01 s without interlacing (dark blue) and 0.01 s with interlacing (orange). There is a clear decrease in the observed displacement with longer integration times. Figure adapted from te Velthuis *et al.* [155]

From an argument posed by Towles *et al.*, the observed microsphere centre for an image is simply the average of all microsphere positions during that integration time (Figure 4-10) [162]. As a result, blurring effects can be minimised by using an integration time shorter than the characteristic relaxation time ($\tau_0$) over which microsphere movement occurs (Equation 4-18) [155,163].

$$\tau_0 = \frac{\gamma}{k_x} = \frac{6\pi\eta R_0}{k_x}$$

**Equation 4-18 – Relaxation time ($\tau_0$) for a tethered spherical particle**
This is a function of the coefficient of friction ($\gamma$) and spring constant ($k_x$). This characteristic property can be further expressed in terms of the medium viscosity ($\eta$) and microsphere radius ($R_0$) [155,163].

Evaluation of relaxation time at the experimentally-relevant conditions discussed in Section 4.3.2 yields the values shown in Table 4-4. For all calculations, the medium viscosity was taken to be 0.001 Pa·s [163] and the spring constant ($k_{WLC}$) approximated using the instantaneous change in applied force and tether extension predicted by the worm-like chain model (Equation 4-13; Section 4.3.2). As is expected from the relationship in Equation 4-18, the relaxation time is greater for the smaller applied forces, where the tether exhibits a lower extensibility. To avoid blurring across all relevant experimental conditions a camera with integration time shorter than 0.1 ms is required.

**Table 4-4 – Estimation of tether relaxation times for experimentally-relevant systems**
Relaxation time ($\tau_0$) is a function of the fluid viscosity (taken to be 0.001 Pa·s [163]) and the spring-constant ($k_{WLC}$), which is extracted from evaluation of the worm-like chain model at the specified applied magnetic force ($F_M$). With increasing trap stiffness and for smaller microsphere radii, relaxation time decreases considerably.

| **Microsphere** | ***R* (µm)** | ***L*$_{ext}$ (µm)** | ***F*$_M$ (pN)** | ***k*$_{WLC}$ (N/m)** | **$\tau_0$ (ms)** |
|---|---|---|---|---|---|
| M280 | 1.475 | 5.26 (77.5%) | 0.416 | $5.0 \times 10^{-7}$ | 56 |
| M280 | 1.475 | 6.54 (96.3%) | 14.0 | $1.1 \times 10^{-4}$ | 0.25 |
| MyOne | 0.595 | 5.26 (77.5%) | 0.416 | $5.0 \times 10^{-7}$ | 36 |
| MyOne | 0.595 | 6.23 (91.8%) | 2.9 | $1.0 \times 10^{-5}$ | 1.8 |

To further probe the influence of camera averaging on observed microsphere displacement, camera characteristics can be applied to the microsphere motion simulations (Section 4.2.3) in an approach reported by Velthuis *et al.* [155]. In accordance with the reported method, lateral microsphere displacement (Equation 4-11) is evaluated with a time-step of 5 µs: an increment, which is significantly shorter than all predicted relaxation

times. Simulation of camera integration time and frame-rate is simply achieved by averaging all microsphere positions for frames where the shutter is open. The additional interlacing effect present in some cameras effectively results in two adjacent frames being present in a given image, albeit on alternating pixel rows. This was factored into simulations by averaging the observed microsphere position in adjacent frames. Cameras available for data collection were simulated: standard CCD camera (902DM2S; Watec Co. Ltd, Tsuruoka, Japan) with and without interlacing as well as an entry level CMOS camera (DMK 22BUC03; The Imaging Source GmBH, Bremen, Germany).

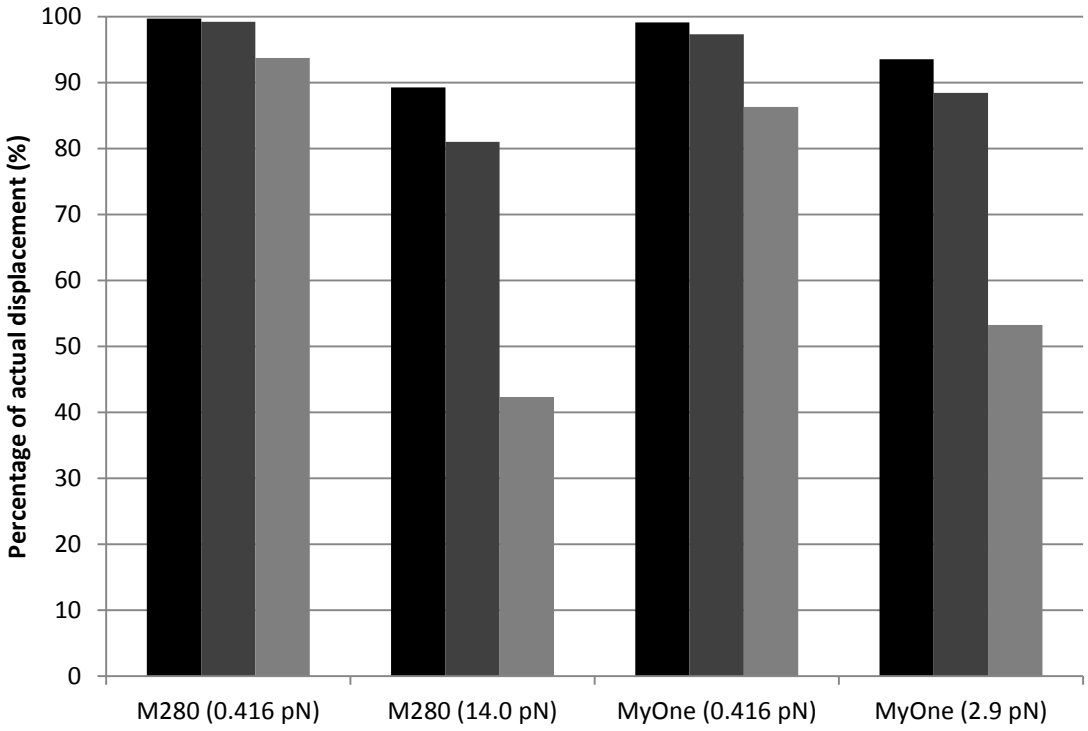


**Figure 4-11 – Effect of camera integration time on microsphere displacement**
Measured variance in microsphere displacement is simulated for four experimentally-relevant conditions, with varying camera conditions applied, expressed as a percentage of the actual displacement value. The four clusters correspond to the experimental conditions outlined in Table 4-4. On the left of each group (black bars) are results for a CMOS camera (5 ms exposure time, 60 fps; DMK 22BUC03; The Imaging Source GmBH, Bremen, Germany), in the centre (dark grey bars) are results for a basic CCD camera without interlacing enabled (10 ms exposure time, 25 fps; 902DM2S; Watec Co. Ltd, Tsuruoka, Japan) and on the right (light grey bars) are results for the same CCD camera with interlacing enabled. There is near-perfect agreement between the CMOS results and in all but one experimental condition the non-interlaced CCD camera exceeds 90% agreement; however, with interlacing enabled the CCD results decrease below 50%.

Analysis of simulated variance for various cameras (Figure 4-11) corroborates with the expectation drawn from the data in Table 4-4, namely that systems with relaxation times greater than the camera integration time exhibit erroneous measurements of displacement. This is most pronounced for configurations using high force, where relaxation times are smaller. At high force, both non-interlacing CCD and CMOS cameras still impose reduced

measured variance; however, these are significantly less pronounced than the interlacing equivalent. The effect of these camera properties on the measured force is shown in Figure 4-12. In the most extreme case (M280 microspheres at 14 pN applied force) the measured force using an interlacing CCD camera is over twice the applied force. With the CMOS camera the greatest variation between applied and measured force is ~12%. Both integrating CCD and CMOS cameras have been used for force characterisation of the magnetic tweezers microscope.

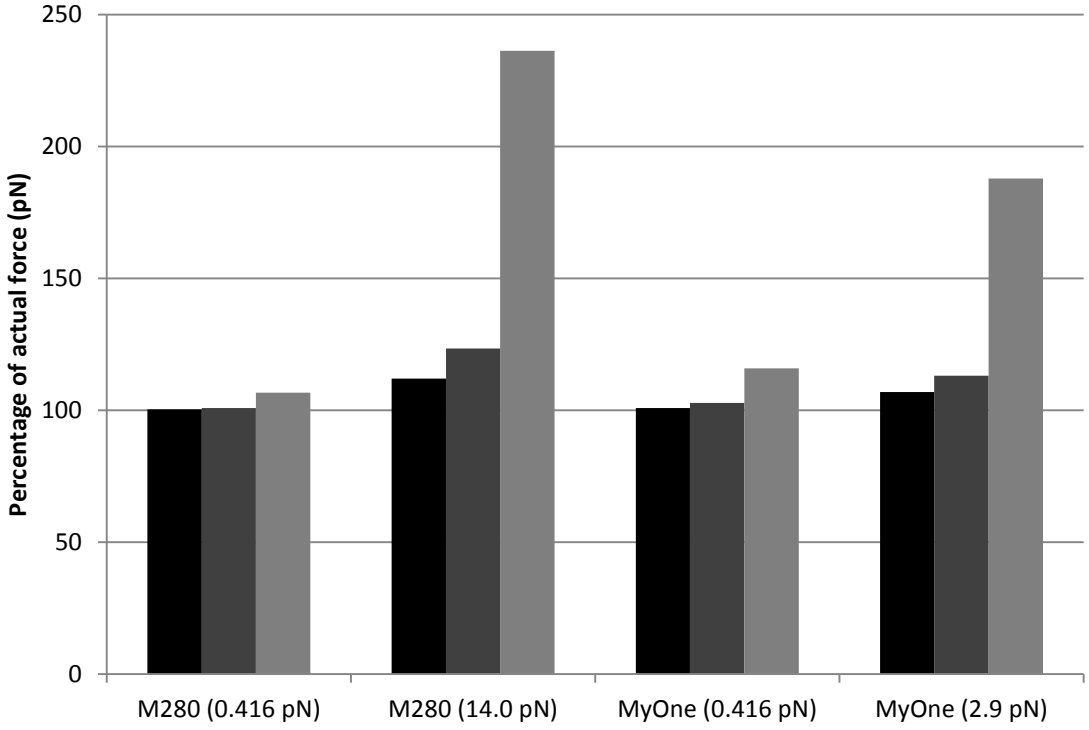


**Figure 4-12 – Effect of camera integration time on measured force**
Application of equipartition theorem (see Section 4.7.1) to variances in microsphere displacement obtained through simulation of different camera integration times (Figure 4-11). The inverse relation between variance in displacement and measured force results in significant disagreement for the interlacing CCD camera at relatively large applied forces. Disagreement between applied and measured forces can be minimised through use of cameras with shorter integration times.

### 4.3.5 Effect of asymmetric microsphere placement

Biot-Savart force estimations described so far have assumed the superparamagnetic microsphere to be positioned perfectly between the magnet pair, thus yielding zero force along the z-axis. In reality, the microsphere is likely to be slightly off-centre and as such, will be subject to this additional force component. The lateral ($B_z$) and longitudinal ($B_y$) magnetic field components can be modelled using a modified version of the biaxial Biot-Savart equation (Equation 4-5). Here, the current elements are related to the off-axis

microsphere position by values $g_L$ (for L-elements) and $g_R$ (for R-elements), where the sum of $g_L$ and $g_R$ is the previously-defined magnet-magnet separation (g) (Figure 4-13). Due to the attachment of microscope components to a single optical breadboard, the magnet pair is assumed to be in near-perfect alignment with the optics, thus yielding a negligible magnetic field component ($B_x$) along the x-axis. The complete equations are included in Appendix B-II, evaluation of which was performed using Maple (*Biot-Savart_off-axis_force_model.mw*; Accompanying Material).

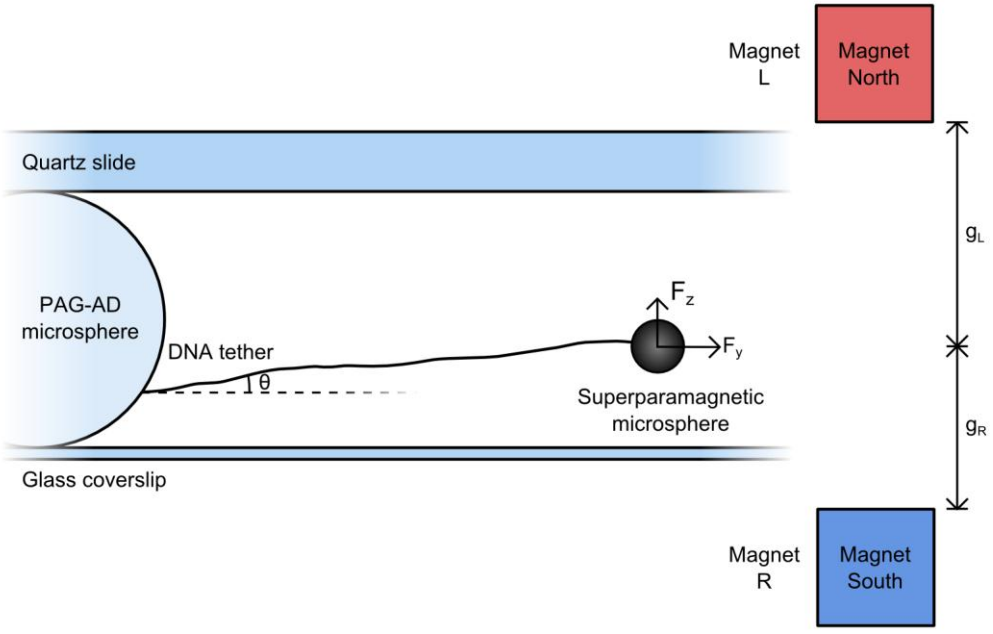


**Figure 4-13 – Forces acting on an off-axis superparamagnetic microsphere**
Schematic diagram showing the horizontal ($F_y$) and vertical ($F_z$) force components acting on a superparamagnetic microsphere positioned asymmetrically between the magnet pair in biaxial configuration. The ratio of forces is determined by the microsphere position between the magnets and directly determines the tether angle relative to the y-axis ($\theta$). Separations $g_L$ and $g_R$ specify the distance between the microsphere and magnet L and R, respectively (*L*, *R* nomenclature used for consistency with Lipfert *et al.* model [99]).

Forces arising from the two modelled magnetic field components are calculated using the equations shown in Appendix C-II. These have been evaluated for experimentally-relevant magnet-pair to microsphere separations and are shown in Figure 4-14a. Taking these forces to have exclusive influence over the tether position, the angle relative to the y-axis (Figure 4-13) has been calculated (Figure 4-14b).

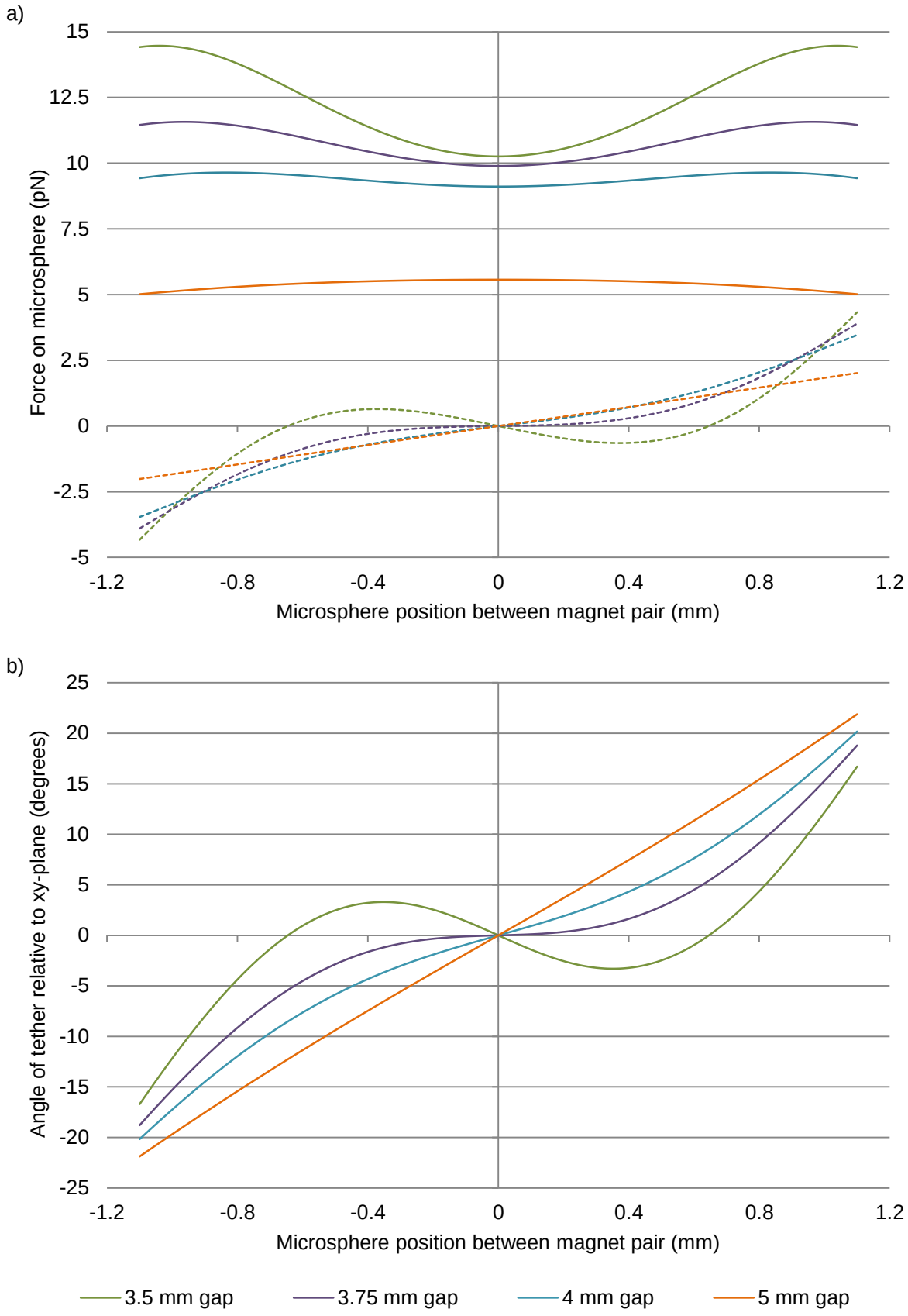


**Figure 4-14 – The effect of off-axis superparamagnetic microsphere placement**
a) Force acting on the microsphere along the y-axis (solid lines) and along the z-axis (dashed lines). With increasing magnet pair to microsphere separation the forces tend towards zero. b) Tether angle relative to the y-axis as calculated based on the ratio between vertical and horizontal forces. At increasing separations the angle is characterised by a linear response in relation to microsphere position between the magnets. All calculations were performed using a magnet-magnet separation of 2.2 mm.

Calculations shown in Figure 4-14 have been performed for M280 microspheres; however, the ratio of magnetic field components is identical for the MyOne alternative. With increasing distance from the magnet pair, both forces tend towards zero, resulting in a linear response for position between the magnets and the tether angle. For magnet pair to microsphere separations greater than approximately 5 mm this linear gradient decreases; however, the DNA compaction accompanying these larger separations begins to dominate any descriptions of tether conformation.

At the minimum achievable microsphere to magnet pair separation of 3.5 mm, the angle subtended between the tether and y-axis does not exceed 3.5° within the central 1.2 mm range. This is due in part to the curve inflexion for an off-axis position of ~0.4 mm. For the larger magnet pair to microsphere separation of 5 mm this response is steeper, resulting in angles exceeding 5° within the central 0.5 mm. Similarly, for separations of 10 mm (data not shown), sub 5° angles are observed for the central 0.6 mm. In practicality, the 2.2 mm magnet to magnet separation is negligibly larger than the sample thickness, thus precluding off-axis microsphere placement greater than 0.5 mm. Therefore, tethers can be assumed to lie within 5° of horizontal.

## 4.4 Construction of the magnetic tweezers microscope

### 4.4.1 Optical components

Fundamental to the unique capabilities of the horizontal magnetic tweezers (HMT) microscope is the ability to simultaneously manipulate both the twist and force acting on individual DNA tethers whilst imaging fluorescently labelled bio-molecules interacting with them. To enable this, it must be possible to image both the magnetic microsphere, onto which the force is applied, and the fluorophore coupled to the bio-molecule. This is achieved using the optical set-up shown in Figure 4-15, which combines both bright-field illumination for monitoring the magnetic microsphere and wide-field laser epifluorescence for illumination of the fluorophores.

Bright-field illumination allows large objects, such as the 2.8 μm diameter magnetic microspheres and 9 μm diameter latex tethering microspheres to be imaged. This is especially important in the case of the magnetic microspheres: the motion of which is used to elucidate the force acting on the DNA tether through use of the equipartition function

(Section 4.7.1). To prevent cross-talk between the bright-field and fluorescence elements of the microscope, the bright-field illumination is restricted to the blue region of the spectrum, with wavelengths in the range 420 nm to 500 nm.

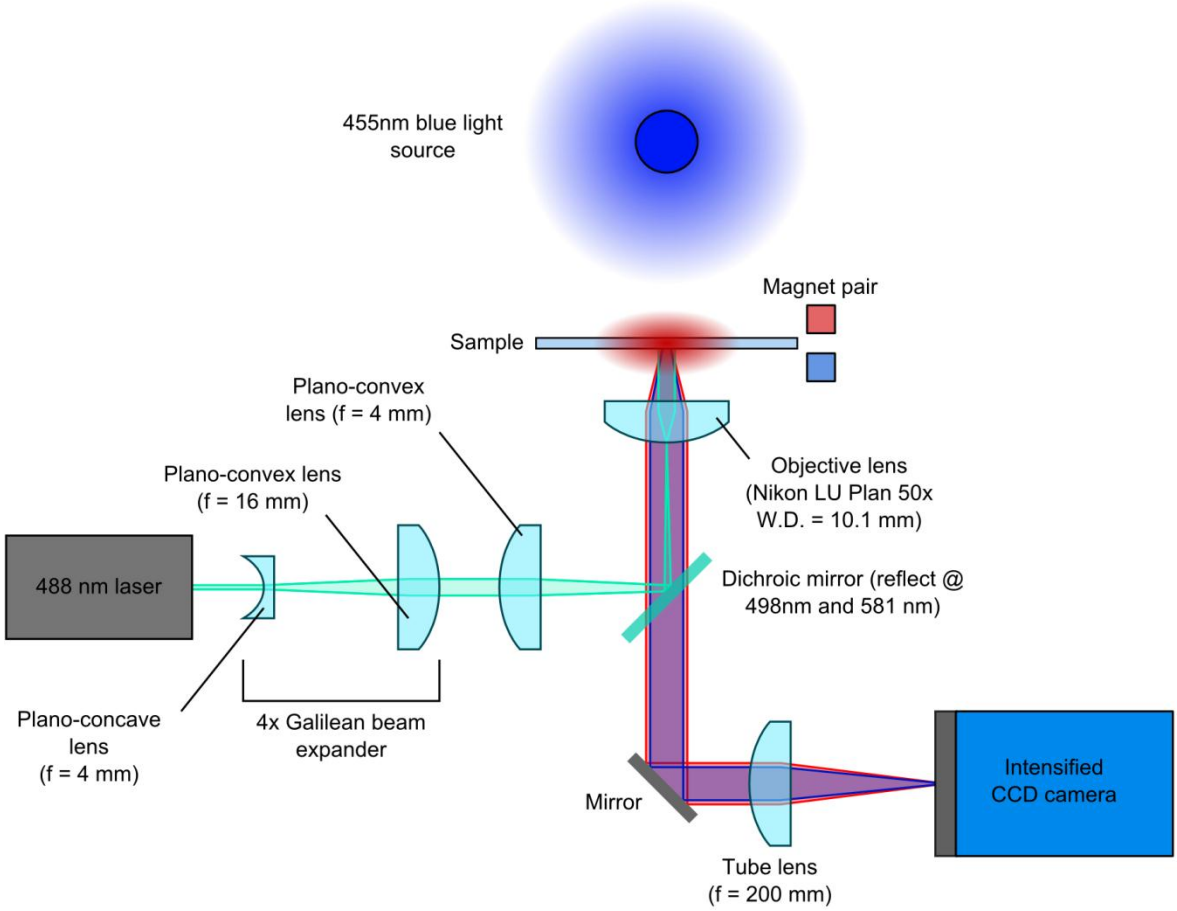


**Figure 4-15 – Optical configuration of magnetic tweezers microscope**
Shown is the light-path for the bright-field illumination and wide-field laser epifluorescence. Bright-field illumination from a blue LED (455 nm) passes through the laser-coupling dichroic and is focused onto the camera CCD by the tube lens. The exciting laser beam (488 nm) is expanded four-fold using a Galilean beam expander and focussed to the back of the objective lens, where it excites fluorophores in the sample. Fluorophore emission follows the same path as transmitted bright-field light, but is also focussed onto the camera CCD. Alternatively, the transmitted bright-field and fluorescence emission light can be chromatically separated using the systems shown in Figure 4-17.

Illumination is provided by a 455 nm Royal Blue LED with collimating optics (M455L2-C3; ThorLabs, New Jersey, USA) placed above the sample. Transmitted light is collected by the long working-distance objective lens (CFI LU Plan EPI ELWD; W.D. = 10.1 mm; N.A. = 0.55; Nikon, Tokyo, Japan) and subsequently passes through the laser-coupling dichroic mirror (reflection maxima at 498 nm and 581 nm; FF498/581; Semrock, Rochester, New York, USA) after which it is reflected with a dielectric turning mirror (CM1-EO2; ThorLabs, New Jersey, USA) towards the achromatic doublet lens (AC254-200-A-ML; ThorLabs, New Jersey, USA), which acts as the tube lens and focuses

the light onto the imaging system (camera, OptoSplit II or DualCam). In accordance with Equation 4-19, there is a simple relationship between the magnification and the focal lengths of the objective ($f_{obj}$) and tube ($f_{tube}$) lenses. As a result of this, the magnification achievable with the 50x objective lens can be doubled by swapping the vendor-recommended 200 mm tube lens with a 400 mm equivalent; however, such an approach ultimately becomes diffraction-limited (Equation 4-20), with the smallest resolvable feature having a length of ~400 nm, when illuminated with the blue LED.

$$M = \frac{f_{tube}}{f_{obj}}$$

**Equation 4-19 – Basic magnification relation**
Magnification ($M$) is a function of objective ($f_{obj}$) and tube ($f_{tube}$) lens focal lengths. It is possible to easily increase magnification through selection of a tube lens with a longer working distance.

$$d = \frac{\lambda}{2(nsin\theta)} = \frac{\lambda}{2NA}$$

**Equation 4-20 – Diffraction limit of an optical system**
The smallest resolvable feature length ($d$) is determined by the illuminating light wavelength ($\lambda$), index of refraction ($n$) and angle over which light can be focused to form the image ($\theta$). The quantity $nsin\theta$ is a property of the objective lens, frequently referred to as the numerical aperture ($NA$).

Fluorescence illumination is provided in the described configuration by a 75 mW 488 nm laser (Sapphire; Coherent, Inc., California, USA); however, the selected dichroic filter is also compatible with laser excitation at 561 nm. The initial 1 mm beam diameter is expanded four-fold to 4 mm with a Galilean beam expander (Figure 4-16a), thus allowing a greater sample area to be homogeneously illuminated. This expander is comprised of two lenses, a plano-concave lens (40-DN-16; Comar Optics Ltd., Cambridge, UK), which causes the laser beam to diverge, followed by a plano-convex lens (160-DQ-25**;** Comar Optics Ltd., Cambridge, UK), which brings it back to infinity-focus [164]. Alternatively, a Keplarian beam expander configuration can be implemented (Figure 4-16b), whereby the laser beam initially converges and is then returned to infinity focus with a divergent lens; however, this can lead to localised heating of the air at the laser focal point, which can in turn result in optical distortion of the beam [165]. Following the beam expander, the laser is focussed onto the back aperture of the objective lens with a plano-convex lens (40-DQ-25; Comar Optics Ltd., Cambridge, UK), resulting in wide-field epifluorescence illumination [166].

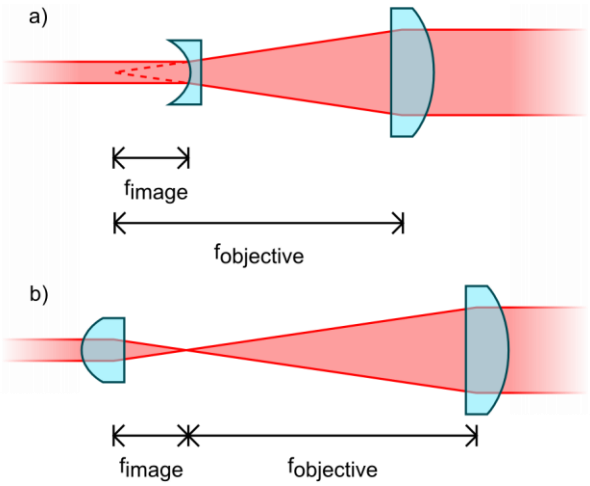


**Figure 4-16 – Schematic diagrams methods for expansion of a laser beam**
For each system the distance between lenses is the sum of the individual focal lengths. a) Galilean beam expander configuration, with initial divergence of the incident laser beam using a plano-concave image lens, followed by convergence back to infinity focus using a plano-convex lens. b) Keplarian beam expander configuration in which the incident laser beam is initially converged with a plano convex lens and then brought back to infinity focus with another plano-convex lens. This method causes the laser to focus to a single point, which can lead to localised heating and result in beam distortion [164]. It also requires a larger distance between lenses to achieve an equivalent magnification to the Galilean expander. Image adapted from [164].

Light emitted from the sample is collected by the objective lens and travels down the optical path in a similar manner to the bright-field illumination. The light is transmitted through the dichroic filter, reflected by the 45° mirror and then focussed onto the imaging system, which can be either a camera array (as in Figure 4-15) or intermediate image manipulation tool (Figure 4-17).

Chromatic separation of the bright-field and fluorescence signals can be achieved through inclusion of either technologies included in Figure 4-17, positioned between the tube lens and camera. Both split the image using a dichroic mirror (FF498/581; Semrock, Rochester, New York, USA) and use the following filters to remove unwanted wavelengths: 452 nm ± 22.5 nm bandpass (FF01-452/45; Semrock, Rochester, New York, USA) for the transmitted bright-field light and 640 nm ± 12.5 nm bandpass (D640/25m; Comar Optics Ltd., Cambridge, UK) for the fluorescence emission. With the Optosplit II (Figure 4-17a; Cairn Research, Faversham, UK), the separated images are directed onto opposite halves of the same CCD chip and with the DualCam (Figure 4-17b; Optical Insights, now part of Photometrics, Tucson, Arizona, USA) they are sent to different cameras. In both instances, the resulting video can be kept as two separate channels, or alternatively, using software described in Sections 4.5.1, assigned to different colour channels of a single RGB video. Spectral details for the various illumination sources, filters and fluorophores used in the microscope are included in Appendix A-I.

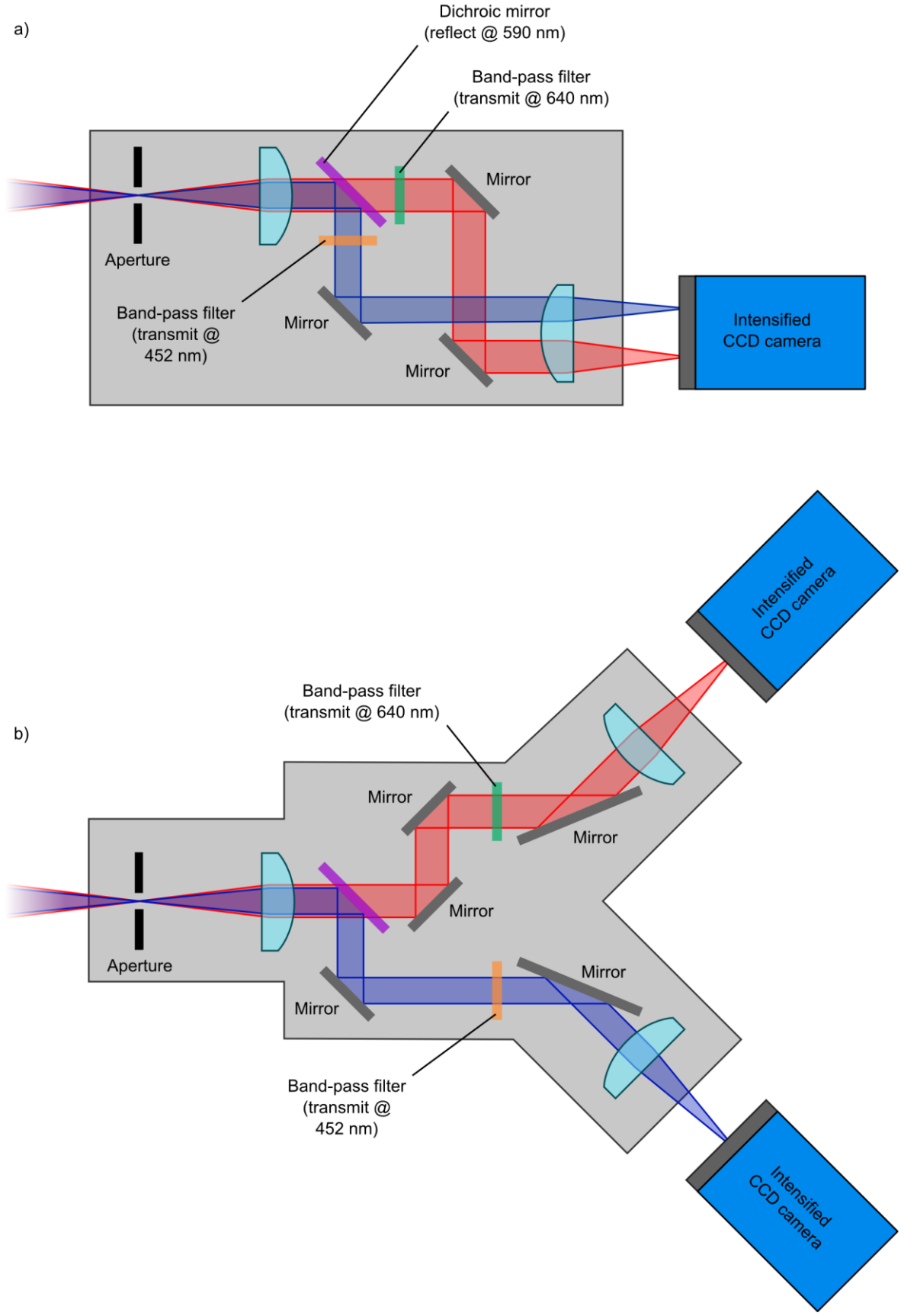


**Figure 4-17 – Two chromatic image splitters compatible with the HMT microscope**
a) The Optosplit II separates the transmitted brightfield (blue) and fluorescence emission (red) onto opposite halves of the camera CCD chip. b) Similarly, the DualCam chromatically splits the image; however, the different light paths are directed to different cameras. Optical path elucidated through mechanical analysis.

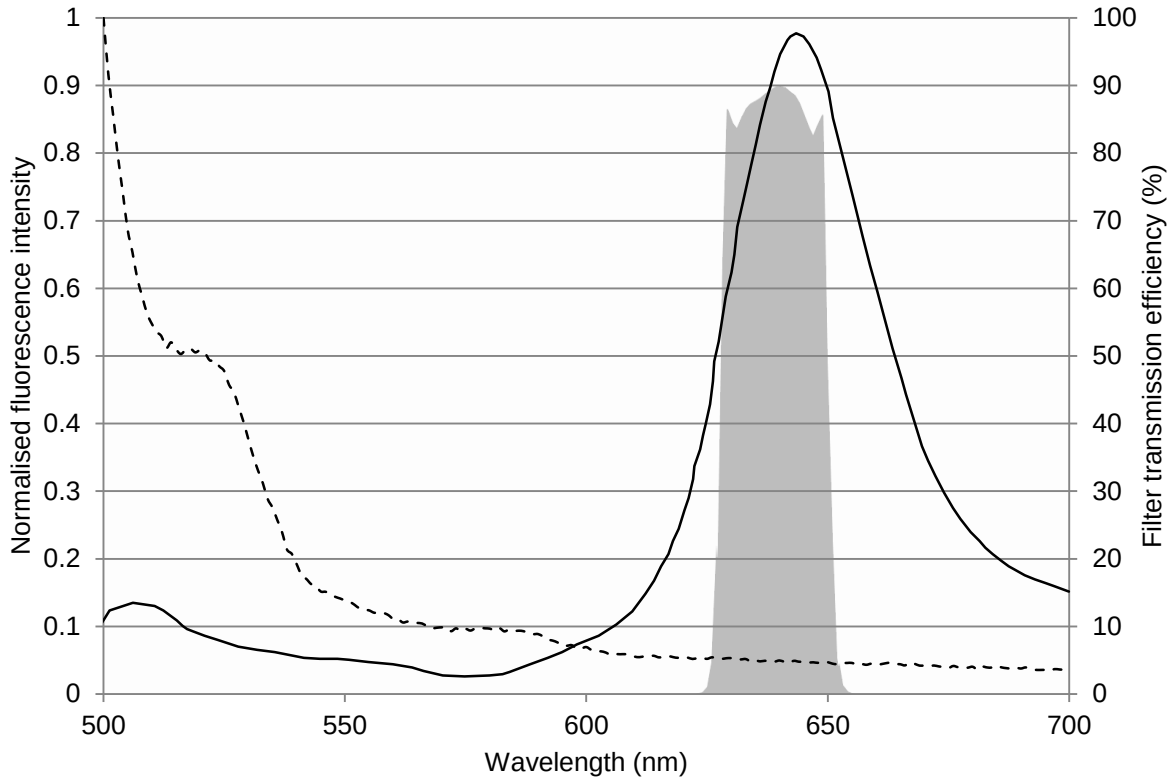


**Figure 4-18 – Analysis of microsphere-scattered excitation light**
Comparison of the normalised fluorescence emission spectrum for TransFluoSpheres (solid black line; primary vertical axis) typically used in the magnetic tweezers microscope and that of a dilution of MyOne microspheres in plain buffer (dashed black line; primary vertical axis). Also included is the transmission efficiency of a band-pass filter selected to give optimal fluorescence signal whilst minimising background from microsphere-scattered light (transmission centred on 640 nm, FWHM = 25 nm; grey shaded area; seconday vertical axis). The spectrum for the 645 nm TransFluoSpheres, reported by Bhalgat, *et al.* [167], was digitised using GetData [168]. Spectra for the MyOne microspheres, collected using a fluorometer at 488 nm excitation, demonstrates the significant increase in long-wavelength emission due to scattering by the microspheres.

Selection of the final filter must not only take into account removal of residual light at the excitation wavelength, but also minimisation of longer wavelengths arising from light scattering by the superparamagnetic microspheres. An example emission spectrum shown in Figure 4-18 demonstrates the significant degree of such scattering and highlight the importance of choosing an appropriate filter. Filter selection is determined by maximisation of the signal-to-noise ratio between the vendor-supplied fluorophore emission spectrum and measured scatting spectrum; in the described microscope configuration, these were the emission spectrum of TransFluoSpheres (645 nm emission peak), manually digitised with GetData [168], and scattering of 488 nm light by MyOne superparamagnetic microspheres (Invitrogen, Carlsbad, California, USA), measured using a fluorometer (FluoroMax 3; Horiba, Ltd., Kyoto, Japan). Maximisation of the signal to noise ratio with a custom MATLAB script (function: *chooseFilter.m*; Accompanying Material) across the wavelength range 497 nm to 700 nm and full width half maxima

(FWHM) range 10 nm to 60 nm yielded an optimal signal (normalised transmission ratio of 18.9) for the theoretical filter centred on 637 nm and with a 13 nm FWHM; criteria which were most closely satisfied by the filter D640/25m (Comar Optics Ltd., Cambridge, UK).

### 4.4.2 Mechanical components

Construction of the horizontal magnetic tweezers (HMT) microscope is achieved using a commercially available 30 mm cage system (ThorLabs, Inc., Newton, New Jersey, USA) and various custom-fabricated components (Figure 4-19). With this approach, standard 1" (or 25 mm) diameter optical components are mounted on plates, held at each corner by metal rods. These plates can be freely-positioned along the rods and subsequently fixed in place with friction screws. Expansion of the optical system beyond this simple one-dimensional configuration is achieved with additional available components, such as mirror cubes, filter mounts and various translational stages. A complete list of components used, as well as schematic diagrams for custom components, is included in Appendix A-II.

The implemented optomechanical configuration (Figure 4-19) makes use of a cage-mounted z-translational stage to control the vertical position of the objective lens and thus provide focussing ability. Below this, a mirror cube directs the optical path parallel to the breadboard surface and towards the tube lens, from where it is sent to the imaging system. A second optical path containing the Gaussian beam expander optics held on xy-translational stages is coupled into the primary path through a dichroic mirror, attached to a rotation-variable filter mount. The relatively short focal length of the laser-focussing lens (40-DQ-25; Comar Optics Ltd., Cambridge, UK) imposes the requirement that the dichroic be positioned directly below the objective lens; hence raising the laser with post-holders (PH1.5 and PH6; Thorlabs, Inc., Newton, New Jersey, USA). To confer mechanical strength, the cage system is screwed directly onto the optical breadboard at regular intervals using metal posts (TR1, TR6 and TR8; Thorlabs, Inc., Newton, New Jersey, USA) and mounts (CP02B; Thorlabs, Inc., Newton, New Jersey, USA).

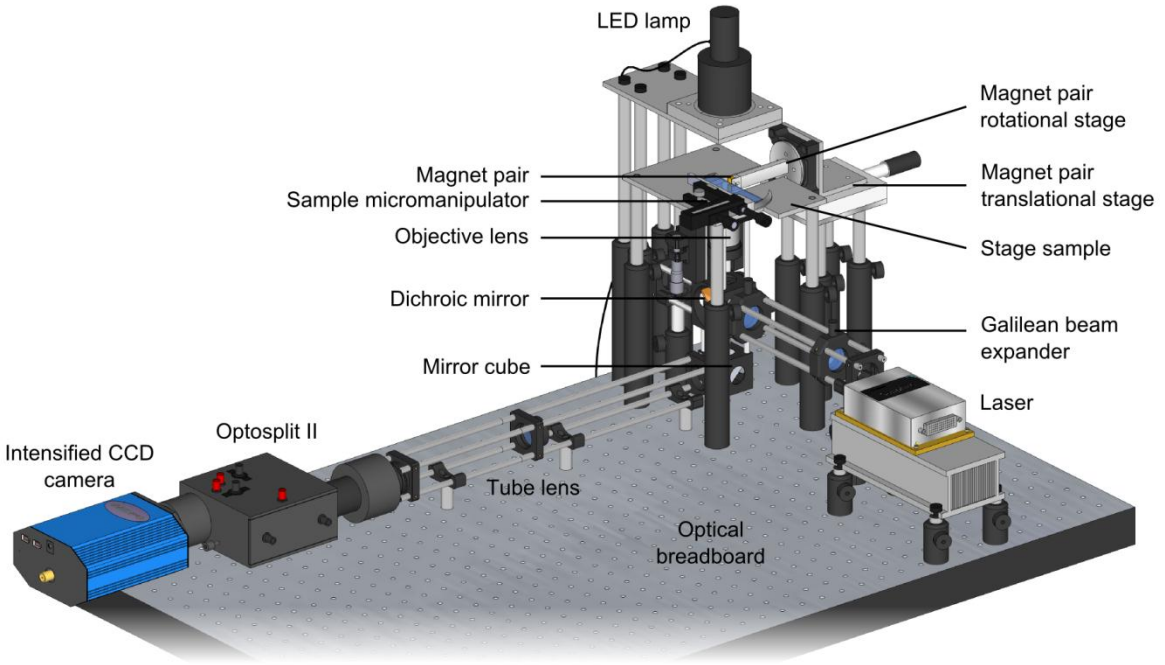


**Figure 4-19 – Horizontal magnetic tweezers microscope configuration**
Google Sketchup model showing an overview of the horizontal magnetic tweezers microscope. Construction is achieved using the ThorLabs 30 mm cage system, which allows modifications to the microscope configuration to be easily implemented. Bright-field illumination comes from a collimated blue LED held above the sample stage and wide-field epifluorescence is achieved through focussing of a 488 nm (or 561 nm) laser onto the back of the objective lens. Transmitted and emitted light are collected by the objective lens and focussed on the camera assembly. In the configuration shown, the bright-field and fluorescence images are split and directed onto different halves of the intensified camera CCD chip. The magnetic tweezers element of the microscope is implemented by holding the magnet-pair to one side of the sample on a stage with rotational and translational capabilities.

Key custom components were designed in-house and fabricated by Mark Bentley (Mechanical Workshops, Department of Biology, University of York, UK); these are the sample stage, LED lamp mount and magnet-pair holder (Figure 4-20). The sample stage is comprised of a 5 mm thick aluminium sheet with recessed section to allow the magnet pair access to the sample; additional holes at each corner permit attachment to metal poles, held at a user-defined height from the sample surface with pole-holders. Using a pair of aluminium plates, the LED lamp is held in place directly above the sample at a user-defined height with adjustable poles; the lamp is secured with a friction-clamped aluminium ring. Finally, the magnet pair is held on the end of an aluminium shaft connected to an assembly comprising a rotational stage and one-dimensional translational stage, also mounted on height-adjustable poles. A friction-clamp holds the magnet pair at a fixed separation; however, the interchangeable design of this clamp allows for 3D-printed holders with fixed magnet-separations to be used instead.

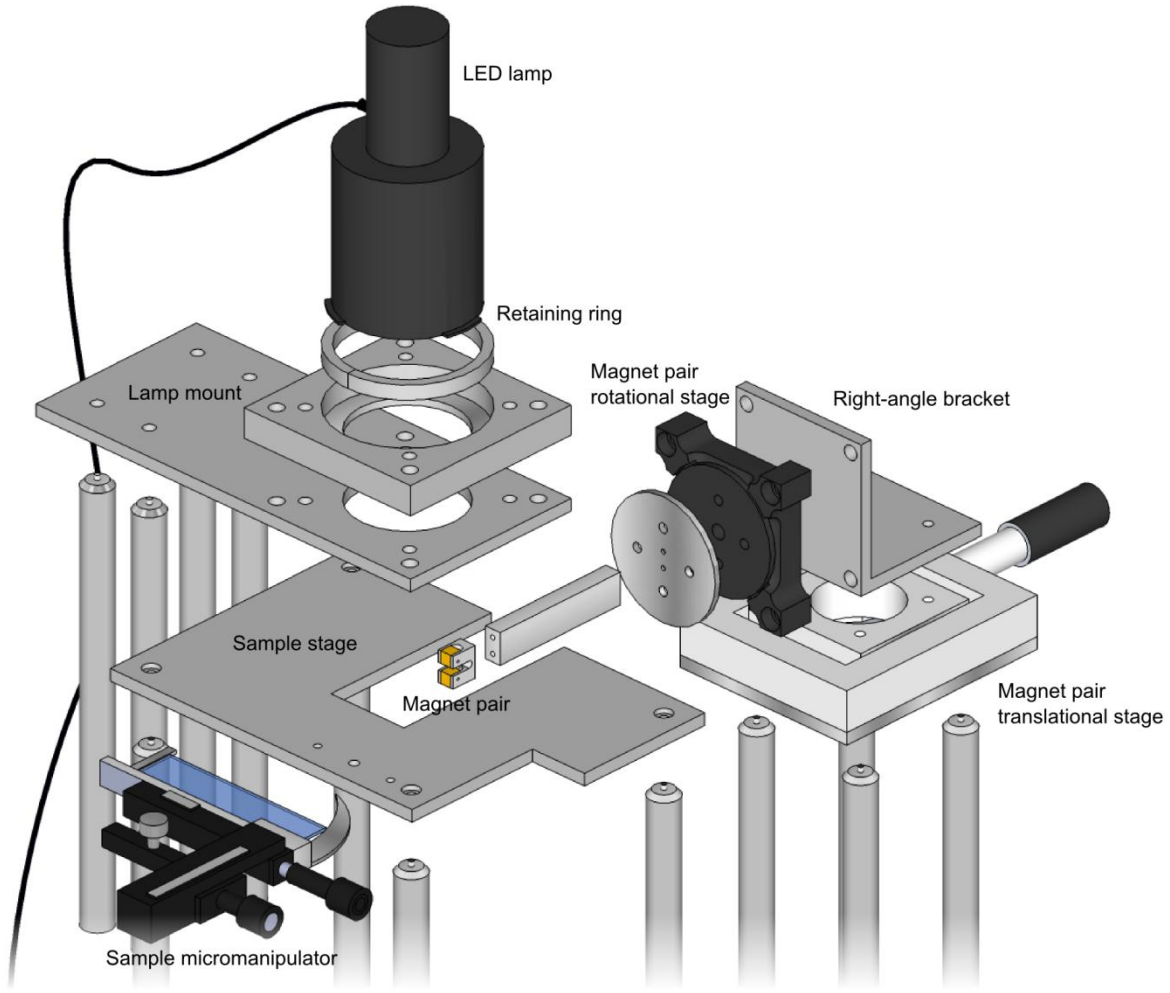


**Figure 4-20 – Components responsible for sample and magnet-pair control**
Samples are held above the objective lens on a custom-fabricated stage with a commercially purchased micromanipulator for accurate sample translational control. A section cut from the stage allows the magnet pair to be brought into close proximity of the sample. The magnet pair is held in a clamp on the end of a rod connected to the rotational stage and the entire magnet-control assembly is placed on a one-dimensional translational stage, permitting precise movement of the magnets towards the sample. Since magnets are held with friction, magnet-pair separation can be easily adjusted.

## 4.5 Software components for horizontal magnetic tweezers microscope

### 4.5.1 Magnification measurement

Measurement of observed magnification is a useful technique to demonstrate the optical components of the microscope are functioning as expected. To act as a calibrated reference, images are acquired of the USAF 1951 resolution test (Edmund Optics Ltd., York, UK): a target which is comprised of arrays of well-defined lines with known spacing. Evaluation of the observed line spacing in relation to the known pixel dimensions of the camera CCD chip yield accurate measurements of magnification.

Automated measurement of collected images is achieved using a custom MATLAB script (function: *measureMag.m*; Accompanying Material), which takes an input image (pre-cropped to the region of interest) and extracts the intensity profile across each column. Comparison of profile intensities to a threshold value (automatically-adjusted relative to the total image pixel intensity range) allows line boundaries to be established, thus yielding observed distance per pixel. Magnification is calculated as the ratio of physical pixel dimension to the measured distance per pixel. Calibration of the microscope for different tube lens focal lengths is included in Section 4.6.1.

### 4.5.2 Image alignment for OptoSplit II

Simultaneous imaging of both bright-field and fluorescence channels can be achieved using the OptoSplit II image splitter (Cairn Research, Faversham, UK) as described in Section 4.4.1. This device is placed in the image path directly before the camera and chromatically splits the image using a built-in dichroic filter. The two image paths are then focussed onto either half of the camera CCD, with coarse alignment of the two images performed manually through manipulation of the steering mirrors. Once the same spatial region of the sample is visible on both halves of the CCD, fine alignment of the two images is achieved using a reference image (for example, a USAF 1951 resolution target) and the custom MATLAB script, *isCalibrateImageSplitter.m* (Accompanying Material). With this system, the user is presented with an interface in which they press one of the two ROI selection buttons on the right of the window and approximately define the corresponding image region by dragging a rectangle to the desired size. Automated alignment of the two images, started with the "Try Alignment" button, rasters one image across the other in two dimensions with a typical range of ±10 px. At each position, the mean pixel intensity residual between the two images is calculated and stored in a two-dimensional array. The position of best alignment is identified as the location with the lowest residual. Each image ROI is stored in the calibration file *imageSplitterSettings.mat* and is valid until the OptoSplit II is mechanically adjusted.

Following calibration, alignment of video obtained with the OptoSplit II is performed using the second custom MATLAB script, *imageSplitter.m* (Accompanying Material). For each frame of the input video, the left and right image ROIs specified by the *imageSplitterSettings.mat* calibration file are combined into a single video frame with one

assigned to each colour channel. The channels used are determined by the user, although they default to red and green.

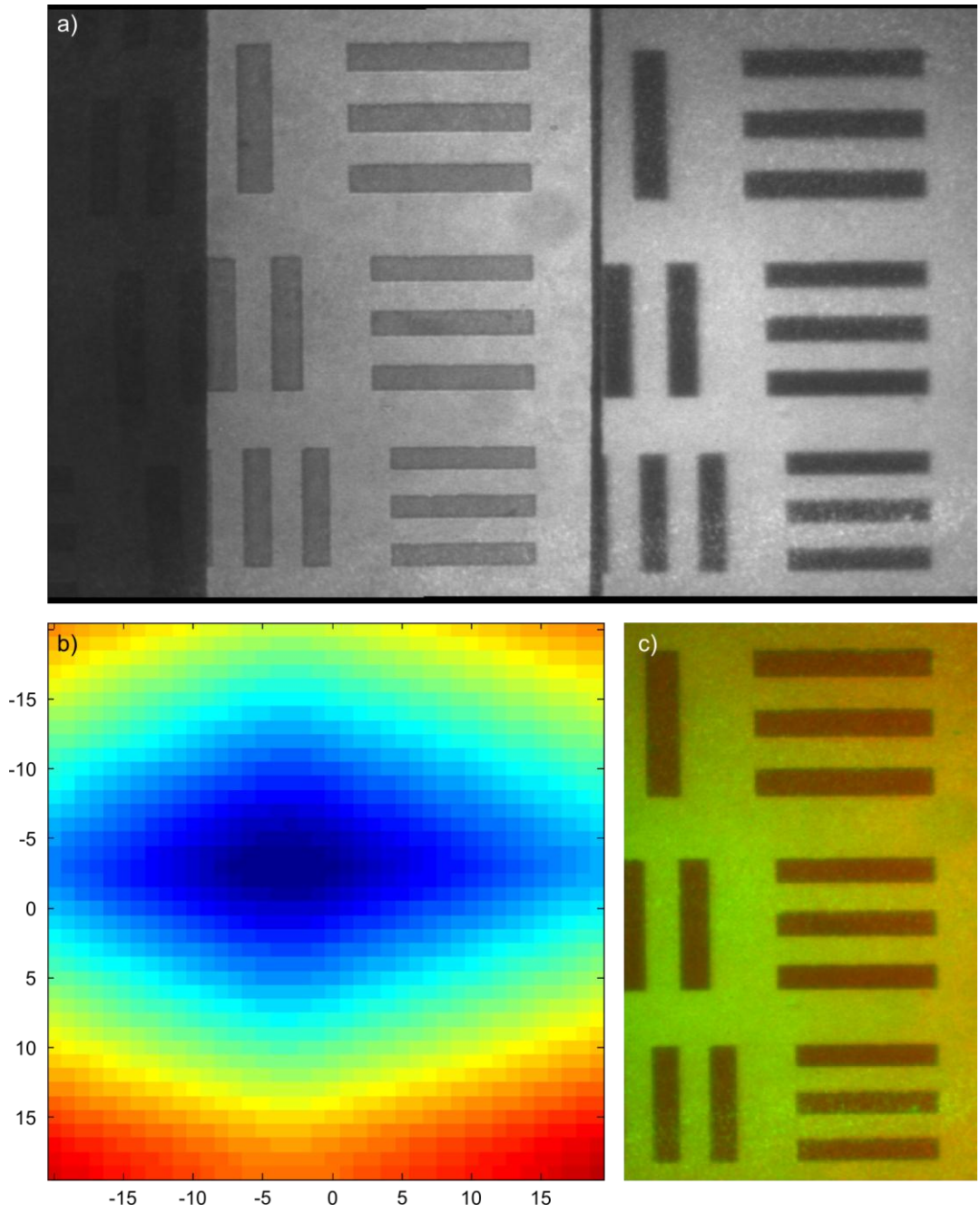


**Figure 4-21 – Calibration of the OptoSplit II using a custom MATLAB system**
a) Example frame obtained from the OptoSplit II showing the same regions on either side of the CCD. b) Following calibration, a two-dimensional plot of the mean pixel intensity residuals is displayed by the system, highlighting the region of best image alignment in blue. c) The output frame has each image assigned to a different colour channel.

An example alignment of the USAF 1951 resolution test used for calibration is shown in Figure 4-21. For this purpose, the image was split using a half mirrored filter, which divides the incident light between the transmitted and reflected paths equally. The two

images were assigned to the red and green channels of the output image. Absence of regions distinctly exhibiting one single colour indicates alignment was successful.

### 4.5.3 High-accuracy particle tracking of microsphere displacement

The measurement of lateral bead displacement for determination of applied force in the magnetic tweezers via the equipartition theorem (Section 4.7.1) is achieved using a custom MATLAB tool (function: *multiTracker.m*; Accompanying Material). This system tracks the motion of user-identified microspheres in a pre-recorded video and returns both the displacement and force acting on the microsphere. While the source code is provided with a full commentary in the appendix, included here is a summary of the key functions.

#### 4.5.3.1 System initialisation and microsphere selection

Microspheres to be tracked are user-selected using a static display of the first frame in the video (function: *mtSelectParticles.m*; Accompanying Material). This initialisation step serves a number of purposes. First, yielding an approximate position for each microsphere, which also allows debris and surface-immobilised microspheres to be discarded from analysis. Second, the user defines the approximate microsphere radius by resizing the region of interest (identified by blue circles); a process which negates any problems with large differences in microsphere radii, such as is the case when using the 9 μm PAG-AD-MS as the static reference point (Section 4.7.3). Finally, the regions of interest are smoothed using the average image pixel intensity, thus yielding a background image from which all subsequent frames can be subtracted.

Key parameters that govern both the detection and tracking algorithms as well as conversion of microsphere trajectories to applied force values are also set in this initialisation phase (function: *mtTrackerDetectionSettings.m*; Accompanying Material). The user is presented with a dialog, pre-completed with typical values, for background pixel intensity threshold (parameter: *top_thres_multiplier)*, microsphere radius (parameter: *R*), the number of consecutive frames a microsphere can go undetected before being discarded (parameter: *disappear_threshold*), acceptable microsphere movement between frames (parameter: *drift_threshold*), DNA tether length (parameter: *tether_length*) and finally, the camera-specific magnification calibration (parameter: *distance_per_pixel*).

These values are saved to a MATLAB .mat parameter file, thereby acting as a useful reference for data analysis.

#### 4.5.3.2 Detection of microsphere centres

Arguably the most important aspect of any tracking system is the ability to accurately detect particle centres in a reproducible manner. For the application here this is especially important, considering microsphere displacement is directly related to the applied force. While systematic errors, such as drift can be easily accounted for with reference markers, such as surface-immobilised microspheres, inaccuracy in particle centre evaluation will result in erroneously large measured forces.

Numerous approaches exist to detect particle centres with sub-pixel resolution, such as two-dimensional cross-correlation of regions of interest to reference images [169,170], calculating the centre-of-mass (centroid approach) [171,172] and fitting Gaussian curves to pixel intensity profiles [173,174]. The technique implemented here is cross-correlation (function: *mtImRegisterFit.m*; Accompanying Material), identified as the most accurate method by Cheezum *et al.* [161].

Cross-correlation as implemented here is based on the built-in MATLAB function, imregister.m (modified to return the transformation matrix, *tform*). With this, two arrays containing the same ROI and centred on the approximate microsphere origin are rotationally offset relative to each other by 180° and registered so as to minimise the residual between the pair. The actual microsphere centre is acquired through the relation that the translation required to overcome the initial image offset is equal to twice the initial error in the microsphere centre position. While the registration function is capable of aligning images both translationally and rotationally, centre-detection with manually rotated images requires it be restricted solely to the former. This restriction proves beneficial in terms of processing speed, with a cross-correlation approach generally reaching equilibrium faster than the profile-fitting equivalent, thanks mainly to the relatively limited number of fit parameters.

#### 4.5.3.3 Tracking microspheres between images

Detected microspheres are tracked between temporally-adjacent frames according to a number of criteria (function: *mtPeakFollow.m*; Accompanying Material). First, the spatial residuals between a specific microsphere position and all the detected positions in the previous frame are calculated. Assuming the smallest measured distance is within the drift threshold (parameter: *drift_threshold*) the two positions are accepted as corresponding to the same microsphere; however, if this criteria is not satisfied, positions are compared to the previous frame (non-adjacent by one frame) and the drift threshold is doubled (Figure 4-22). This is repeated until either a positional match is identified, or the number of frame regressions exceeds the user-defined parameter, *disappear_threshold*.

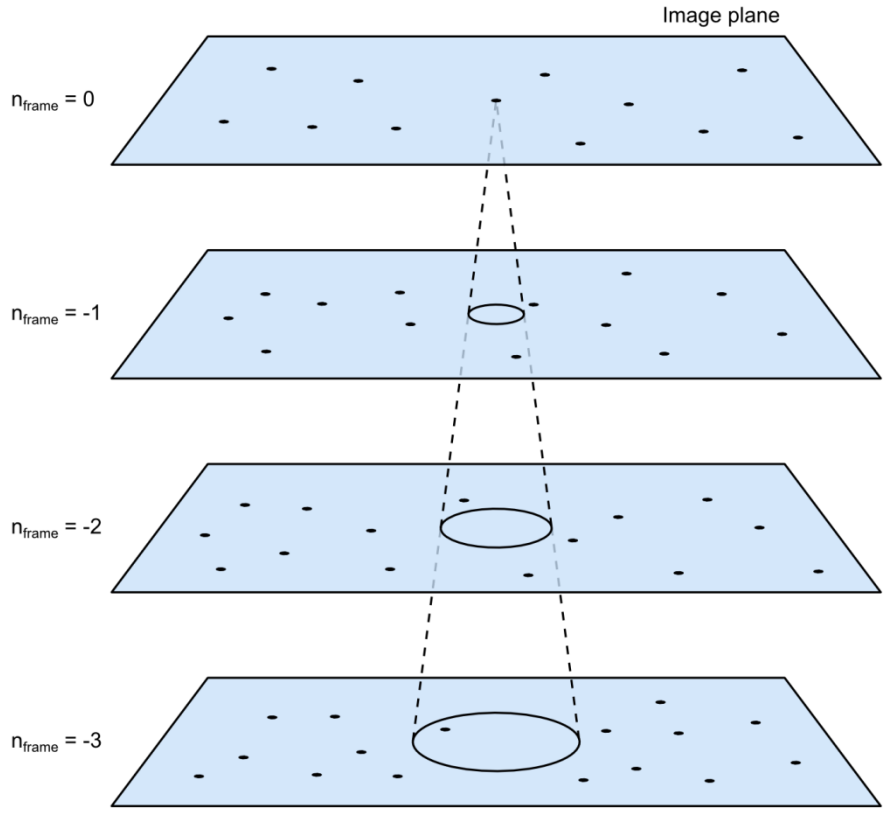


**Figure 4-22 – Process to track microspheres between adjacent frames in a video**
Initially, the spatial residual between the microsphere of interest ($n_{frame}$ = 0) and all microspheres in the previous frame ($n_{frame}$ = -1) is calculated. A match is registered if the smallest residual is within the user-defined drift threshold (perimeter of allowed region identified by black line). Failure to identify such a match leads to comparison with the next previous frame ($n_{frame}$ = -2) and a corresponding doubling in the drift threshold. The process is repeated until a match is identified, or the maximum number of allowed frame regressions is exceeded. In three dimensions, the volume swept out by the drift threshold can be visualised as a cone (dashed line).

Adopting a three-dimensional view of this approach (two spatial dimensions and one temporal dimension), the volume in which detected positions in different frames can be considered to correspond to the same microsphere is described by a cone (Figure 4-22).

Ultimately, while this approach is useful for tracking fast-moving particles, the typically small displacement observed for magnetically-trapped microspheres rarely results in frame regression beyond the immediately previous frame.

#### 4.5.3.4 Evaluation of microsphere trajectories

Following completion of particle tracking, the data is stored in a pair of Microsoft Excel spreadsheet files (function: *mtAnalyseTrackedParticles.m*; Accompanying Material); the first acting as a summary of the key tracking results and the second providing spatial coordinates of each tracked microsphere as a function of frame number. For each tracked microsphere, the first file contains the average detected position, the variance in displacement along x and y-axes (provided in terms of both pixels and nanometres) and the force calculated from the application of equipartition theorem (Section 4.7.1). Using the information stored in the second file, the trajectory of each microsphere is drawn onto a single video frame along with reference numbers relating each microsphere to the stored positional data (function: *mtLineDraw.m*; Accompanying Material). This visualisation can be further extended through creation of a video showing the microsphere trajectory, traced out in real-time (function: *mtMakeMovie.m*; Accompanying Material).

#### 4.5.3.5 Implementation to a video series

Semi-automation of the particle tracking system offers improvements in throughput due to a reduction in the necessary user input. Rather than sequentially loading each video manually, the system reads fundamental video and sample parameters from a user-created, tab-delimited text file (*VideoList.txt*). In the typical configuration, this text file contains a list of both the full video filenames (including file extension) and microsphere to magnet-pair separations, required for force analysis. Prior to initiation of the tracking system the user is required to select microspheres of interest and create settings files for all videos. While the amount of user input is largely unchanged from entirely manual initialisation, this approach groups all necessary user interaction to a single instance, thus allowing the software to run uninterrupted for the duration of analysis.

#### 4.5.3.6 Evaluation of particle tracking accuracy

Accuracy of the custom MATLAB particle tracking system was evaluated through measurement of variance in displacement for surface-immobilised M280 microspheres.

Surface-immobilised microsphere positions were extracted from videos intended for force calibration (Section 4.7). Only M280-based samples exhibited sufficiently high numbers of these stationary microspheres to achieve a statistically-relevant measure of particle detection accuracy ($n$ = 15).

Analysis of identified surface-immobilised particles yielded an average positional standard error of 6.5 ± 0.7 nm (n = 15). This is comparable with other reported values of 2 nm [175], 8.7 ± 2.5 nm [176], 26 nm [177] and 25 nm [173] for similar systems; however, these are estimates as provided in the literature and likely use different approaches to assess accuracy. When compared to superparamagnetic microsphere motion arising from force application in a typical magnetic tweezers experiment, the accuracy in detection was shown to have negligible deleterious effect. In terms of the expected variance measurements (see Section 4.7 for a description of the relationship between microsphere variance and applied force), this corresponds to an error of less than 2.2%. The upper bound of this error being estimated for the highest force, and thus lowest displacement, case of an M280-bound microsphere at 14 pN applied force (Section 4.2.2) .

Owing to the high accuracy of microsphere detection, measured microsphere positions used for force calibration (Section 4.7) are used without noise subtraction or other manipulation.

## 4.6 Verification of optical systems

### 4.6.1 Calibration of magnification

Magnification in the magnetic tweezers microscope is determined simply by the ratio of tube lens to objective lens focal lengths, as shown in Equation 4-19 (Section 4.5.1). Through implementation of the calibration approach described in Section 4.5.1, it is possible to reliably demonstrate the successful implementation of the microscope optical components via comparison of predicted to measured magnifications. In the analysis described here, the microscope is shown to operate as predicted across a range of cameras (standard CCD and CMOS) and for tube lens focal lengths of 150 mm, 200 mm and 400 mm, yielding predicted magnifications between 37.5x and 100x (Table 4-5). Measured magnifications differ from the expected values by just 4.4% at 37.5x, 0.12% at 50x and 0.03% at 100x.

**Table 4-5 – Magnification calibration using CMOS, CoolSnap EZ and Watec cameras**
Comparison of measured microscope magnifications to predicted values for the implemented camera and tube lens. Observed magnification depends on the camera pixel size ($L_{pixel}$) and tube lens focal length ($f_{tube}$). To demonstrate successful implementation of the microscope optics, the measured magnification ($M_{obs}$) is compared to the predicted magnification ($M_{pred}$). For all measurements, the same objective lens was used (CFI LU Plan EPI ELWD; Nikon), with focal length of 4 mm.

| **Camera** | **$L_{pixel}$ (µm)** | **$f_{tube}$ (mm)** | **$M_{pred}$** | **$M_{obs}$** |
|---|---|---|---|---|
| CMOS | 6.00 | 150 | 37.5 | 37.9 |
| CMOS | 6.00 | 200 | 50 | 49.7 |
| CMOS | 6.00 | 400 | 100 | 100.2 |
| CoolSnap EZ | 6.45 | 150 | 37.5 | 38.7 |
| CoolSnap EZ | 6.45 | 200 | 50 | 49.9 |
| CoolSnap EZ | 6.45 | 400 | 100 | 99.3 |
| Watec | 8.33 | 150 | 37.5 | 40.8 |
| Watec | 8.33 | 200 | 50 | 50.5 |
| Watec | 8.33 | 400 | 100 | 100.5 |

For each microscope configuration detailed in Table 4-5, a single calibration image was acquired and analysed using a custom MATLAB script (function: *measureMag.m*; Accompanying Material). In order to allow for the large range of magnifications tested, the line-group observed in the USAF 1951 target was varied between configurations, to give the largest possible distance per pixel. The same long working-distance objective lens (CFI LU Plan EPI ELWD; W.D. = 10.1 mm; N.A. = 0.55; Nikon, Tokyo, Japan) was used in all experiments for the purpose of consistency. Pixel edge lengths ($L_{pixel}$) were vendor-supplied for CMOS (6.00 µm/px; DMK 22BUC03; The Imaging Source GmBH, Bremen, Germany) and CoolSnap EZ (6.45 µm/px; Photometrics, Tucson, Arizona, USA) cameras and were measured by Urban Seger in the case of the Watec CCD camera (8.33 µm/px; 902DM2S; Watec Co. Ltd, Tsuruoka, Japan).

### 4.6.2 Characterisation of fluorescence and photobleaching

Implementation of truly horizontal tethers in the magnetic tweezers microscope necessitated the use of epi-illumination rather than higher signal to noise approaches, such as TIRF (Section 2.7.5). To facilitate investigation on the single-molecule level, RNAP is labelled with 40 nm diameter fluorescent TransFluoSpheres (TFS; Invitrogen, California, USA). These probes are ideal, since they are comprised of polystyrene spheres

impregnated with large quantities of fluorophore. As a result, not only do they yield significantly higher fluorescence signals than individual fluorophores, but they have greatly improved lifetimes of observation; exhibiting a gradual reduction in fluorescence intensity, rather than undergoing single-step photobleaching.

**Figure 4-23 – Individual TransFluoSpheres observed at 488 nm excitation**
Example image of 40 nm TransFluoSpheres (TFS) observed in the horizontal magnetic tweezers microscope using 488 nm laser excitation and the optical components described in Section 4.4.1. The image was collected using a scientific CMOS camera (pco.edge 5.5; PCO AG, Kelheim, Germany) at an integration time of 30 ms. TFS were immobilised between a quartz slide and glass coverslip in a solidified 2% agarose gel (in TAE buffer). Individual TFS are easily identifiable, thus indicating that at appropriate labelled stoichiometries, it should be possible to identify single RNAP enzymes.

The ability to resolve individual fluorophores in the horizontal magnetic tweezers microscope is demonstrated through immobilisation of TFS to a final concentration of 0.24 nM in 2% agarose gel (in TAE buffer). A similar sample design to that described in Section 2.7.3 was used, with a quartz slide and glass coverslip maintained at a uniform separation by 9 µm latex microspheres (Section 2.5.1). To prevent premature agarose polymerisation, the 9 µm microspheres, TFS and agarose were combined to a single solution; a 10 µl volume of which was deposited straight onto the quartz slide and covered with the glass coverslip. Following polymerisation, the sample was illuminated using the typical microscope optics (Section 4.4.1) and a 488 nm laser (Sapphire 488-30 CDRH; Coherent, Inc., Santa Clara, California, USA) operated at 30 mW. Imaging used a scientific CMOS camera (pco.edge 5.5; PCO AG, Kelheim, Germany**)** operated with an

integration time of 30 ms, 1120 x 1000 $px^2$ image size and 16-bit pixel intensity scale. Data was cropped to the intensity range 77 to 262 and saved in an 8-bit tif format (Figure 4-23).

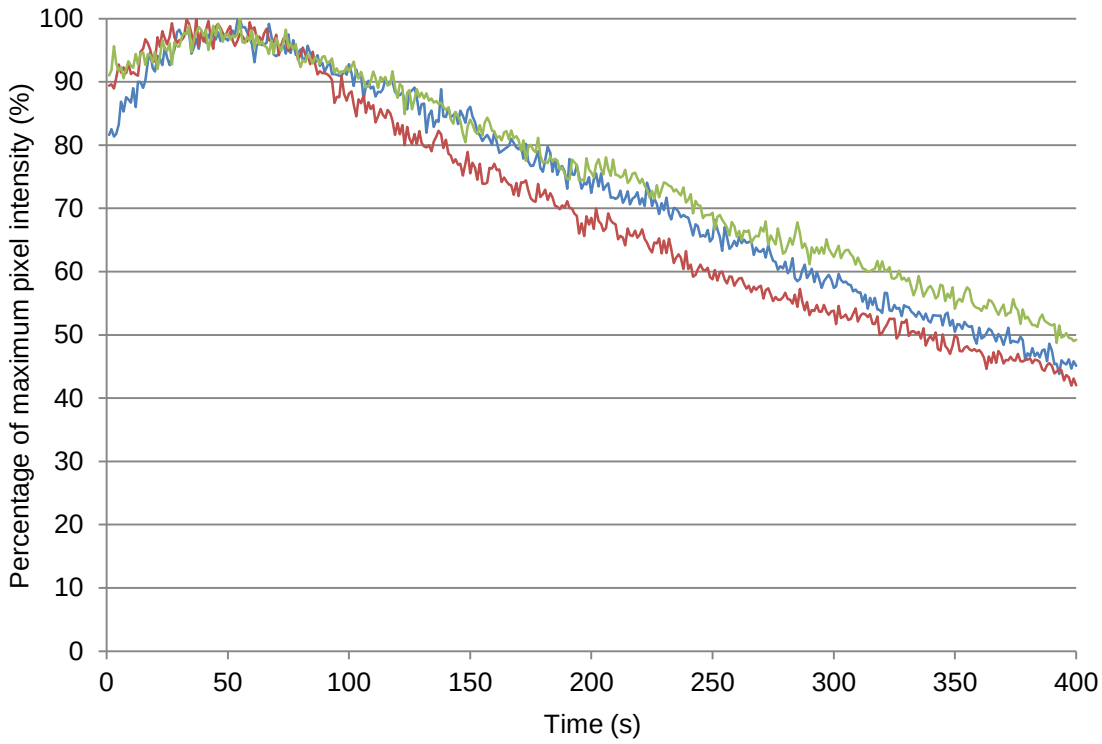


**Figure 4-24 – Photobleaching of TFS across a 400 second period**
At three different sample regions, fluorescence intensity was measured for 100 TFS and 100 background positions. Data shown is mean TFS intensity with mean background intensity subtracted and subsequently scaled to the percentage of maximum pixel intensity. All three sample areas show similar characteristic curves, with a slight initial increase in fluorescence, followed by a linear decrease in fluorescence intensity. The origin of the initial increase in fluorescence is unknown; however, its presence in all samples indicates it may be an intrinsic property of TFS; possibly one mediated by sample heating when illuminated. The linear photobleaching region exhibits a reduction of approximately 0.152 ± 0.01 $\%s^{-1}$ (SD; n = 3), where 100% intensity is the maximum observed value. As such, the TFS fluorescence half-life can be estimated as approximately 310 ± 31 s (SD; n = 3).

Through acquisition of video data at a frame-rate of 1 fps for a total duration of 400 seconds it was possible to observe TFS photobleaching. Prior to data acquisition, the region of interest was identified and focussed as quickly as possible to minimise premature photobleaching. Three videos were collected of the sample, each using identical camera settings, and varying only in sample position. These videos were analysed using a custom MATLAB script (function: *measureTFSIntensity.m*; Accompanying Material), whereby the user selects each TFS centre using a graphical user interface (GUI) similar to that described in Section 4.5.3.1. The mean pixel intensity of each selected region is monitored as a function of time and output to an Excel spreadsheet. Similarly, pixel intensity background data is collected by repeating the approach, but selecting regions void of any

TFS. For each video, 100 TFS and 100 background positions were measured. Average TFS intensities were subtracted from average background intensities and scaled to the maximum value observed (Figure 4-24).

All three measured intensity profiles show very similar characteristics, with an initial increase (time, $t$ = 0 to 50 s) followed by a linear decrease in intensity. The origin of this initial increase is not immediately clear; however, it may result from temperature dependence of the fluorophores as the TFS are heated by the incident laser. Through fitting a simple linear relation to each data set, the rate of photobleaching is estimated at $0.152 \pm 0.01$ $\%s^{-1}$ (SD; n = 3), where 100% intensity occurs for the maximum observed fluorescence. Accordingly, the photobleaching rate can be used to calculate an approximate TFS fluorescence half-life of 310 ± 31 s (SD; n = 3).

## 4.7 Force characterisation of horizontal magnetic tweezers

### 4.7.1 Equipartition theorem

Acquisition of biologically-relevant information from the horizontal magnetic tweezers microscope relies on the tethered substrate being manipulated in a well-defined and reproducible manner. One fundamental aspect of this is both accurate prediction and measurement of the force acting on the superparamagnetic microsphere, since over-extension has been demonstrated elsewhere to have a considerable effect on the stability of the pre-initiation transcription complex [41]. The first requirement has been implemented in the form of the Biot-Savart law (Section 4.2.2), which is used to model the field generated by a pair of cubic permanent magnets. When applied to the known magnetic properties of the superparamagnetic microspheres, a prediction of force as a function of microsphere to magnet pair separation can be extracted [99]. Complementing this, force acting on the superparamagnetic microsphere can be measured indirectly via equipartition analysis, which relates thermally-induced superparamagnetic microsphere displacement to the restoring force resulting from the applied magnetic field [178,30,179].

At sufficiently large microsphere to magnet pair separations the magnetic force experienced by the tethered microsphere is negligible, thus its motion can be described solely in terms of Brownian motion. Decreases in this separation are coupled with a proportional increase in the applied magnetic force, attracting the microsphere towards the

region of highest magnetic flux density. For increasing magnetic attraction, the tethered bead begins to act as a simple pendulum, with amplitude of displacement determined by Brownian motion. At thermal equilibrium, the magnetic force acting on the microsphere and the thermal energy are equal [179], allowing the system to be expressed using the equipartition function [30] (Equation 4-21). Variance in displacement perpendicular to the long-axis of the tether is measured using sub-pixel accuracy particle tracking (Section 4.5.3) and calculated with Equation 4-22.

$$F = \frac{k_B T l}{\delta x^2}$$

**Equation 4-21 – Equipartition theorem applied to tethered particle motion**
This relates thermally-induced lateral displacement of a magnetically-trapped bead to the applied magnetic force. Applied magnetic force ($F$) is a function of the Boltzmann constant ($k_B$), temperature ($T$; measured in K), the DNA tether length ($l$) and the lateral bead displacement ($\delta x$) [30].

$$\delta x^2 = \langle x^2 \rangle - \langle x \rangle^2$$

**Equation 4-22 – Method for calculating variance in displacement**
Variance in displacement is the difference between the mean squared position (first term) and the squared mean position (second term) [30].

### 4.7.2 Application of equipartition theorem

Force was measured for six different tether, microsphere and immobilisation combinations (Table 4-6). These conditions were chosen primarily to demonstrate the effect of tether length and superparamagnetic microsphere radius on force determination. Additionally, comparison between force curves collected for tethers attached to PAG-AD-MS and tethers attached directly to the surface was used to yield information about the influence of the tethering substrate. In particular, this influence may manifest as partial binding of the tether to the PAG-AD-MS, resulting in a lower than expected free tether length and overestimation of the applied force (Equation 4-21).

Typical sample preparation followed the protocol outlined in Section 2.7.3. The magnetic tweezers microscope was operated at 50x magnification with the long working-distance objective lens (CFI LU Plan EPI ELWD; W.D. = 10.1 mm; N.A. = 0.55; Nikon, Tokyo, Japan) and manufacturer-recommended tube lens focal length of 200 mm (AC254-200-A-ML; ThorLabs, New Jersey, USA). For each identified tether, a 400 frame video was recorded using either a standard CCD camera (10 ms integration time, 25 fps frame-rate; Watec Co. Ltd, Tsuruoka, Japan) or an entry-level CMOS camera (5 ms integration time,

60 fps frame-rate; DMK 22BUC03; The Imaging Source GmBH, Bremen, Germany) at 15 microsphere to magnet pair separations, ranging from 4 mm to 14.5 mm. Microsphere motion in all videos was measured with the custom MATLAB system described in Section 4.5.3 and forces calculated using equipartition theorem (Section 4.7.1). Results are only available for microsphere to magnet pair separations greater than 4 mm; the first 2.5 mm being excluded because of occlusion by the magnets and the second 1.5 mm excluded due to optical distortion arising from inhomogeneous illumination when magnets are close to the field of view. It should be noted that approximately 50% of the dig-SfiI-biotin T7 DNA results were collected using a template subsequently digested with the restriction endonuclease PmlI (New England Biolabs, Massachusetts, USA). The purpose of this was to inactivate the 4000 bp tether, which can result in unwanted short tethers (Figure 2-17; Section 2.3.9). Continued integrity of the 36 kbp template following digestion and sample purification was verified using gel electrophoresis, thus this additional step should have no effect on force response measurements.

**Table 4-6 – Summary of sample configurations for force calibration**
The various sample configurations used either the 6.79 µm dig-StuI-biotin T7 DNA template or the 12.2 µm dig-SfiI-biotin T7 DNA (Section 2.3.9). Superparamagnetic microspheres were either 1.19 µm diameter MyOne or 2.95 µm diameter M280 and tethering of all DNA was either to the channel surface or a 9.23µm diameter PAG-AD-MS substrate. Two cameras were used; one with an interlacing CCD sensor and the other a CMOS sensor.

| **Tether** | **Superparamagnetic microsphere** | **Camera** | **Attachment point** | **Number** |
|---|---|---|---|---|
| Dig-StuI-biotin T7 DNA (20 kbp) | M280 ($R$ = 1.475 µm) | CCD | PAG-AD-MS | 23 |
| Dig-StuI-biotin T7 DNA (20 kbp) | M280 ($R$ = 1.475 µm) | CMOS | PAG-AD-MS | 6 |
| Dig-SfiI-biotin T7 DNA (36 kbp) | M280 ($R$ = 1.475 µm) | CMOS | PAG-AD-MS | 23 |
| Dig-SfiI-biotin T7 DNA (36 kbp) | M280 ($R$ = 1.475 µm) | CMOS | Surface | 16 |
| Dig-SfiI-biotin T7 DNA (36 kbp) | MyOne ($R$ = 0.595 µm) | CMOS | PAG-AD-MS | 22 |
| Dig-SfiI-biotin T7 DNA (36 kbp) | MyOne ($R$ = 0.595 µm) | CMOS | Surface | 21 |

Measured force curves for each experiment configuration are shown in Figure 4-25 along with the associated standard error values shown separately in Figure 4-26 (for the purpose of clarity). In all experimentally collected data there is clear and significant disagreement with the Biot-Savart prediction (Section 4.2.2). Interestingly, while the measured and predicted force response curves fail to align, there is strong agreement between all measured data. Such discrepancy could be attributed to a variety of causes; however, all foreseeable origins of error in the experiment have been identified and addressed as described below.

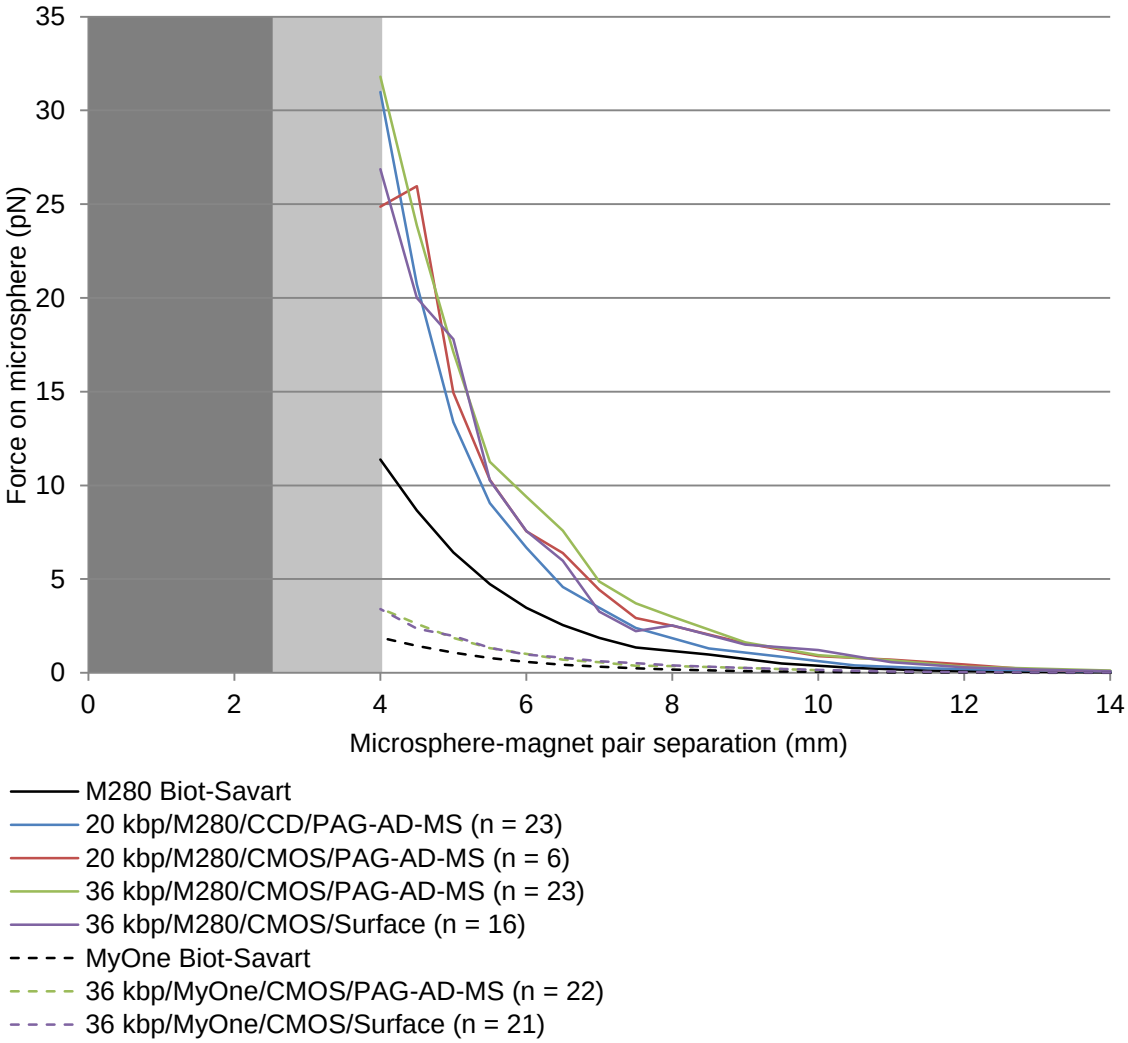


**Figure 4-25 – Comparison of predicted and measured force calibration curves**
Forces calculated through application of equipartition theorem (Section 4.7.1) to the variance in displacement measurements for each sample configuration have been averaged. The various sample configurations have been summarised in the format, tether-length/microsphere/camera/attachment-point and are stated along with the number of measurements taken (n). Measured forces are compared to those predicted by the Biot-Savart model (black lines), with all M280 microsphere data shown as solid lines and MyOne microsphere data shown as dashed lines. Standard error of the data comprising each curve is shown in Figure 4-26.

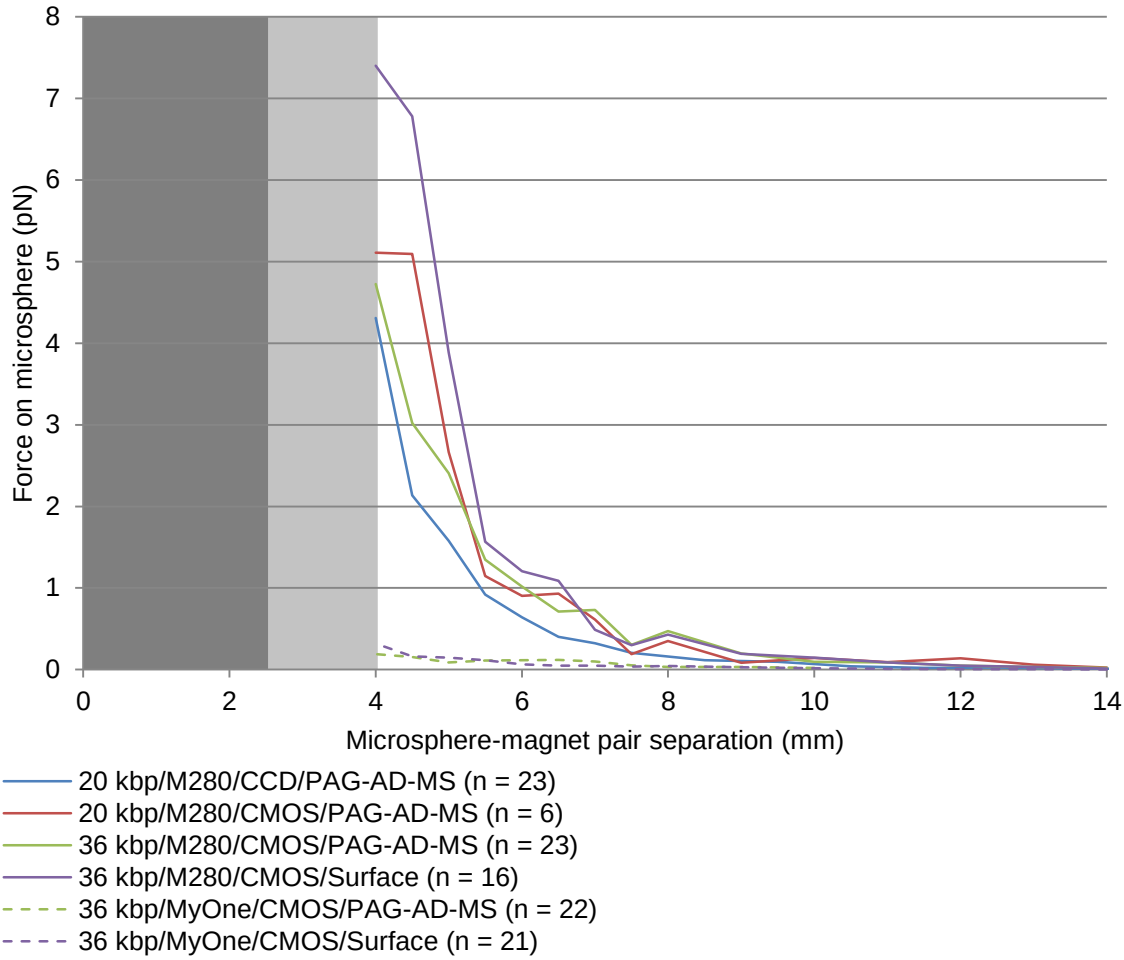


**Figure 4-26 – Standard error of measured force calibration data**
For purposes of figure clarity, the standard error of each average force curve shown in Figure 4-25 has been plotted separately. Standard error for each averaged force response curve increases with decreasing microsphere to magnet separation; this corresponds to the higher force region, where tethers have a higher probability of shearing. Resultantly, the number of measurements comprising each average decreases, leading to greater error.

Components fundamental to the experiment have been tested for agreement of the vendor-stated properties to measured values. In particular, this involved measurement of superparamagnetic microsphere radii using SEM-collected images and a custom MATLAB script (Section 2.5.2). Both the MyOne and M280 microspheres were observed to have radii larger than those specified by the manufacturer: 13% larger for the former and 5% larger for the latter. In the case of MyOne microspheres, a similar value has been reported elsewhere [99]. Assuming homogeneous distribution of magnetic particles within the polystyrene, larger microspheres would experience a greater force. Therefore, the Biot-Savart predictions in Figure 4-25 were based upon these measured radii. Similarly, magnetic remanence ($B_r$) of the cubic NdFeB magnets was measured using a Hall probe (Section 2.5.3). Across 48 measurements, an average value of $B_r = 1.26 \pm 0.05$ T was obtained. This is slightly less than that specified by the manufacturer, but is corroborated

by independent measurements [99]. As with the microsphere measurements, the Biot-Savart prediction was based upon the measured magnetic remanence.

Equipartition theorem-based estimation of force acting on microspheres is directly proportional to the tether length. Accordingly, incorrectly high tether lengths will result in overestimation of the force acting on the microsphere. For a tether immobilised on a PAG-AD-MS, such a situation could manifest through binding of part of the tether to the tethering substrate surface. Indeed, this is likely to occur in cases where the tether attachment point lies on the opposite side of the PAG-AD-MS to the magnet pair. Since it is not possible to determine the path of each tether, this effect was probed through measurement of tethers attached directly to the channel surface. Using this approach for both M280 and MyOne microspheres (green line for PAG-AD-MS-immobilised tethers and purple line for surface-immobilised tethers; Figure 4-25), no significant improvement in agreement with the Biot-Savart predicted force response was observed.

As discussed in Section 4.3.4, long camera integration times can result in blurring in the observed data. The magnitude of this effect was simulated for the two cameras used to collect data and was demonstrated to have the most severe effect on the interlacing CCD camera. Despite this, there is no discernible difference between data collected with the interlacing CCD or CMOS cameras; an effect most apparent for identical experimental configurations using the different cameras (blue line for CCD and red line for CMOS; Figure 4-25), where the CCD measurements are slightly lower than those collected with the CMOS camera. Failure to exhibit any appreciable improvement in agreement between predicted and measured forces indicates influence of a significantly more dominant factor.

Interaction of the microsphere with the channel surface may account for the so far unresolved disagreement between theory and experiment. As detailed in Section 4.3, up to 50% of M280 and 30% of MyOne microspheres may come into contact with the channel surface as a result of thermal motion, gravity and asymmetry in the applied magnetic field. While it is not possible to determine the absolute effect of this contact, the indirect effect on microsphere displacement has been observed. Comparison of equivalent force response curves for the two types of microsphere show a closer agreement experimental agreement with theory for the MyOne data. This is demonstrated in Figure 4-27, where the MyOne data has been scaled to be directly comparable to that of the M280 microspheres. An

appropriate scaling factor was identified as the value required for alignment of the Biot-Savart curves for MyOne and M280 microspheres, since the applied magnetic field profile is unaffected by microsphere composition. Resultantly, the two curves differ solely in magnitude and not shape.

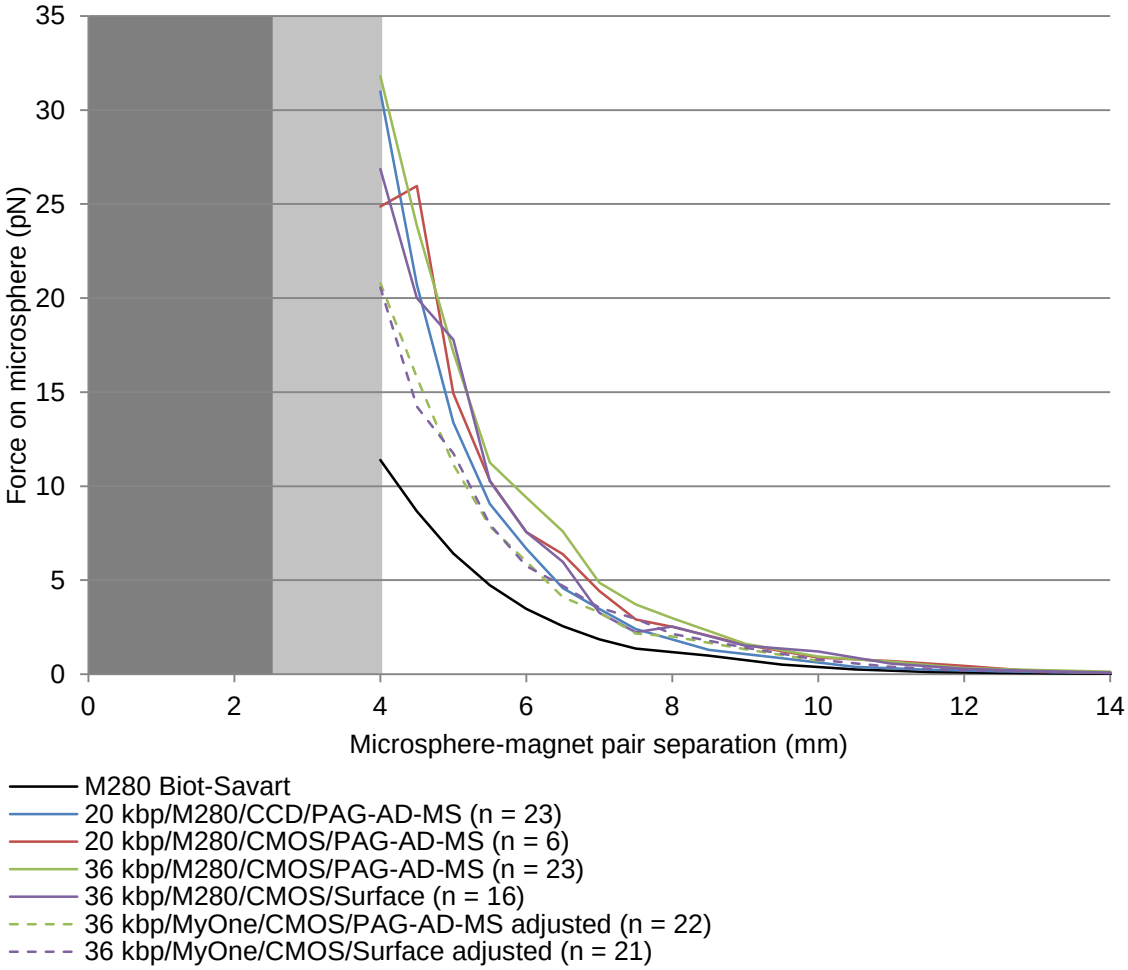


**Figure 4-27 – Alignment of MyOne and M280 force response curves**
To facilitate improved comparison of the MyOne and M280 force response curves the MyOne data has been rescaled to match the M280 data. The scaling factor used was that which gave exact alignment of the predicted Biot-Savart force curves, since they posess identical shapes, but with magnitudes dictated by the microsphere properties. The scaled curves demonstrate an improvement in agreement between theory and experiment for the smaller, MyOne microspheres, thus indicating an influence of microsphere diameter no measured force.

While there is still a significant disagreement between the theoretical and experimental data, there appears to be correlation between the measured force and microsphere diameter. This effect could be further probed through reconfiguration of the microscope to a standard vertical system (Section 1.4.3). Such an approach would allow the tethered microsphere to be extended much further from the surface, where interactions can be considered negligible. Implementation of this would require incorporation of a vertically-inclined translational stage for magnet positioning and modification to the magnet holder to permit

passage of bright-field light to the sample; however, fundamentally the experiment would remain unchanged, as microsphere displacement would remain along the same axis. In the absence of such data, it is not possible to determine conclusively if the disagreement results entirely from surface effects, such as a higher probability of surface contact, or from an incomplete description of the magnetic field using Biot-Savart law.

### 4.7.3 Tether extension in response to applied magnetic force

An alternative approach to characterise the force response of the magnetic tweezers system is to measure tether extension as a function of the applied force. Theoretically, this response can be described using the worm-like chain model (WLC; Section 4.3.2), which describes the double-stranded DNA polymer like a semi-flexible rod. Taking the average microsphere positions from the data collected for equipartition analysis as a function of microsphere to magnet pair separation, the observed tether extension can be inferred. In a surface-tethered scenario, the time-averaged position of the superparamagnetic microsphere at zero applied force would coincide with the tethering point; however, the presence of the PAG-AD-MS tethering substrate prevents this from occurring. To overcome this, extensions are calculated relative to the position at maximum measured applied force, with the extension at this point assumed to correlate with the WLC prediction. Mechanical drift of the sample is accounted for using the average position of the PAG-AD-MS as a stationary reference.

Tether extension as a function of the measured applied force has been calculated for the *36 kbp/M280/CMOS/PAG-AD-MS* and *36 kbp/MyOne/CMOS/PAG-AD-MS* data sets shown in Figure 4-25. Any data sets where the microsphere was disabled, either through non-specific immobilisation on the channel surface or through dissociation from the PAG-AD-MS, were discarded from this analysis. For the M280 data, this resulted in a significant decrease from 22 to 8 sets, whereas only 3 of the initial 21 MyOne sets were removed. This supports the observation described in Section 4.3 that a greater proportion of the M280 microspheres are likely to be in either continuous or intermittent contact with the channel surface.

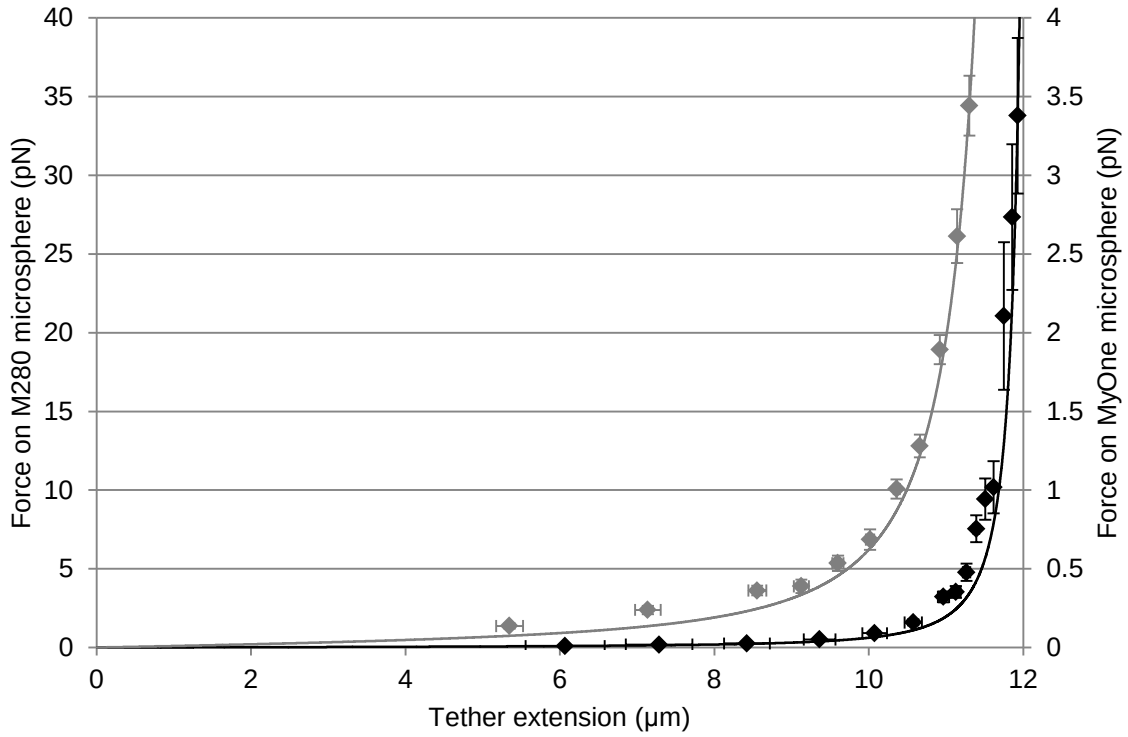


**Figure 4-28 – Measured force as a function of tether extension**
Data was recorded for M280 (n = 8; black symbols; primary axis) and MyOne (n = 18; grey symbols; secondary axis) tethered DNA (dig-SfiI-biotin T7 DNA; $l_c$ = 12.2 μm). A small initial force (< 1 pN) is required to achieve extension to ~80%; however, the force necessary to continue extension increases greatly beyond this point. Average measured extension is compared to the theoretical Worm-Like Chain (WLC) model, which is plotted to suit the different M280 (black line; primary axis) and MyOne (grey line; secondary axis) force ranges. Unlike the equipartition force measurements (Section 4.7.2), there is strong agreement between the experimentally-obtained data and theoretical prediction for both data sets. This indicates the force measurement is accurate and disagreement to the Biot-Savart model likely originates from an incomplete magnetic description of the system. Agreement here further demonstrates the successful and reliable manipulation of single dsDNA tethers.

There is strong agreement between the measured tether extension data and theoretical WLC model evident for both species of microsphere across the full extension range (Figure 4-28). Minor disagreement is observed for the MyOne-tethered DNA at low applied forces; however, this can be attributed to the spatial obstruction from the PAG-AD-MS as described above. Such strong agreement for both data sets supports the use of the equipartition theorem for force characterisation and indicates the implemented Biot-Savart model may not offer a complete description of the magnetic field.

Tether extension also represents an alternative route to force characterisation of the magnetic tweezers microscope. Issues with low experimental throughput, compared to the equipartition approach which only requires a single force measurement, could be addressed through automation. Integration of a piezoelectric-controlled x-y translational stage for magnet positioning with the data acquisition system would remove the need for user intervention between measurements.

# Tethered DNA experiments

## Chapter 5

## 5.1 Introduction

Real-time observation of transcription on the single-molecule level requires DNA tethers to be extended within the focal plane of the objective lens. It is on these tethers that RNAP undergo transcription, visualised via conjugated fluorescent probes, such as TransFluoSpheres (TFS; Life Technologies, Carlsbad, California, USA) or quantum dots (Q-Dots; Life Technologies, Carlsbad, California, USA). These individual components have thus far been successfully demonstrated: reproducible tether extension in Section 4.7 and functionally active biotinylated wild-type T7 RNAP in Section 2.4.1. In this chapter, the two experimental strands are brought together to facilitate the final goal of probing transcription in manners not previously possible; however, prior to this it is necessary to optimise the tethering system. Such an analysis is especially important for single-molecule experiments, where failure to achieve optimal conditions can preclude attainment of biologically-relevant information through a combination of high background fluorescence, unwanted surface immobilisation, photo-mediated sample degradation and low experimental through-put.

In order to address the various aspects identified, initial experiments have been conducted utilising microfluidic sample delivery and Total Internal Reflection Fluorescence (TIRF) microscopy. These two techniques may not offer the torsional control available with a magnetic tweezers assay, but for the purpose of biological optimisation, the unrivalled signal contrast available is essential. In particular, TIRF is suited to a study of surface-immobilisation, since the technique is limited to fluorescent observation within ~100 nm from the channel surface; a restriction imposed by the exponential intensity decay of the fluorophore-exciting evanescent wave (see Section 2.7.5) [107]. Microfluidic sample delivery also befits the required optimisation experiments, offering hydrodynamic extension of DNA and rapid buffer exchange (as described in Section 5.3.1). Furthermore, the independence of hydrodynamically-extended DNA permits a higher experimental through-put than is available with magnetic tweezers, where interactions between superparamagnetic microspheres can limit surface tether density.

## 5.2 A microfluidic platform for characterisation of tethered DNA experiments

### 5.2.1 Evaluation of existing technologies for microfluidic device fabrication

Over the past two decades microfluidics has become a valuable tool in the world of science and technology, having far reaching impact in fields as diverse as point-of-care medicine [180], consumer electronics (e.g. printer cartridges and tactile touchscreen displays) and molecular biology [181,182]. One area which has begun seeing increased influence from microfluidics is single-molecule biophysics, where microfluidics has enabled experiments incorporating buffer exchange [183,184] and hydrodynamic force application [82,103,185,186]. However, numerous standard single-molecule techniques, such as optical and magnetic tweezers and prism-coupled Total Internal Fluorescence (TIRF) microscopy have not yet benefitted from the establishment of a standard microfluidic approach. This is due to considerable spatial constraints imposed by these techniques, in particular, a limit on sample thickness (Figure 5-1). While approaches to tackle this have been reported, none have seen wide-scale adoption owing to costly materials, equipment or facilities [187,188], incompatibility with high-numerical aperture microscopy [189] or an inability to offer consistent reproduction of complex channel configurations [190–192]. The described microfluidic design addresses each of these issues, offering quick and easy photolithographic fabrication of 30 μm high, multi-flow channels compatible with the aforementioned techniques, whilst maintaining an initial financial outlay of less than £800.

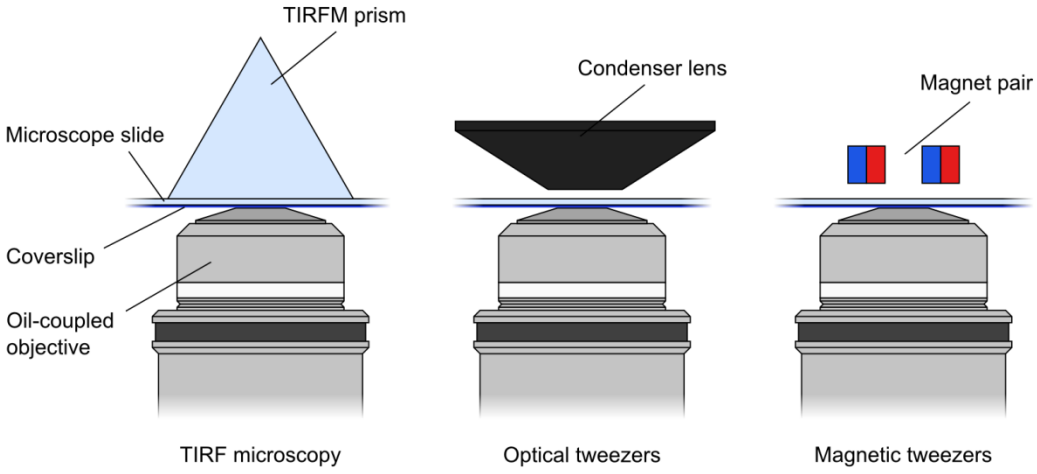


**Figure 5-1 – Spatial constraints imposed by three single-molecule techniques**
Example techniques are TIRF microscopy (left), optical tweezers (centre) and magnetic tweezers (right). Prism-coupled TIRF microscopy requires a quartz prism to be placed directly above the observable region to couple in the reflected laser. Optical tweezers require a condenser lens in close proximity to the upper surface for brightfield illumination of the sample. Magnetic tweezers requires a magnet pair to be in close proximity to the sample, since magnetic field strength decreases with an increasing distance. For the high resolution imaging required, each technique uses high numerical aperture oil-coupled objectives in contact with the underside of the sample.

Early microfluidic device fabrication generally involved using etched glass as the channel-forming layer [193–195]. However, this method relies on the use of expensive equipment and a clean-room environment, thus preventing microfluidics seeing wide-scale adoption. Over the past few years, alternative structural materials, including poly(dimethylsiloxane) (PDMS) [61], Cyclic Olefin Copolymer (COC) [196,197] and SU-8 photoresist [198,199] have been demonstrated. Working with these often involves additional steps, such as fabrication of intermediate moulds and while glass and COC-based devices exhibit greater mechanical strength, for the purpose of rapid channel-configuration prototyping, materials which do not require so many intermediary steps generally have the upper hand.

Today PDMS has become widely adopted as the microfluidics material of choice (examples include: [61,200–203]) offering several significant advantages, such as ease of moulding, biocompatibility, optical transparency above 280 nm and auto-sealing to surfaces mediated via van der Waals interactions [204]. Despite this wealth of benefits, it also has several shortcomings, many intrinsic in the properties that make them so suitable for rapid prototyping in the first place. PDMS lacks the requisite mechanical strength to withstand techniques that apply undue force to the polymer, resulting in deformation and channel warping. While it is possible to construct TIRF and optical/magnetic tweezer-compatible devices from PDMS, flow generation must be achieved with low pressure methods, such as electrophoresis [189] or gravity-driven flow [205]. However, these low flow-rates do not allow the fast interface switching achievable with more robust construction solutions. Similarly, exertion of excessive levels of compression from high numerical aperture, oil-coupled objectives must be avoided, thus restricting use to air-objectives.

Devices constructed with double-sided adhesive tape offer an alternative to PDMS, addressing the problem of deformability [191,206–208]. However, channels constructed in this manner must be kept relatively simple and are not highly reproducible, since the tape is cut by hand. Therefore, this method is not a viable proposition for experiments where accurate spatial control of flow is required.

### 5.2.2 Photoresist as a channel-forming layer compatible with TIRF microscopy

Described here is a novel, low-cost method for the rapid and reliable fabrication of simple, thin microfluidic devices. They can be manufactured and altered on demand in small

batches using off-the-shelf equipment and without the need for a clean-room environment. These devices are compatible with high spatial resolution microscopies, such as prism and objective-coupled TIRF and with micro-manipulation optical and magnetic tweezer systems, whilst providing chemically clean surfaces onto which bio-molecules or cells can be immobilised. The convergence of multiple single-molecule approaches onto one device is possible due to its thin design, comprising a quartz slide-photoresist-coverslip sandwich.

Photoresist is well documented as a material for microfluidic device construction and has been used in a variety of different applications [209–214]. Device fabrication with this material can be completed within a day, making it comparable to its PDMS counterpart. PDMS-based fabrication is frequently performed using an SU-8 [215,216,61,217,218,201,219,213] channel master onto which the polymer is moulded. Therefore, when prototyping many channel configurations (for which many masters would need to be made), using photoresist structurally, rather than as an intermediate, can significantly reduce manufacturing time. Further time and complexity can be saved by laminating solid dry-film photoresists onto the glass substrate, rather than using liquid photoresists (examples include: [220,198,221–223,199,224–226]), which require spin-coating and curing.

The devices described here exhibit advantages over their PDMS counterparts in a couple of key areas, whilst losing none of the advantages that make PDMS so suitable for microfluidics fabrication. By sandwiching photoresist between rigid materials, such as glass and quartz, channels are significantly less deformable, allowing for higher flow-rates to be employed and unlocking the ability for fast interface switching (3-5 seconds) by altering the ratio between fluid flow rates. Additionally, thermal bonding of photoresist to the glass and quartz substrates is achieved using a standard office laminator and hot-plate, thus negating the need for expensive, specialised plasma-bonding equipment as used in the covalent attachment of PDMS to glass.

Use of low-cost materials, such as dry-film photoresist on coverslips and $Na_2CO_3$ as the developer, permits over-fabrication of semi-assembled devices, with only those exhibiting the best properties being used for producing complete assemblies. Also, the fluidic devices presented here can optionally be easily disassembled after use, which is a cost saving advantage in cases where expensive quartz slides have been used.

The benefits of TIRF microscopy compatibility are not necessarily available to thicker systems with complex 3D channel geometries [209,202,227] or to devices with certain polymer-based surface coatings used to assist device assembly (such as SU-8 or PMMA [220]) as these reduce the optical transparency and continuity of refractive index required for TIRF.

### 5.2.3 Optical systems

High numerical aperture objectives provide excellent temporal and spatial resolutions; however, they come at the cost of a short focal-length, thus imposing sample thicknesses of <20 μm. Furthermore, implementation of TIRF microscopy in the prism-coupled configuration requires the sample to be within a few hundred nanometres of the opposite channel surface to ensure fluorophores are within the evanescent field region. Once again, the channel can have a thickness, no greater than a few tens of micrometres. These spatial constraints are addressed in our design using a single, 30μm thick, photoresist layer sandwiched between a quartz slide and glass coverslip.

Imaging with prism-coupled TIRF is performed at the quartz slide-observation volume interface as this presents minimal background fluorescence due to the low auto-fluorescence of quartz and the chemically-clean state of the surface. The latter can be assumed as the quartz slide is only attached following complete channel development. However, for use of these devices with objective-coupled TIRF the incident laser and emitted fluorescence pass through the glass coverslip; therefore, the ability to completely remove fluorescent material from the glass coverslip is vital. SEM (Figure 5-2a and Figure 5-2b) and fluorescence analyses (see Section 5.3.2) at this surface confirm its clarity and the high channel contrast ratio.

### 5.2.4 Design of the microfluidic device

The microfluidic devices described here were designed by Urban Seger, with optimisation of production and characterisation (Section 5.3) conducted by myself.

Flow in the microfluidic channels is generated by applying pressure above the solutions in the inlet reservoirs. Using a resistive pneumatic network [228], relative flow-rates can be adjusted by altering the ratio of applied pressures. The resistive pneumatic network divides a pressure difference (of applied and atmospheric pressures) between the two

outlets in a manner analogous to Ohm's Law for electrical resistance [229]. In this analogy, resistance arises from tubing radii and lengths, and the pressure ratio between the two outlets is adjusted by a valve, equivalent to a variable resistor (circuit diagram included in Appendix B-I). This system provides a constant total down-stream flow-rate independent of the ratio, which would be much more difficult to achieve using syringe pumps, where decreased pressure in one branch needs to be matched by an equal increase in the other, thus requiring computer control [230,231]. Furthermore, the inclusion of an inversion switch allows the ratio between the two pressures to be swapped, with transition of the laminar flow interface from initial to final positions taking less than five seconds (transition time depends on flow-rate).

Solutions are stored on-device in PDMS reservoirs positioned to one side of the observation volume (Figure 5-2). The block is held in place with adhesive tape between the device and a support lid constructed from a glass slide, thus avoiding the need for plasma-bonding. Placement of the block is such that it does not obstruct the exiting TIRF microscopy laser, yet is close enough to the observation volume that considerable fluid wastage is not incurred by having long connecting channels or tubing. Additionally, storing solutions in reservoirs on the device reduces flow instabilities due to variations in hydrostatic pressure, as would be likely encountered with off-device storage and interconnecting tubing.

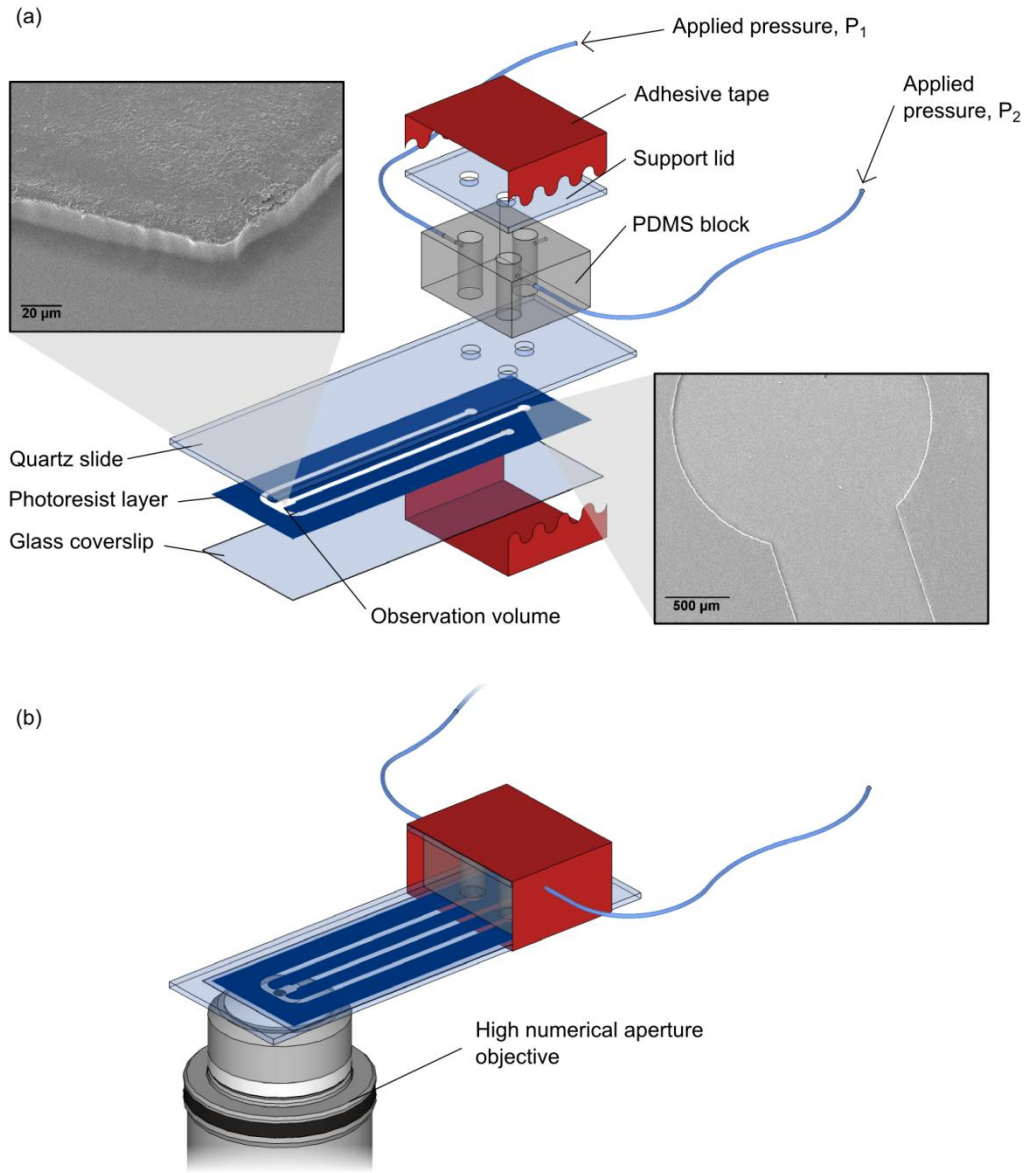


**Figure 5-2 – Exploded diagram of microfluidic device**
a) Diagram of device assembly showing the photoresist channel layer sandwiched between a quartz slide and glass coverslip. Solutions are stored on-device in the PDMS block, which is connected to the photoresist channels via pre-drilled holes in the slide. (Inset) SEM images (5 kV; JSM 6490LV; JEOL, Tokyo, Japan) showing the corner of the observation volume and a channel inlet. These images demonstrate the photoresist to be well resolved, with minimal debris where photoresist has been removed by $Na_2CO_3$ development. b) Diagram of the assembled device with the high numerical aperture objective placed below the observation volume and adhesive tape fully sealing the PDMS block and surrounding components.

### 5.2.5 Fabrication and assembly

Glass coverslips and quartz slides were prepared using the protocol outlined in Section 2.7.2. 30 µm thick dry-film photoresist (Ordyl Alpha 930; Elga Europe Ltd., Milan, Italy) was laminated onto cleaned coverslips using a standard office hot roll laminator (SPLa3; Fellowes, Inc., Itasca, Illinois, USA) operating at 1 cm/s and 100 °C with blotting paper acting as a support substrate (Figure 5-3). Blotting paper was removed

using a sharp blade and any examples where bubbles had formed due to dust trapped in the photoresist were discarded.

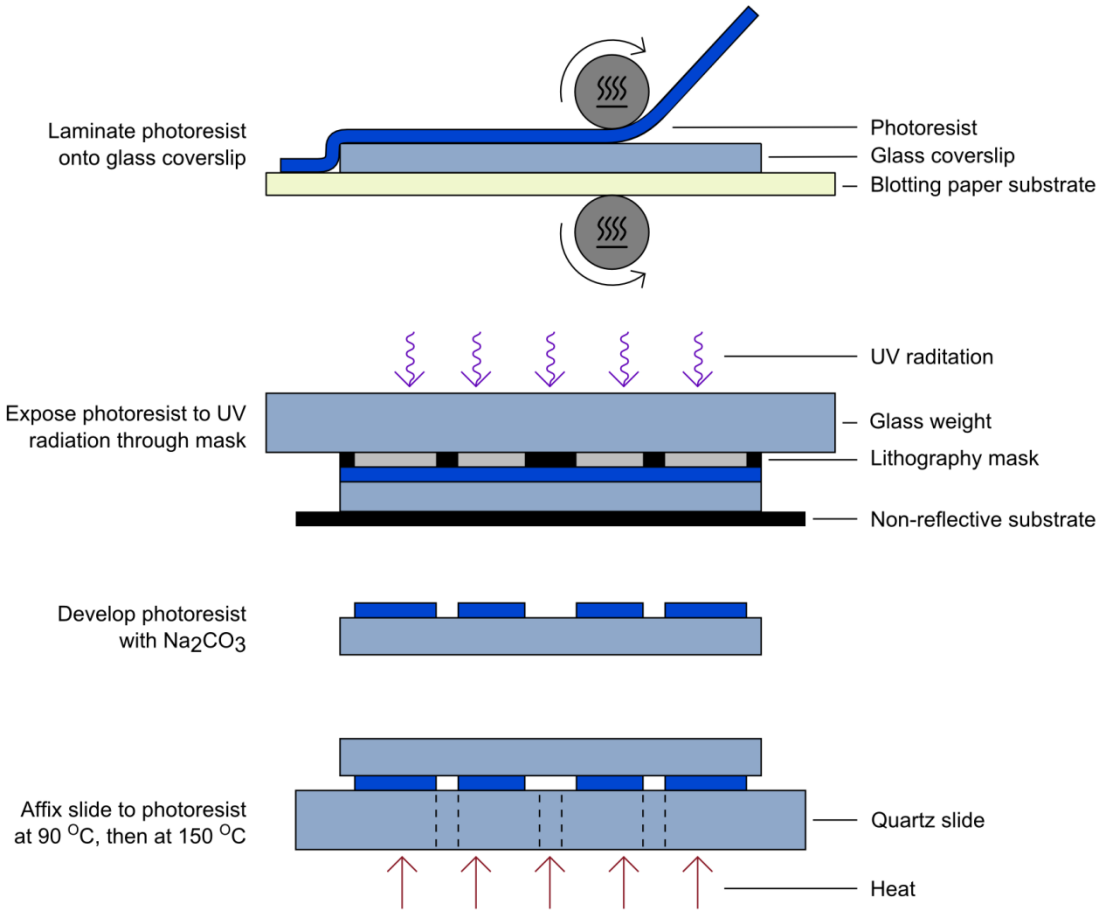


**Figure 5-3 – Guide to fabrication of microfluidic devices**
Photoresist is initially laminated onto a glass coverslip, and then patterned with the channel configuration via standard photolithography. Channels are sealed with a quartz slide with pre-drilled holes (dashed lines), allowing connection to the reservoir PDMS block.

Channel configurations were designed using vector graphics software (Inkscape) and professionally printed onto Lithofilm (Reprotech Studios Ltd., York, UK). However, Bao *et al.* have demonstrated the production of lithography masks in-house onto transparency film using a laser printer (>1200 dpi) [232]. Laminated coverslips were aligned with the lithography mask and weighted with a glass plate, then exposed to 370 nm ± 5 nm UV radiation (12 $Wm^{-2}$; SpecBright UV LED Arealights; StockerYale, Inc., now ProPhotonix Ltd., Salem, New Hampshire, USA) for 35 seconds at a light source-photoresist separation of 21 cm (Figure 5-3). Parasitic exposure of photoresist due to reflections from the supporting surface was prevented by placing the glass coverslip on a non-reflective substrate. Photoresist was developed in a 1% $Na_2CO_3$ (Sigma-Aldrich, Missouri, USA) solution for 150 seconds at room temperature using a hand agitated plastic coverslip holder

(custom built) to produce constant movement of the developer solution with respect to the polymer. Channels were rinsed thoroughly with deionised water and blown dry with filtered air.

Attachment of photoresist coated coverslips to quartz slides was performed at 90 °C using a hotplate (HP139110-60, Thermo Fisher Scientific, Massachusetts, USA), followed by cooling. Photoresist was annealed at 150 °C for 10 minutes, with pressure applied using the flat surface of silicon wafer handling tweezers to assist uniform adhesion. The device was allowed to cool at the same rate as the hotplate over a period of approximately 30 minutes. During annealing, the photoresist undergoes a colour change from light to dark blue. Tests showed excessive heating led to significant and terminal bubbling of photoresist, while heating for too long causes photoresist discolouration. Optimisation of experimental parameters including UV-exposure time and intensity, photoresist development time and annealing temperature is necessary; however this one-off outset can be completed within a few working days.

The PDMS (Sylgard 184 Silicone Elastomer; Dow Corning Corp., Midland, Michigan, USA) reservoir block was formed by injecting degassed liquid polymer mixture into a pre-fabricated Perspex (PMMA) mould by syringe and allowing it to set overnight at 70 °C. Reservoirs were defined by pins inserted into the Perspex mould prior to PDMS injection (various reservoir radii are achievable by inserting the pins into short lengths of plastic tubing). Small access holes were punched into the side of the PDMS block by a sharpened glue-gun tip (14 gauge; IDS, Inc., Agoura Hills, California, USA) and allow interfacing with the resistive pneumatic network (Figure 5-2). A full protocol for PDMS reservoir-block fabrication is provided in Appendix B-II.

Device assembly is summarised in Figure 5-2. The PDMS block is placed on slide-photoresist-coverslip sandwich in alignment with the pre-drilled channel-interface holes on the slide. Sufficient bonding should be achieved by the PDMS-slide van der Waals interactions to hold the block in place. The support lid is placed on the upper PDMS surface in alignment with the reservoirs. Secure sealing of the system is achieved by wrapping a single layer of electrical adhesive tape around the PDMS block, slide and support lid. Access to the reservoirs and resistive pneumatic network connections are

made by cutting away regions of the electrical tape. Solutions are pipetted into each inlet reservoir and the reservoir tops resealed with another piece of adhesive tape.

All materials used during fabrication are low cost and therefore discarded following device use, except the quartz slides, which are soaked for approximately 24 hours in 2% (v/v) Decon 90 (Decon Laboratories Ltd., Hove, UK) solution, causing the photoresist to dissociate, sonicated for 10 min in 1 M KOH, rinsed with deionised water and then ethanol, and reused. Quartz slides are routinely reused for device fabrication without an increase in residual background fluorescence.

## 5.3 Characterisation of the microfluidic device

### 5.3.1 Demonstration using staining of surface-immobilised DNA

Rapid interface switching in the device has been demonstrated with repeated staining and photobleaching of surface-immobilised DNA using the fluorescent intercalating dye YOYO-1 [105]. The interface between a non-fluorescent buffer and a solution containing YOYO-1 is switched across the observation volume multiple times, thus cycling exposure of DNA in the imageable region to the fluorophore. When exposed to the YOYO-1 flow, intercalation of dye into the DNA occurs, resulting in an increase in observed fluorescence with TIRF microscopy. This observed fluorescence decays away when DNA is switched into the buffer flow through a combination of fluorophore dissociation and photobleaching. Using a fluorophore concentration well in excess of the $K_d$ should permit restaining of the DNA through replacement of photobleached YOYO-1. Ultimately, the staining rate is dependent on the rate of switching and not on the YOYO-1 binding rate.

Flow serves a dual purpose in this experiment. In addition to providing a delivery method for the fluorophore, the hydrodynamic drag exerted upon the surface-immobilised DNA molecules extends it from the compacted state it adopts in static conditions into an elongated form, thus keeping it within the 100 nm deep evanescent field of the exciting TIRF laser.

To immobilise DNA in microfluidic devices produced as described in this paper, the channels were first functionalised with 1 mg/ml biotin-BSA in TE buffer at room temperature for 20 minutes, followed by incubation with 100 μg/ml streptavidin in a

TE-based buffer at room temperature for 5 minutes, then finally with a 30 minute incubation of 0.29 nM biotin-dUTP-end-labelled T7 DNA (see Section 2.3.9.1) digested at the single restriction site StuI approximately half way along the molecule (yielding ~20000 bp fragments). Devices were assembled in the manner depicted in Figure 5-2 and described in Section 5.2.5.

Staining was observed using an inverted microscope (IM35; Carl Zeiss AG, Jena, Germany) in a prism-coupled TIRF configuration using a 488 nm laser (Sapphire 488-30 CDRH; Coherent, Inc., Santa Clara, California, USA) and 100x oil-immersion objective lens (Plan-Apochromat; W.D. = 0.17 mm, N.A. = 1.4; Carl Zeiss AG, Jena, Germany). This was connected to a camera (IC-300; Photon Technology International, Inc., Birmingham, New Jersey, USA) with image acquisition performed using a custom LabVIEW VI (National Instruments Corp., Austin, Texas, USA). Time-points for the inversion of driving pressures (interface switching events) were recorded, so switching times could be calculated.

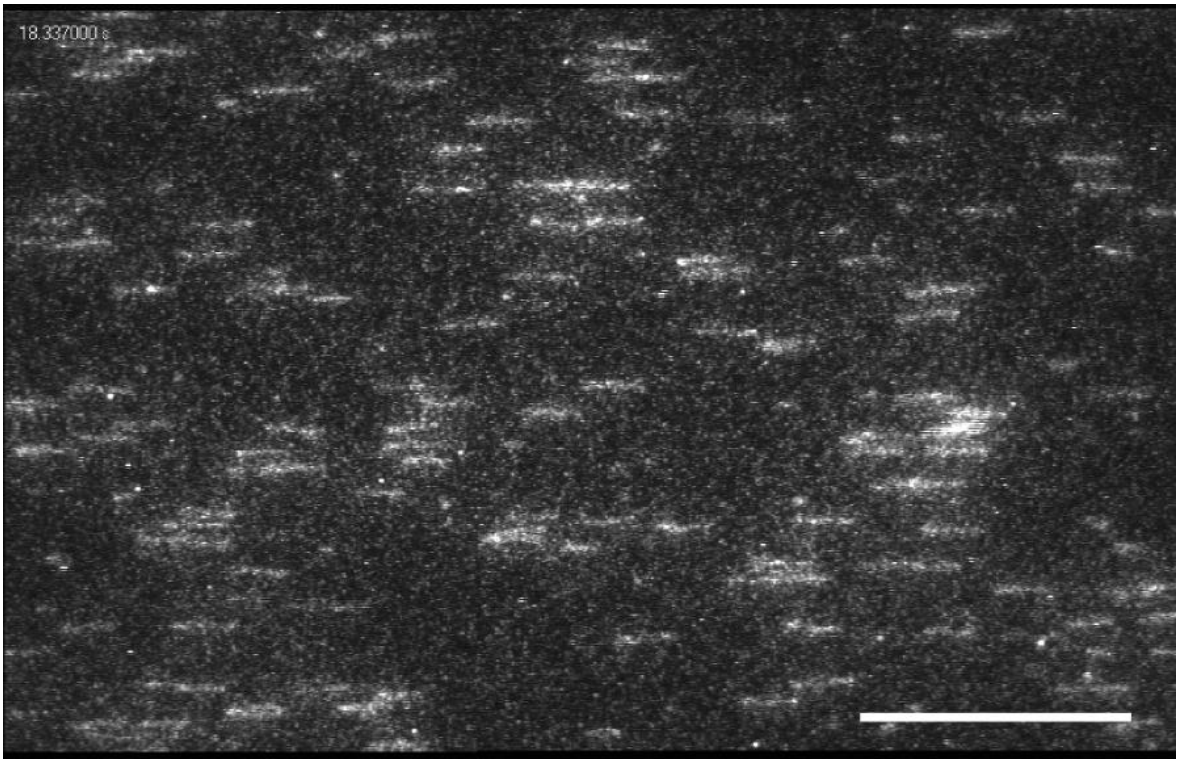


**Figure 5-4 – Example frame from microfluidic device flow-switching demonstration**
DNA is immobilised in the microfluidic chamber at one end and extended through application of flow. Introduction of the intercalating dye, YOYO-1 stains the DNA molecules, which subsequently appear as bright lines on a dark background. DNA molecules appear misleadingly wide; this is a result of imaging objects smaller than the diffraction limit of the microscope. The high level of noise present in the image is due to free fluorophore in solution and to the thermal noise of the intensified CCD camera. The scale bar corresponds to a length of 20 μm.

PBS (pH 7.39) was added to one PDMS reservoir and YOYO-1 (diluted to 500 nM in PBS) added to the other. Flow-driving pressure balance was initially set to leave PBS dominant in the channel to prevent premature exposure of DNA to YOYO-1. An approximate flow-rate of 0.52 ± 0.02 µl/s (n = 30) has been estimated by measuring the velocity of fluorescent particles free in solution and applying a parabolic velocity profile (assuming the fastest particles were at the maximum evanescent field depth of 100 nm). Once stained, DNA molecules appear as homogeneous bright lines on a dark background. Noise in the collected images is mostly attributable to free fluorophores in solution and to the thermal noise of the intensified CCD camera (Figure 5-4).

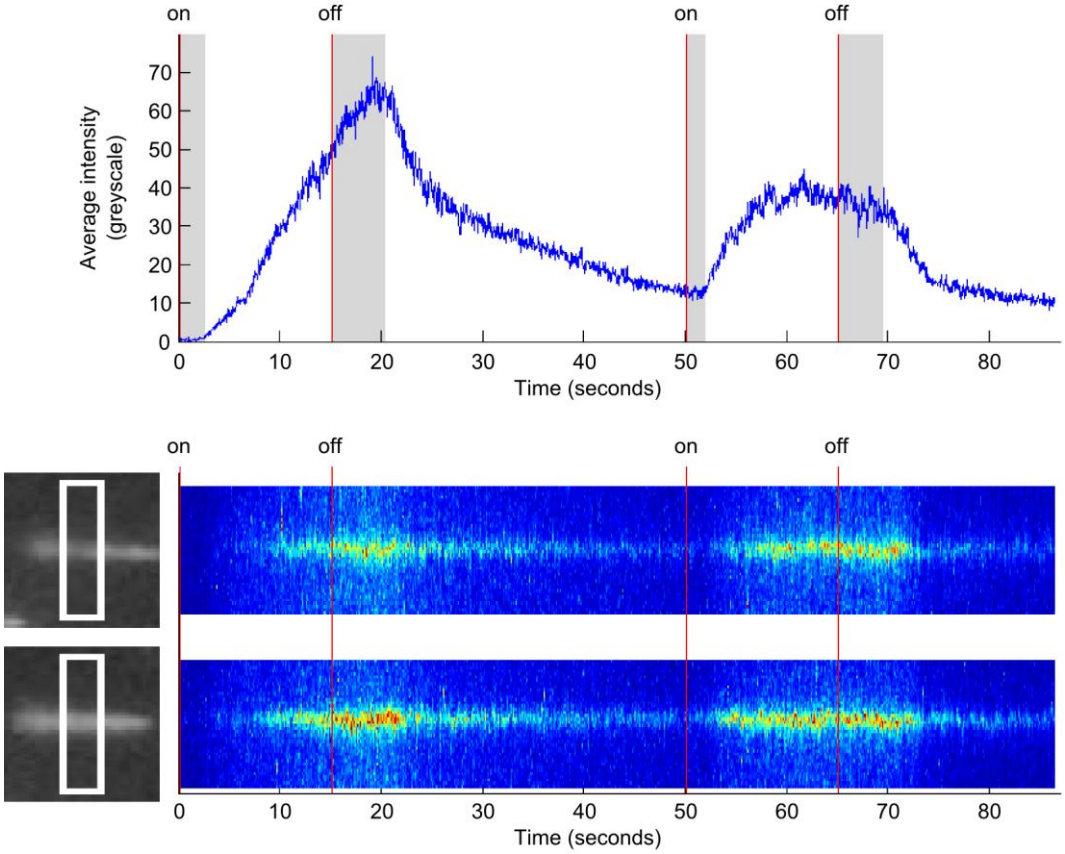


**Figure 5-5 – Evaluating interface switching using DNA and YOYO-1**
Fluorescence intensity for surface-immobilised DNA molecules being repeatedly stained with YOYO-1 as a function of time. The average intensity profile for an 80 pixel high region of 36 molecules as a function of time (top) and averaged cross section across individual molecules depicted by white boxes as a function of time. The times at which the flow-driving pressures were inverted are shown as red lines, with "on" signifying a switch to YOYO-1 dominance and "off" signifying the switch to PBS dominance in the channel. Flow switching times (from inversion of driving pressures to passage of the interface across the observed region) are highlighted with grey shading. There are clear changes in DNA intensity approximately 3-5 seconds after each switching event. Intensities have been rescaled to take advantage of the full dynamic range of the plotting tools.

Fluorescence profiles transecting single surface-immobilised DNA molecules have been measured as a function of time using a custom MATLAB system (Figure 5-5). To reduce

noise in the data, each cross-section time-point is the average of 11 adjacent cross-sections in that frame. These averaged regions are shown along the left-side of Figure 5-5 in white boxes.

Figure 5-5 demonstrates that the interface can be moved across the sample with switching times on the order of 3-5 s at a flow-rate of 0.52 μl/s ± 0.02 μl/s (n = 30). Switching from PBS to YOYO-1 solution occurs slightly more quickly than the reverse switching. This is due to the observed molecules lying off-centre in the switching region; however, these differences are only on the order of 1-2 s and become less significant towards the centre of the channel. Due to the relatively low YOYO-1 dissociation rate, fluorophore molecules are not replenished as frequently as photobleaching events occur. This leads to saturation of the DNA with an increasingly high proportion of photobleached YOYO-1 molecules, resulting in the lower maximum average intensity observed for the second staining event.

An average length for 40 DNA molecules (across 50 frames at the peak of YOYO-1 exposure) has been measured to be 4.1 μm ± 0.05 μm (n = 40) at the 0.71 μl/s flow-rate. Measurement was performed using an automated system, which identifies molecule end-points as the most extreme pixel locations along each molecule long-axis. The resolution of measurement does not permit realisation of the 0.68 μm difference between the long and short DNA fragment contour lengths of 7.14 μm and 6.46 μm (T7 DNA digested at StuI), thus the average value was taken. This measured length accounts for just 63% and 57% of the long and short contour lengths respectively, thus indicating the force was insufficient to extend DNA fully. Further extension of molecules was possible by employing higher flow-rates; however, this led to an increase in the rate of the DNA dissociation from the surface.

Since all DNA molecules are visible within the 100 nm deep evanescent field and show no significant decrease in fluorescence intensity towards the free-terminus it can be assumed the angle between DNA and the surface is less than 1.4° and thus the entire molecule length is measured. Through extrapolation of the relation between flow velocity and relative tether extension relationship reported by Perkins et al. [233] it is possible to estimate an end-to-end extension of 5.0 ± 0.1 μm; where error in this measure is based on predicted accuracy in extrapolation. This extension is notably longer than that measured through

analysis of the YOYO-1 stained sample and could be indicative of partial photocleavage of the DNA.

### 5.3.2 Quality and reliability of the devices

Fundamental to the microfluidic device fabrication process is complete removal of the fluorescent photoresist from the channel. SEM analysis shows the in-channel coverslip surface to be free from photoresist and other contaminating materials (Figure 5-2a and Figure 5-2b). This observation is supported by cross-sectional fluorescence (Zeiss filter set 15) intensity profiles measured with ImageJ (National Institutes of Health, Bethesda, Maryland, USA) for channels of different development times (30, 60 and 150 seconds; Figure 5-6). These studies showed improved channel definition with increasing development time up to 150 seconds, with 120, 150 and 180 second development times all producing near-identical results. It is expected that at excessive development times, photoresist would become overdeveloped and channel definition would be degraded, however this was not apparent for times ≤ 180 seconds.

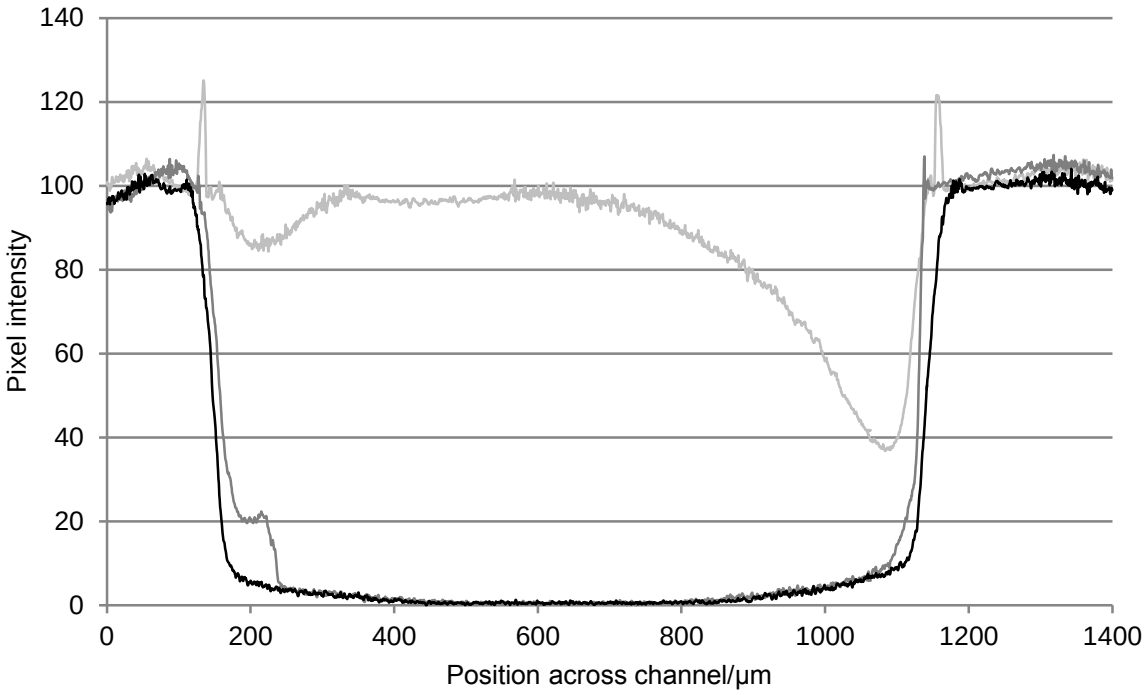


**Figure 5-6 – Evaluating photolithographic development of channels**
Fluorescence microscopy profiles demonstrate improved cross-sectional channel definition with longer development times, up to 150 seconds. At 30 seconds (light grey line) large quantities of photoresist remain undeveloped, however by 60 seconds (dark grey line) the channel is almost clear. The chosen time, 150 seconds (black line), is also representative of channel definitions at 120 seconds and 180 seconds.

In the case where different materials are used, e.g. borosilicate glass coverslips on quartz slides, differences in thermal expansion coefficients (here 7.2 $x10^{-6}$ $K^{-1}$and 0.54 $x10^{-6}$ $K^{-1}$, respectively) give rise to internal stresses when assembled devices are cooled, following the high temperature annealing phase. Tests showed the frequency of mechanical coverslip failure to become significantly high for coverslips damaged prior to assembly. Pre-assembly coverslip damage, such as chipping at the edges, provides a point of structural weakness from which cracks can propagate; however this can be avoided with careful handling.

Reusability of photolithographic masks and low material costs permit several devices to be fabricated simultaneously. Coupled with high success rates, this reduces the negative impact of failed attempts, thus negating the need for modified photoresist patterns [194] or adaptive layers [209] to increase structural stability, which would otherwise add further complexity to the fabrication process.

### 5.3.3 Long-term usage

As expected, at high pHs, the photoresist exhibits degradation and subsequent leaching into solution. However, this only becomes significant over extended periods of exposure (>20 hours). The effects of photoresist degradation would be negligible for non-static solutions and for short observation periods. Under standard laminar flow conditions, where mixing is minimal, photoresist-contaminated solutions would be restricted to the channel edges.

### 5.3.4 Example channel configurations

Rapid prototyping of channel designs was a key design consideration for this microfluidic system. Channel configurations can be quickly and easily designed using either freely available (Inkscape) or commercial (Adobe Illustrator, CorelDraw) vector graphics software. Compatibility with the resistive pneumatic network is achieved using a standardised, three port connection configuration (Figure 5-7), which interfaces with the PDMS reservoir block via holes drilled in the quartz slides.

Single channel configurations (Figure 5-7a) are well suited to tethered particle motion experiments, where buffer switching is unnecessary, but for which large observation volumes are required to increase the number of potential tethers. This design utilises the

versatility of the pneumatic network interface, as the central port is redundant, with the outer two acting as inlet and outlet. The configurations shown in Figure 5-7b and Figure 5-7c are designed for use with TIRF microscopy, with the direction of flow being parallel and perpendicular, respectively, to the axis of symmetry for the laser-coupling prism. This allows the observable region to be shifted either along the direction of flow (Figure 5-7b) or perpendicular to it (Figure 5-7c) without needing to move the prism and angle of laser incidence.

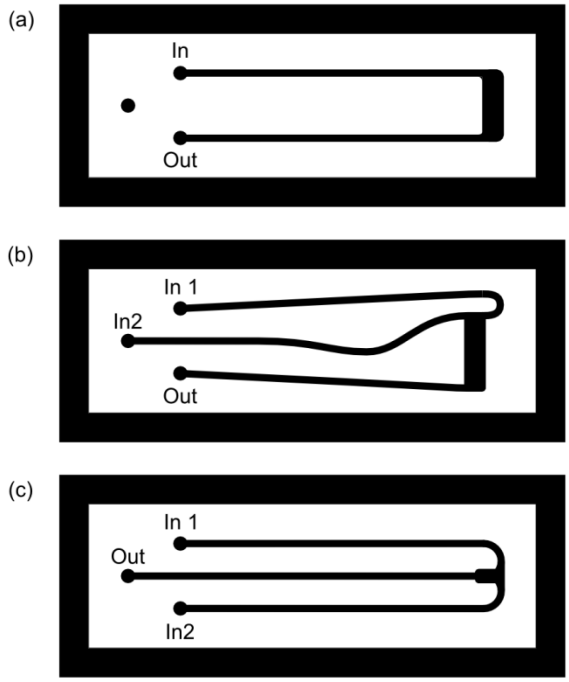


**Figure 5-7 – Example microfluidic channel configurations**
Each configuration has been designed to cater for a specific purpose. a) Simple flow chambers featuring one solution are ideal for tethered particle force measurements, b) Channels parallel to prism axis of symmetry allow the observable region to be moved parallel to the flow direction without reconfiguration of the optical system when using prism-coupled TIRF microscopy. Bends in the inlet channels are used to ensure channels are of equal lengths, c) Similarly, channels perpendicular to the prism allow easy movement perpendicular to the flow direction, across the fluid interface.

Channels b and c in Figure 5-7 have dual inputs, thus providing the ability for a switchable fluid interface in the observation volume. Such a system has been demonstrated by Tan *et al.* for buffer exchange when probing the assembly and disassembly of MuB target complexes on surface-immobilised DNA [183]. Using a switchable fluid interface, buffers can be exchanged across the observation volume on a sub-second time scale. This is significantly faster than for equivalent single-inlet and valve systems, which require flow to be temporarily brought to a halt. Valve-based systems also suffer from notable solution mixing during the switching process due to the parabolic flow profile within microfluidic channels. However, this effect is negligible for a switchable interface system, where

mixing only arises from diffusion between adjacent solutions. Minor alterations to the PDMS block configuration also permits different experiments to be conducted. For example, incorporation of a second outlet reservoir can facilitate the implementation of stagnation point assays as used by Dylla-Spears *et al.* to trap and manipulate DNA [234].

## 5.4 Optimisation of tethered DNA experiments

### 5.4.1 Quantifying photocleavage of DNA stained with YOYO-1

Experiments using individual DNA tethers stained with intercalating dyes, such as YOYO-1, are susceptible to high-rates of DNA damage from photocleavage. This can rapidly lead to a loss of samples in the observable region and an associated reduction in experimental precision and accuracy. Photocleavage occurs due to the formation of reactive oxygen species (ROS) via excitation of the dye; these ROS then attack the DNA backbone resulting in single-strand nicks [101–103]. As the single-strand nick density increases there is an increased probability of forming a double-strand break, which eventually results in the observed removal of the downstream region of the tethered DNA when single-strand nicks overlap or are separated by less than approximately 15 base-pairs [235,102]. Several ways to reduce the frequency of photocleavage events have been reported in the literature and mostly focus on the removal, or reduction, of oxygen in the buffer [103,105,102,106,236–238].

In addition to photocleavage of DNA, single-molecule fluorescence experiments are susceptible to problems stemming from photobleaching, arising from ROS-mediated degradation of the fluorophore [239]. It is necessary to address this problem in conjunction with photocleavage, since a reduction in photocleavage rate can lead to photobleaching becoming the predominant cause for the disappearance of molecules from the observed region. Fortunately, some techniques for preventing photocleavage also serve to reduce photobleaching rates.

Simple degassing of the buffer can be achieved using either a vacuum chamber or by bubbling nitrogen through the sample [102,105,106]; however, while this is easy to implement, it is unable to prevent photobleaching. A more comprehensive approach is to use the free-radical scavenger, β-mercaptoethanol (βME), which removes the reactive oxygen radicals from solution [102,105,103]. An alternative to βME is an oxygen scavenging system which uses

glucose and glucose oxidase to remove oxygen from the solution; however, this produces hydrogen peroxide, which is reduced to water by the addition of catalase [236–238]. In this study three buffer preparations are compared; untreated buffer, degassed buffer and the glucose oxidase oxygen scavenging system diluted with degassed buffer.

#### 5.4.1.1 Experimental method

Three single-inlet/outlet photoresist channels were prepared as described in Section 5.2.5 with 0.5 µg/ml digoxigenin-BSA (production described in Section 2.4.2), 1 mg/ml acetylated BSA, 2.5 µg/ml whole anti-digoxigenin antibody (polyclonal IgG antibody from sheep; AbD Serotech, now part of Bio-Rad Laboratories, California, USA) and 0.29 nM dig-StuI-biotin T7 DNA (production described in Section 2.3.9). One of the channels was imaged in plain buffer, the second with degassed buffer and the third with the oxygen scavenging system diluted in degassed buffer. For each sample, YOYO-1 was initially added at 10 nM and was increased as necessary during the experiment until the photocleavage rate became sufficiently high that it would not be conducive to use with tethered DNA experiments.

The plain buffer used for the first channel was 1x T7 RNAP transcription buffer (40 mM Tris-HCl, 10 mM NaCl, 6 mM $MgCl_2$). This buffer was also used in the other two samples, albeit with degassing, which was performed for 1 hour in a vacuum. The glucose system oxygen scavenger comprised 960 µl 1x T7 RNAP transcription buffer, 20 µl 1 M DTT, 10 µl 300 mg/ml glucose (Massachusetts), 5 µl 10 mg/ml glucose oxidase (Sigma-Aldrich, St. Louis, Missouri, USA) and 5 µl 2 mg/ml catalase (Sigma-Aldrich, St. Louis, Missouri, USA). To quantify the degree of variability with this technique, a second sample with plain buffer was run on a different day, but using the same preparation and means of data collection as conducted previously.

Each sample was imaged via TIRF microscopy using a 100x magnification oil-coupled objective (Plan-Apochromat; W.D. = 0.17 mm, N.A. = 1.4; Carl Zeiss AG, Jena, Germany) and an intensified CCD camera (IC-300; Photon Technology International, Inc., Birmingham, New Jersey, USA).

#### 5.4.1.2 Approaches for an automated system to measure photocleavage

In order to obtain a statistically significant number of photocleavage time points, hundreds of molecules were measured per sample. Such a labour-intensive analysis would greatly benefit from a degree of automation for the detection of photocleavage events. To achieve this, a custom MATLAB system (function: *measurePhotoCleavage.m*; Accompanying Material) was designed to analyse the mean pixel intensity of user specified regions of interest (ROI) in each video, coinciding with surface-tethered DNA molecules.

Upon initialisation of the photocleavage measurement system, the user is presented with the first frame of the selected input video (pre-decomposed into individual frames using software such as ImageJ or VirtualDub) onto which they highlight surface tethered DNA molecules using the line drawing tool (enabled by default). The system extracts the coordinates of each line and stores them as individual regions of interest for which to measure the mean pixel intensity at each frame.

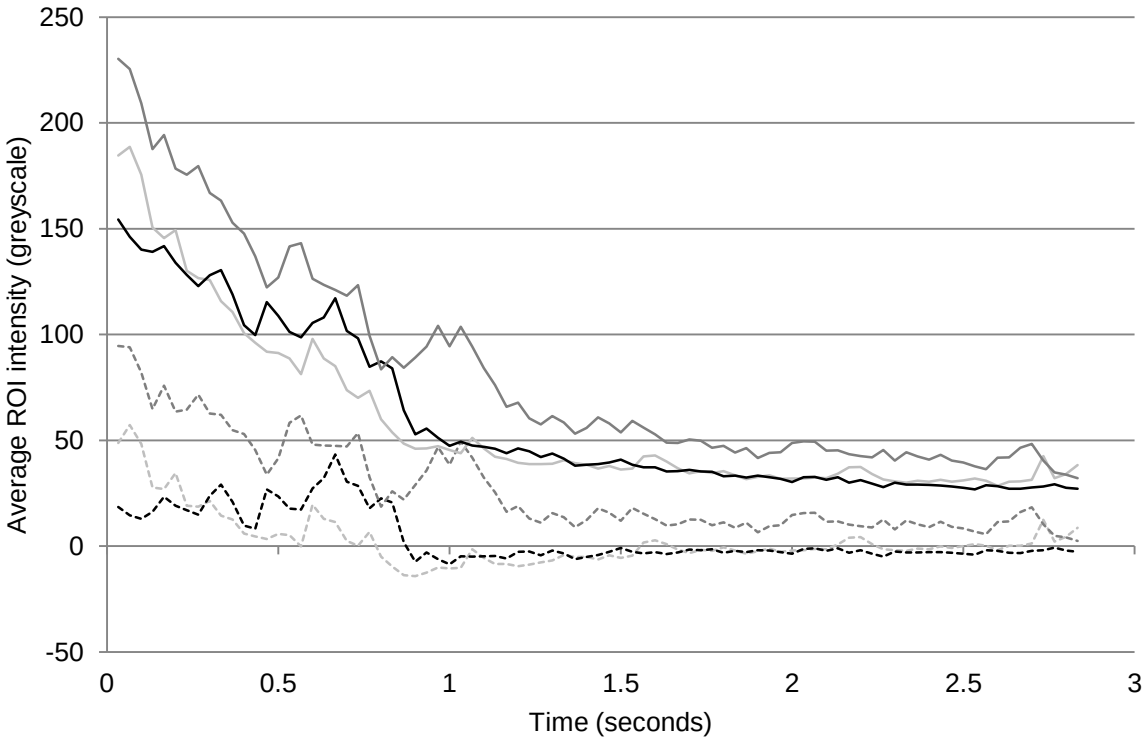


**Figure 5-8 – DNA and YOYO-1 photo-bleaching intensity profiles**
Intensity profiles as a function of time for three user-specified regions of interest. Shown are the raw intensity profiles (solid lines) and intensity profiles with the mean frame intensity subtracted (dashed lines) to account for sample photobleaching. There is a high level of noise in the data even after removal of the photobleaching background, which makes automatic identification of photocleavage events difficult. Example data is taken from the plain buffer sample.

The intention of the automated system is to interpret sudden changes in the mean intensity of each ROI as photocleavage events; however, this proved difficult to implement since the signal-to-noise ratio, especially for more photobleached samples, was very low (solid lines in Figure 5-8). Improvements could be obtained through subtraction of the entire frame mean intensity from the mean ROI intensities (dashed lines in Figure 5-8), but samples with low levels of fluorescence still proved problematic.

Two methods were attempted for identification of photocleavage events. The first was simply identification of the time-point which exhibited the greatest reduction in intensity; however, spontaneous events, such as dissociated DNA molecules passing through the region of interest, led to frequent misidentification via this method. A second, more complicated, approach was to measure the average intensities preceding and following each time point. The difference between the "before" and "after" averages was calculated at each point and a photocleavage event taken to be the time point with the greatest difference between the two values. This method also proved inadequate, since it was unable to take into account multiple photocleavage events for a single tether or cases where a tether did not break.

While it is probably possible to create a reliable automated system for identification of photocleavage events, the time required to implement this was estimated to be far greater than that required to measure photocleavage manually. Future development of this system may implement multiple detection algorithms, with photocleavage events being identified through a consensus approach. There would also be need for filters to identify cases where no photocleavage event occurred or where sudden changes in intensity were due to fluorescent material passing through the ROI.

#### 5.4.1.3 Manual measurement of photocleavage

An immediately more reliable system for identification of photocleavage events was deemed to be through manual identification. To achieve high throughput of data, another custom MATLAB script (function: *numberImageStack.m*; Accompanying Material) was written. With this tool the user is presented with the first frame in the video to be analysed (pre-decomposed into individual frames using software such as ImageJ or VirtualDub) onto which they identify DNA tethers with a mouse right-click. At each click the script

assigns a unique identifier number for the specific molecule. Once all molecules have been identified the numbers are automatically written to each image in the stack and converted to an uncompressed video. Using this video, the user can easily step the video frame by frame to identify photocleavage events whilst keeping track of which molecules have already been measured.

#### 5.4.1.4 Results

Through manual analysis of the data it was possible to measure at least 100 molecules per sample (and on average a much higher number). For instances where a tether had multiple breakage events, the first event was recorded. Histograms of photocleavage time were calculated for each data set and these used to calculate the cumulative percentage of tethers that had broken as a function of time (Figure 5-9). Figure 5-9 clearly shows significant differences between the sample preparations. As observed previously during single-molecule transcription assays, the plain channel underwent fast photocleavage. This can be addressed through simple degassing of the buffer; however, while degassing reduced the photocleavage rate, photobleaching became the dominant problem. As a result, it was not possible to observe individual tethers for a significantly improved time. This problem could be solved slightly by increasing the concentration of YOYO in the buffer, with concentrations of 10 nM, 30 nM and 50 nM tested, although this led to increased photocleavage rates.

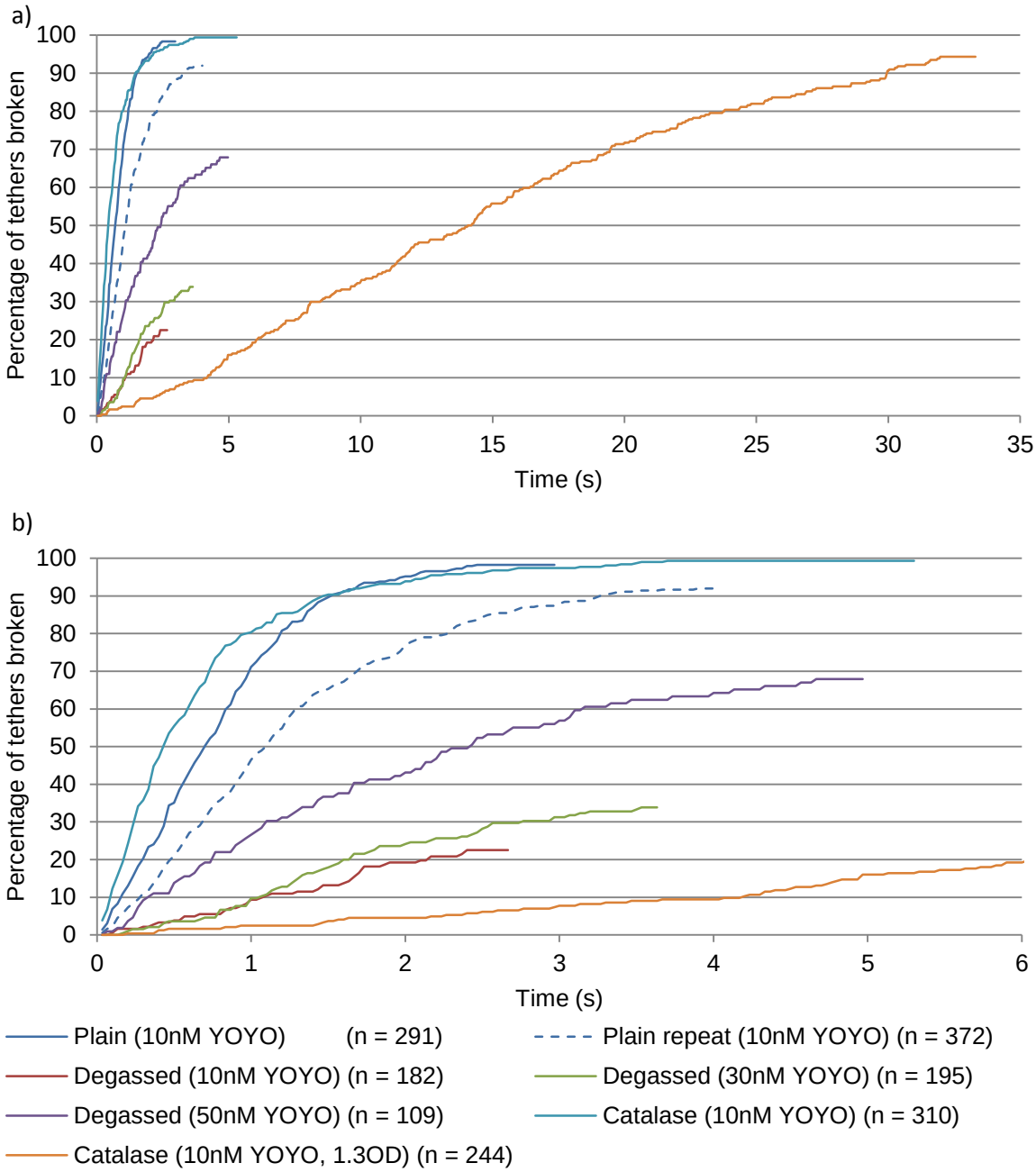


**Figure 5-9 – Cumulative percentage of broken tethers as a function of time**
a) The full range of times measured shows a significant improvement in both photobleaching and photocleavage rates for the glucose system with 1.3 OD neutral density filter. b) The same data truncated at 6 seconds to show the faster breaking samples in more detail. Termination of each curve corresponds with a lack of identifiable DNA tethers, either resulting from photobleaching or photocleavage.

The most significant improvement came from the oxygen scavenging system, which demonstrated a marked reduction in photobleaching rates. However, this came at the cost of resurgence in photocleavage events, presumably because the higher concentrations of active, DNA-bound, YOYO was producing levels of reactive oxygen species, which could not be counteracted by the oxygen scavenger and degassed buffer (Figure 5-10). The adopted solution was to attenuate the incident laser intensity using a 1.3 OD neutral density

filter, which reduced the laser brightness by a factor of approximately 20. With this, photocleavage was brought to an acceptable rate, while photobleaching was also kept sufficiently low so that tethers could be observed for up to 30 seconds, marking an improvement of approximately 10-fold compared to the untreated sample.

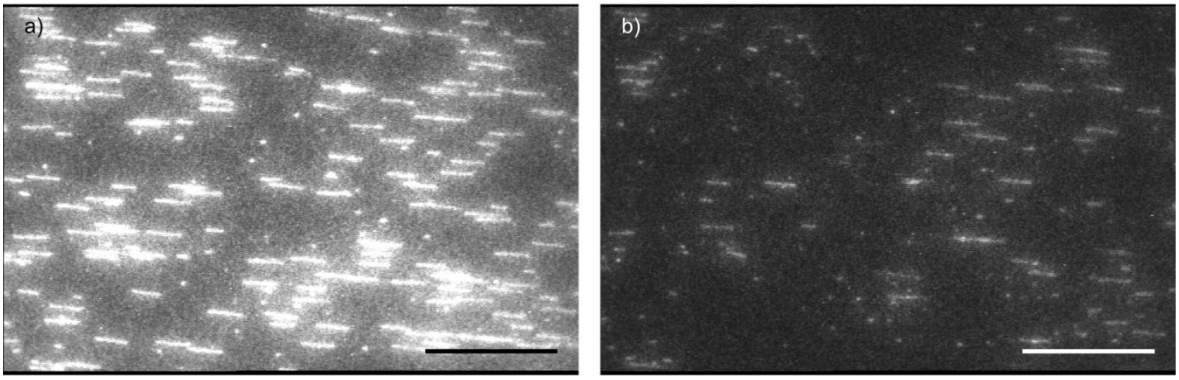


**Figure 5-10 – Photocleavage and photobleaching in catalase-present sample**
Two frames from the acquired video of photocleavage and photobleaching in the sample with glucose oxidase and catalase present. a) Initially the DNA has high fluorescence due to the intercalated YOYO-1. Tether lengths, extended through hydrodynamic flow, are approximately the same; this is indicative of high sample homogeneity. b) Following 1.25 seconds exposure to laser illumination the sample has undergone significant photobleaching. Additionally, large quantities of DNA molecules have undergone photocleavage. Scale bars both represent distances of 20 μm.

Despite the large difference between the various samples shown in Figure 5-9 there is also a considerable disagreement between the two plain channel photocleavage curves. This variability is likely due to laser alignment in the TIRF microscope since the rate of ROS generation is highly dependent on the intensity of the incident laser, as shown by the difference between the glucose sample with and without the 1.3 OD neutral density filter. As the sample is moved on the microscope stage the angle of laser incidence needs to be adjusted, so the point of total internal reflection is directly above the objective; however, with photocleavage occurring almost instantly after illumination for some samples there is no time for this adjustment to occur. This could be solved with the use of objective-coupled TIRF microscope, rather than its prism-coupled counterpart.

### 5.4.2 Evaluating systems for surface passivation

Observation of transcription on torsionally constrained DNA tethers is conducted in sealed chambers. While this condition is necessary for experimental stability, minimising fluid flow around tethers, it introduces potential limitations arising from bulk fluorescence of samples, since removal of unused reagents is not possible. Ultimately, a state of compromise must be reached whereby the concentration of conjugated RNAP-TFS

(TransFluoSpheres; Life Technologies, Carlsbad, California, USA) is sufficiently high to enable transcription, whilst not exceeding levels where bulk fluorescence prevents individual transcription events from being observed. In the case of T7 RNAP, the minimum acceptable concentration is taken as equivalent to the dissociation constant for promoter binding ($K_d$ = 4.8 nM [240]). For experiments where the RNAP-TFS concentration is very close to the $K_d$ for promoter binding, non-specific surface immobilisation can potentially lead to deleterious levels of enzyme depletion from the reaction mixture.

Optimisation of DNA tethering density whilst evaluating passivation systems was performed using TIRF microscopy. For this application, TIRF offers two key benefits: firstly, the high signal to noise ratio permits clear identification of individual fluorescent probes; secondly, the ~100 nm field-depth of the TIRF evanescent field befits a study of surface immobilisation by reducing the influence of bulk fluorescence.

Unless otherwise stated, TransFluoSpheres (TFS; Invitrogen, California, USA) were added to a final concentration of 2.4 nM in 1x T7 RNAP transcription buffer (200 mM Tris-HCl, 30 mM $MgCl_2$, 50 mM NaCl). Microfluidic devices were all of the single-inlet/single-outlet design and fabricated using a single layer of 30 µm high photoresist (Section 5.2). Channels were functionalised using the standard protocol outlined in Section 5.2.5 up to and including incubation with the whole anti-digoxigenin antibody. Following functionalisation, the diluted TFS mixture was incubated in the device for approximately 5 minutes prior to imaging with TIRF microscopy (488 nm excitation) under a continuous flow of 1x T7 RNAP transcription buffer. Video of the sample was obtained with the PTI intensified camera, operated through the custom LabVIEW system (National Instruments Corp., Austin, Texas, USA). All images shown in the following analysis were averaged across 30 frames of raw video data.

Attempts were made to implement an automated system for quantification of TFS immobilisation; however, the experimental variability in camera voltage gain and laser alignment precluded such an analysis. While low immobilisation levels permitted identification of individual TFS, with increasing concentration the overlap in fluorescence profiles and saturation of the detector led to a significant loss in information, thus imposing unacceptable inaccuracy in measurements. Despite this, the large variability in fluorescence observed as a result of functionalisation and passivation modifications

permitted sufficient qualitative analysis of images that significant improvements in immobilisation could be achieved.

#### 5.4.2.1 Non-specific immobilisation resulting from standard surface functionalisation

Initially, the associated influence of non-specific immobilisation of TFS was tested for each component of the standard surface-functionalisation protocol. First, TFS were introduced into an untreated channel to get an estimate on the level of non-specific immobilisation due solely to the microspheres. This sample demonstrates that the TFS do bind to some extent without any channel functionalisation (Figure 5-11a); however, it is not possible to discern the origin of this immobilisation, be it via the streptavidin microsphere-functionalisation or electrostatic interactions. Such high immobilisation is sufficient to severely restrict the ability to perform single-molecule transcription assays.

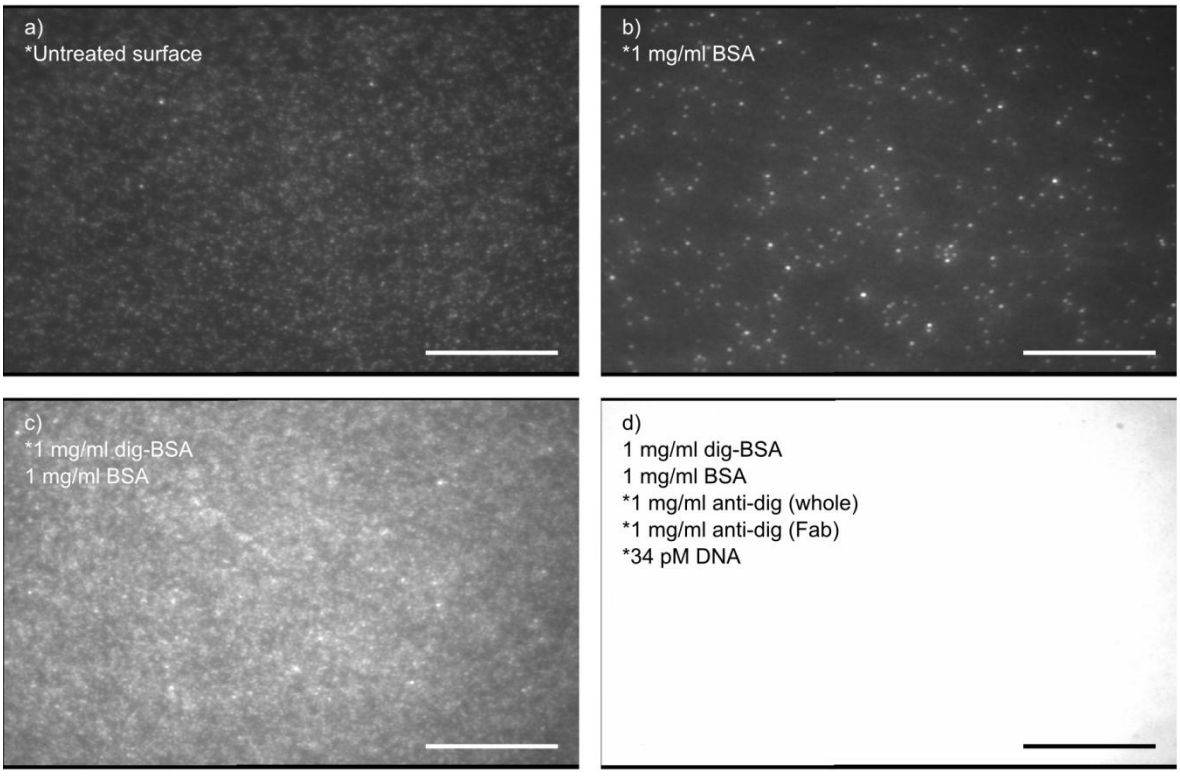


**Figure 5-11 – Effect of key functionalization components of TFS immobilisation**
Representative images for observed non-specific immobilisation of TFS in microfluidic channels functionalised using the standard protocol (Section 2.7.4). In each case, the present functionalisation components are listed, with the key components highlighted with an asterisk. a) An untreated channel gives an indication of background TFS immobilisation levels. b) BSA passivates the channel surface, yielding a significant reduction in non-specific immobilisation. c) Addition of dig-BSA counters the positive effect of the unlabelled BSA, returning immobilisation levels equivalent to the untreated channel. d) For a typical transcription assay functionalisation, the whole anti-digoxigenin antibody undergoes a significant degree of interaction with the TFS. This is evident as near-complete saturation of the camera. Scale bars each represent a 20 μm distance.

A potential upper limit on the ability to reduce TFS immobilisation was provided through passivation with 1 mg/ml acetylated BSA (B8894; Sigma-Aldrich, Missouri, USA). Predictably, a significant improvement in TFS binding was observed in the presence of BSA (Figure 5-11b) to a degree considered acceptable for single-molecule transcription assays. This immobilisation rate would permit easy identification of transcription-mediated RNAP-DNA co-localisation events.

The first surface functionalisation probed was 1 mg/ml dig-BSA (see Section 2.4.2 for preparation), following which the channel was also incubated with unlabelled BSA, in accordance with the standard protocol. Despite the continued presence of unlabelled BSA in the sample there was a clear increase in non-specific adsorption of TFS (Figure 5-11c), with immobilisation returned to similar levels to those seen in the untreated sample (Figure 5-11a).

To simulate a typical transcription assay, a channel was incubated with 1 mg/ml full anti-digoxigenin antibody (polyclonal IgG antibody from sheep; AbD Serotech, now part of Bio-Rad Laboratories, California, USA). In addition to this 1 mg/ml anti-dig Fab fragment (Roche Applied Science, Penzberg, Germany) was incubated for 15 minutes at room temperature to pacify any exposed digoxigenin groups on the surface-immobilised dig-BSA. Finally, 34 pM dig-StuI-biotin T7 DNA (see Section 2.3.9 for preparation) was incubated in the functionalised channel for 30 minutes at room temperature. Clearly there is a significant interaction between the TFS and full antibody (Figure 5-11d), one possible explanation for which is the formation of disulphide linkages.

#### 5.4.2.2 Passivation through incorporation of additional functionalisation components

Following establishment of TFS immobilisation levels in the presence of standard functionalisation components, passivation through addition of further reagents can be probed. The most significant increase in immobilisation was observed upon addition of the whole anti-dig antibody. To investigate if this interaction arises from the formation of disulphide linkages forming between cysteine residues, 1 mM DTT was added to all buffers. Upon addition of DTT there was a notable decrease in fluorescence, indicative that fewer TFS were being immobilised (Figure 5-12a). A ten-fold increase in DTT

concentration for a subsequent sample did not yield an observable improvement in immobilisation, thus implying 1 mM was sufficient to reduce all disulphide linkages.

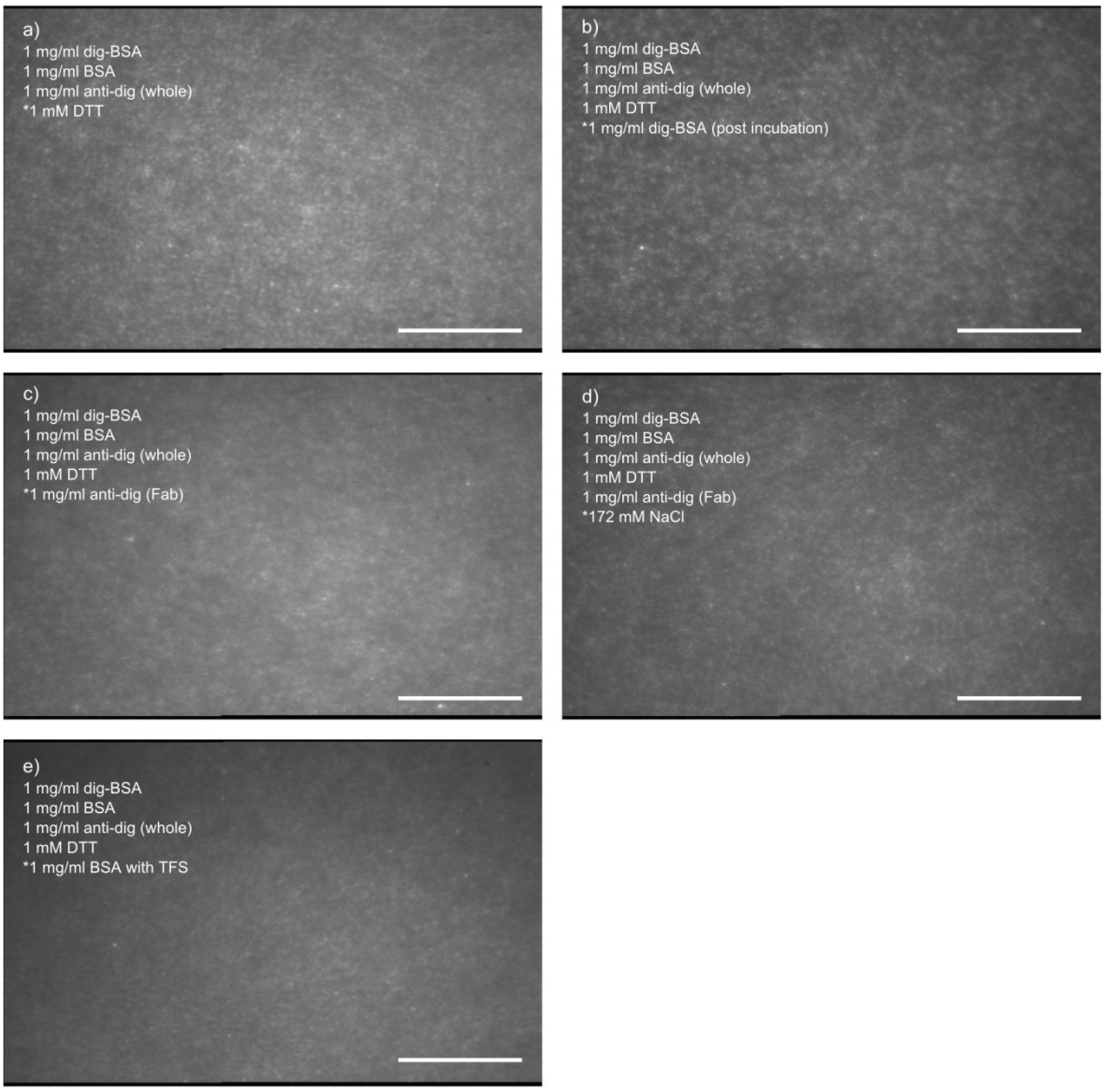


**Figure 5-12 – Effect of surface passivation approaches on immobilisation of TFS**
Representative images for observed non-specific immobilisation of TFS in microfluidic channels functionalised using the standard protocol (Section 2.7.4). In each case, the present functionalisation components are listed, with the key components highlighted with an asterisk. a) There is a significant reduction in TFS immobilisation upon addition of 1 mM DTT to all buffers (compared to Figure 5-11d); DTT has been added to all subsequently prepared samples. b) Incubation of channels with 1 mg/ml dig-BSA to block unbound Fab regions on the anti-dig antibody did not appear to yield an improvement in immobilisation. c) Addition of 1 mg/ml anti-dig Fab fragment to passivate unbound dig-BSA on the channel surface also yielded no observable improvement. d) Buffer exchange (10 mM NaCl to 172 mM NaCl) of a sample with pre-immobilised TFS did not result in TFS dissociation; indicating the interaction does not have an electrostatic origin. e) Pre-incubation of TFS with BSA to passivate the exposed polystyrene surface had no observable effect on TFS immobilisation, thus indicating the interaction is protein-protein mediated or that BSA adsorbs poorly to polystyrene. Scale bars each represent a 20 μm distance.

Interestingly, while multiple surface-accessible cysteine residues are present at the interface between Fc and Fab regions of IgG (PDB: 1IGT), they are generally sequestered

in a structural role. Furthermore, the sequence of streptavidin is devoid of cysteine, thus hinting at a different mechanism for the interaction between TFS and anti-dig. Owing to the positive impact of DTT on surface passivation this reagent was present in all subsequently-prepared samples.

An alternative source for the observed immobilisation is the unoccupied antibody Fab region; a hypothesis addressed through functionalisation with 1 mg/ml dig-BSA prior to addition of the TFS. This is analogous to an approach used by Finkelstein *et al.*, who used free biotin to passivate a streptavidin-functionalised surface [241]. Addition of dig-BSA had no apparent effect on TFS immobilisation (Figure 5-12b); however, any positive effect on immobilisation may be masked by additional interaction with the attached BSA group.

In order to address the potential interaction of TFS with exposed dig-BSA (that not bound to antibody), 1 mg/ml anti-dig Fab fragment was incubated in the channel prior to addition of TFS. Hypothetically, this approach would facilitate blocking of binding sites that may be inaccessible to the full antibody due to steric clashing. Nonetheless, this addition provided no discernible improvement in reduction of TFS immobilisation (Figure 5-12c). One possible conclusion from this is that the saturation of all surface-immobilised dig-BSA occurred with the full antibody. With this sample a second hypothesis was probed: that interaction arises from an electrostatic origin. The standard final monovalent salt concentration in the transcription mixture is usually 10 mM, which is significantly less than the tethering buffer (TetBu+; 172 mM NaCl). Incubation of the channel with pre-immobilised TFS yielded no obvious improvement, thus indicating the electrostatic effect to be non-present or negligible.

Clarification whether TFS interaction with the channel surface is mediated either via the streptavidin functionalisation or polystyrene microsphere material is accomplished using a method proposed by Dr. Mark Wallace (Department of Chemistry, University of Oxford). Addition of BSA to the TFS mixture should allow passivation of the exposed (non-streptavidin functionalised) bead surface. This sample was prepared following the standard protocol, but using TFS pre-incubated with 1 mg/ml acetylated BSA. There appears to be no improvement in reducing TFS binding from incubation of TFS with BSA, which indicates any exposed polystyrene is not responsible for the non-specific

immobilisation. Instead, this observation implies the interaction is protein-protein mediated.

#### 5.4.2.3 Reducing functionalisation concentration

Instead of pursuing surface passivation through addition of further reagents, it is possible to achieve the same goal via reduction of surface functionalisation density. This represents another compromise in the experimental configuration, since a decrease in channel functionalisation will result in a corresponding decrease in ability to generate DNA tethers.

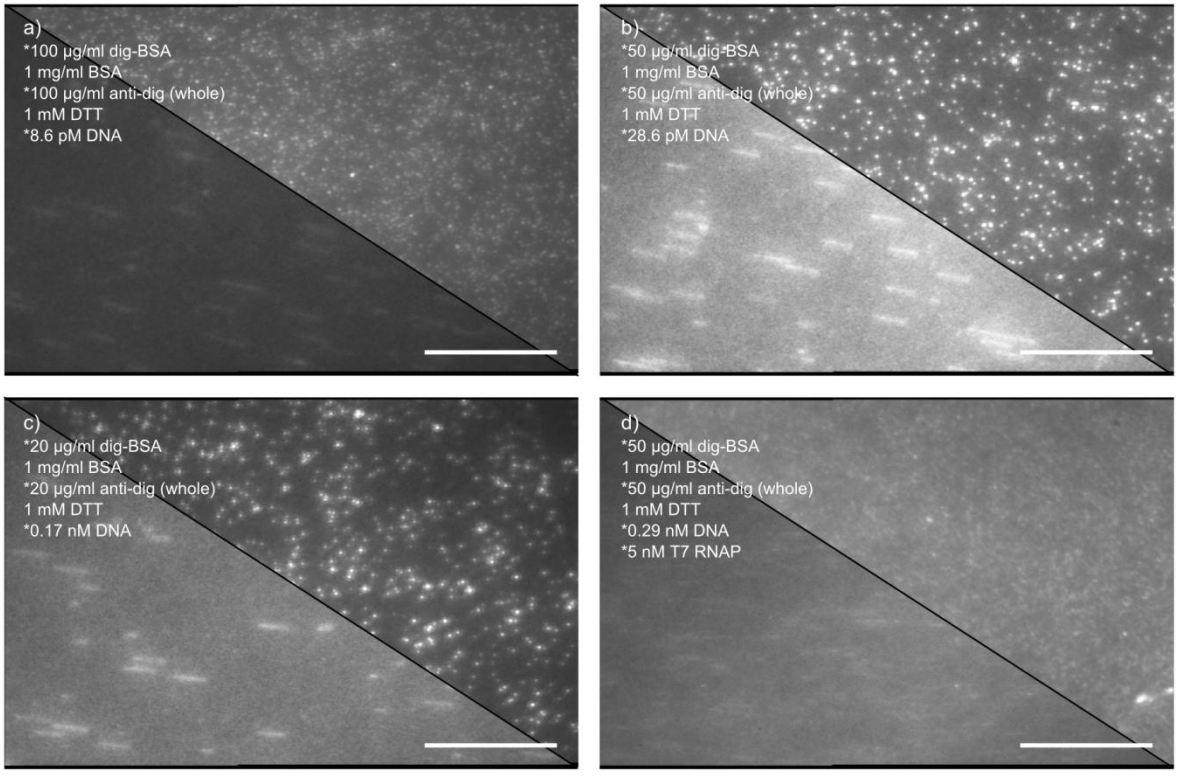


**Figure 5-13 – Effect of reduced functionalisation densities on immobilisation of TFS**
Split images showing the red channel with TFS (top right) and the green channel with DNA (bottom left) for the same image region. In each case, the present functionalisation components are listed, with the key components highlighted with an asterisk. Progressive improvements in immobilisation were observed for the three dig-BSA and anti-dig antibody concentrations investigated: 100 µg/ml (a), 50 µg/ml (b) and 20 µg/ml (c). Despite a 6-fold higher DNA concentration for the 20 µg/ml sample, the reduced functionalisation density yielded undesirably low tethering rates. d) Introduction of biotinylated wild-type T7 RNAP into the assay resulted in a significant increase in TFS immobilisation. Mediated by the RNAP, this increase is incompatible with reliable single-molecule transcription assays. Scale bars each represent a 20 µm distance.

Three concentrations were trialled, with dig-BSA and the full anti-dig antibody held at equal weight per volume concentrations, corresponding to a 2.2-fold molar excess of dig-BSA; concentrations were 100 µg/ml (Figure 5-13a), 50 µg/ml (Figure 5-13b) and 20 µg/ml (Figure 5-13c). For the first two conditions DNA was used at a final molecular

concentration of 28.6 pM, but increased to 0.17 nM for the third in order to overcome the reduced functionalisation. These modifications to the standard protocol yielded a clear improvement in TFS immobilisation, with individual microspheres being identifiable across all concentration ranges (Figure 5-13). These results further hint towards a protein-mediated origin for non-specific immobilisation.

Despite concentrations of 20 μg/ml exhibiting immobilisation approaching the theoretical minimum identified in Figure 5-11b for functionalisation with BSA only, the reduction in tethering rate was deemed too severe and 50 μg/ml channel functionalisation was identified as optimal. For this condition falsely occurring colocalisation of DNA and RNAP (identified by TFS) would be undesirably high; however, this can be relatively easily isolated from legitimate transcription events through statistical analysis and omission of TFS not displaying linear motion along tethers.

With the semi-optimised conditions identified in Figure 5-13b the ability to image single-molecule transcription was probed. Following 50 μg/ml surface functionalisation using the standard protocol, the transcription assay was incubated in the channel for 10 minutes at room temperature. DNA was incubated in the channel at a final concentration of 0.29 nM to further probe improvements in tethering that could be attained. The transcription assay was comprised of 3.7μl 340 nm biotinylated wild-type T7 RNAP (Section 2.4.1) and 5.2 μl 240 nM TFS incubated together on ice for 30 minutes prior to addition of 50 μl 5x T7 RNAP transcription buffer (Section 2.1), 25 μl 100 mM DTT (Melford, Ipswich, UK), 100 μl 2.5 mM rNTPs (2.5 mM per species) and 66.1 ultra-pure water (18.2 MΩ•cm; PureLab Ultra; Elga Process Water, Marlow, UK).

Inclusion of RNAP yielded a drastic increase in TFS immobilisation, likely due to direct interaction of the TFS-labelled enzyme with the channel surface (Figure 5-13d). Although such a result is indicative of successful RNAP-TFS conjugation, the high background fluorescence is not conducive to realisation of reliable single-molecule transcription assays. Despite this, increased DNA concentration was highlighted as a source of improved tethering density and thus, a potential route for further reduction in TFS surface-immobilisation (Section 5.4.2.4).

#### 5.4.2.4 The effect of RNAP on non-specific immobilisation of TFS

The concentrations used for functionalisation in Section 5.4.2.3 do not offer optimal tethering, since typical experiments see DNA added to a final concentration of ~30 pM. Although this is born out of a necessity to conserve valuable DNA stocks, it represents concentrations 140-fold lower than the average dissociation constant for similar interactions ($K_d$ = 1 nM for digoxin-antidigoxigenin [242], 11.5 nM for digoxin-antidigoxin [243] and 0.1 nM for digoxigenin-anti digoxin [244]). As such, the ability to form tethers on the channel surface is greatly reduced. Significant improvements can potentially be achieved through increasing the final DNA concentration to 0.3 nM. With this, it is possible to reduce the surface functionalisation density, whilst avoiding any reduction in tether formation rates.

All samples were prepared using the standard surface functionalisation protocol with 50 µg/ml dig-BSA (Section 2.4.2), 1 mg/ml acetylated BSA for passivation and 50µg/ml anti-dig full antibody (polyclonal IgG antibody from sheep; AbD Serotech, now part of Bio-Rad Laboratories, California, USA). Each component contained 1 mM DTT to reduce disulphide linkages as shown to be beneficial in Section 5.4.2.2. In a reversal of the approach described in Sections 5.4.2.1 to 5.4.2.3, a 5-fold weight per volume excess of antibody to dig-BSA (dig-BSA concentrations of 10 µg/ml, 2 µg/ml, 1 µg/ml and 200 ng/ml) was used. This corresponds to a 2.2-fold excess of antibody, thus favouring saturation of dig-BSA.

There is a clear decrease in both TFS immobilisation and DNA tether formation rates as dig-BSA concentration is reduced from 10 µg/ml to 200 ng/ml (Figure 5-14). These represent an overall dilution of between 100 and 5000-fold from the standard protocol initially used. TFS immobilisation reaches acceptable levels for dig-BSA concentrations less than 1 µg/ml; yielding a low probability of chance colocalisation between DNA and TFS. These modifications to the surface functionalisation protocol should permit observation of transcription events on the single-molecule level, whilst maintaining RNAP concentrations above the $K_d$ for promoter binding.

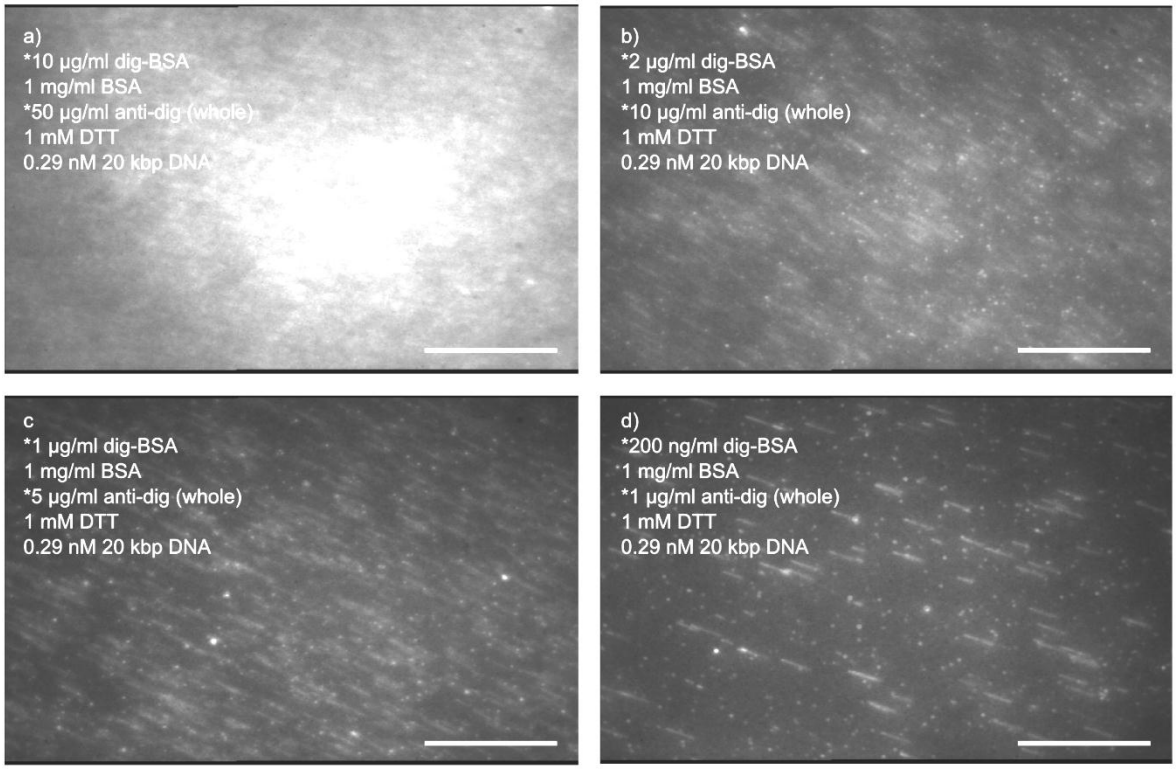


**Figure 5-14 – Effect of reduced functionalization density on immobilisation of TFS**
Improvements in non-specific TFS immobilisation in the presence of 5 nM biotinylated wild-type T7 RNAP. Each sample utilises a 5-fold weight per volume excess of antibody over dig-BSA to assist saturation of dig-BSA. In each case, the present functionalisation components are listed, with the key components highlighted with an asterisk. Concentrations of dig-BSA used are 10 µg/ml (a), 2 µg/ml (b), 1 µg/ml (c) and 200 ng/ml (d). A clear decrease in both TFS immobilisation and DNA tether formation is observed with less dense surface functionalisation. At 200 ng/ml the chance instances of DNA and RNAP colocalisation are deemed to be acceptable. Scale bars each represent a 20 µm distance.

# Diffusion simulations of the colE9-BtuB complex

Chapter 6

## 6.1 Background on colicin E9

In a climate of increasing resistance from bacterial strains, new and novel antibiotic approaches are being sought. The development of these approaches is informed by the study of naturally-occurring bacteriocins; enzymes produced by bacteria as a weapon for use in inter-strain competition [245,246]. The specific role of bacteriocins is to kill or inhibit growth of competing bacterial strains in order to gain local dominance and capitalise on limited-resources present; as a result, bacteriocins are often only produced in response to SOS signals [246].

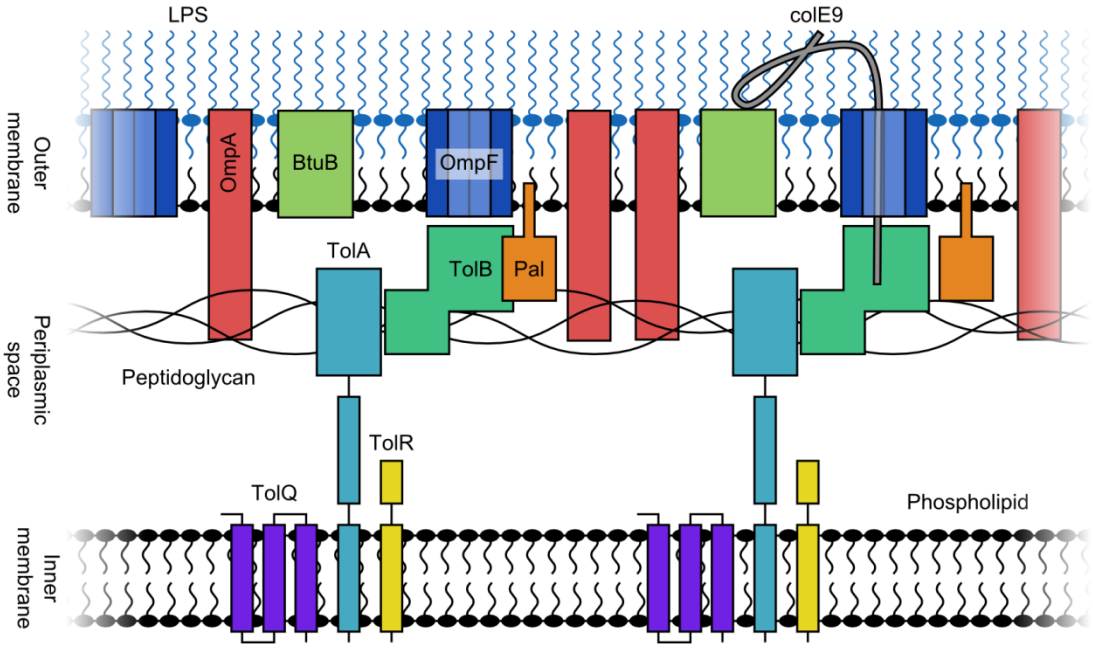


**Figure 6-1 – Key components of the colicin import pathway**
Schematic diagram of the *E. coli* cell wall, highlighting the key components required for colicin import into the cell; the vitamin $B_{12}$ receptor, BtuB; nutrient import channel, OmpF and the structural Tol complex. In the absence of colE9, the lipoprotein, Pal interacts with TolB. Upon binding of the colE9 R-domain to BtuB, the unstructured region of the N-terminal domain feeds through OmpF, where it interacts with TolB, subsequently disrupting the TolB-Pal interaction. Exact details of the colicin import mechanism and how the Tol system is parasitised for this purpose has yet to be fully understood. OmpA is a major outer membrane protein, which interacts with the peptidoglycan layer. Simulations described in Section 6.4 probe a possible picket fence restriction to diffusion arising from the stationary OmpA.

Of particular research interest are the *E. coli*-specific bacteriocins, known as colicins, due mainly to the wealth of existing knowledge about this organism. Colicins are divided into two main groups depending on the cell entry mechanism utilised; group A colicins (sub-groups A, E and N [247]) using the Tol system and group B colicins (sub-groups B, D, I and M [247]) using the Ton system [248]. The evolved purpose of the Tol-Pal system is believed to play a structural role (Figure 6-1), aiding integrity of the *E. coli* outer membrane [248,247], while the Ton system uses force transduction to enable interactions with the outer

membrane [248]. Further classification into the aforementioned sub-groups is determined in a receptor-specific manner; in the case of the group E colicins this receptor is the vitamin $B_{12}$ binding site, BtuB [249,250].

Cell killing activity is achieved through a range of mechanisms, depending on the type of bacteriocin; common methods encompass pore-formation [251–253] and nuclease activity [254–256]. Generally, protection for the colicin-producing cell strain is achieved through simultaneous expression of a corresponding immunity protein, which binds very tightly ($K_d = 9.3 \times 10^{-17}$ M for the colE9-Im9 interaction [257]) to the colicin whilst present in the parent cell [258–260].

The 61 kDa colE9 colicin [261] is formed from three distinct regions: two alpha helices comprising the receptor R-domain, responsible for BtuB binding (Figure 6-1); a structured C-terminal (CT) domain exhibiting endonuclease activity; and a 380 residue N-terminal (NT) domain. Of this NT domain, the most extreme 300 residues form an unstructured region necessary for membrane translocation and are thus accordingly referred to as the T-domain [246].

Following outer membrane binding, the BtuB-colE9 complex undergoes two-dimensional diffusion until encountering the trimeric porin, OmpF. This behaviour is described by the fluid mosaic model, which states that cell membranes behave as two-dimensional fluids and thus, embedded proteins are free to undergo lateral diffusion [262,263]. Upon localisation with OmpF, the colicin is imported into the cell interior in a mechanism mediated by the T-domain. While this process has yet to be fully described, it is known to involve interaction with the Tol complex; in particular, displacing TolB from its interaction with Pal [264]. In a mechanism still not entirely elucidated, colE9 translocates across the cytoplasmic membrane and in doing so dissociates from the bound immunity protein [265,248]. Once through the cytoplasmic membrane, colE9 is able to exert its intrinsic DNase activity to achieve cell killing.

## 6.2 Summary of experimental diffusion observations

Experimental observation of diffusion by a fluorescently-labelled colE3 –BtuB [266] and colE9-BtuB (Copeland, N.A., Toth, C., Seger, U., Cross, S.J., Pullen, J.R., Quinn, D.M.,

Garrod, T.J., Kleanthous, C. and Baumann, C.G., unpublished data) complex on the outer membrane of JM83 *E. coli* cells have demonstrated restricted behaviour. Restriction occurs when diffusing particles are confined within a specific region, thus limiting the maximum distance they can travel relative to their origin of travel. This quantity is typically described by the mean square displacement (MSD), which is a measure of the average straight-line distance a particle has travelled relative to its origin of movement at any given time. When considering simple two-dimensional Brownian diffusion, three distinct scenarios can arise: free diffusion (black line; Figure 6-2), directed diffusion (blue line; Figure 6-2) and restricted diffusion (red line; Figure 6-2) [170]. Free diffusion occurs in the absence of any external influence, directed diffusion arises when particle motion is forced in a particular direction and restricted diffusion occurs when particles are unable to move beyond an imposed boundary [170].

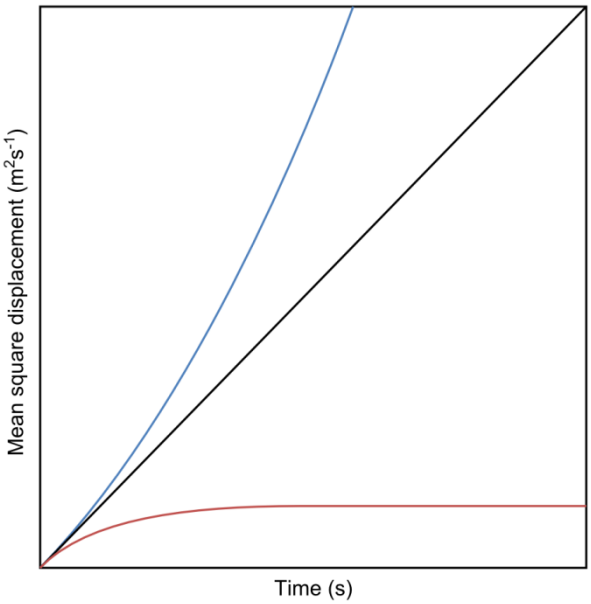


**Figure 6-2 – Basic model of diffusion scenarios**
Mean square displacement (MSD) from two-dimensional Brownian diffusion can adopt three basic forms depending on external influences on particle motion. The most basic scenario, free diffusion (black line), arises when there are no external influences on the diffusive behaviour, thus the MSD curve conforms to a straight line The diffusion coefficient can be extracted from the gradient of this straight line, where the gradient is $4D_{2D}$. Direct diffusion (blue line) arises in cases of an external influence forcing the particle in a particular direction and as such, the rate of displacement from the origin increases with time. Finally, restricted diffusion occurs when particles are prevented from diffusing beyond a specific boundary. In this case, the maximum displacement from the origin is limited by the size of the restricting compartment. Image adapted from [170].

For the purpose of experimentally-measuring diffusion of the BtuB-colE9 complex, an engineered version of colE9 was used. This mutant has engineered thiol groups at both extents of the R-domain (Y324C and L447C), which form a "top-lock", thus permitting OmpF binding of this domain, but preventing complete protein translocation. An

additional thiol was engineered at K469C to which an Alexa-488 fluorophore was attached using maleimide chemistry. Diffusion was observed on the outer membrane of JM83 *E. coli* cells using an inverted microscope (IM35; Carl Zeiss AG, Jena, Germany) in a prism-coupled TIRF configuration using a 488 nm laser (Sapphire 488-30 CDRH; Coherent, Inc., Santa Clara, California, USA), 100x oil-immersion objective lens (Plan-Apochromat; W.D. = 0.17 mm, N.A. = 1.4; Carl Zeiss AG, Jena, Germany**)** and intensified CCD camera (IC-300; Photon Technology International, Inc., Birmingham, New Jersey, USA). Data was collected using a custom LabVIEW (National Instruments Corp., Austin, Texas, USA) script written by Urban Seger (University of York) at 30 fps. This work was conducted by Nikki Copeland, Csaba Toth and Diana Quinn.

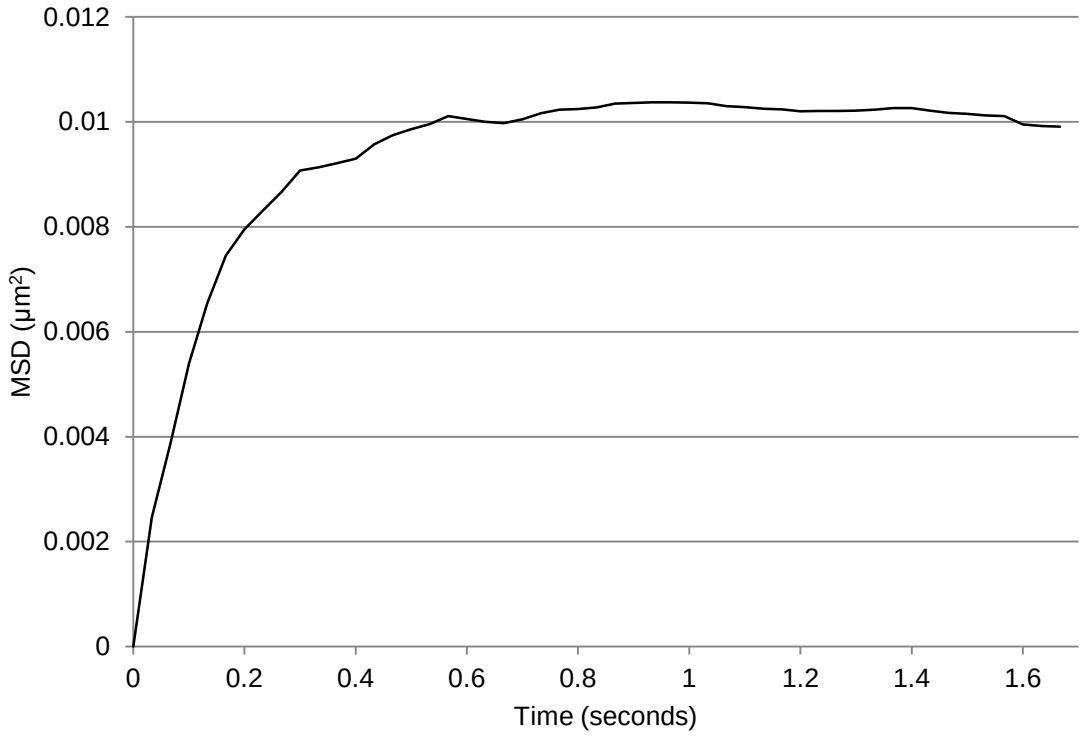


**Figure 6-3 – Experimentally-observed MSD for colE9-BtuB on JM83 *E. coli* cells**
The observed diffusion curve displays clear evidence of restricted diffusion, with an MSD plateau reached within 0.6 seconds. There is no elucidated physical origin for this diffusion; however the work described in this section focuses on determining the nature of the restriction. Of particular focus are the effects of data acquisition (transformation of three-dimensional diffusion trajectories to an acquired two-dimensional image), the rate of diffusion and the size of the restricting compartments. Data is averaged over 95 diffusing particles for the full experiment duration.

There is clear evidence of restriction to colE9-BtuB diffusion in the measured MSD data (Figure 6-3); however, the origin of this effect is unknown. The experiments described in this section probe the diffusive nature of colE9-BtuB through comparison to simulated trajectories. While this approach does not necessarily highlight a particular origin for the

observed effect, it can yield information of diffusion and restriction characteristics, such as rate of movement and the size of any restricting compartments.

## 6.3 The Monte Carlo method for modelling diffusion

The Monte Carlo method is characterised by repetition of an operation numerous times to obtain an averaged outcome [267]. In the case of a diffusion simulation, this involves treating the trajectory of each particle as a series of discrete steps (*dl*), taking place over a short period (*dt*) [170,268,269,266]. This motion can be applied to unrestricted planar diffusion through inclusion of an angular term ($\theta$), randomly drawn from the standard normal distribution (over the range 0 to $2\pi$), where the two perpendicular vectors are defined by Equation 6-1 and Equation 6-2.

$$dx = \sqrt{4Ddt}\cos(\theta)$$

**Equation 6-1 – Constant diffusion step for Monte Carlo simulations in the x-axis**
Step size in the x-axis (*dx*) is a function of the diffusion coefficient (*D*), the duration of the step (*dt*) and an angle ($\theta$) randomly selected from the standard normal distribution.

$$dy = \sqrt{4Ddt}\sin(\theta)$$

**Equation 6-2 – Constant diffusion step for Monte Carlo simulations in the y-axis**
Similar to the x-axis step, the y-axis step (*dy*) is a function of the particle diffusion coefficient (*D*), step duration (*dt*) and a randomly selected angle ($\theta$). To maintain a constant step length, the angle is the same for the x-axis calculation.

Simulations of outer membrane protein diffusion using the Monte Carlo approach have been reported many times in the literature [170,270–272]. Of particular note is the work of Deich *et al.*, who simulated diffusion of several thousand (2,000 to 10,000) copies of the membrane-bound histidine kinase, PleC on a curved surface representative of a Caulobacter cell [269]. This idealised cell surface comprised a cylinder ($L_{cell}$ = 3 μm; $R_{cell}$ = 0.5 μm), with hemispherical capped ends ($R_{cap} = R_{cell}$). Three-dimensional coordinates were subsequently projected onto a two-dimensional plane to simulate experimental observation in a standard wide-field microscope [269].

While the method of Deich *et al.* has been implemented elsewhere [268,273], of significant implication to the present work is the report by Spector *et al.*, who were also probing the diffusive behaviour of the colE3-BtuB complex on the surface of *E. coli* ($L_{cell}$ = 1 μm, $R_{cell}$ = 0.5 μm) [266]. Their approach utilised a very short time step of 1 μs to accurately

model particle motion, but with only every 25,000$^{th}$ frame extracted to simulate a camera frame rate of 40 fps [266].

All MATLAB code used for the described simulations is included in the Accompanying Material.

### 6.3.1 Planar diffusion

In accordance with theory, the mean square displacement (MSD) gradient is 4D (Figure 6-4), with an intercept at an MSD of zero. Planar diffusion was evaluated for 5000 particles, with diffusion coefficient (D) of 0.05 $\mu m^2 s^{-1}$, simulated for a total time (*T*) of 1.7 seconds at intervals (*dt*) of 1 µs [266] and then fit with a straight line in Microsoft Excel. Short interval times produce more physically-relevant particle trajectories; however, only every 33,333$^{th}$ data point was recorded. This corresponds to a frame rate of 30 fps, which is equivalent to the experimentally collected data. The same treatment was applied to all simulated data reported.

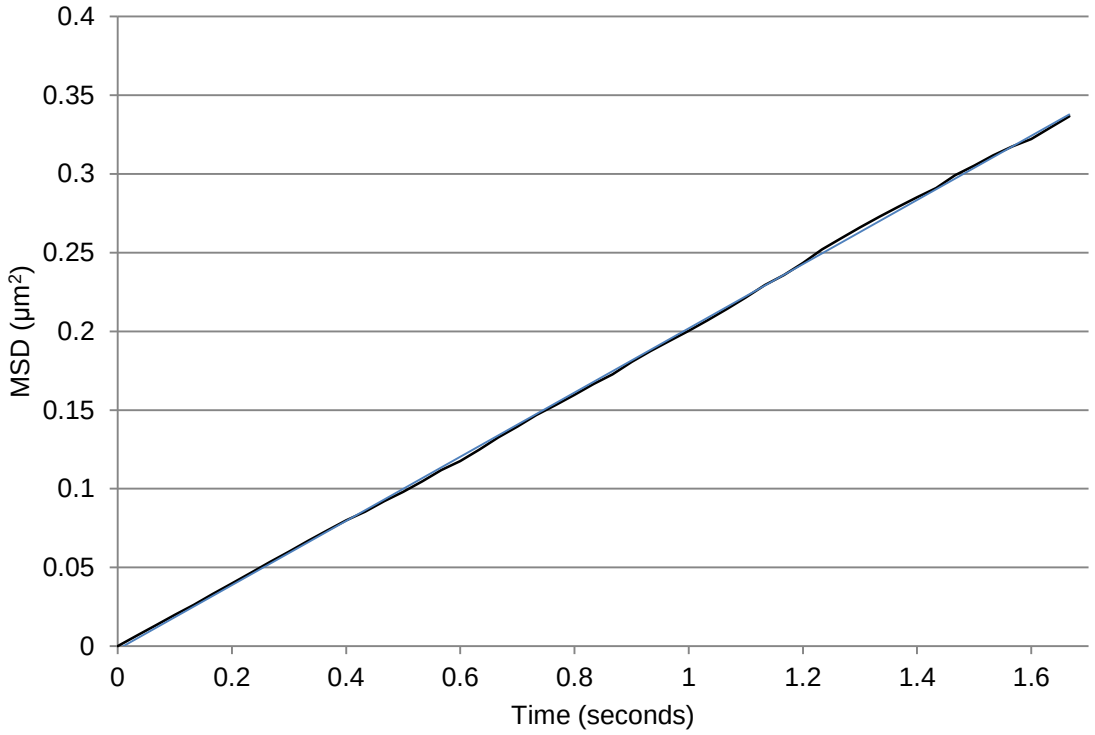


**Figure 6-4 – Plot of mean square displacement (MSD) for unrestricted planar diffusion**
Mean square displacement (MSD) of 5000 diffusing particles (black line), with diffusion coefficient (*D*) of 0.05 $\mu m^2 s^{-1}$, simulated over a total time (*T*) of 1.7 s at step intervals (*dt*) of 1 µs. The data can be accurately fit using a straight line (blue line) with an intercept of 0.001 $\mu m^2$ and gradient of 2.03 $\mu m^2 s^{-1}$; equal to 4D, as predicted by theory.

All simulations described are based upon planar diffusion, onto which various operations are imposed in order to model effects such as cell membrane curvature (Section 6.3.2), random orientation of the cell (Section 6.3.4) and diffusion restriction (Sections 6.3.5 and 6.3.6). The simulation was written in MATLAB and run from the parent function, *monteCarloDiffusion.m*.

### 6.3.2 Membrane curvature

When observed with the TIRF microscope, the three-dimensional particle position is projected onto a two-dimensional plane (i.e. the camera plane). The resulting loss of information in a direction away from the long axis of the bacterial cell has the potential to influence the measured MSD and accordingly may be responsible for the observed diffusion restriction. To probe the effect of membrane curvature, the planar diffusion coordinates were transformed onto a basic representation of an *E. coli* cell, modelled as a cylinder (radius, $R_{cell}$, and length, $L_{cell}$) with hemispherical capped ends. Due to the non-physical nature of mapping a two-dimensional plane to a spherical surface, the probability of a particle residing at any given location increased towards the extremes of the capped ends (Figure 6-5); however, as a consequence of the exponentially decaying TIRF microscopy field included in Section 6.3.3, diffusion in the region where the end-effect was most significant was never evaluated.

Curvature is enabled in the simulation through specification of a non-zero radius of cell surface curvature ($R_{cell}$) and length ($L_{cell}$). This allows the function *cellCurvature.m* to be called during each time-step iteration and convert the planar coordinates to three dimensions. To simulate the random binding of colE9 to the membrane receptor, the diffusion start locations are randomly distributed across the cell surface using the function *randomStart.m*, which draws locations from the standard uniform distribution.

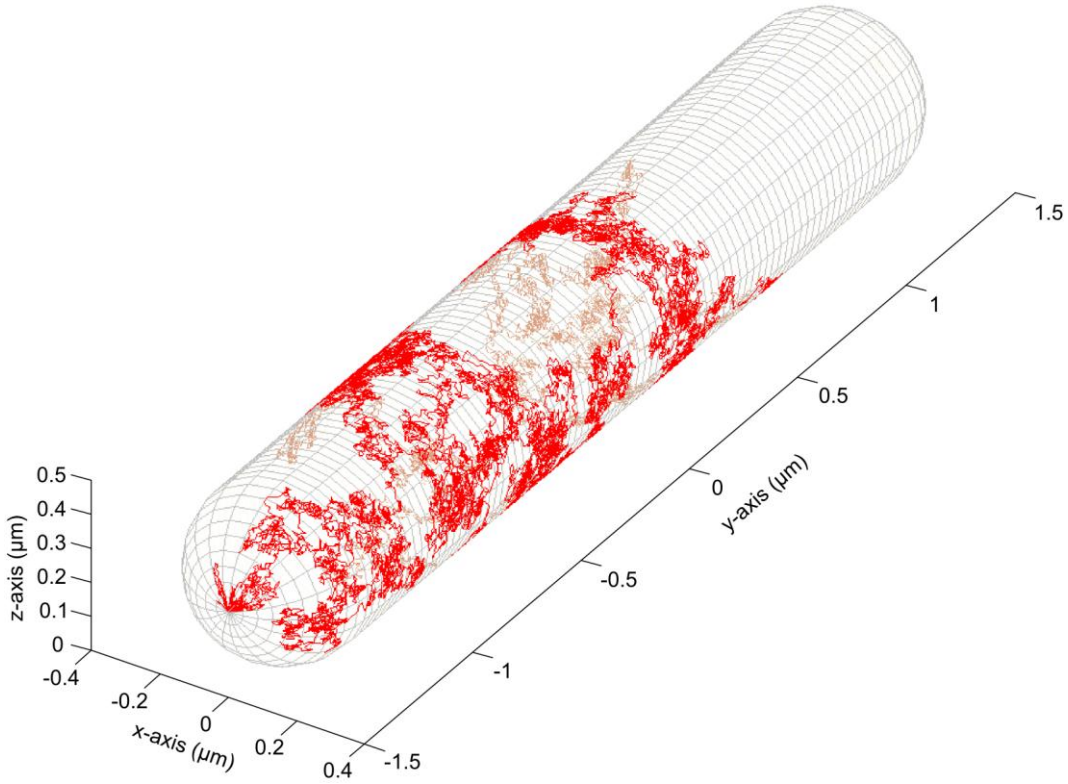


**Figure 6-5 – Transformation of planar coordinates onto the curved bacterial surface**
A single planar diffusion trajectory modelled using the Monte Carlo method ($D$ = 0.05 µm$^2$s$^{-1}$, $T$ = 20 s, $dt$ = 1 ms) has been transformed onto a curved surface representative of a typical *E. coli* cell. The cell surface (grey mesh) is idealised as a cylinder ($R_{cell}$ = 0.25 µm and $L_{cell}$ = 3 µm) with hemispherical capped ends ($R_{cell}$ = 0.25 µm). Mapping of Cartesian trajectories to a spherical polar coordinate system results in the non-uniformity observed at cell ends.

Comparison of MSD values for planar diffusion and equivalent two-dimensional diffusion projected from surface-transformed data is shown in Figure 6-6. This data shows two equivalent simulations featuring 5000 particles with diffusion coefficients ($D$) of 0.05 µm$^2$s$^{-1}$, simulated for a total time ($T$) of 1.7 seconds at intervals ($dt$) of 1 µs [266]. One data set is shown for planar diffusion (black line, Figure 6-6; data from Section 6.3.1) and the other mapped onto a cell with parameters characteristic of typical *E. coli* cells (blue line, Figure 6-6); these were radius of curvature of 0.25 µm and length of 3 µm.

Transformation of planar diffusion trajectories onto the curved bacterial surface leads to a significant reduction in the rate of increase in MSD, as shown in Figure 6-6. This arises from an inability to resolve particle movement perpendicular to the observable plane (z-axis when adopting the coordinate system from Figure 6-5). As such, the most marked impact on measured MSD occurs at the edges of the bacteria, where all motion in the xz-plane is along the z-axis.

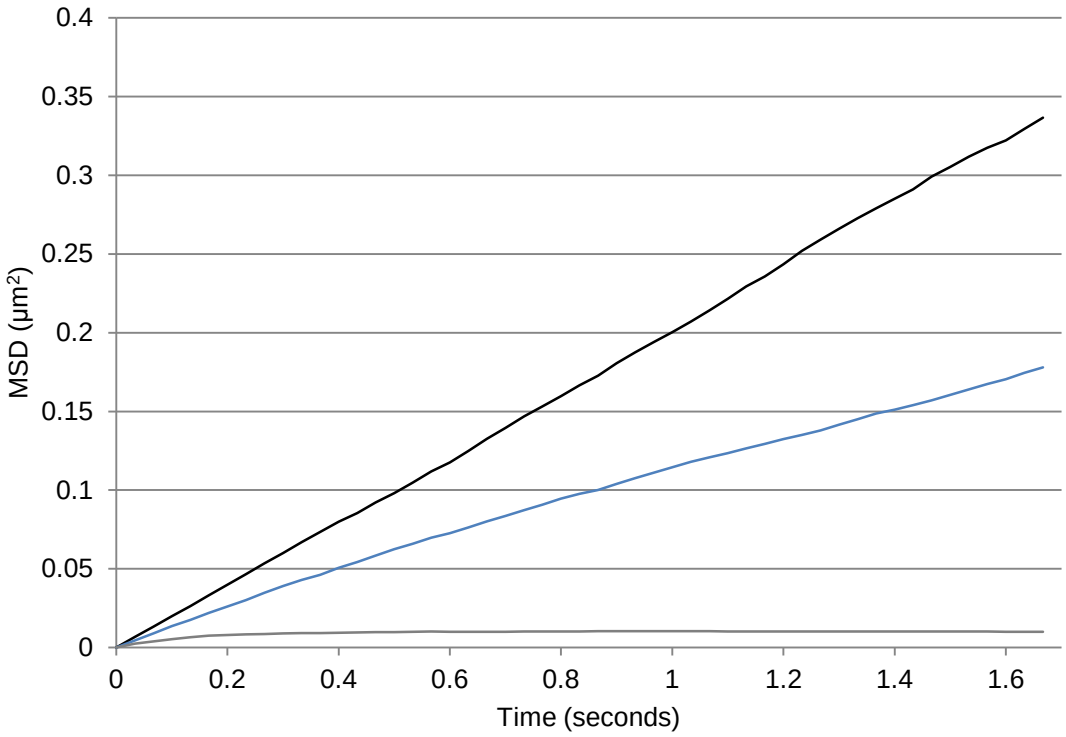


**Figure 6-6 – Comparison of MSD for diffusion on flat and curved surfaces**
Simulated diffusion for two equivalent sets of 5000 particles ($D$ = 0.05 μm$^2$s$^{-1}$, $T$ = 1.7 s, $dt$ = 1 μs), with one set preserved as planar diffusion (black line) and the other transformed onto a surface characteristic of an *E. coli* cell ($R_{cell}$ = 0.25 μm, $L_{cell}$ = 3 μm; blue line). For reference, the experimentally-obtained data is also shown (grey line). The slight deviation observed for the surface-transformed data is significantly less pronounced than that evident in the experimentally-obtained data. This indicates factors other than cell curvature are responsible for the MSD plateau.

While the deviation of the surface-transformed data tends towards a reduction in MSD gradient with increasing time, as is evident with the experimentally-observed data, the magnitude of this effect is much less pronounced. Despite this, membrane curvature may contribute to the observed MSD plateau; therefore, all simulations performed henceforth were transformed in this manner.

### 6.3.3 TIRF microscopy evanescent field depth

The experimentally-acquired data was obtained using TIRF microscopy; an approach which utilises the evanescent field generated by a totally internally reflected laser at the sample/substrate interface (described in detail in Section 2.7.5). Briefly, high signal to noise measurements are achieved through excitation of only the fluorophores within approximately 100-200 nm of this interface. The result of this is that only particles diffusing on the lowest regions of the cell are observed.

Implementation of the evanescent field depth is achieved simply through termination of any particles which diffuse further than a user-specified distance from the lowest cell surface. While it is feasible these particles may diffuse back into the evanescent field region, experimentally they would be classified as a new fluorophore. To reduce the computational cost of this approach, start locations are only generated within the evanescent field region (function: *randomStart.m*).

Further to inclusion of a simple threshold, the estimated fluorescence intensity of each particle is calculated as a function of distance from the lowest cell surface (*z*). This is achieved through evaluation of the evanescent field decay constant (*d*) using the relation in Equation 6-3, followed by inclusion of this value in the exponential decay equation (Equation 6-4) [107].

$$d = \frac{\lambda_0}{4\pi}\sqrt{\mathrm{n}_1^2 \sin^2(\phi) - n_2^2}$$

**Equation 6-3 – Characteristic exponential decay depth for the TIRF evanescent field**
The characteristic decay depth (d) for the evanescent field generated through TIRF illumination is a function of the incident wavelength ($\lambda_0$), angle of laser incidence ($\varphi$) and the refractive indices of the incident and transmitted media ($n_1$ and $n_2$, respectively) [107].

$$I = I_0 \exp(-z/d)$$

**Equation 6-4 – Evanescent field intensity**
The evanescent field decays exponentially with increasing distance from the TIRF interface. As such, the intensity at a distance (*z*) into the sample is a function of the intensity at the interface ($I_0$) and the characteristic exponential decay depth (*d*) given by Equation 6-3.

Influence of the TIRF evanescent field depth was characterised through five equivalent simulations using 5000 particles with diffusion coefficients (*D*) of 0.05 $\mu m^2 s^{-1}$, simulated for a total time (*T*) of 1.7 seconds at intervals (*dt*) of 1 µs [266]. One data set was preserved as standard planar diffusion (black line, Figure 6-7; data from Section 6.3.1); another was transformed onto the cell surface in the absence of any evanescent field depth restrictions (blue line, Figure 6-7; data from Section 6.3.2) and the final three were all surface-transformed and subjected to field depths of 100 nm (red line, Figure 6-7), 150 nm (green line, Figure 6-7) and 200 nm (purple line, Figure 6-7).

The most significant result of imposing a finite field depth is the reduction in diffusing particles with increasing simulation time, leading to a less accurate MSD prediction. This is most evident for the narrowest evanescent field (100 nm; red line, Figure 6-7). When

simulating restricted diffusion (Sections 6.3.5 to 6.3.7) this effect becomes less pronounced as fewer particles are capable of passing the evanescent field boundary. A subtler effect on the data is that shallower field depths eliminate the regions of the cell which have the greatest gradient normal to the imaging plane. Since these are the areas where most spatial information is lost in the projection of trajectories onto a two-dimensional image, implementation of a finite field depth tends the observed MSD towards the planar diffusion case.

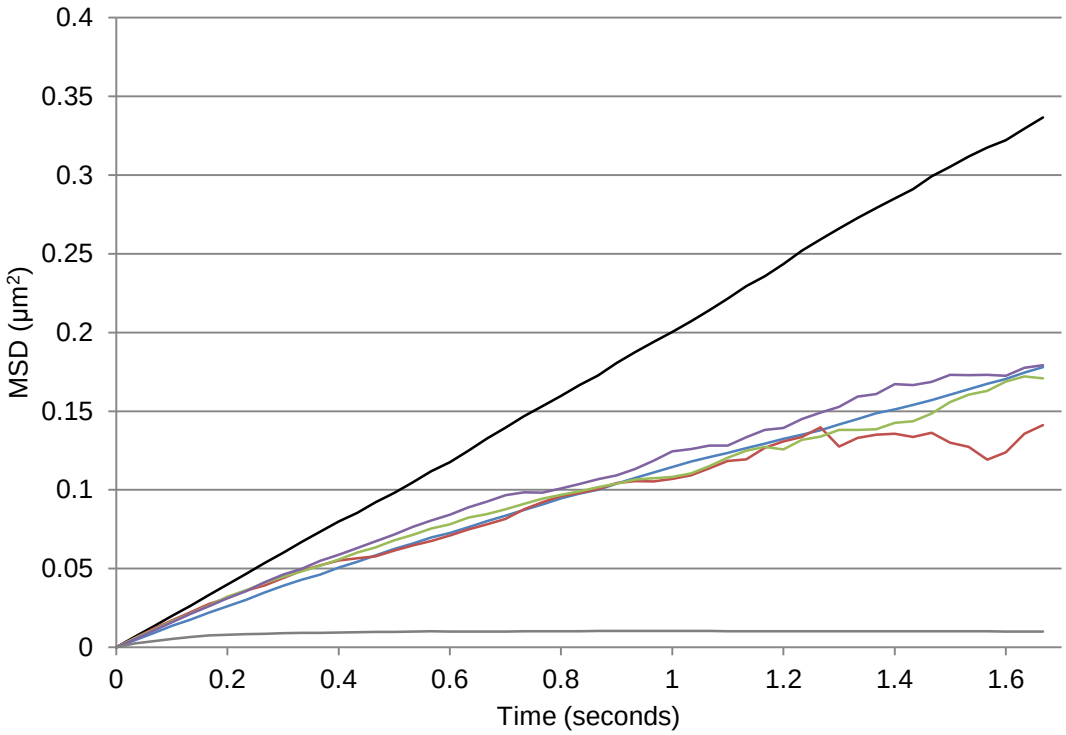


**Figure 6-7 – Effect of TIRF illumination field of depth on observed MSD**
Unrestricted diffusion simulated on a two-dimensional plane (black line), on the curved cell surface (blue line) and on the cell surface with varying evanescent field depths: 100 nm (red line), 150 nm (green line) and 200 nm (purple line). Each simulation is conducted for 5000 particles ($D$ = 0.05 μm$^2$s$^{-1}$, $T$ = 1.7 s, $dt$ = 1 μs) and where relevant, for a curved surface characteristic of an *E. coli* cell ($R_{cell}$ = 0.25 μm, $L_{cell}$ = 3 μm). For reference, the experimentally-obtained data is also shown (grey line). Reduction in the number of diffusing particles with increasing simulation time results in less accurate MSD prediction, as is most evident with a field depth of 100 nm. Another result, less evident in these plots, is a tendency towards an MSD characterised by planar diffusion for shallower field depths. This arises from exclusion of the steepest gradients, which occur around the bacteria midpoint.

It is not possible to explain the experimentally-observed MSD plateau in terms of the illumination limitations of TIRF microscopy. Nonetheless, for similarity to the experimental system, all simulations reported hereafter include finite TIRF field depths of 150 nm. This value reaches a compromise between modelling a realistic illumination system and maintaining statistically-relevant numbers of diffusing particles.

### 6.3.4 Random cell orientation

Simulations conducted thus far have been based on cells with aligned long axes; however, experimentally there will be a random distribution of orientations. To simulate this, planar coordinates are passed through the transformations described by Equation 6-5 and Equation 6-6 (function: *cellRotation.m*), where the degree of rotation ($\theta$) is randomly selected from the standard uniform distribution. Following transformation of trajectories to the curved cellular surface (Section 6.3.2) the rotation operation is reversed.

$$dx = dx\cos(\theta) - dy\sin(\theta)$$

**Equation 6-5 – Rotational transformation of x-coordinates**
Operation applied to x-coordinate values (*dx*) to achieve a rotation of magnitude $\vartheta$. This is necessary to simulate cell rotation during Monte Carlo diffusion simulations.

$$dy = dx\sin(\theta) + dy\cos(\theta)$$

**Equation 6-6 – Rotational transformation of y-coordinates**
Operation applied to y-coordinate values (*dy*) to achieve a rotation of magnitude $\vartheta$. This is necessary to simulate cell rotation during Monte Carlo diffusion simulations.

Two equivalent simulations were performed using 5000 particles with diffusion coefficients ($D$) of 0.05 $\mu m^2 s^{-1}$, simulated for a total time ($T$) of 1.7 seconds at intervals ($dt$) of 1 μs [266]. In both cases the diffusion was mapped onto a curved surface characteristic of the E. coli outer membrane ($R_{cell}$ = 0.25 μm, $L_{cell}$ = 3 μm; see Section 6.3.2) with a finite TIRF microscopy field depth (see Section 6.3.3) of 150 nm. One set of trajectories was then rotationally-transformed by an angle randomly selected for each diffusing particle (red line, Figure 6-8). For purposes of continuity with previously reported data, the simulations are plotted along with the MSD curve for unrestricted planar diffusion (black line, Figure 6-8; data from Section 6.3.1).

As should be expected for rotation about an axis normal to the imaging plane, there is no appreciable difference between simulations with all bacteria aligned and randomly oriented. Divergence of the two curves is purely due to the random nature of Monte Carlo simulations, especially at later time-points, where the number of diffusing particles has been reduced via the evanescent field limit (see Section 6.3.3).

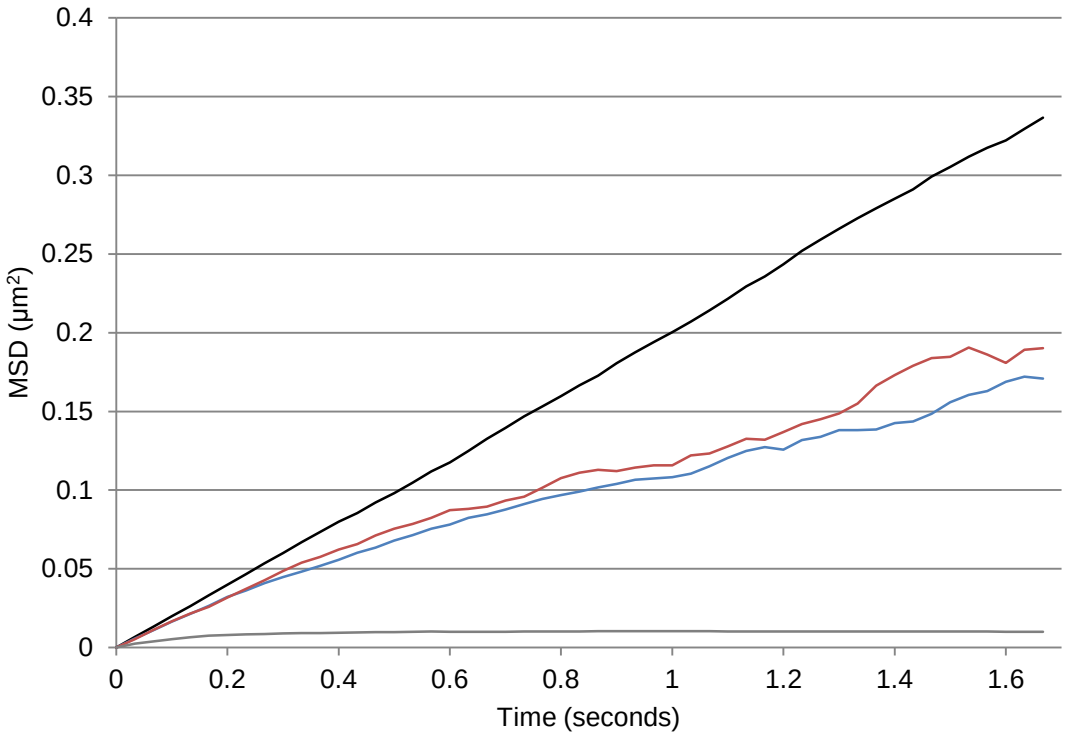


**Figure 6-8 – Effect of random bacterial cell rotation on MSD**
Simulating the experimental condition that not all cells are aligned as has been assumed thus far. Shown is planar diffusion (black line) and diffusion mapped to a curved surface characteristic of an *E. coli* cell ($R_{cell}$ = 0.25 μm, $L_{cell}$ = 3 μm) with all cell axes aligned (blue line) and random cell alignment (red line). For reference, the experimentally-obtained data is also shown (grey line). Each simulation is conducted for 5000 particles ($D$ = 0.05 μm$^2$s$^{-1}$, $T$ = 1.7 s, $dt$ = 1 μs) capable of unrestricted diffusion. There appears to be no appreciable difference between aligned and randomly oriented cells.

While rotation may have an effect on the experimentally-measured MSD, it would only manifest in the case of some form of optical aberration or camera inhomogeneity, whereby the image was stretched in one dimension. Simulations described henceforth do not have random cell rotation.

### 6.3.5 Square mesh membrane compartmentalisation restricting diffusion

Factors thus far included in the simulation have been unable to account for the experimentally-observed MSD plot (Section 6.2). As such, this implies that experimental factors (for example, projection of three-dimensional coordinates onto a two-dimensional plane) do not affect the unrestricted diffusion trajectories in ways as to yield pseudo-restriction. Typically, restricted diffusion can be explained in terms of membrane compartmentalisation [263], whereby diffusing particles are confined to specific regions on the cell surface.

The approach described here imposes a square mesh (element edge length, $L_{mesh}$) onto the planar diffusion trajectories, where each mesh compartment has an associated coordinate (function: *meshFind.m*). Particles are only free to diffuse within a single mesh compartment; any steps finishing beyond this current mesh square are discarded and the particle is assumed to have remained stationary. Restricted trajectories are mapped onto the curved bacterial surface model as previously described (Section 6.3.2). Figure 6-9 shows example restricted diffusion for 100 particles ($D$ = 0.05 μm$^2$s$^{-1}$, $T$ = 1 s, $dt$ = 1 ms, $R_{cell}$ = 0.25 μm, $L_{cell}$ = 3 μm, $L_{mesh}$ = 0.2 μm), where each particle is randomly assigned a colour for clarity.

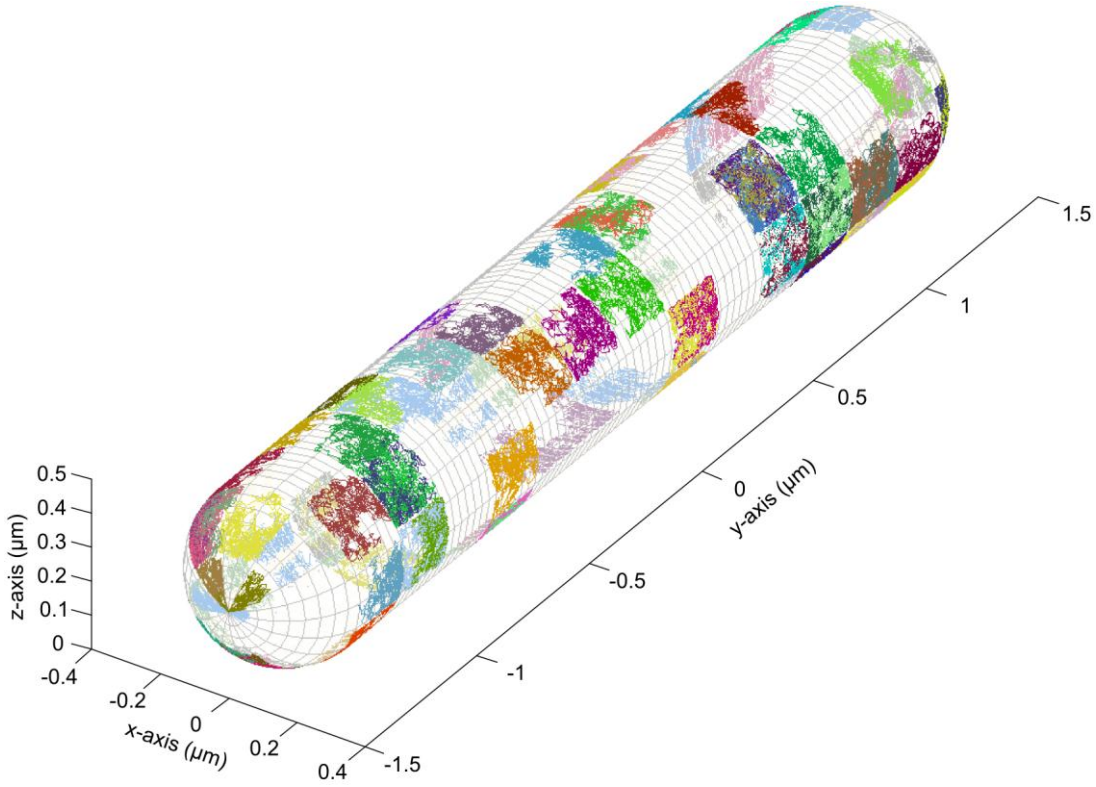


**Figure 6-9 – Effect of membrane compartmentalisation on diffusion trajectories**
Each diffusing particle is confined to a square compartment of user-defined edge length ($L_{mesh}$), with each compartment arranged in a tessellating mesh. These diffusion trajectories are mapped to the modelled cell surface using the previously-described technique (see Section 6.3.2). Trajectories are shown for 100 particles ($D$ = 0.05 μm$^2$s$^{-1}$, $T$ = 1 s, $dt$ = 1 ms, $L_{edge}$ = 0.2 μm) on a curved surface characteristic of an *E. coli* cell ($R_{cell}$ = 0.25 μm, $L_{cell}$ = 3 μm) with 150 nm evanescent field depth. For ease of visualisation, each particle is randomly assigned a colour.

Experimentally, mesh coordinates will not align for all bacteria due to axial rotation and presumed variations in bacterial composition. To simulate this, mesh coordinates can be randomised for each diffusing particle with the mesh displacement vectors ($dx_{mesh}$ and $dy_{mesh}$) drawn from the standard uniform distribution. The effect of this is shown in Figure 6-10 for a simulation otherwise equivalent to that shown in Figure 6-9.

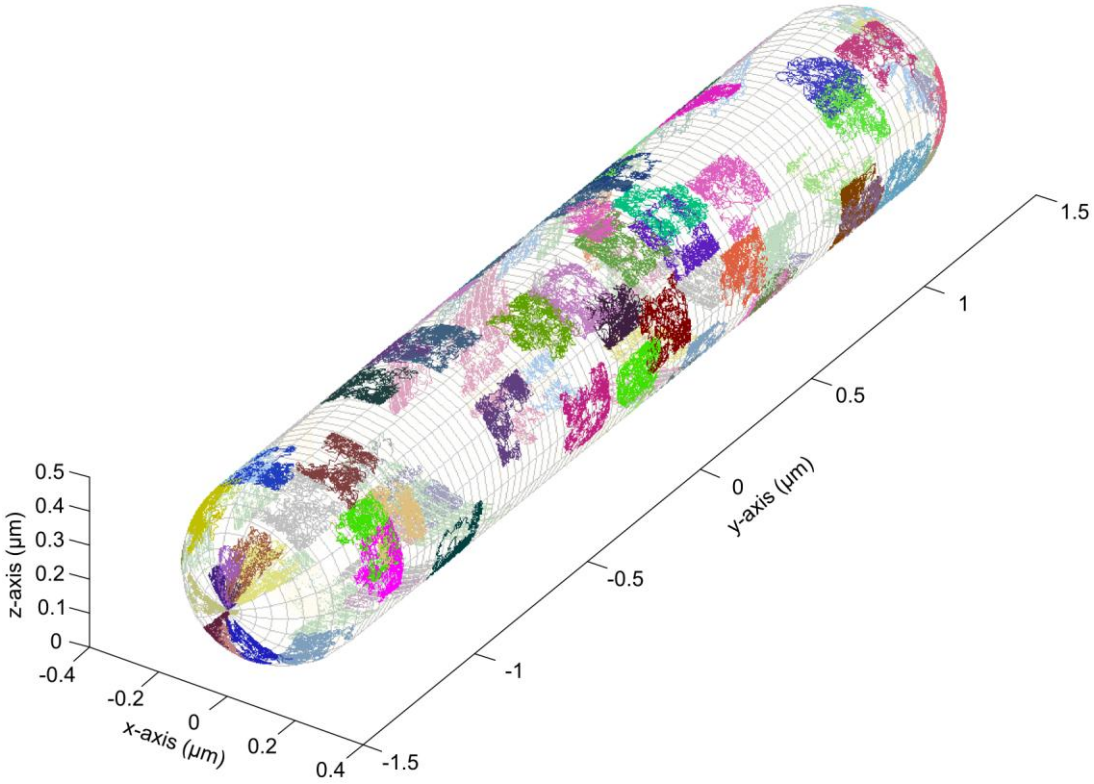


**Figure 6-10 – Randomisation of mesh coordinates for each diffusing particle**
Restricting compartment coordinates for each diffusing particle are randomised, which results in loss of the tessellated mesh pattern seen in Figure 6-9. Simulation conditions are otherwise the same as for the tessellated mesh model (100 particles, $D$ = 0.05 µm$^2$s$^{-1}$, $T$ = 1 s, $dt$ = 1 ms, $R_{cell}$ = 0.25 µm, $L_{cell}$ = 3 µm, $L_{mesh}$ = 0.2 µm). This simulates random axial-rotation of the cell as well as random positioning of the mesh along the bacterial long axis. For ease of visualisation, each particle is randomly assigned a colour.

To probe the effect of restricted diffusion on observed MSD for aligned and randomised meshes two sets of simulations were performed. These featured 5000 particles with diffusion characteristics described previously ($D$ = 0.05 µm$^2$s$^{-1}$, $T$ = 1.7 s, $dt$ = 1 µs; Section 6.3.1) mapped onto a curved surface representative of the *E. coli* outer membrane ($R_{cell}$ = 0.25 µm, $L_{cell}$ = 3 µm; Section 6.3.2) and subjected to a TIRF microscopy evanescent field depth of 150 nm (Section 6.3.3). A square mesh ($L_{mesh}$ = 0.2 µm) with conserved (red lines; Figure 6-11) and randomised (green lines; Figure 6-11) position relative to the bacterial cell was imposed on diffusion trajectories.

Inclusion of restricted diffusion in the simulation has a drastic effect on the observed MSD (Figure 6-11). After approximately 0.5 seconds the MSD has reached a plateau, very similar to that observed in the experimentally-measured data. This MSD profile appears to be characterised by two linear regimes; the first corresponding to near-unrestricted diffusion and the second corresponding to the diffusive confinement by the mesh. Whilst the absolute MSD plateau values are different between the experiment and simulation,

these are a function of user-specified variables; namely the diffusion coefficient ($D$) and mesh edge length ($L_{mesh}$).

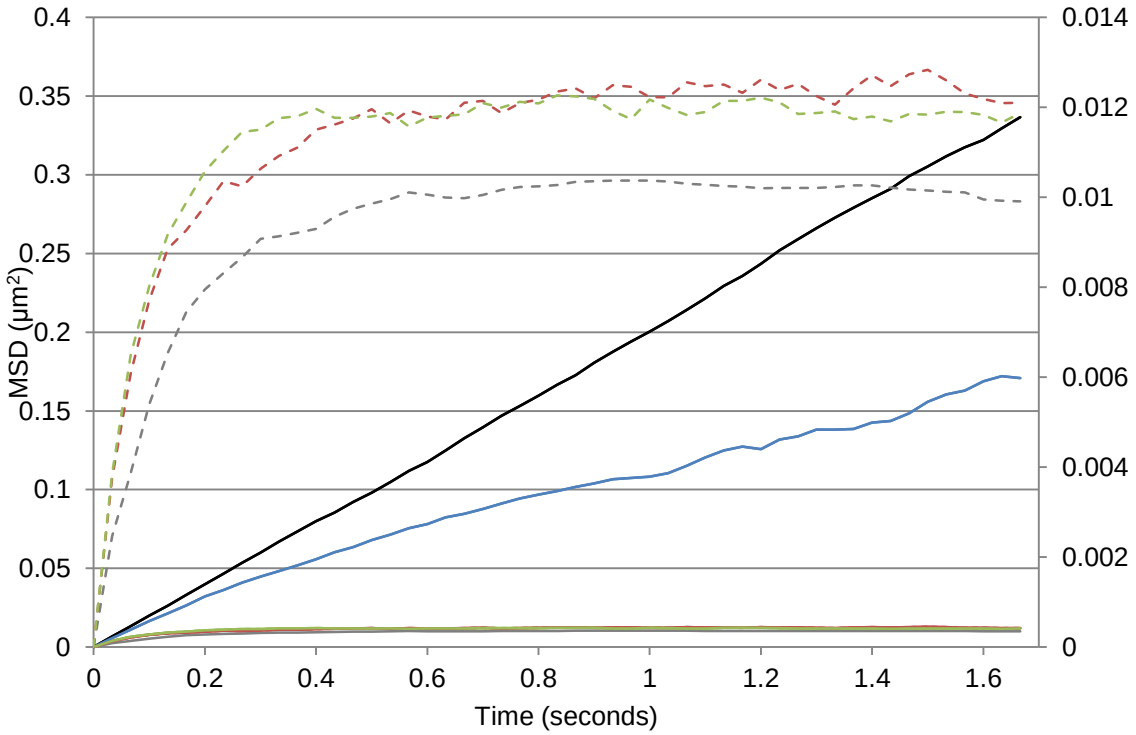


**Figure 6-11 – Effect of membrane compartmentalisation on observed MSD**
Restriction of diffusion due to membrane compartmentalisation has been simulated for 5000 particles ($D$ = 0.05 μm$^2$s$^{-1}$, $T$ = 1.7 s, $dt$ = 1 μs) with each trajectory is mapped onto a curved surface characteristic of an *E. coli* cell ($R_{cell}$ = 0.25 μm, $L_{cell}$ = 3 μm; Section 6.3.2) and subjected to a 150 nm evanescent field depth (Section 6.3.3). Particles are restricted to diffusing within a single element of the square mesh ($L_{mesh}$ = 0.2 μm) (red lines). Axial rotation of bacteria has been simulated through randomisation of mesh coordinates (green lines). For reference, simulated unrestricted planar (black line; Section 6.3.1), unrestricted diffusion on the bacterial surface inside a 150 nm deep evanescent field (blue line; Section 6.3.3) and the experimentally-obtained data (grey lines) are also shown. For improved visibility, restricted diffusion data has also been plotted relative to the secondary axis (dashed lines).

There appears to be negligible difference between simulations using constant and randomised mesh coordinates; therefore, all data reported henceforth includes a randomised mesh.

Despite not yielding a direct indication on the source of restriction, through comparison to the experimentally-obtained MSD data, parameters such as restricting compartment size ($L_{mesh}$) and diffusion constants ($D$) can be elucidated. These parameters are varied in Section 6.3.7 in order to improve agreement between the data sets.

### 6.3.6 Semi-permeable membrane compartmentalisation

Since no origin has been elucidated for the observed restricted diffusion, it is likely the physical picture is more complex than has thus far been simulated. One manner in which this complexity could manifest is semi-permeability of the membrane compartments. To incorporate this into the simulation, potential mesh boundary pass events are treated in a probabilistic manner, based on a user-defined threshold value (*boundary_pass_threshold*, range: 0 to 1). At each boundary pass event a random number is drawn from the standard uniform distribution; if this value is above the threshold value, the particle can proceed to the adjacent compartment, otherwise the particle remains stationary.

While this approach does not assume a physical origin for the gating of adjacent compartments, feasible sources are size exclusion [274], angle of boundary approach or velocity of approach.

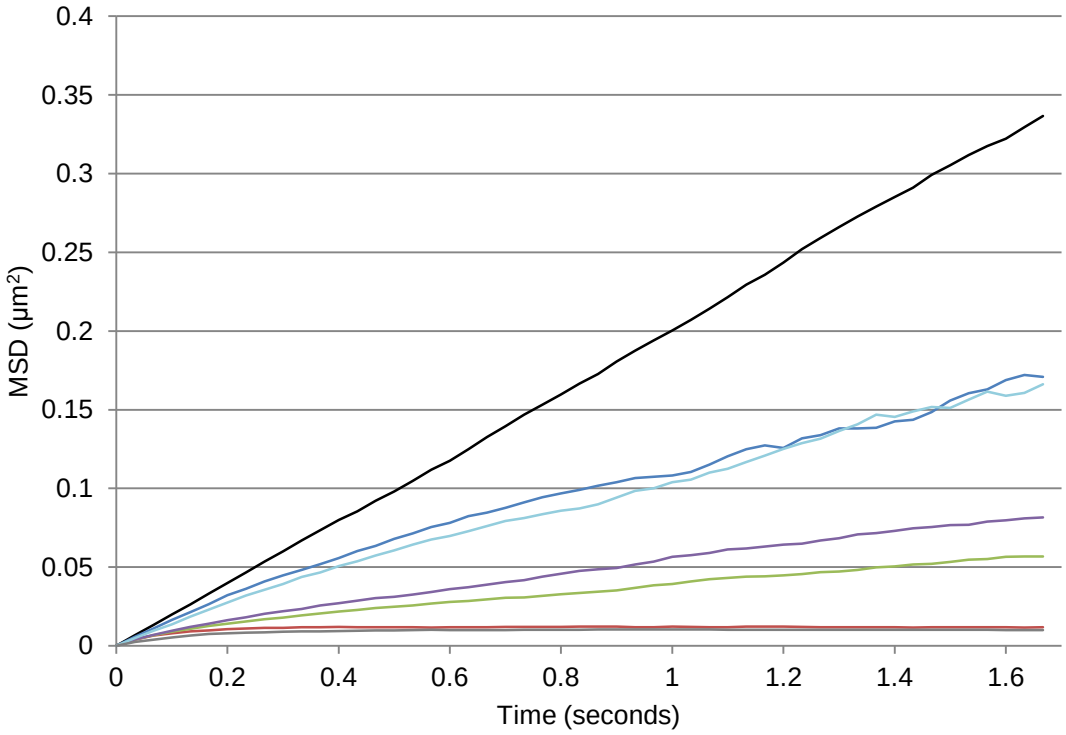


**Figure 6-12 – MSD for diffusion constrained by semi-permeable compartments**
Simulations of 5000 particles ($D$ = 0.05 µm$^2$s$^{-1}$, $T$ = 1.7 s, $dt$ = 1 µs) diffusing on a curved surface ($R_{cell}$ = 0.25 µm, $L_{cell}$ = 3 µm; Section 6.3.2) inside a 150 nm evanescent field (Section 6.3.3) are restricted by a semi-permeable square mesh ($L_{mesh}$ = 0.2 µm). Successful mesh boundary pass percentages of 0.05% (green line), 0.1% (purple line) and 1% (cyan line) have been simulated. Reference lines are also included; unrestricted planar diffusion (black line; Section 6.3.1), unrestricted diffusion on a curved surface (blue line; Section 6.3.2), restricted diffusion with a non-permeable square mesh (red line) and the experimentally-obtained data (grey line). Only moderate permeability (~1%) leads to MSD convergence with the unrestricted cahowever, this relation is not absolutely quantifiable, since the probability of a boundary passage event is inversely proportional to the time step duration ($dt$). The non-permeable mesh result bears the greatest similarity to the experimentally-observed MSD data.

Three data sets were simulated with *boundary_pass_threshold* values of 0.9995 (green line; Figure 6-12), 0.999 (purple line; Figure 6-12) and 0.99 (cyan line; Figure 6-12); corresponding to 0.05%, .01% and 1% of boundary crossing attempts succeeding, respectively. These thresholds are semi-arbitrary, since the number of boundary pass attempts is influenced by the time-step duration (*dt*) for a fixed simulation time (*T*). Other simulation parameters were identical to those described for restricted diffusion with a non-permeable mesh ($D$ = 0.05 μm$^2$s$^{-1}$, $T$ = 1.7 s, $dt$ = 1 μs, $R_{cell}$ = 0.25 μm, $L_{cell}$ = 3 μm, $L_{mesh}$ = 0.2 μm; Section 6.3.5).

With increasing membrane permeability the gradient of the MSD plateau region, observed for non-permeable membranes (Section 6.3.5), also increases. This is to be expected since the imposed square mesh no longer offers absolute confinement to diffusing particles. For a 1% boundary passage success rate, the observed MSD converges with the unrestricted diffusion result. Since the experimentally-obtained data shows a complete MSD plateau following the initial unrestricted diffusion regime it can be concluded the physical membrane compartmentalisation is completely impermeable.

### 6.3.7 Varying simulation parameters to fit experimental data

Key parameters determining the profile of the restricted diffusion MSD curves are the diffusion constant ($D$) and edge length of the restricting mesh ($L_{mesh}$). These parameters have been varied across a relevant range ($D$ = 0.015 μm$^2$s$^{-1}$ to 0.04 μm$^2$s$^{-1}$, $L_{mesh}$ = 0.18 μm to 0.2 μm) for the purpose of achieving optimal correlation with the experimentally-observed data (Section 6.2). All simulations were based on diffusion of 5000 particles restricted by an impermeable square mesh, with particle trajectories mapped to the curved *E. coli* surface ($T$ = 1.7 s, $dt$ = 1 μs, $R_{cell}$ = 0.25 μm, $L_{cell}$ = 3 μm, $L_{mesh}$ = 0.2 μm). This configuration was previously determined to give an MSD profile reaching a constant plateau following initial fast diffusion, similar to the experimental case (Section 6.3.5).

Following coarse identification of approximate values for $D$ and $L_{mesh}$ using a trial-and-error approach (data not shown), final simulations were conducted with one parameter held constant whilst the other was varied (Figure 6-13 and Figure 6-14). Figure 6-13 demonstrates the characteristic response of varying the diffusion coefficient on the initial diffusion gradient and MSD plateau value. For a constant $L_{mesh}$ of 0.185 μm there is

optimal agreement between the simulation and experimental data for a diffusion coefficient of $0.03 \pm 0.0025$ $\mu m^2 s^{-1}$. The two curves within $0.005$ $\mu m^2 s^{-1}$ of this value exhibit significant divergence. This observation is consistent with that measured by Spector *et al.* for BtuB complexed with a fluorescent antibody ($D = 0.05 \pm 0.01$ $\mu m^2 s^{-1}$) and to a slightly lesser degree when complexed with colicin ($D = 0.1 \pm 0.02$ $\mu m^2 s^{-1}$) [266].

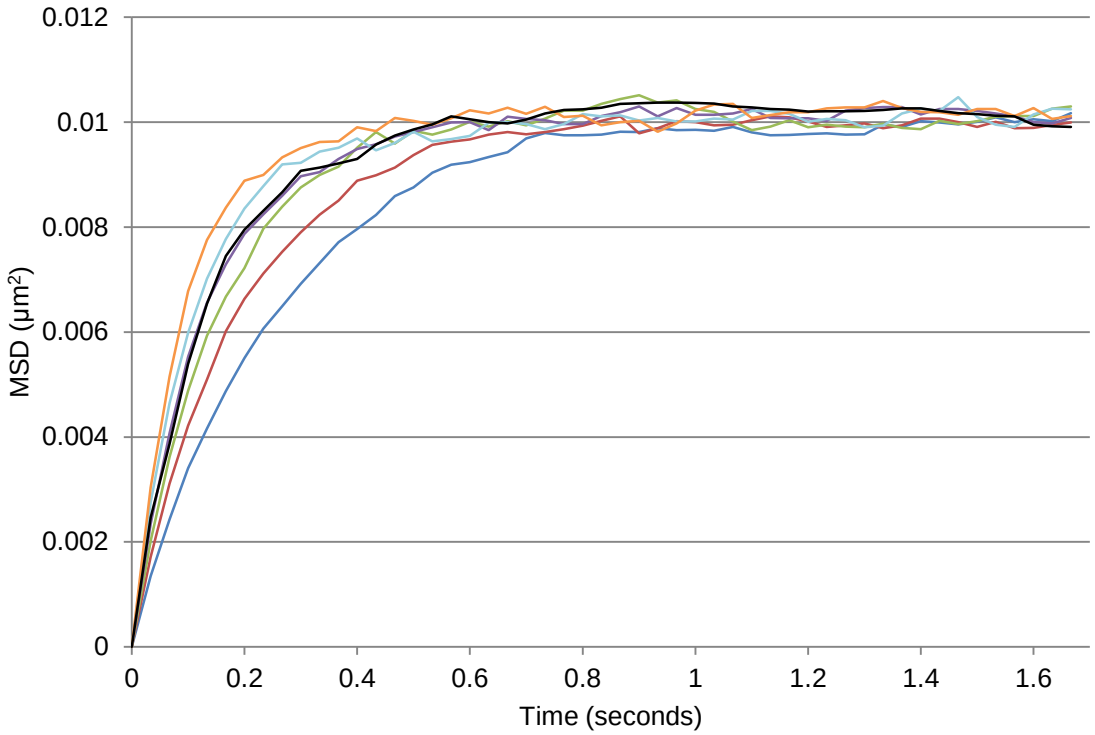


**Figure 6-13 – Varying *D* (constant $L_{mesh}$) to fit experimental MSD data**
Standard restricted diffusion simulations ($T = 1.7$ s, $dt = 1$ µs, $R_{cell} = 0.25$ µm, $L_{cell} = 3$ µm, $L_{mesh} = 0.185$ µm, 150 nm evanescent field depth) have been run using various diffusion constants to fit the experimentally observed MSD curve (black line). Diffusion coefficient values were 0.015 $\mu m^2 s^{-1}$ (blue line), 0.02 $\mu m^2 s^{-1}$ (red line), 0.025 $\mu m^2 s^{-1}$ (green line), 0.03 $\mu m^2 s^{-1}$ (purple line), 0.035 $\mu m^2 s^{-1}$ (cyan line) and 0.04 $\mu m^2 s^{-1}$ (orange line). Strongest correlation between simulated and experimentally-obtained MSD curves occurs for a diffusion coefficient of $0.03 \pm 0.0025$ $\mu m^2 s^{-1}$.

Similarly, mesh edge length ($L_{edge}$) was varied between 0.18 µm and 0.2µm whilst maintaining the diffusion coefficient ($D$) at 0.03 $\mu m^2 s^{-1}$. The obtained data, shown in Figure 6-14, demonstrates an optimal agreement between the experimentally-observed data (Section 6.2) and simulation for $L_{edge}$ of $0.1875 \pm 0.00125$ µm. This is in strong agreement with compartment diameters simulated by Spector *et al.*, who report sizes of 190 nm when BtuB is in complex with fluorescently-labelled anti-BtuB [266].

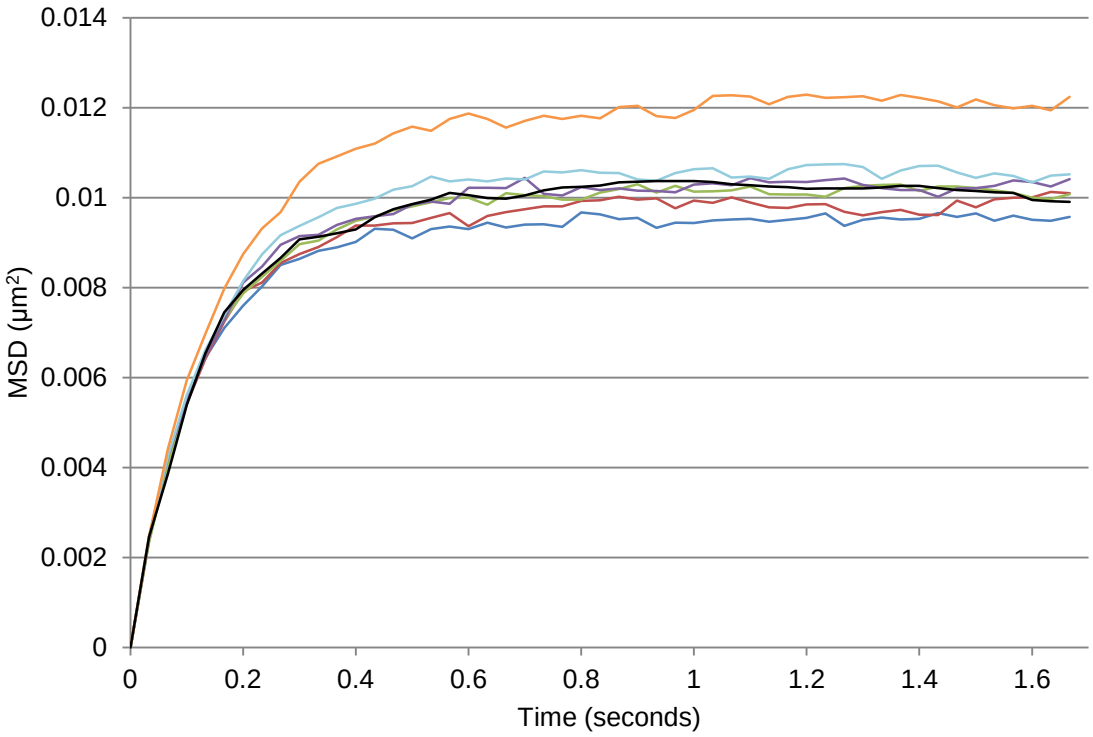


**Figure 6-14 – Varying $L_{mesh}$ (constant *D*) to fit experimental MSD data**
Standard restricted diffusion simulations (D = 0.03 $\mu m^2 s^{-1}$, $T$ = 1.7 s, $dt$ = 1 μs, $R_{cell}$ = 0.25 μm, $L_{cell}$ = 3 μm, 150 nm evanescent field depth) have been run using various mesh edge lengths to fit experimentally observed MSD data (black line). Mesh edge lengths were 0.18 μm (blue line), 0.1825 μm (red line), 0.185 μm (green line), 0.1875 μm (purple line), 0.19 μm (cyan line) and 0.2 μm (orange line). The strongest correlation between experimentally-obtained and simulated data occurred for a mesh edge length of 0.1875 ± 0.00125 μm.

## 6.4 Restricted diffusion arising from outer membrane vacancies

Simulations modelling diffusion of experimentally-observed colE9-BtuB complexes demonstrated restricted behaviour which could be explained in terms of a non-permeable square mesh (Section 6.3.5). While this approach facilitated strong agreement between experimental and simulated MSD curves it cannot be attributed to a physical origin. A strong candidate for this physical origin is vacancy diffusion, which takes into consideration the volume (or area, since the simulations are all planar) of the diffusing BtuB as well as that of two other significant outer membrane proteins, OmpF and OmpA. Inclusion of OmpA is necessary since this is a major outer membrane protein and one which has connections to the peptidoglycan layer [275]. Peptidoglycan interactions have the potential to inhibit OmpA diffusion, thus causing it to act as a picket fence that corrals the diffusing BtuB. As described in Section 6.1, the trimeric porin OmpF is a key protein in the cellular import mechanism of colE9, providing entry to the periplasmic space [264].

### 6.4.1 Reported examples of membrane vacancy diffusion

Vacancy diffusion has been previously modelled using a voxel approach, whereby proteins are confined to a square lattice, with a single occupancy per element (voxel) [271,272]. Proteins are randomly distributed on the lattice and permitted to move a specific number of unoccupied voxels per time step. Instances of attempted protein movement into occupied voxels can either be discarded or subjected to stochastic biomolecular reactions [276,277,271]. In the latter scenario, occurrence of a reaction between the two proteins is determined by user-specified probabilities, compared against randomly generated numbers [276,277].

Advantages of the voxel approach are a significant minimisation in computational overheads. These owe primarily to the reduced memory allocation necessary for storing integer protein coordinates and to simplified calculations used to track protein-protein interactions; however, they come at the expense of a loss in spatial precision and the ability to define protein shapes.

An alternative approach is the simulation of restricted diffusion in rat kidney fibroblasts by Fujiwara, *et al.*, who utilised a square mesh populated by anchored-protein pickets [274]. These proteins were hypothesised to be bound to the actin skeleton of the cell, onto which they formed a semi-permeable square mesh. To accurately model their experimentally-observed diffusion, each mesh square edge ($L_{mesh}$ = 0.2 μm) was populated with 31, 24 or 23 anchored proteins with diameters of 1 nm, 2 nm or 3 nm, respectively [274]. This method represents a combination of the finite protein volume modelled by vacancy diffusion and the square mesh described in Sections 6.3.5 and 6.3.6).

### 6.4.2 Population of the simulated membrane

Protein volume is approximated for two-dimensional diffusion using a simple model whereby each protein is represented by a circle of given radius; OmpF ($R_{OmpF}$ = 1.7 nm, monomer radius), OmpA ($R_{OmpA}$ = 1.3 nm) and BtuB ($R_{BtuB}$ = 2.3 nm), as measured using NMR or crystallography. This simplification is not too dissimilar from the physical picture for the porins OmpF and OmpA or for the vitamin $B_{12}$ receptor, BtuB, which have cylindrical β-barrel structures (Figure 6-15).

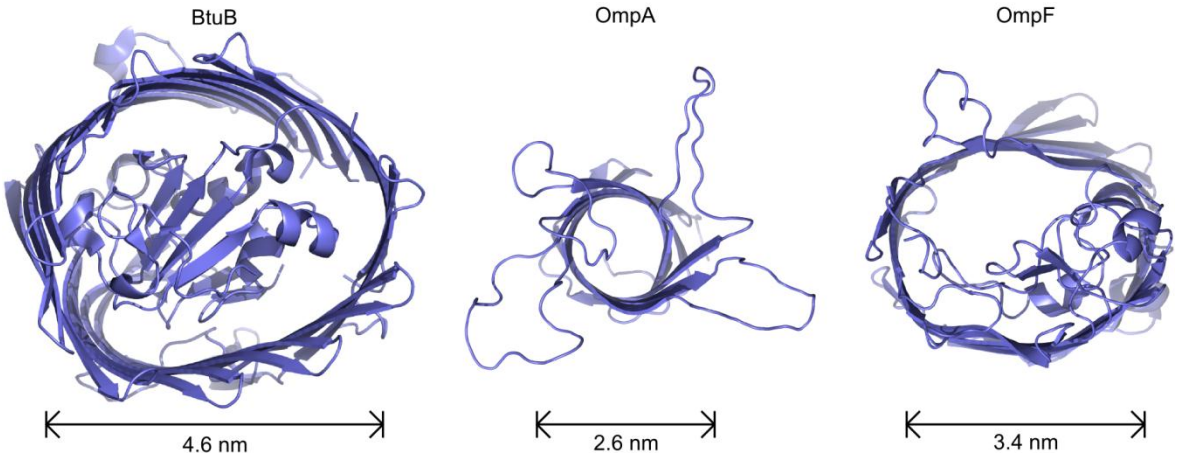


**Figure 6-15 – Protein structures of BtuB, OmpA and an OmpF monomer**
Each protein is based on a cylindrical β-barrel structure, thus facilitating insertion into the cellular outer membrane. Approximate barrel diameters have been measured using PyMol (Version 1.5.0.4 Schrödinger, LLC.) and are shown below each structure. Structures were taken from the Protein Data Bank (PDB): BtuB (PDB ref. 2GUF [278]), OmpA (PDB ref. 2GE4 [279]) and an OmpF monomer (PDB ref. 2ZFG [280]). Approximately to scale.

An estimation of outer membrane occupancy can be obtained using reported populations for the various proteins; ~300 copies of BtuB per cell [250,266], ~1 x$10^5$ copies of OmpA per cell [281,282] and also ~1 x$10^5$ copies of OmpF monomer per cell [283]. Assuming the stated radii, these populations give an approximate protein surface area of 1.4 μm$^2$, which is similar to the value of 1.8 μm$^2$ stated by Nikaido [284]. Taking the same physical properties of an *E. coli* cell used in Section 6.3.2 ($R_{cell}$ = 0.25 μm, $L_{cell}$ = 3 μm), a protein surface area of 1.4 μm$^2$ corresponds to 29.7% occupancy of the cell surface. This is an approximation, with similar published work using a range of *E. coli* cell sizes, which yield occupancies of 14.6% [285], 14.9% [268], 15.9% [286] and 22.3% [266] when treated in the same manner (identical protein populations). To probe the effect of protein volume on diffusion, a range of membrane occupancies spanning the aforementioned values from 10% to 30%, at 5% intervals, has been simulated.

Prior to simulation of colE9-BtuB diffusion, a model area of the outer membrane must be populated with BtuB, OmpA and OmpF. The range of this area is determined by the user-specified *E. coli* cell size such that the planar simulated region will wrap once round the cell surface. To avoid problems arising from the non-periodicity of the simulated region, a TIRF field depth shallower than the bacterial diameter must be used to prevent diffusion around the cell.

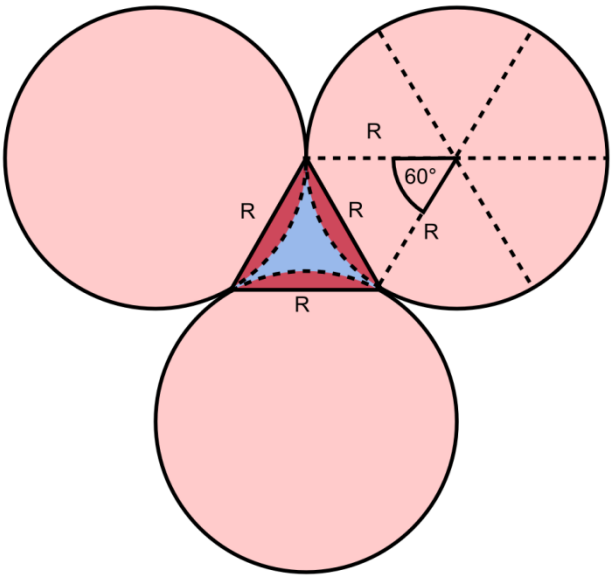


**Figure 6-16 – Dissection of area calculations for outer membrane packing**
OmpF trimers can be simplified as three circles and the area they enclose. Calculation of the OmpF area involves summation of the three monomer areas (light red circles) and the equilateral triangle with edge lengths $R_{OmpF}$ (shaded blue), followed by subtraction of the three overlapping segments (shaded dark red).

The area of the monomer proteins OmpA and BtuB can be easily approximated using the standard equation for the area of a circle. Calculation of the OmpF trimer occupancy is more complicated since it is the sum of the three monomers and the area between them. Dissection of this central area (shaded blue; Figure 6-16) requires the subtraction of three segments (shaded dark red; Figure 6-16), with chord length $R_{OmpF}$, from the equilateral triangle with edge length $R_{OmpF}$. The final OmpF area is given by Equation 6-7.

$$Area_{OmpF\ trimer} = \left(\frac{5\pi}{2} + \sqrt{3}\right) {R_{OmpF}}^2$$

**Equation 6-7 – Calculation of OmpF trimer area**
OmpF trimer area can be simplified as the sum of three circles and the region between them; the configuration of these components is shown in Figure 6-16b. Area is a function of the OmpF monomer radius ($R_{OmpF}$), taken to have a value of 3.3 nm.

Since the BtuB population is very low compared to the Omp proteins, the initial protein placement and diffusion is based solely upon OmpA and OmpF. In order to generate statistically significant numbers of BtuB diffusion paths without great computational expense, BtuB positions do not influence other membrane proteins. This enables multiple BtuB positions to be simulated independently for a single membrane distribution. At the low occupancies used in the simulation this has a negligible effect on BtuB trajectories.

### 6.4.3 Simulating diffusion using populated membrane

Taking the diffusion coefficient identified in Section 6.3.7 as best representing the experimentally-observed data ($D$ = 0.03 μm$^2$s$^{-1}$), diffusion of 5000 particles was measured for a series of membrane occupancies spanning the range 10% to 30%, at 5% intervals. An example of membrane population is shown in Figure 6-17 along with its influence on a single diffusing BtuB. Calculated planar trajectories were mapped to a curved surface representing the *E. coli* outer membrane ($R_{cell}$ = 0.25 μm, $L_{cell}$ = 3 μm), as described in Section 6.3.2 and subjected to a 150 nm evanescent field depth (Section 6.3.3). For reasons of minimising computational expense, the total simulated time was halved to 0.85 seconds. Since the characteristic plateau in the experimentally-obtained MSD data occurs within the first 0.6 seconds this should not prevent meaningful comparison with the simulations. Time step for the simulations was maintained at 1 μs and converted to 30 fps for the purpose of data analysis (as described in Section 6.3.1).

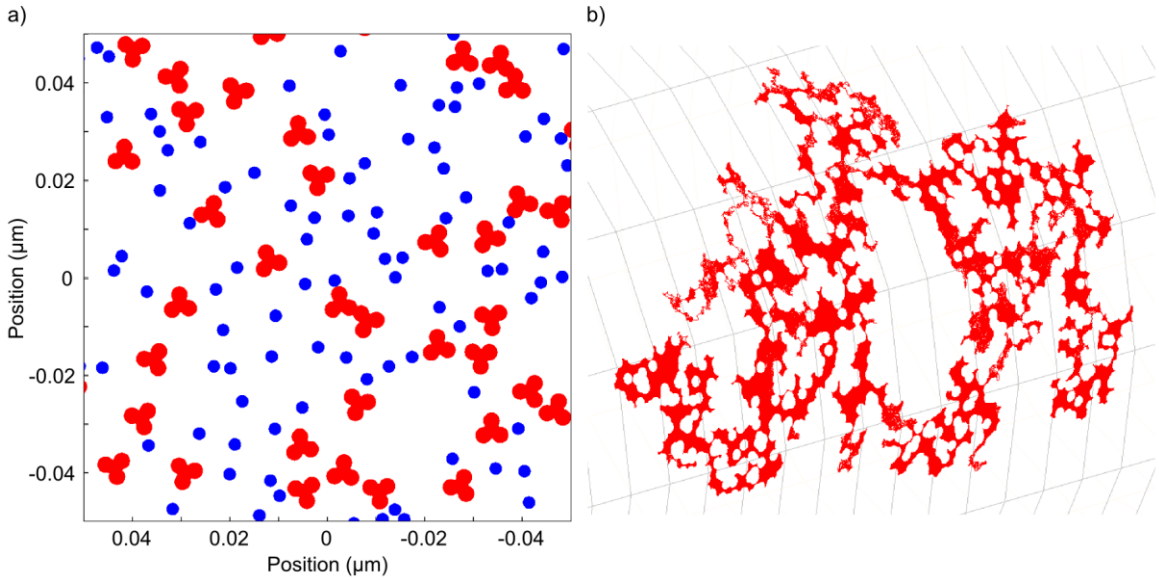


**Figure 6-17 – Simulated *E. coli* outer membrane for diffusion studies**
a) Example region of the simulated outer membrane showing OmpF trimers (red) and OmpA monomer (blue) at a final occupancy of 15%. Homogeneous protein distribution is assumed, with protein coordinates selected randomly. b) Effect of incorporating finite protein size into diffusion simulations. A BtuB trajectory (traced as a red line) is highly influenced by the presence of OmpF and OmpA. The example simulation was run for a total of 10 seconds at a time step of 10 μs, with a diffusion coefficient of 0.05 μm$^2$s$^{-1}$ and membrane occupancy of 15%.

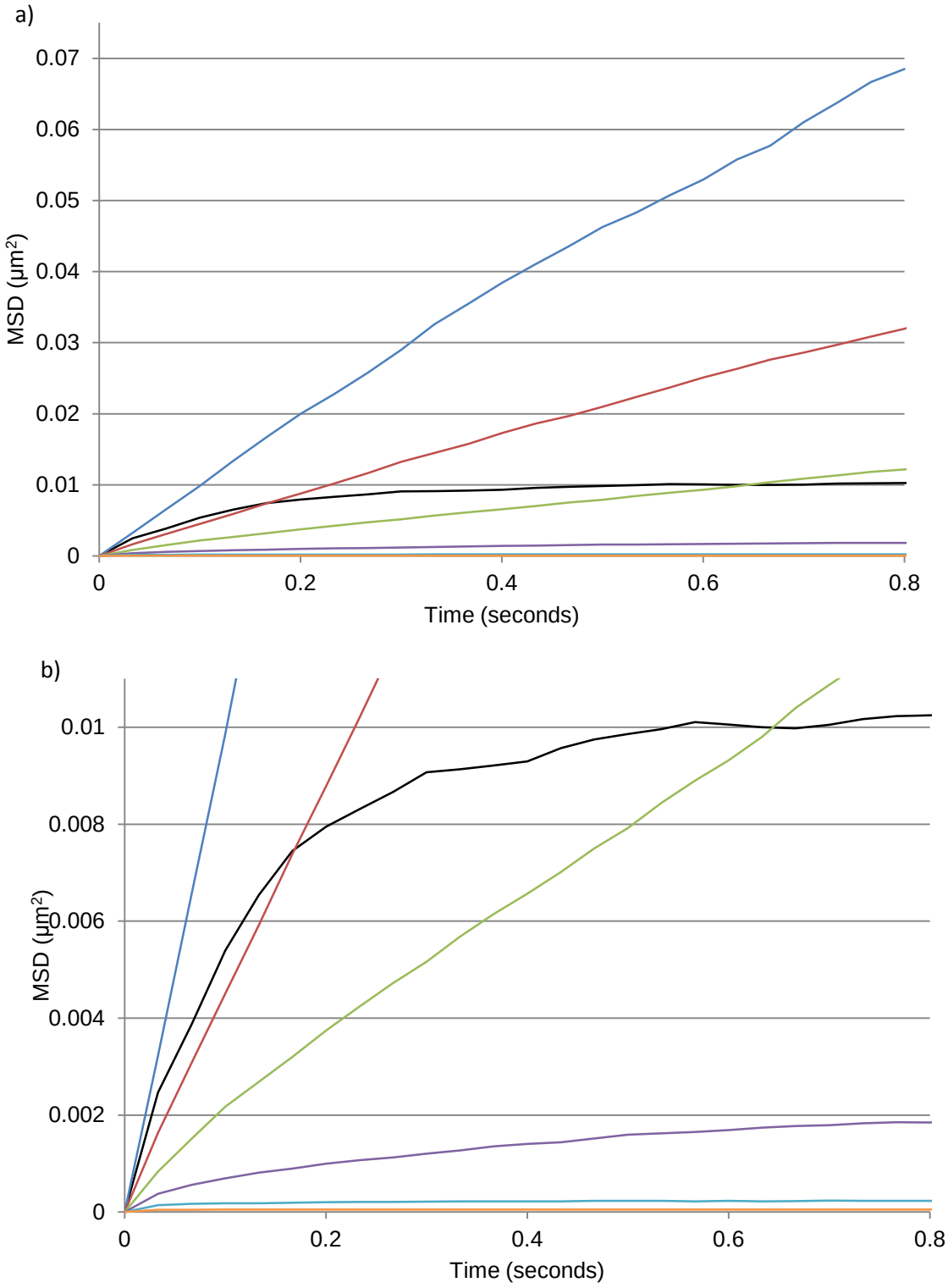


**Figure 6-18 – Effect of finite protein volume on BtuB-colE9 diffusion**
Mean square displacement (MSD) curves for simulated diffusion of BtuB in the *E. coli* outer membrane taking into consideration the finite size of BtuB and other common proteins, OmpA and OmpF. Simulations were conducted for 5000 diffusing particles ($D$ = 0.03 µm$^2$s$^{-1}$, $T$ = 0.8 s, $dt$ = 1 µs, $R_{cell}$ = 0.25 µm, $L_{cell}$ = 3 µm and an evanescent field depth of 150 nm) in a membrane populated to occupancies of 10% (red line), 15% (green line), 20% (purple line), 25% (cyan line) and 30% (orange line). The same data is shown at two different MSD scales to assist analysis; full range (a) and restricted range (b). For the purpose of comparison, MSD curves for the experimentally-obtained data (black line) and unrestricted diffusion on the curved cell surface (blue line) are also shown. Diffusion through vacancies in the outer membrane simply appears to attenuate the ability for the protein to move, resulting in a lower gradient. There is no indication of restriction occurring on the length scales observed in the experimental data.

Restriction of BtuB diffusion to vacancies in the outer membrane has a significant effect on the rate of diffusion from the starting point. This is particularly evident through comparison of unrestricted diffusion (blue line; Figure 6-18) to diffusion through a membrane with 10% occupancy (red line; Figure 6-18) under otherwise identical conditions; the latter experiences an approximately four-fold reduction in rate of diffusion. With increasing occupancy the ability to diffuse is further reduced; however, there is no indication of the protein being confined to a specific region, as hypothesised.

While restriction is observed for sufficiently high occupancies (25% and 30%), it is on a length scale barely greater than the size of the BtuB itself and as such cannot account for the restricted diffusion observed experimentally. This indicates the current model of vacancy diffusion in the outer membrane is incomplete, with further modifications possibly arising from diffusion of OmpF or the inclusion of inhomogeneities in protein population. These are discussed in more detail in Section 7.5.1.

# Discussion

## Chapter 7

## 7.1 Rationale for studying the effect of torsion on transcription

Common to numerous DNA-dependent enzymatic activities, such as transcription by RNA polymerase, is the separation of the two single-strands in the double helix. Processes resulting in the translocation of this separated region along the DNA would ideally be coupled with rotation of the enzyme complex around the helical twist of the substrate. *In vivo*, the effect of hydrodynamic drag acting on the enzyme and DNA substrate prevents such behaviour and results in twin supercoiled domains [1]; a compaction of supercoil density (overwinding) downstream of the enzyme and a relaxation of supercoil density (underwinding) upstream.

Supercoiling has been previously demonstrated to have a significant effect on the efficiency of transcription initiation and accordingly has been postulated to pose a regulatory role. The careful curation of torsion *in vivo* is performed by the topoisomerase class of enzymes, which are capable of introducing and removing supercoiling as necessary. Despite holding such an important role, DNA torsion is an effect often neglected during *in vitro* single-molecule experiments, where it remains uncharacterised. The aim of the described work is to develop a system capable of reproducibly controlling DNA tether torsion and applied force whilst conducting single molecule fluorescence experiments. With such an instrument, it is possible to perform multiple novel experiments, centred on the effect of transcription-coupled DNA supercoiling; these include probing the efficiency of promoters under specific torsion and investigating the interaction of multiple transcribing polymerases on a single DNA tethers. Experiments are conducted using T7 RNAP, allowing experiments to draw on the benefit of a well characterised single-subunit enzyme, which exhibits significant mechanistic homology with its multi-subunit counterparts from higher organisms.

## 7.2 Atomic force microscopy

AFM is a scanning probe microscopy technique, which can be used in both air and liquid environments. For the application discussed here it excels at imaging individual DNA molecules deposited onto atomically flat substrates, such as mica. This provides a static snapshot of samples, which is useful for both experimental verification that the transcription system is working and to probe inter-RNAP effects, such as enzyme spacing on the template.

Deposition of DNA onto mica was performed reproducibly using a protocol developed by Gassan Suliman. This permitted both characterisation of DNA integrity through contour-length analysis and establishment of an immobilisation baseline that could be used for comparison when introducing transcription complexes. Observation of transcription complexes bound to the DNA substrates proved a more difficult task, with disruption of immobilisation evident. Two hypotheses for this were the decreased stability of DNA on the mica, leading to easier dissociation during sample washing, and the potential formation of aggregates in the sub-optimal conditions of the AFM buffer.

Several experimental modifications were trialled, centred mostly on improving the ability to form stalled transcription complexes and optimising the deposition conditions, yielding stronger links to the mica. Firstly, pre-incubated transcription assays were passed through NucAway spin columns to transfer the buffer from one optimised for transcription (see Section 2.1 for composition) to one more suited for immobilisation on mica (see Section 2.1 for composition). This yielded no observable improvement, highlighting the possibility for sample retention in the spin columns. Due to this concern, subsequent samples were not treated in this manner; simply being deposited in transcription buffer.

To ensure formation of stalled transcription complexes, two methods were used. The first was nucleotide starvation, a common approach to halting transcription whereby the polymerase is unable to progress through omission of one or more nucleotide species. Success of this approach was potentially prevented by the need for incorporation of all four nucleotide species in the first 11 incorporation events at each promoter, thus precluding the ability to fully escape the abortive cycling phase of transcription and form a stable complex. To overcome this, a modified strategy using 3'-dATP was implemented. Incorporation of a nucleotide into the nascent RNA chain requires a hydroxyl group on the 3' ribose carbon; therefore, addition of 3'-dATP (cordycepin) during transcription should cause complexes to stall. As with nucleotide starvation, there was no evidence of an improvement in transcription complex immobilisation. This result indicated that the lack of observed immobilisation may simply originate from poor adhesion between the DNA and mica; an issue amplified by the potentially-destabilising effect of stalled transcription complexes.

The trivalent cationic molecule, spermidine, had been used elsewhere to affect immobilisation of samples on mica for AFM imaging. Implementation here was intended to benefit from mediation of an interaction between the negative charges of the DNA backbone and mica surface. This did appear to facilitate improved immobilisation of DNA; however, as observed elsewhere it was coupled with a condensation of the DNA substrate, which is undesirable due to an increased occurrence of DNA-crossovers. Furthermore, an increase in unbound RNAP was observed, which is highly problematic for identification of legitimate colocalisation events between DNA and enzyme.

Finally, the effect of DNA template length was investigated, since all other reported experiments had been conducted with templates less than 1500 bp. It was possible the longer templates were providing an excessive volume for hydrodynamic drag (during sample washing) to act upon, thus removing them from the mica. For this investigation, a template of 644 bp length was used; however, this did not appear to improve immobilisation. Instead, a reduction in the DNA immobilisation frequency was observed, which implied there may be a more fundamental issue preventing immobilisation of short DNA, such as the buffer conditions.

Ultimately, it was decided that the perceived benefits from analysis of static images of transcription did not offset the time outlay necessary to optimise the system.

### 7.2.1 Future approaches to facilitate observation of transcription complexes

#### 7.2.1.1 Varying buffer salt concentrations to affect sample immobilisation

Buffer concentration is known to have a significant effect on immobilisation properties, as has been demonstrated in numerous published works [91,133]. In particular, variation of divalent salt concentration will affect the ability to immobilise samples as described in Section 3.1.3. However, in all likelihood, this will have a similar effect to the inclusion of the trivalent cation, spermidine, which increased mica-binding of both the DNA template and unbound RNAP (Section 3.3.4). Initial salt concentrations range from omission to 10 mM for both NaCl and $MgCl_2$, since these span the concentrations present in the examples included in Table 3-1.

#### 7.2.1.2 Increasing RNAP radius with T7 RNAP monoclonal antibody

Throughout the previous work it has not been possible to conclusively identify T7 RNAP transcription complexes bound to the template DNA using AFM. It had been assumed this was due to poor sample immobilisation on mica; however, an alternative explanation is an inability to resolve the relatively small, 98 kDa T7 RNAP complex [96] with the current AFM apparatus; indeed, the majority of equivalent experiments (Table 3-1) use the larger, 449 kDa *E. coli* RNAP $\sigma^{70}$ holoenzyme [287]. To address this, it is possible to artificially increase the complex size through addition of T7 RNAP monoclonal antibody, which has a size of 150 kDa [23].

When augmenting any enzyme, the fundamental concern is one of activity inhibition; fortunately, the antibody-binding epitope is positioned at the C-terminus (residues 861-883), well away from the active site [27]. In addition to this, T7 RNAP labelled in this way has been previously shown by Kim and Larson to retain transcriptional activity [27].

$$R_{min} = 0.066M^{\frac{1}{3}}$$

**Equation 7-1 – Minimum protein radius**
Estimating minimum protein radius ($R_{min}$, nm) based on the molecular weight (M, Da) [288]. This relationship assumes a spherical protein shape and partial specific volume of 0.73 ml·g$^{-1}$.

Through the simple relationship shown in Equation 7-1 it is possible to estimate the radius of a protein, assumed spherical in shape, based on its molecular weight [288]. For the application at hand, such an analysis permits a quantitative evaluation of the benefit of conjugating T7 RNAP with its antibody. In the case of T7 RNAP ($M_r$ = ~98 kDa [96]) the estimated minimum radius is ~3 nm, which is in agreement with the average size measured from the crystal structure of the elongation complex (PDB: 1H38) of ~3.5 nm. Similarly, the estimated minimum radius for a typical antibody ($M_r$ = ~150 kDa [23]) is 3.5 nm; however, this differs by a greater degree from an equivalent antibody crystal structure (PDB: 1IGT), which yields a radius of ~ 7 nm in the plane of the protein and 2.4 nm normal to it. This difference is due to the elongated, rather than globular, form of the antibody. Irrespective of the exact protein size, when observed through AFM, addition of T7 RNAP antibody should offer at least a two-fold increase in complex size with no clear side-effects.

### 7.3 Horizontal magnetic tweezers microscope

Several techniques exist, which are capable of providing physical manipulation of individual tethers; however, they come with disadvantages, precluding their implementation here. Optical tweezers provide a large force range, but implementation of torsional control is unnecessarily complicated, requiring complex optical geometries. Conversely, hydrodynamic extension of tethers is relatively simple to implement and can yield force-control; however, it is incompatible with torsional control of tethers. Generally, torsional control of individual DNA molecules is achieved using a magnetic tweezers system, where the molecule is tethered between a stationary surface and superparamagnetic microsphere. This microsphere is manipulated using an applied magnetic field, thus permitting both force and torsional control. Despite this advantage, the standard magnetic tweezers configuration uses a tether perpendicularly-orientated with respect to the microscope focal plane. As such, biological activity has to be elucidated from motion of the microsphere rather than through direct single-molecule fluorescence observation.

An emerging method for combining the micromanipulation benefits of magnetic tweezers with single-molecule fluorescence imaging is the horizontal magnetic tweezers microscope. Fundamentally similar to the standard magnetic tweezers configuration, the tethers are pulled horizontally using a pair of magnets to the side of the sample. Due to the common requirement that magnets be brought close to the sample, systems often have to reach a compromise between magnitude of force, magnification (and resolution limit) and the formation of truly horizontal tethers. The approach implemented here was designed for a balance between all three, unlike existing systems where generally two are chosen at the detriment of the third [74,76,75,77].

In the reported configuration, horizontal tethers are formed between 9 µm diameter microspheres and superparamagnetic (1 µm or 2.8 µm diameter) microspheres. In addition to acting as the vertical tethering substrate, the 9 µm microspheres serve a structural role, separating the upper and lower microfluidic chamber substrates (such as a glass coverslip and quartz slide). The thin channel minimises the background fluorescence arising from bulk excitation of the reaction mixture. Tethering to each microsphere is achieved using end-functionalisation of the DNA; digoxigenin to anti-digoxigenin at the 9 µm microsphere interface and biotin to streptavidin at the superparamagnetic microsphere interface. Using

this labelling system and a simple microfluidic chamber preparation protocol, tethers have been reliably generated and characterised.

The novel nature of the microscope required custom fabrication using a combination of the commercially-available ThorLabs 30 mm cage system and components designed and manufactured in-house. This design permits easy configuration rearrangements and augmentation. Optically, the microscope uses a dual illumination system; necessary for simultaneous force characterisation and fluorescence imaging. Bright-field, confined to the blue end of the spectrum (~450 nm) is used for microsphere visualisation, where microsphere displacement is indicative of the applied magnetic force. Wide-field laser epifluorescence illumination ($\lambda_{ex}$ = 488 nm) is used to fluorescently excite the fluorophore labelling the polymerase. Both illumination systems can be visualised simultaneously, thus permitting real-time force feedback; achieved either on the same CCD chip (OptoSplit II) or on separate cameras (DualCam). Through appropriate choice of tube lens focal length, magnifications up to 100x can be observed. Although the optics are diffraction limited at 50x, this additional magnification spreads the image over more pixels on the camera CCD, thus improving the ability to localise observed particle centres.

Force calibration was performed using equipartition analysis, which relates thermally-induced microsphere displacement to the restoring force arising from applied force acting parallel to the tether equilibrium position. This is measured as a function of distance between the superparamagnetic microsphere and magnet pair. For calibration, a theoretical force response is calculated using the Biot-Savart law, which models the applied magnetic field, from which the force acting on the superparamagnetic microsphere can be calculated. Moderate agreement between theory and experimental data was observed for a variety of experimental conditions encompassing different tether lengths, superparamagnetic microsphere stocks and cameras. While the averaged force response curves were in good agreement, they differed from the Biot-Savart prediction significantly in terms of magnitude, but not characteristic shape. Through characterisation of key components of the magnetic tweezers system it was not possible to ascertain an origin for this discrepancy; however improved agreement was observed for data collected using smaller microspheres, thus indicating some form of microsphere size-related influence. Such a relation agrees with the trend predicted through analysis of spatial, thermal and

gravitational factors that the larger microspheres would interact with the channel surface significantly more frequently.

Tethers were also characterised through analysis of the extension in response to an equipartition function-measured applied force. Spatial occlusion preventing the superparamagnetic microsphere occupying a time-averaged position coincident with the tethering point necessitated measurements relative to the position at maximum possible extension. The extension at this point was based on assumed agreement between the predicted and measured forces described previously, with this force value used to calculate tether extension according to the worm-like chain model (WLC) [149]. Strong agreement between the WLC-predicted extension curve and that obtained through analysis of the superparamagnetic microsphere position relative to stationary markers in the sample (such as the 9 μm diameter microspheres) was observed. Slight disagreement in the low-force values is likely due to the aforementioned inability for the observed tether extension to reach zero. This observation contributes to validation of the particle tracking and equipartition force measurement approach described above. Furthermore, it highlights an incomplete picture of the magnetic tweezers being provided by the Biot-Savart method as the source for the observed force response disagreement.

### 7.3.1 Future modifications to the microscope configuration

#### 7.3.1.1 Vertical position measurement of superparamagnetic microsphere

At low applied forces, the superparamagnetic microsphere undergoes relatively large thermally-induced displacements perpendicular to the DNA tether. These displacements can potentially bring the microsphere into contact with the microfluidic channel surface. This contact may result in attenuation of microsphere displacement and thus erroneous force measurements via equipartition analysis.

It is possible to identify microspheres significantly close to the channel surface through relative analysis of the diffraction patterns arising from the 9 μm tethering-substrate microsphere and the superparamagnetic microsphere. This technique is well established and is routinely applied in the standard vertical magnetic tweezers configuration, where it is used to determine changes in DNA end-to-end length. Reference lookup tables for the diffraction pattern profile are pre-compiled by scanning the microscope focal plane in

bright-field illumination through the microsphere of interest. These are subsequently used to calculate the distance between the three-dimensional microsphere centre and the microscope focal plane, thus yielding a measure of vertical position. With separate lookup tables for the 9 μm diameter and superparamagnetic microspheres and the assumption that the microfluidic channel centre coincides with the 9 μm microsphere centre, the distance between the superparamagnetic microsphere and channel surface could be elucidated.

Implementation of such a system has thus far not been possible due to the low vertical resolution of the objective lens control; 10 μm for the z-axis translational stage (CT1; ThorLabs, New Jersey, USA). To accurately measure the height-dependence of the diffraction pattern, greater control over either the sample or objective lens position is necessary; this could be easily achieved for the magnetic tweezers configuration using a one-dimensional motorised translational stage (MT1/M-Z8; ThorLabs, New Jersey, USA), which has a vertical resolution of 0.1 μm.

#### 7.3.1.2 High throughput tethering substrate

Force characterisation of the magnetic tweezers microscope (Section 4.7) has used DNA tethered to a 9 μm diameter latex microsphere (PAG-AD-MS). While this simple approach to tethering is adequate for the relatively low through-put nature of the experiments conducted, a more robust and higher capacity technique is sought for general use. Specific improvements required of an advanced tethering system are a larger tethering area, compatibility with microfluidics and an easily identifiable tether attachment point. With the existing system, magnetisation and subsequent interaction of proximate superparamagnetic microspheres limits a single tether to each PAG-AD-MS. In addition to this, the assumed homogeneous PAG-AD-MS functionalisation precludes identification of the exact tethering location. One possible approach to address this is the use of established micro-fabrication techniques to generate well-defined structures on the slide surface. A hypothesised method for achieving this has been developed in conjunction with Steven Johnson and Jonathan Cremer from the Department of Electronics (University of York) and is shown in Figure 7-1.

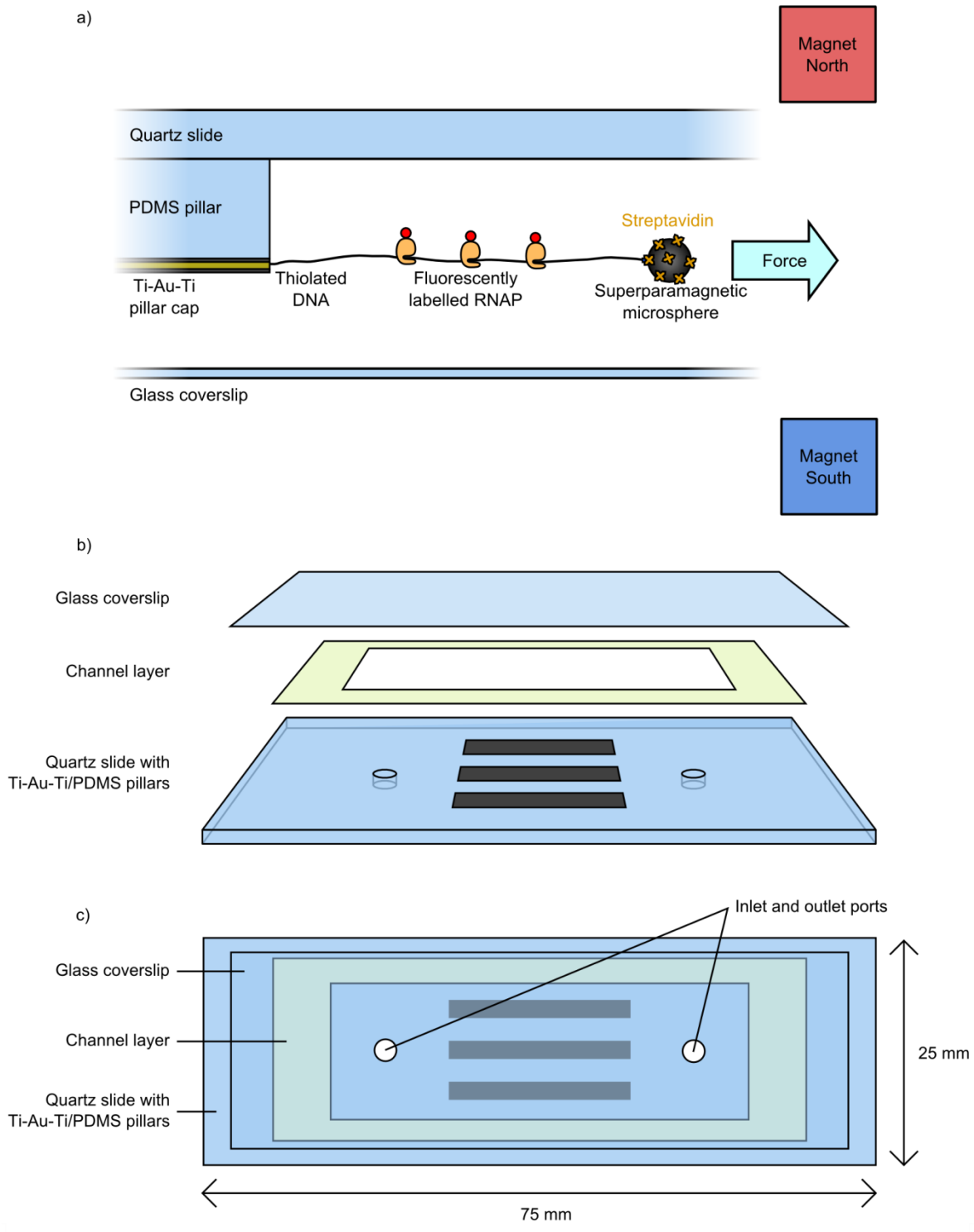


**Figure 7-1 – Micro-fabricated pillars for DNA tethering**
Proposed system for DNA tethering in horizontal magnetic tweezers microscope using micro-fabricated PDMS pillars capped with titanium and gold. a) DNA is tethered at one end via thiol-gold coupling and extended using the typical magnet-pair configuration. b) Exploded diagram of the microfluidic cell. Three metal-capped pillars are formed on the quartz slide surface and enclosed by a polymer channel forming material and glass coverslip. The channel forming material would likely be a thin PDMS film or SecureSeal adhesive sheets (Grace Bio-Labs, Inc., Oregon, USA). c) Buffer exchange is implemented using a basic microfluidic system comprising a thin chamber with a single inlet and outlet port at either end.

The proposed method involves creating pillars on the quartz slide with a titanium-gold-titanium layered caps (Figure 7-1a). Several possible approaches exist for the formation of such pillars, but likely routes include spin-coating and development of PDMS using reactive ion etching [289,290] or direct patterning of the quartz slide using hydrofluoric acid [291–294]. During fabrication, thin layers of gold and titanium would be deposited using standard evaporative methods. The role of the lowest titanium layer is as an adhesive between the PDMS pillar and gold layer and the upper titanium layer as a protective layer above the gold. Through thiol coupling between the gold layer and a thiol group introduced onto the end of the DNA tethers, covalent bonds between the micro-fabricated structures and DNA tethers would form.

Pillars are housed inside a simple, single-inlet single-outlet microfluidic device, which could be constructed from either SecureSeal adhesive sheets (Grace Bio-Labs, Oregon, USA) or thinly spun PDMS (Figure 7-1b and c). PDMS benefits from a number of material advantages explained in detail in Section 5.2.1; of particular use here are chemical inertness, optical transparency, mechanical rigidity and the ability to be spun to user-defined thicknesses.

Following successful development of the described system it is intended that multiple tethers are visible in a single image region. An ideal tether density has been demonstrated by Danilowicz *et al.* for a basic system using a functionalised glass capillary placed inside a square microcell (discussed in Section 1.4.4.1) [74]. Key improvements over the published approach would be the ability to immobilise tethers at a well-defined vertical position coinciding with the thin gold layer. Additionally, through well-characterised spin-coating of PDMS, the channel height could be kept at a minimum to reduce background fluorescence.

## 7.4 Tethered DNA experiments

Characterisation and optimisation of the DNA tethering system was conducted using laminar flow extension. While this is not capable of exerting torsional control over the substrate it can be coupled with high numerical aperture fluorescence microscope techniques, allowing for easy optimisation of surface passivation and to limit photobleaching, photocleavage.

Compatibility of laminar flow extension with fluorescence techniques, such as prism-coupled Total Internal Reflection Fluorescence (TIRF) microscopy requires specially adapted microfluidic sample delivery systems. These devices have a nominal thickness barely more than a typical microscope slide and coverslip combination, thus allowing use of oil-immersion objective lenses with working distances of below 150 µm. Such physical properties are possible using solid photoresist (30 µm thick) as the channel forming material and keeping the air-interface and storage reservoirs off-centre, away from the observation volume. Lithographic development of the fluid-handling layer permits rapid prototyping of channel configurations. Flow is generated using a resistive pressure network, which divides an applied pressure difference in two in a manner analogous to Ohm's law for electrical resistance. The output pressures are applied to hermetically-sealed chambers above the reagent reservoirs, resulting in flow towards the outlet reservoir. Varying the pressure ratio alters the reagent flow velocities relative to each other, shifting the laminar flow interface, whilst maintaining a constant downstream flow-rate.

A functional demonstration of the microfluidic system was performed using repeated staining of surface-immobilised DNA using the intercalating fluorophore, YOYO-1. With this, complete buffer exchange across the observation volume was recorded for times less than 5 seconds. Notably, the developed microfluidic platform also benefits from easy implementation facilitated by a non-reliance on expensive equipment and clean-room facilities.

For optimisation of DNA tethers and single-molecule fluorescence conditions, TIRF microscopy is ideal. The limited depth of the fluorescence excitation volume (~100 nm with exponentially decaying intensity from the channel surface) provides a significant contrast improvement over epi-illumination. Such high signal to noise ratio was used to optimise buffer conditions, in particular minimising photocleavage of tethered DNA substrates. Photocleavage arises due to the generation of reactive oxygen species (ROS) by laser-excitation, but can be attenuated through inclusion of oxygen scavenger systems. Of the two systems trialled, degassed buffer and the glucose oxidase-catalase oxygen scavenger system, the latter showed the most significant improvement. Manual identification of photocleavage events gave an approximate 10-fold increase in tether

lifetime when using the oxygen scavenger; specifically, an improvement in maximum observed lifetime from 3 seconds to 30 seconds. The presence of glucose also served to curtail the rate of photobleaching, thus enabling the use of lower concentrations of YOYO-1.

Further optimisation was required in the form of surface passivation, minimising non-specific immobilisation of the TransFluoSphere (TFS) microspheres used to individually label the polymerases. Early investigations in this area concentrated on identifying the surface functionalisation components responsible for mediating the TFS interaction. From these tests a significant increase in immobilisation was observed upon addition of the whole anti-digoxigenin antibody. Having identified this source, further attempts were made to passivate any unbound protein using the reducing agent DTT, digoxigenin-BSA (dig-BSA), the anti-dig FAB fragment and incubation of the TFS with BSA. Significant improvements were finally obtained through increasing the DNA concentration to a value closer to the dissociation constant for the anti-digoxigenin - digoxigenin bond, yielding vastly improved tethering rates. Accordingly, it was possible to reduce the surface functionalisation concentrations whilst maintaining sufficient DNA coverage to permit parallel experiments.

### 7.4.1 Future work to probe transcription-coupled DNA supercoiling

#### 7.4.1.1 Single-molecule fluorescence observations of transcription

Reliable and reproducible conditions for immobilisation of individual DNA molecules in a microfluidic device compatible with the TIRF microscope have been developed. In addition to this, wild-type T7 RNAP has been labelled and purified with a biotin group. This enables attachment to streptavidin-conjugated fluorophores such as TransFluoSpheres (TFS) or quantum dots. The next step towards observation of transcription at the single molecule level will combine these two achievements to enable the active fluorophore-labelled polymerase to be visualised transcribing in real-time.

It is preferable to conduct these optimisation experiments using the TIRF microscope due to the superior contrast resulting from limited bulk volume excitation. Through implementation of a dual-inlet microfluidic device, as described in Section 5.2.4, surface-immobilised DNA can be exposed to separate initiation and viewing mixtures. In this

scenario, the former would contain a sufficiently high concentration of pre-incubated RNAP/TFS conjugates, in addition to all the necessary components for transcription, to facilitate frequent transcription initiation events. Conversely, the viewing mixture would contain all the necessary transcription components, but lack RNAP and TFS; therefore, limiting the fluorescence signal to those RNAP/TFS conjugates transcribing the substrate.

#### 7.4.1.2 Observation of transcription using magnetic tweezers microscope

Following optimisation of the single-molecule transcription assay, experiments can be conducted using the horizontal magnetic tweezers microscope. Unlike the aforementioned microfluidic system for TIRF, the current protocol for the magnetic tweezers microscope uses irreversible sealing of sample chambers prior to imaging. *In situ* buffer exchange is not possible due to the need for samples to be introduced via the capillary action of tissue paper (Section 2.7.3). Additionally, chamber sealing assists in minimising fluid flow, which may arise from sample movement and would result in inconsistent force application on tethered microspheres.

The inability to perform buffer and sample exchange imposes a limit on the fluorophore concentration such that the fluorescence signal isn't dominated by unbound RNAP/TFS conjugates. Although this can be overcome with reduced RNAP/TFS concentrations of ~1 nM, it is approximately 5-fold below the dissociation constant for promoter binding by T7 RNAP [240]. For a system already at sub-optimal conditions of room temperature this represents an undesirable restriction. An alternative approach uses transcription elongation complexes pre-stalled either through nucleotide starvation (Section 0) or use of 3'dATP (Section 3.3.3); however, this precludes observation of active complexes. The limitations of the current sample preparation protocol are one of the main reasons for development of a more robust tethering system (Section 7.3.1.2).

Irrespective of sample chamber design, the magnetic tweezers microscope permits torsional control of tethers and facilitates the observation of transcription at user-defined DNA superhelical densities. Implementation of torsional control requires substrate DNA to be attached at either end through both backbone strands; a process for which a protocol has been published by Seol and Neuman [70]. This protocol involves PCR production of short DNA handles with a reaction mixture doped with a small amount of a relevant

nucleotide analogue, such as biotin-dUTP. The PCR products are chosen to contain a single restriction endonuclease site, which yields sticky ends, and has a single equivalent site in the substrate DNA. Digestion and subsequent ligation of the PCR handles and substrate DNA yields the final double end-labelled template.

### 7.5 Diffusion simulations of the colE9-BtuB complex

Competition between bacterial strains has led to the evolution of cytotoxic proteins, known as bacteriocins. These proteins are released by the producing cell in situations of limited local resources and are intended to kill closely related competing strains. Of particular interest are the *E. coli* bacteriocins, known as colicins. Colicin E9 (colE9), an endonuclease type colicin, is formed from three domains; a coiled-coil comprising the R domain, which binds the vitamin $B_{12}$ receptor in the outer membrane of the target cell; a structured C-terminal domain, which exhibits endonuclease activity; and an unstructured N-terminal domain, which is required for translocation of the protein into the periplasm of the target cell.

Experimentally-obtained data for diffusion of the colE9-BtuB shows clear evidence of restricted two-dimensional motion. This is characterised by a reduction of the mean square displacement (MSD) from the origin of diffusion as a function of time, to an eventual plateau. The origin of such behaviour is unknown; however, parameters describing the behaviour of this motion can be elucidated through computational simulation. Such simulations were performed using the Monte Carlo approach, whereby protein motion is decomposed into a series of time steps, which take place over a short time interval in a random direction.

From an initial simulation solely describing unrestricted diffusion in a two-dimensional plane, additional experimental conditions were introduced and their effect on the measured MSD analysed. First, the effect of diffusion on the curved *E. coli* cell outer membrane and subsequent transformation to a two-dimensional image, as viewed in the microscope, was modelled. This served to notably decrease the MSD and introduce a slight time-dependence; however, it was not characteristic of the experimental data. The depth of the evanescent field used to excite fluorophores in the experiment was also implemented, since this would only permit visualisation of the first 100-200 nm of the sample from the

microscope slide surface. Across this range there was negligible effect on the measured MSD, with the main effect being a reduction in the number of particles diffusing in the observable region and the resulting reduction in precision. The final experimental condition probed was random cell orientation in the plane of observation. This yielded no appreciable difference in measured MSD, as would be expected, since no positional data is lost; instead, it is merely rotationally transformed.

With no clear evidence of the experimentally-observed restricted diffusion resulting from the process of data acquisition, compartmentalisation of the outer membrane was investigated. Initially, a basic square mesh model was implemented, whereby proteins are free to diffuse within a square compartment, but are subject to probabilistically-determined access to adjacent compartments. With this approach, good agreement between the experimental and simulated MSD curves was obtained when using non-permeable compartments. Agreement was reduced significantly with only minor compartment permeability, indicating an absolute restriction to movement within the mesh. Through optimisation of the diffusion coefficient ($D$) and mesh cell edge length ($L_{mesh}$) it was possible to align the experimentally-obtained and simulated MSD data with high confidence. This approach yielded optimal values of $D = 0.03 \pm 0.0025\ \mu m^2 s^{-1}$ and $L_{mesh} = 0.1875 \pm 0.00125\ \mu m$, both of which are in good agreement with measurements reported elsewhere [266].

A physical origin for the observed restriction was investigated in terms of finite protein size for both BtuB and two major outer membrane components, the porin trimer OmpF and monomer OmpA. Diffusion of BtuB through a stationary matrix of randomly positioned OmpF and OmpA was performed for outer membrane occupancies spanning the biologically-relevant range 10% to 30%. At low occupancies (10% and 15%), diffusion through vacancies in the simulated region resulted in no appreciable restriction; however, the ability of BtuB to diffuse was greatly reduced. This effect was increased at higher occupancies to the point where restriction did occur (25% and 30%), but on length scales barely larger than the protein itself. Such a result is not consistent with the experimentally-obtained data and indicates additional factors need to be considered.

### 7.5.1 Future modifications to Monte Carlo diffusion simulations

#### 7.5.1.1 Including inhomogeneities in membrane population

While implementation of an impermeable square mesh was successful at describing the experimentally-observed restricted diffusion, it has no apparent physical origin. Conversely, permitting the colE9-BtuB complex to diffuse through vacancies between OmpF and OmpA has biological relevance, but was unable to describe the physical picture. Further modifications to the diffusion simulation could probe the effect of inhomogeneities in the outer membrane.

A similar approach has been reported by Fujiwara *et al.* for a eukaryotic system, whereby diffusing species are confined within a square mesh, but where the compartment boundaries are formed by finite volume proteins [274]. While this isn't directly applicable to the present bacterial system, due to the assumption that proteins are immobilised on the cell's actin skeleton, it demonstrates how membrane compartmentalisation and vacancy diffusion can be combined.

An alternative approach would be the inclusion of a time dependency on the membrane population, with OmpF diffusing in addition to BtuB. Such a dynamic environment is biologically relevant since OmpF has been reported to diffuse at a rate of 0.006 $\mu m^2 s^{-1}$ within a restricted compartment of approximately 100 nm [266]. Indeed, the observation that OmpF also undergoes restricted diffusion across a shorter range than BtuB supports the vacancy diffusion hypothesis; with the larger OmpF size (~6.8 nm across the trimer compared to ~4.6 nm for BtuB) preventing passage to regions accessible to BtuB.

# Appendix

# Appendix A. Construction details for the magnetic tweezers microscope

## I. Optical component spectral details

The following are optical component spectra for the horizontal magnetic tweezers microscope (Section 4.4.1).

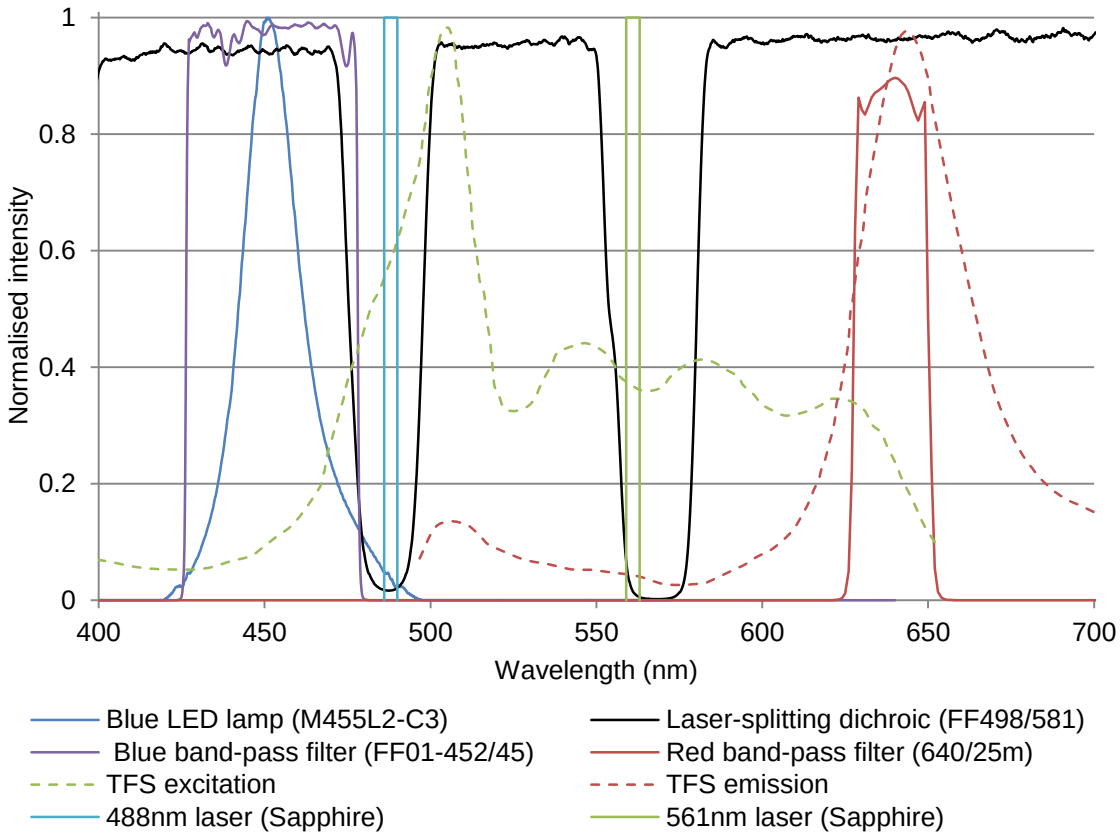


**Figure 8-1 – Spectra for optical components in horizontal magnetic tweezers system**
Included in this plot are vendor-supplied transmission spectra for dichroic filter (FF498/581; Semrock, Rochester, New York, USA), blue band-pass filter (FF01-452/45; Semrock, Rochester, New York, USA), red band-pass filter (D640/25m; Comar Optics Ltd., Cambridge, UK), blue LED lamp (M455L2-C3; ThorLabs, New Jersey, USA), two lasers (488 nm and available 561 nm; both Sapphire; Coherent, Inc., California, USA) and the excitation and emission spectra for the TransFluoSpheres (TFS; Invitrogen).

## II. Components list

The following components were ordered from ThorLabs (New Jersey, USA).

| Item | Code | Qty. |
|---|---|---|
| Cage Assembly Rod, 1" Long, Ø6 mm | ER1 | 2 |
| Cage Assembly Rod, 2" Long, Ø6 mm | ER2 | 4 |
| Cage Assembly Rod, 3" Long, Ø6 mm | ER3 | 4 |
| Cage Assembly Rod, 6" Long, Ø6 mm | ER6 | 4 |
| Cage Assembly Rod, 8" Long, Ø6 mm | ER8 | 8 |
| Cage Assembly Rod, 10" Long, Ø6 mm | ER10 | 4 |
| Cage Assembly Rod, 12" Long, Ø6 mm | ER12 | 4 |
| Rod Adapter for Ø6 mm ER Rods | ERSCA | 4 |
| 30 mm Cage Plate Adapter | CP02B | 4 |
| 30 mm Cage Plate with 35 mm Clear Aperture | CP03/M | 1 |
| 30 mm Cage System, XY Translating Lens Mount for Ø1" Optics | CXY1 | 2 |
| Post-Mounted Iris Diaphragm, Ø8.0 mm Max Aperture | ID8/M | 1 |
| SM1 Threaded 30 mm Cage Plate, 0.35" | CP02/M | 2 |
| SM1 (Ø1.035"-40) Coupler, External Threads, 0.5" Long | SM1T2 | 1 |
| Adapter with External M25 x 0.75 Threads and Internal SM1 Threads | SM1A11 | 1 |
| Adapter with External SM1 Threads and Internal M25 x 0.75 Threads | SM1A12 | 1 |
| Mounted Ø1" Achromatic Doublet, f=150 mm, ARC: 400-700 nm | AC254-150-A-ML | 1 |
| Mounted Ø1" Achromatic Doublet, f=200 mm, ARC: 400-700 nm | AC254-200-A-ML | 1 |
| Mounted Ø1" Achromatic Doublet, f=400 mm, ARC: 400-700 nm | AC254-400-A-ML | 1 |
| Cube-Mounted E02 Dielectric Turning Mirror, 400-750 nm | CM1-E02 | 1 |
| 30 mm Cage System Cube, 4-Way | C4W | 1 |
| Rotatable Cage Cube Platform for C4W/C6W | B3C | 1 |

| | | |
|---|---|---|
| Blank Cover Plate with Rubber O-Ring for C4W/C6W, Metric | B1C/M | 1 |
| Cage-Compatible Dichroic Filter Mount | FFM1 | 1 |
| 1/2" Travel Translator with CT101 for 30 mm Cage System | CT1 | 1 |
| Cold White Collimated LED for Nikon Eclipse, 1600 mA | MCWHL2-C3 | 1 |
| Royal Blue (455 nm) Collimated LED for Nikon Eclipse, 1600 mA | M455L2-C3 | 1 |
| T-Cube LED Driver, 1200 mA Max Drive Current | LEDD1B | 1 |
| 15 V Power Supply Unit for a Single T-Cube | TPS001 | 1 |

## Appendix B. Construction details for microfluidic devices

### I. Schematic diagram of the resistive pressure divider

Flow in the microfluidic devices is generated by applying pressures to sealed voids above fluid reservoirs connected to the channels. The pressure can be divided between two outlets using a system analogous to Ohm's circuital law (Figure 8-2) [228], with the ratio between the two varying whilst maintaining a constant net rate. In this analogy, the potential difference is the difference between applied pressure from the building's filtered air supply, $P_{wall}$ and atmospheric pressure. Tubing resistances, $R$, $R_{v1}$, $R_{v2}$ and $xR$, are characteristic of the length and radii of the respective tubing. Net flow rate can be altered using the valve, $R_{v1}$. The ratio between pressures $P_1$ and $P_2$ is altered using a valve, $R_{v2}$. It is possible to switch the ratio using the inversion dial represented by the curved arrow. Earth symbols signify tubing which is open to atmospheric pressure at one end.

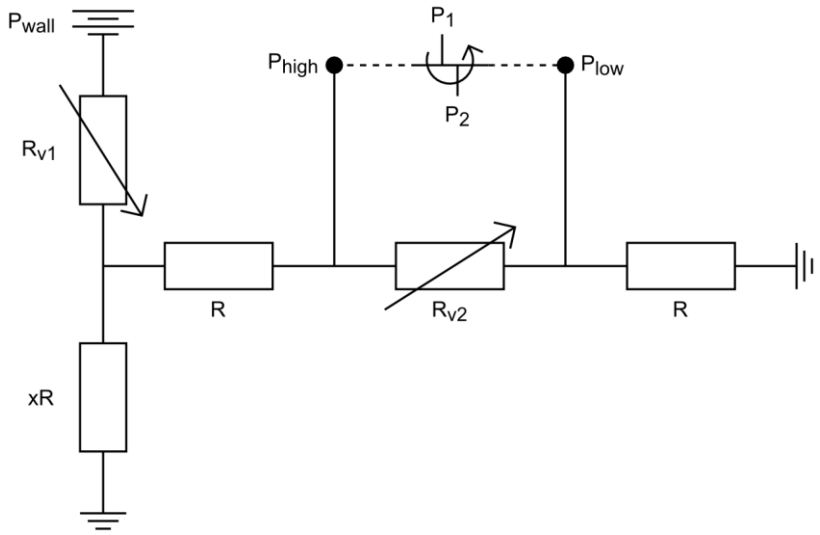


**Figure 8-2 – Schematic diagram of the resistive pressure divider**
This system is analogous to Ohm's circuital law for electrical resistance, with resistances ($R$) generated by tubing of different lengths and radii. An input pressure from a compressed air supply is divided between two outlets, $P_{high}$ and $P_{low}$. The Figure adapted from Braschler *et al.* [228]

## II. PDMS block preparation

Reservoir preparation:

- Disassemble the PDMS mould (Figure 8-3)
- Clean each piece of the mould using a cloth
- To resize pins to desired radii, push into ~9 mm lengths of plastic tubing
- Slide the pins back into the mould, with tubing on inner side of mould
- Place three glass slides on the top surface of the bottom mould piece
- Reassemble mould, so the central glass slide completely covers the bottom of the reservoir void (Figure 8-3a)
- To check the mould is tight, tap the corners of the overhanging slides. If they move, the mould is not tight enough

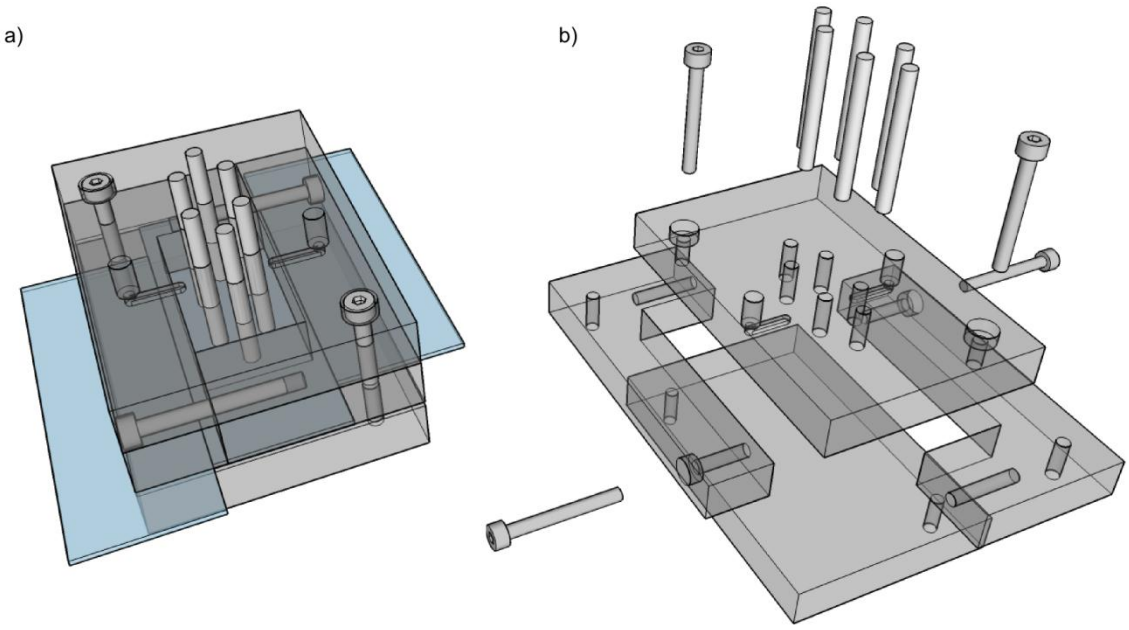


**Figure 8-3 – Diagram of the custom-made PDMS mould**
The PDMS mould is constructed from four plastic blocks, held together using four bolts. a) A glass slide is placed between the bottom two layers of the mould for the PDMS block to form onto. An addition two slides are placed either side to provide support when the mould is tightened. Reservoirs are created using six pins, pushed through holes in the top layer of the mould. PDMS is injected through one of the two side ports, with the other used to vent the escaping air. b) Exploded view showing mould in disassembled state.

Preparation and moulding of PDMS:

- Remove the base and curing agent (Sylgard 184 Silicone Elastomer; Dow Corning Corp., Midland, Michigan, USA) from the refrigerator
- Add 10 parts base and 1 part curing agent in a plastic tray and mix thoroughly
- Pour the PDMS into a syringe and replace the piston to a position where approximately half of the syringe is air

- Place the syringe, nozzle-up, in a de-gassing chamber for 10 minutes
- Repeat de-gassing if bubbles are still present
- Push the PDMS in the syringe to the tip of the nozzle
- Put the nozzle firmly into the filling hole in the mould
- Fill the mould to ¾ capacity
- For the final ¼, tilt the mould left and right to ensure all bubbles are removed through the venting hole (opposite the filling hole)
- Place the mould flat and fill the filling and venting holes with PDMS, so any space in the mould created by escaping bubbles is filled with PDMS
- Cure the polymer at 70 $^{0}$C overnight

Removal of PDMS:

- Clear any excess PDMS from the top of the mould
- Remove all the screws from the mould using the hex key
- Carefully ‘wiggle’ the mould pieces until they separate from the PDMS block
- Use a hex key to push on the pins through the PDMS block and top mould
- Remove any remaining tubing pieces in the PDMS using tweezers
- Use a razor blade to remove any excess PDMS from the block
- Use the razor blade to cut the block in half

## Appendix C. Derivations of equations

### I. Biot-Savart law

Derivation expanded from that reported by Lipfert *et al.* [99]. Force (*F*) acting on a superparamagnetic microsphere from an externally-applied magnetic field is given by Equation 4-1 (Section 4.2.2). This shows that force is a function of gradient of the dot-product of microsphere magnetisation (*m*) and the magnetic field (*B*). As such, it is necessary to compute the magnetic field as a function of distance from the magnet pair (Equation 4-3).

In the monoaxial case (Figure 4-2), all elements need to be evaluated; however, the contributions from L2, L4, R2 and R4 can be grouped together, as can those from L1 and R1 and from L3 and R3. The magnetic field along the z-axis is therefore given by Equation 8-1.

$$B_z = \frac{B_r}{4\pi}\left[\int \frac{2L}{r^3}dzdy + \int \frac{2h-L}{r^3}dzdx + \int \frac{2h+L}{r^3}dzdx\right]$$

**Equation 8-1 – Magnetic field along the z-axis (monoaxial case)**
Evaluation of Equation 4-3 for the monoaxial case yields a series of three integrals; each describing the field from a series of equivalent elements. The numerator of the first integral is the sum of the distance between the microsphere position and the element along the y-axis for elements L2, L4, R2 and R4, for the second integral it is the equivalent distance along the x-axis for elements L1 and R1 and for the third integral it is the equivalent distance along the x-axis for elements L3 and R3. A description of the distance (*r*) between the microsphere and element is included in Equation 8-2.

$$\begin{aligned} B_z = \frac{B_r}{4\pi}\Bigg[&\int_{g/2}^{g/2+L}\int_{-L/2}^{L/2}\frac{2L}{(z^2+(L/2)^2+(h-y)^2)^{3/2}}dydz \\ &+\int_{g/2+L}^{g/2}\int_{-L/2}^{L/2}\frac{2h-L}{(z^2+x^2+(h-L/2)^2)^{3/2}}dxdz \\ &+\int_{g/2}^{g/2+L}\int_{-L/2}^{L/2}\frac{2h+L}{(z^2+x^2+(h+L/2)^2)^{3/2}}dxdz\Bigg] \end{aligned}$$

**Equation 8-2 – Inclusion of microsphere to integral element separation (monoaxial)**
A full geometric description of the monoaxial configuration z-axis magnetic field is obtained through inclusion of the microsphere to element separation (*r*). Magnetic field along the z-axis is a function of the magnet remanence ($B_r$), magnet edge length (*L*), magnet separation (*g*) and the microsphere to coordinate origin separation (*h*; see Figure 4-2).

For the biaxial case, Figure 4-2 demonstrates that contributions to the magnetic field along the z-axis from elements L2 and L4 will cancel with R2 and R4 (respectively). Therefore, only the "side" edges (L1, L3, R1 and R3) contribute to the magnetic field. The magnetic field along the z-axis is given by Equation 8-3.

$$B_z = \frac{B_r}{4\pi}\left[\int \frac{-2(h-y)}{r^3}\,dydx + \int \frac{2(h-y)}{r^3}\,dydx\right]$$

**Equation 8-3 – Magnetic field along the z-axis (biaxial case)**
As with the monoaxial case, the Biot-Savart representation can be described by grouped integrals. Since elements L2, L4, R2 and R4 cancel, there are only two integrals. The first of these describes elements L1 and R3, with a numerator equal to the distance between the microsphere and integral element. Similarly, the second integral corresponds to elements L3 and R1.

$$B_z = \frac{B_r}{4\pi}\left[\int_{-L/2}^{L/2}\int_{-L/2}^{L/2} \frac{-2(h-y)}{(x^2+(h-y)^2+(g+L)^2)^{3/2}}\,dydx + \int_{-L/2}^{L/2}\int_{-L/2}^{L/2} \frac{2(h-y)}{(x^2+(h-y)^2+g^2)^{3/2}}\,dydx\right]$$

**Equation 8-4 – Inclusion of microsphere to integral element separation (biaxial)**
A full geometric description of the biaxial configuration z-axis magnetic field is obtained through inclusion of the microsphere to element separation ($r$). Magnetic field along the z-axis is a function of the magnet remanence ($B_r$), magnet edge length ($L$), magnet separation ($g$) and the microsphere to coordinate origin separation ($h$; see Figure 4-2).

## II. Biot-Savart law for off-axis superparamagnetic microsphere placement

Evaluating the Biot-Savart law for each current element in terms of the split magnet-magnet separation distances $g_L$ and $g_R$ (Figure 4-13) yields magnetic field components in the y and z directions. This follows the same approach used in Appendix C-I, but without cancellation of equivalent elements.

$$
\begin{aligned}
B_y = \frac{B_r}{4\pi}\Bigg[ & \int_{-L/2}^{L/2}\int_{-L/2}^{L/2} \frac{g_L + L}{(x^2 + (h-y)^2 + (g_L + L)^2)^{3/2}}\, dxdy \\
& - \int_{-L/2}^{L/2}\int_{g_L+L}^{g_L} \frac{L/2}{((L/2)^2 + (h-y)^2 + z^2)^{3/2}}\, dzdy \\
& - \int_{-L/2}^{L/2}\int_{-L/2}^{L/2} \frac{g_L}{(x^2 + (h-y)^2 + g_L^2)^{3/2}}\, dxdy \\
& - \int_{-L/2}^{L/2}\int_{g_L}^{g_L+L} \frac{L/2}{((L/2)^2 + (h-y)^2 + z^2)^{3/2}}\, dzdy \\
& + \int_{-L/2}^{L/2}\int_{-L/2}^{L/2} \frac{g_R}{(x^2 + (h-y)^2 + {g_R}^2)^{3/2}}\, dxdy \\
& + \int_{-L/2}^{L/2}\int_{g_R+L}^{g_R} \frac{L/2}{((L/2)^2 + (h-y)^2 + z^2)^{3/2}}\, dzdy \\
& - \int_{L/2}^{L/2}\int_{L/2}^{L/2} \frac{g_R + L}{(x^2 + (h-y)^2 + (g_R + L)^2)^{3/2}}\, dxdy \\
& + \int_{-L/2}^{L/2}\int_{g_R}^{g_R+L} \frac{L/2}{((L/2)^2 + (h-y)^2 + z^2)^{3/2}}\, dzdy \Bigg]
\end{aligned}
$$

**Equation 8-5 – Y-axis component of off-axis biaxial configuration**
A full geometric description of the y-axis component of the magnetic field arising for the off-axis biaxial configuration is obtained through individual evaluation of all eight integral elements. Magnetic field along the y-axis is a function of the magnet remanence ($B_r$), magnet edge length ($L$), split magnet separations relative ($g_L$ and $g_R$; see Figure 4-13) and the microsphere to coordinate origin separation ($h$).

$$B_z = \frac{B_r}{4\pi}\left[-\int_{-L/2}^{L/2}\int_{-L/2}^{L/2}\frac{h-y}{(x^2+(h-y)^2+(g_L+L)^2)^{3/2}}\,dydx + \int_{-L/2}^{L/2}\int_{-L/2}^{L/2}\frac{h-y}{(x^2+(h-y)^2+g_L^2)^{3/2}}\,dydx + \int_{-L/2}^{L/2}\int_{-L/2}^{L/2}\frac{h-y}{(x^2+(h-y)^2+g_R^2)^{3/2}}\,dydx - \int_{-L/2}^{L/2}\int_{-L/2}^{L/2}\frac{h-y}{(x^2+(h-y)^2+(g_R+L)^2)^{3/2}}\,dydx\right]$$

**Equation 8-6 – Z-axis component of off-axis biaxial configuration**
A full geometric description of the z-axis component of the magnetic field arising for the off-axis biaxial configuration is obtained through individual evaluation of all eight integral elements. Magnetic field along the z-axis is a function of the magnet remanence ($B_r$), magnet edge length ($L$), split magnet separations relative ($g_L$ and $g_R$; see Figure 4-13) and the microsphere to coordinate origin separation ($h$). This is an expanded version of Equation 8-4.

## Appendix D. DNA sequences

### I. pUC-Φ600

TCGCGCGTTTCGGTGATGACGGTGAAAACCTCTGACACATGCAGCTCCCGGAGACGGTCACAGCTTGTCTGTA
AGCGGATGCCGGGAGCAGACAAGCCCGTCAGGGCGCGTCAGCGGGTGTTGGCGGGTGTCGGGGCTGGCTTAAC
TATGCGGCATCAGAGCAGATTGTACTGAGAGTGCACCATATGCGGTGTGAAATACCGCACAGATGCGTAAGGA
GAAAATACCGCATCAGGCGCCATTCGCCATTCAGGCTGCGCAACTGTTGGGAAGGGCGATCGGTGCGGGCCTC
TTCGCTATTACGCCAGCTGGCGAAAGGGGGATGTGCTGCAAGGCGATTAAGTTGGGTAACGCCAGGGTTTTCC
CAGTCACGACGTTGTAAAACGACGGCCAGTGAATTCGAGCTCGGTACCCGGGGATCCTTCTGATGTTCGTCTG
CCTCATGATTTCCATAGCTTGACGACGACCAGCAGCGGTCTGAGCGGCAATCATTTTGGCCTGAGCGTTCTGA
CCACTGATAGCCTGAGCGCCAGATATAGCGATAGGTATTGCGGCTGCCCAACACATATGGTTATCCTCCTTTC
GTGATTGTAAATAACTGAAATTGACCATCTCGTGTGTACTCTTCATGGAATACCGCACCGATAGTCTTGAGGA
AACGAATGTGGGACGTATTGCCTACCCATACGTAATTCCAAAGAGTATCATACTTCTCAAGCATCTTATCGCG
ATACTCCATGATTAACTTACGGAACTTTCGCTTAGCCTTTCCACTAAGTCGCCACACTTGGTCGCTCGTAACG
AACCAGCACTGGTCCCCGCAGTTACCACCGATAGCTAGAGGGAACCCATAGAGGCTCAACGTGACACACTCGG
AAGCATCAGGGAAACTCGGCTCAATACCAGCAGCCTTAGCTTCAAGAATGTCATGGTGAGCCGGAGTGAATAC
CTCAAAGTCTGTACTTTTAGTAGGTCTTATAGTCATCATAAGAAAACCCTCCCGTAGTCGTATTGTTCTCCCT
ATAGTGAGTCGTATTAATTTCGAGCCACCACAGGGAGAATATTTAATTAAATACCGGAACTTCTCCGTAAGTA
GTTACCTTCCCAGCCACACCCAATGATGTTCAGAGGGGTAGTCTCATCTGACAAGATGAAGCTTGGCGTAATC
ATGGTCATAGCTGTTTCCTGTGTGAAATTGTTATCCGCTCACAATTCCACACAACATACGAGCCGGAAGCATA
AAGTGTAAAGCCTGGGGTGCCTAATGAGTGAGCTAACTCACATTAATTGCGTTGCGCTCACTGCCCGCTTTCC
AGTCGGGAAACCTGTCGTGCCAGCTGCATTAATGAATCGGCCAACGCGCGGGGAGAGGCGGTTTGCGTATTGG
GCGCTCTTCCGCTTCCTCGCTCACTGACTCGCTGCGCTCGGTCGTTCGGCTGCGGCGAGCGGTATCAGCTCAC
TCAAAGGCGGTAATACGGTTATCCACAGAATCAGGGGATAACGCAGGAAAGAACATGTGAGCAAAAGGCCAGC
AAAAGGCCAGGAACCGTAAAAAGGCCGCGTTGCTGGCGTTTTTCCATAGGCTCCGCCCCCCTGACGAGCATCA
CAAAAATCGACGCTCAAGTCAGAGGTGGCGAAACCCGACAGGACTATAAAGATACCAGGCGTTTCCCCCTGGA
AGCTCCCTCGTGCGCTCTCCTGTTCCGACCCTGCCGCTTACCGGATACCTGTCCGCCTTTCTCCCTTCGGGAA
GCGTGGCGCTTTCTCATAGCTCACGCTGTAGGTATCTCAGTTCGGTGTAGGTCGTTCGCTCCAAGCTGGGCTG
TGTGCACGAACCCCCCGTTCAGCCCGACCGCTGCGCCTTATCCGGTAACTATCGTCTTGAGTCCAACCCGGTA
AGACACGACTTATCGCCACTGGCAGCAGCCACTGGTAACAGGATTAGCAGAGCGAGGTATGTAGGCGGTGCTA
CAGAGTTCTTGAAGTGGTGGCCTAACTACGGCTACACTAGAAGAACAGTATTTGGTATCTGCGCTCTGCTGAA
GCCAGTTACCTTCGGAAAAAGAGTTGGTAGCTCTTGATCCGGCAAACAAACCACCGCTGGTAGCGGTGGTTTT
TTTGTTTGCAAGCAGCAGATTACGCGCAGAAAAAAAGGATCTCAAGAAGATCCTTTGATCTTTTCTACGGGGT
CTGACGCTCAGTGGAACGAAAACTCACGTTAAGGGATTTTGGTCATGAGATTATCAAAAAGGATCTTCACCTA
GATCCTTTTAAATTAAAAATGAAGTTTTAAATCAATCTAAAGTATATATGAGTAAACTTGGTCTGACAGTTAC
CAATGCTTAATCAGTGAGGCACCTATCTCAGCGATCTGTCTATTTCGTTCATCCATAGTTGCCTGACTCCCCG
TCGTGTAGATAACTACGATACGGGAGGGCTTACCATCTGGCCCCAGTGCTGCAATGATACCGCGAGACCCACG
CTCACCGGCTCCAGATTTATCAGCAATAAACCAGCCAGCCGGAAGGGCCGAGCGCAGAAGTGGTCCTGCAACT
TTATCCGCCTCCATCCAGTCTATTAATTGTTGCCGGGAAGCTAGAGTAAGTAGTTCGCCAGTTAATAGTTTGC
GCAACGTTGTTGCCATTGCTACAGGCATCGTGGTGTCACGCTCGTCGTTTGGTATGGCTTCATTCAGCTCCGG
TTCCCAACGATCAAGGCGAGTTACATGATCCCCCATGTTGTGCAAAAAAGCGGTTAGCTCCTTCGGTCCTCCG

ATCGTTGTCAGAAGTAAGTTGGCCGCAGTGTTATCACTCATGGTTATGGCAGCACTGCATAATTCTCTTACTG
TCATGCCATCCGTAAGATGCTTTTCTGTGACTGGTGAGTACTCAACCAAGTCATTCTGAGAATAGTGTATGCG
GCGACCGAGTTGCTCTTGCCCGGCGTCAATACGGGATAATACCGCGCCACATAGCAGAACTTTAAAAGTGCTC
ATCATTGGAAAACGTTCTTCGGGGCGAAAACTCTCAAGGATCTTACCGCTGTTGAGATCCAGTTCGATGTAAC
CCACTCGTGCACCCAACTGATCTTCAGCATCTTTTACTTTCACCAGCGTTTCTGGGTGAGCAAAAACAGGAAG
GCAAAATGCCGCAAAAAAGGGAATAAGGGCGACACGGAAATGTTGAATACTCATACTCTTCCTTTTTCAATAT
TATTGAAGCATTTATCAGGGTTATTGTCTCATGAGCGGATACATATTTGAATGTATTTAGAAAAATAAACAAA
TAGGGGTTCCGCGCACATTTCCCCGAAAAGTGCCACCTGACGTCTAAGAAACCATTATTATCATGACATTAAC
CTATAAAAATAGGCGTATCACGAGGCCCTTTCGTC

## II. PCR pUC-Φ600

GGGGCCATGGCCTGAGCGCCAGATATAGCGATAGGTATTGCGGCTGCCCAACACATATGGTTATCCTCCTTTC
GTGATTGTAAATAACTGAAATTGACCATCTCGTGTGTACTCTTCATGGAATACCGCACCGATAGTCTTGAGGA
AACGAATGTGGGACGTATTGCCTACCCATACGTAATTCCAAAGAGTATCATACTTCTCAAGCATCTTATCGCG
ATACTCCATGATTAACTTACGGAACTTTCGCTTAGCCTTTCCACTAAGTCGCCACACTTGGTCGCTCGTAACG
AACCAGCACTGGTCCCCGCAGTTACCACCGATAGCTAGAGGGAACCCATAGAGGCTCAACGTGACACACTCGG
AAGCATCAGGGAAACTCGGCTCAATACCAGCAGCCTTAGCTTCAAGAATGTCATGGTGAGCCGGAGTGAATAC
CTCAAAGTCTGTACTTTTAGTAGGTCTTATAGTCATCATAAGAAAACCCTCCCGTAGTCGTATTGTTCTCCCT
ATAGTGAGTCGTATTAATTTCGAGCCACCACAGGGAGAATATTTAATTAAATACCGGAACTTCTCCGTAAGTA
GTTACCTTCCCAGCCACACCCAATGATGTTCAGAGGGGTAGTCTCATCTGACAAGATGGTCGACGGGG

### III. pSR-550

TTGGGGATCCCCGGGAATTCCGATCCGGACAACCGATGAAAGCGGCGACGCGCAGTTAATCCCACAGCCGCCA
GTTCCGCTGGCGGCATTTTAACTTTCTTTATCACACAGGAAACAGCTATGACCATGATTACGGATTCACTGGC
CGTCGTTTTACAACGTCGTGACTGGGAAAACCCTGGCGTTACCCAACTTAATCGCCTTGCAGCACATCCCCCT
TTCGCCAGCTGGCGTAATAGCGAAGAGGCCCGCACCGATCGCCCTTCCCAACAGTTGCGCAGCCTGAATGGCG
AATGGCGCTTTGCCTGGTTTCCGGCACCAGAAGCGGTGCCGGAAAGCTGGCTGGAGTGCGATCTTCCTGAGGC
CGATACTGTCGTCGTCCCCTCAAACTGGCAGATGCACGGTTACGATGCGCCCATCTACACCAACGTAACCTAT
CCCATTACGGTCAATCCGCCGTTTGTTCCCACGGAGAATCCGACGGGTTGTTACTCGCTCACATTTAATGTTG
ATGAAAGCTGGCTACAGGAAGGCCAGACGCGAATTATTTTTGATGGCGTTAACTCGGCGTTTCATCTGTGGTG
CAACGGGCGCTGGGTCGGTTACGGCCAGGACAGTCGTTTGCCGTCTGAATTTGACCTGAGCGCATTTTTACGC
GCCGGAGAAAACCGCCTCGCGGTGATGGTGCTGCGTTGGAGTGACGGCAGTTATCTGGAAGATCAGGATATGT
GGCGGATGAGCGGCATTTTCCGTGACGTCTCGTTGCTGCATAAACCGACTACACAAATCAGCGATTTCCATGT
TGCCACTCGCTTTAATGATGATTTCAGCCGCGCTGTACTGGAGGCTGAAGTTCAGATGTGCGGCGAGTTGCGT
GACTACCTACGGGTAACAGTTTCTTTATGGCAGGGTGAAACGCAGGTCGCCAGCGGCACCGCGCCTTTCGGCG
GTGAAATTATCGATGAGCGTGGTGGTTATGCCGATCGCGTCACACTACGTCTGAACGTCGAAAACCCGAAACT
GTGGAGCGCCGAAATCCCGAATCTCTATCGTGCGGTGGTTGAACTGCACACCGCCGACGGCACGCTGATTGAA
GCAGAAGCCTGCGATGTCGGTTTCCGCGAGGTGCGGATTGAAAATGGTCTGCTGCTGCTGAACGGCAAGCCGT
TGCTGATTCGAGGCGTTAACCGTCACGAGCATCATCCTCTGCATGGTCAGGTCATGGATGAGCAGACGATGGT
GCAGGATATCCTGCTGATGAAGCAGAACAACTTTAACGCCGTGCGCTGTTCGCATTATCCGAACCATCCGCTG
TGGTACACGCTGTGCGACCGCTACGGCCTGTATGTGGTGGATGAAGCCAATATTGAAACCCACGGCATGGTGC
CAATGAATCGTCTGACCGATGATCCGCGCTGGCTACCGGCGATGAGCGAACGCGTAACGCGAATGGTGCAGCG
CGATCGTAATCACCCGAGTGTGATCATCTGGTCGCTGGGGAATGAATCAGGCCACGGCGCTAATCACGACGCG
CTGTATCGCTGGATCAAATCTGTCGATCCTTCCCGCCCGGTGCAGTATGAAGGCGGCGGAGCCGACACCACGG
CCACCGATATTATTTGCCCGATGTACGCGCGCGTGGATGAAGACCAGCCCTTCCCGGCTGTGCCGAAATGGTC
CATCAAAAAATGGCTTTCGCTACCTGGAGAGACGCGCCCGCTGATCCTTTGCGAATACGCCCACGCGATGGGT
AACAGTCTTGGCGGTTTCGCTAAATACTGGCAGGCGTTTCGTCAGTATCCCCGTTTACAGGGCGGCTTCGTCT
GGGACTGGGTGGATCAGTCGCTGATTAAATATGATGAAAACGGCAACCCGTGGTCGGCTTACGGCGGTGATTT
TGGCGATACGCCGAACGATCGCCAGTTCTGTATGAACGGTCTGGTCTTTGCCGACCGCACGCCGCATCCAGCG
CTGACGGAAGCAAAACACCAGCAGCAGTTTTTCCAGTTCCGTTTATCCGGGCAAACCATCGAAGTGACCAGCG
AATACCTGTTCCGTCATAGCGATAACGAGCTCCTGCACTGGATGGTGGCGCTGGATGGTAAGCCGCTGGCAAG
CGGTGAAGTGCCTCTGGATGTCGCTCCACAAGGTAAACAGTTGATTGAACTGCCTGAACTACCGCAGCCGGAG
AGCGCCGGGCAACTCTGGCTCACAGTACGCGTAGTGCAACCGAACGCGACCGCATGGTCAGAAGCCGGGCACA
TCAGCGCCTGGCAGCAGTGGCGTCTGGCGGAAAACCTCAGTGTGACGCTCCCCGCCGCGTCCCACGCCATCCC
GCATCTGACCACCAGCGAAATGGATTTTTGCATCGAGCTGGGTAATAAGCGTTGGCAATTTAACCGCCAGTCA
GGCTTTCTTTCACAGATGTGGATTGGCGATAAAAAACAACTGCTGACGCCGCTGCGCGATCAGTTCACCCGTG
CACCGCTGGATAACGACATTGGCGTAAGTGAAGCGACCCGCATTGACCCTAACGCCTGGGTCGAACGCTGGAA
GGCGGCGGGCCATTACCAGGCCGAAGCAGCGTTGTTGCAGTGCACGGCAGATACACTTGCTGATGCGGTGCTG
ATTACGACCGCTCACGCGTGGCAGCATCAGGGGAAAACCTTATTTATCAGCCGGAAAACCTACCGGATTGATG
GTAGTGGTCAAATGGCGATTACCGTTGATGTTGAAGTGGCGAGCGATACACCGCATCCGGCGCGGATTGGCCT
GAACTGCCAGCTGGCGCAGGTAGCAGAGCGGGTAAACTGGCTCGGATTAGGGCCGCAAGAAAACTATCCCGAC
CGCCTTACTGCCGCCTGTTTTGACCGCTGGGATCTGCCATTGTCAGACATGTATACCCCGTACGTCTTCCCGA

GCGAAAACGGTCTGCGCTGCGGGACGCGCGAATTGAATTATGGCCCACACCAGTGGCGCGGCGACTTCCAGTT
CAACATCAGCCGCTACAGTCAACAGCAACTGATGGAAACCAGCCATCGCCATCTGCTGCACGCGGAAGAAGGC
ACATGGCTGAATATCGACGGTTTCCATATGGGGATTGGTGGCGACGACTCCTGGAGCCCGTCAGTATCGGCGG
AATTCCAGCTGAGCGCCGGTCGCTACCATTACCAGTTGGTCTGGTGTCAAAAATAATAATAACCGGGCAGGCC
ATGTCTGCCCGTATTTCGCGTAAGGAAATCCATTATGTACTATTTAAAAAACACAAACTTTTGGATGTTCGGT
TTATTCTTTTTCTTTTACTTTTTTATCATGGGAGCCTACTTCCCGTTTTTCCCGATTTGGCTACATGACATCA
ACCATATCAGCAAAAGTGATACGGGTATTATTTTTGCCGCTATTTCTCTGTTCTCGCTATTATTCCAACCGCT
GTTTGGTCTGCTTTCTGACAAACTCGGGCTGCGCAAATACCTGCTGTGGATTATTACCGGCATGTTAGTGATG
TTTGCGCCGTTCTTTATTTTTATCTTCGGGCCACTGTTACAATACAACATTTTAGTAGGATCGATTGTTGGTG
GTATTTATCTAGGCTTTTGTTTTAACGCCGGTGCGCCAGCAGTAGAGGCATTTATTGAGAAAGTCAGCCGTCG
CAGTAATTTCGAATTTGGTCGCGCGCGGATGTTTGGCTGTGTTGGCTGGGCGCTGTGTGCCTCGATTGTCGGC
ATCATGTTCACCATCAATAATCAGTTTGTTTTCTGGCTGGGCTCTGGCTGTGCACTCATCCTCGCCGTTTTAC
TCTTTTTCGCCAAAACGGATGCGCCCTCTTCTGCCACGGTTGCCAATGCGGTAGGTGCCAACCATTCGGCATT
TAGCCTTAAGCTGGCACTGGAACTGTTCAGACAGCCAAAACTGTGGTTTTTGTCACTGTATGTTATTGGCGTT
TCCTGCACCTACGATGTTTTTGACCAACAGTTTGCTAATTTCTTTACTTCGTTCTTTGCTACCGGTGAACAGG
GTACGCGGGTATTTGGCTACGTAACGACAATGGGCGAATTACTTAACGCCTCGATTATGTTCTTTGCGCCACT
GATCATTAATCGCATCGGTGGGAAAAACGCCCTGCTGCTGGCTGGCACTATTATGTCTGTACGTATTATTGGC
TCATCGTTCGCCACCTCAGCGCTGGAAGTGGTTATTCTGAAAACGCTGCATATGTTTGAAGTACCGTTCCTGC
TGGTGGGCTGCTTTAAATATATTACCAGCCAGTTTGAAGTGCGTTTTTCAGCGACGATTTATCTGGTCTGTTT
CTGCTTCTTTAAGCAACTGGCGATGATTTTTATGTCTGTACTGGCGGGCAATATGTATGAAAGCATCGGTTTC
CAGGGCGCTTATCTGGTGCTGGGTCTGGTGGCGCTGGGCTTCACCTTAATTTCCGTGTTCACGCTTAGCGGCC
CCGGCCCGCTTTCCCTGCTGCGTCGTCAGGTGAATGAAGTCGCTTAAGCAATCAATGTCGGATGCGGCGCGAC
GCTTATCCGACCAACATATCATAACGGAGTGATCGCATTGAACATGCCAATGACCGAAAGAATAAGAGCAGGC
AAGCTATTTACCGATATGTGCGAAGGCTTACCGGAAAAAAGACTTCGTGGGAAAACGTTAATGTATGAGTTTA
ATCACTCGCATCCATCAGAAGTTGAAAAAAGAGAAAGCCTGATTAAAGAAATGTTTGCCACGGTAGGGGAAAA
CGCCTGGGTAGAACCGCCTGTCTATTTCTCTTACGGTTCCAACATCCATATAGGCCGCAATTTTTATGCAAAT
TTCAATTTAACCATTGTCGATGACTACACGGTAACAATCGGTGATAACGTACTGATTGCACCCAACGTTACTC
TTTCCGTTACGGGACACCCTGTACACCATGAATTGAGAAAAAACGGCGAGATGTACTCTTTTCCGATAACGAT
TGGCAATAACGTCTGGATCGGAAGTCATGTGGTTATTAATCCAGGCGTCACCATCGGGGATAATTCTGTTATT
GGCGCGGGTAGTATCGTCACAAAAGACATTCCACCAAACGTCGTGGCGGCTGGCGTTCCTTGTCGGGTTATTC
GCGAAATAAACGACCGGGATAAGCACTATTATTTCAAAGATTATAAAGTTGAATCGTCAGTTTAAATTATAAA
AATTGCCTGATACGCTGCGCTTATCAGGCCTACAAGTTCAGCGATCTACATTAGCCGCATCCGGCATGAACAA
AGCGCAGGAACAAGCGTCGCATCATGCCTCTTTGACCCACAGCTGCGGAAAACGTACTGGTGCAAAACGCAGG
GTTATGATCATCAGCCCAACGACGCACAGCGCATGAAATGCCCAGTCCATCAGGTAATTGCCGCTGATACTAC
GCAGCACGCCAGAAAACCACGGGGCAAGCCCGGCGATGATAAAACCGATTCCCTGCATAAACGCCACCAGCTT
GCCAGCAATAGCCGGTTGCACAGAGTGATCGAGCGCCAGCAGCAAACAGAGCGGAAACGCGCCGCCCAGACCT
AACCCACACACCATCGCCCACAATACCGGCAATTGCATCGGCAGCCAGATAAAGCCGCAGAACCCCACCAGTT
GTAACACCAGCGCCAGCATTAACAGTTTGCGCCGATCCTGATGGCGAGCCATAGCAGGCATCAGCAAAGCTCC
TGCGGCTTGCCCAAGCGTCATCAATGCCAGTAAGGAACCGCTGTACTGCGCGCTGGCACCAATCTCAATATAG
AAAGCGGGTAACCAGGCAATCAGGCTGGCGTAACCGCCGTTAATCAGACCGAAGTAAACACCCAGCGTCCACG
CGCGGGGAGTGAATACCACGCGAACCGGAGTGGTTGTTGTCTTGTGGGAAGAGGCGACCTCGCGGGCGCTTTG

CCACCACCAGGCAAAGAGCGCAACAACGGCAGGCAGCGCCACCAGGCGAGTGTTTGATACCAGGTTTCGCTAT
GTTGAACTAACCAGGGCGTTATGGCGGCACCAAGCCCACCGCCGCCCATCAGAGCCGCGGACCACAGCCCCAT
CACCAGTGGCGTGCGCTGCTGAAACCGCCGTTTAATCACCGAAGCATCACCGCCTGAATGATGCCGATCCCCA
CCCCACCAAGCAGTGCGCTGCTAAGCAGCAGCGCACTTTGCGGGTAAAGCTCACGCATCAATGCACCGACGGC
AATCAGCAACAGACTGATGGCGACACTGCGACGTTCGCTGACATGCTGATGAAGCCAGCTTCCGGCCAGCGCC
AGCCCGCCCATGGTAACCACCGGCAGAGCGGTCGACCGATGCCCTTGAGAGCCTTCAACCCAGTCAGCTCCTT
CCGGTGGGCGCGGGGCATGACTATCGTCGCCGCACTTATGACTGTCTTCTTTATCATGCAACTCGTAGGACAG
GTGCCGGCAGCGCTCTGGGTCATTTTCGGCGAGGACCGCTTTCGCTGGAGCGCGACGATGATCGGCCTGTCGC
TTGCGGTATTCGGAATCTTGCACGCCCTCGCTCAAGCCTTCGTCACTGGTCCCGCCACCAAACGTTTCGGCGA
GAAGCAGGCCATTATCGCCGGCATGGCGGCCGACGCGCTGGGCTACGTCTTGCTGGCGTTCGCGACGCGAGGC
TGGATGGCCTTCCCCATTATGATTCTTCTCGCTTCCGGCGGCATCGGGATGCCCGCGTTGCAGGCCATGCTGT
CCAGGCAGGTAGATGACGACCATCAGGGACAGCTTCAAGGATCGCTCGCGGCTCTTACCAGCCTAACTTCGAT
CACTGGACCGCTGATCGTCACGGCGATTTATGCCGCCTCGGCGAGCACATGGAACGGGTTGGCATGGATTGTA
GGCGCCGCCCTATACCTTGTCTGCCTCCCCGCGTTGCGTCGCGGTGCATGGAGCCGGGCCACCTCGACCTGAA
TGGAAGCCGGCGGCACCTCGCTAACGGATTCACCACTCCAAGAATTGGAGCCAATCAATTCTTGCGGAGAACT
GTGAATGCGCAAACCAACCCTTGGCAGAACATATCCATCGCGTCCGCCATCTCCAGCAGCCGCACGCGGCGCA
TCTCGGGCAGCGTTGGGTCCTGGCCACGGGTGCGCATGATCGTGCTCCTGTCGTTGAGGACCCGGCTAGGCTG
GCGGGGTTGCCTTACTGGTTAGCAGAATGAATCACCGATACGCGAGCGAACGTGAAGCGACTGCTGCTGCAAA
ACGTCTGCGACCTGAGCAACAACATGAATGGTCTTCGGTTTCCGTGTTTCGTAAAGTCTGGAAACGCGGAAGT
CAGCGCCCTGCACCATTATGTTCCGGATCTGCATCGCAGGATGCTGCTGGCTACCCTGTGGAACACCTACATC
TGTATTAACGAAGCGCTGGCATTGACCCTGAGTGATTTTTCTCTGGTCCCGCCGCATCCATACCGCCAGTTGT
TTACCCTCACAACGTTCCAGTAACCGGGCATGTTCATCATCAGTAACCCGTATCGTGAGCATCCTCTCTCGTT
TCATCGGTATCATTACCCCCATGAACAGAAATTCCCCCTTACACGGAGGCATCAAGTGACCAAACAGGAAAAA
ACCGCCCTTAACATGGCCCGCTTTATCAGAAGCCAGACATTAACGCTTCTGGAGAAACTCAACGAGCTGGACG
CGGATGAACAGGCAGACATCTGTGAATCGCTTCACGACCACGCTGATGAGCTTTACCGCAGCTGCCTCGCGCG
TTTCGGTGATGACGGTGAAAACCTCTGACACATGCAGCTCCCGGAGACGGTCACAGCTTGTCTGTAAGCGGAT
GCCGGGAGCAGACAAGCCCGTCAGGGCGCGTCAGCGGGTGTTGGCGGGTGTCGGGGCGCAGCCATGACCCAGT
CACGTAGCGATAGCGGAGTGTATACTGGCTTAACTATGCGGCATCAGAGCAGATTGTACTGAGAGTGCACCAT
ATGCGGTGTGAAATACCGCACAGATGCGTAAGGAGAAAATACCGCATCAGGCGCTCTTCCGCTTCCTCGCTCA
CTGACTCGCTGCGCTCGGTCGTTCGGCTGCGGCGAGCGGTATCAGCTCACTCAAAGGCGGTAATACGGTTATC
CACAGAATCAGGGGATAACGCAGGAAAGAACATGTGAGCAAAAGGCCAGCAAAAGGCCAGGAACCGTAAAAAG
GCCGCGTTGCTGGCGTTTTTCCATAGGCTCCGCCCCCCTGACGAGCATCACAAAAATCGACGCTCAAGTCAGA
GGTGGCGAAACCCGACAGGACTATAAAGATACCAGGCGTTTCCCCCTGGAAGCTCCCTCGTGCGCTCTCCTGT
TCCGACCCTGCCGCTTACCGGATACCTGTCCGCCTTTCTCCCTTCGGGAAGCGTGGCGCTTTCTCAATGCTCA
CGCTGTAGGTATCTCAGTTCGGTGTAGGTCGTTCGCTCCAAGCTGGGCTGTGTGCACGAACCCCCCGTTCAGC
CCGACCGCTGCGCCTTATCCGGTAACTATCGTCTTGAGTCCAACCCGGTAAGACACGACTTATCGCCACTGGC
AGCAGCCACTGGTAACAGGATTAGCAGAGCGAGGTATGTAGGCGGTGCTACAGAGTTCTTGAAGTGGTGGCCT
AACTACGGCTACACTAGAAGGACAGTATTTGGTATCTGCGCTCTGCTGAAGCCAGTTACCTTCGGAAAAAGAG
TTGGTAGCTCTTGATCCGGCAAACAAACCACCGCTGGTAGCGGTGGTTTTTTTGTTTGCAAGCAGCAGATTAC
GCGCAGAAAAAAAGGATCTCAAGAAGATCCTTTGATCTTTTCTACGGGGTCTGACGCTCAGTGGAACGAAAAC
TCACGTTAAGGGATTTTGGTCATGAGATTATCAAAAAGGATCTTCACCTAGATCCTTTTAAATTAAAAATGAA

GTTTTAAATCAATCTAAAGTATATATGAGTAAACTTGGTCTGACAGTTACCAATGCTTAATCAGTGAGGCACC
TATCTCAGCGATCTGTCTATTTCGTTCATCCATAGTTGCCTGACTCCCCGTCGTGTAGATAACTACGATACGG
GAGGGCTTACCATCTGGCCCCAGTGCTGCAATGATACCGCGAGACCCACGCTCACCGGCTCCAGATTTATCAG
CAATAAACCAGCCAGCCGGAAGGGCCGAGCGCAGAAGTGGTCCTGCAACTTTATCCGCCTCCATCCAGTCTAT
TAATTGTTGCCGGGAAGCTAGAGTAAGTAGTTCGCCAGTTAATAGTTTGCGCAACGTTGTTGCCATTGCTGCA
GGCATCGTGGTGTCACGCTCGTCGTTTGGTATGGCTTCATTCAGCTCCGGTTCCCAACGATCAAGGCGAGTTA
CATGATCCCCCATGTTGTGCAAAAAAGCGGTTAGCTCCTTCGGTCCTCCGATCGTTGTCAGAAGTAAGTTGGC
CGCAGTGTTATCACTCATGGTTATGGCAGCACTGCATAATTCTCTTACTGTCATGCCATCCGTAAGATGCTTT
TCTGTGACTGGTGAGTACTCAACCAAGTCATTCTGAGAATAGTGTATGCGGCGACCGAGTTGCTCTTGCCCGG
CGTCAACACGGGATAATACCGCGCCACATAGCAGAACTTTAAAAGTGCTCATCATTGGAAAACGTTCTTCGGG
GCGAAAACTCTCAAGGATCTTACCGCTGTTGAGATCCAGTTCGATGTAACCCACTCGTGCACCCAACTGATCT
TCAGCATCTTTTACTTTCACCAGCGTTTCTGGGTGAGCAAAAACAGGAAGGCAAAATGCCGCAAAAAAGGGAA
TAAGGGCGACACGGAAATGTTGAATACTCATACTCTTCCTTTTTCAATATTATTGAAGCATTTATCAGGGTTA
TTGTCTCATGAGCGGATACATATTTGAATGTATTTAGAAAAATAAACAAATAGGGGTTCCGCGCACATTTCCC
CGAAAAGTGCCACCTGACGTCTAAGAAACCATTATTATCATGACATTAACCTATAAAAATAGGCGTATCACGA
GGCCCTTTCGTCTTCAAGAATTGATCCGCTGTAATCCGGGCAGCGCAACGGAACATTCATCAGTGTAAAAATG
GAATCAATAAAGCCCTGCGCAGCGCGCAGGGTCAGCCTGAATACGCGTTTAATGACCAGCACAGTCGTGATGG
CAAGGTCAGAATAGCGCTGAGGTCTGCCTCGTGAAGAAGGTGTTGCTGACTCATACCAGGCCTGAATCGCCCC
ATCATCCAGCCAGAAAGTGAGGGAGCCACGGTTGATGAGAGCTTTGTTGTAGGTGGACCAGTTGGTGATTTTG
AACTTTTGCTTTGCCACGGAACGGTCTGCGTTGTCGGGAAGATGCGTGATCTGATCCTTCAACTCAGCAAAAG
TTCGATTTATTCAACAAAGCCACGTTGTGTCTCAAAATCTCTGATGTTACATTGCACAAGATAAAAATATATC
ATCATGAACAATAAAACTGTCTGCTTACATAAACAGTAATACAAGGGGTGTTATGAGCCATATTCAACGGGAA
ACGTCTTGCTCGAGGCCGCGATTAAATTCCAACATGGATGCTGATTTATATGGGTATAAATGGGCTCGCGATA
ATGTCGGGCAATCAGGTGCGACAATCTATCGATTGTATGGGAAGCCCGATGCGCCAGAGTTGTTTCTGAAACA
TGGCAAAGGTAGCGTTGCCAATGATGTTACAGATGAGATGGTCAGACTAAACTGGCTGACGGAATTTATGCCT
CTTCCGACCATCAAGCATTTTATCCGTACTCCTGATGATGCATGGTTACTCACCACTGCGATCCCCGGGAAAA
CAGCATTCCAGGTATTAGAAGAATATCCTGATTCAGGTGAAAATATTGTTGATGCGCTGGCAGTGTTCCTGCG
CCGGTTGCATTCGATTCCTGTTTGTAATTGTCCTTTTAACAGCGATCGCGTATTTCGTCTCGCTCAGGCGCAA
TCACGAATGAATAACGGTTTGGTTGATGCGAGTGATTTTGATGACGAGCGTAATGGCTGGCCTGTTGAACAAG
TCTGGAAAGAAATGCATAAGCTTTTGCCATTCTCACCGGATTCAGTCGTCACTCATGGTGATTTCTCACTTGA
TAACCTTATTTTTGACGAGGGGAAATTAATAGGTTGTATTGATGTTGGACGAGTCGGAATCGCAGACCGATAC
CAGGATCTTGCCATCCTATGGAACTGCCTCGGTGAGTTTTCTCCTTCATTACAGAAACGGCTTTTTCAAAAAT
ATGGTATTGATAATCCTGATATGAATAAATTGCAGTTTCATTTGATGCTCGATGAGTTTTTCTAATCAGAATT
GGTTAATTGGTTGTAACACTGGCAGAGCATTACGCTGACTTGACGGGACGGCGGCTTTGTTGAATAAATCGAA
CTTTTGCTGAGTTGAAGGATCAGATCACGCATCTTCCCGACAACGCAGACCGTTCCGTGGCAAAGCAAAAGTT
CAAAATCACCAACTGGTCCACCTACAACAAAGCTCTCATCAACCGTGGCTCCCTCACTTTCTGGCTGGATGAT
GGGGCGATTCAGGCCTGGTATGAGTCAGCAACACCTTCTTCACGAGGCAGACCTCAGCGCTATTCTGACCTTG
CCATCACGACTGTGCTGGTCATTAAACGCGTATTCAGGCTGACCCTGCGCGCTGCGCAGGGCTTTATTGATTC
CATTTTTACACTGATGAATGTTCCGTTGCGCTGCCCGGATTACAGCGGATCAATTCCCAATTCCAGGCATCAA
ATAAAACGAAAGGCTCAGTCGAAAGACTGGGCCTTTCGTTTTATCTGTTGTTTGTCGGTGAACGCTCTCCTGA
GTAGGACAAATCCGCCGGGAGCGGATTTGAACGTTGCGAAGCAACGGCCCGGAGGGTGGCGGGCAGGACGCCC

GCCATAAACTGCCAGGAATTAATTCCAGGCATCAAATAAAACGAAAGGCTCAGTCGAAAGACTGGGCCTTTCG
TTTTATCTGTTGTTTGTCGGTGAACGCTCTCCTGAGTAGGACAAATCCGCCGGGAGCGGATTTGAACGTTGCG
AAGCAACGGCCCGGAGGGTGGCGGGCAGGACGCCCGCCATAAACTGCCAGGAATTAATTCCAGGCATCAAATA
AAACGAAAGGCTCAGTCGAAAGACTGGGCCTTTCGTTTTATCTGTTGTTTGTCGGTGAACGCTCTCCTGAGTA
GGACAAATCCGCCGGGAGCGGATTTGAACGTTGCGAAGCAACGGCCCGGAGGGTGGCGGGCAGGACGCCCGCC
ATAAACTGCCAGGAATTAATTCCAGGCATCAAATAAAACGAAAGGCTCAGTCGAAAGACTGGGCCTTTCGTTT
TATCTGTTGTTTGTCGGTGAACGCTCTCCTGAGTAGGACAAATCCGCCGGGAGCGGATTTGAACGTTGCGAAG
CAACGGCCCGGAGGGTGGCGGGCAGGACGCCCGCCATAAACTGCCAGGAA

## IV. pSJC-Φ13

TTGGGGATCCCCGGGAATTCCGATCCGGACAACCGATGAAAGCGGCGACGCGCAGTTAATCCCACAGCCGCCA
GTTCCGCTGGCGGCATTTTAACTTTCTTTATCACACAGGAAACAGCTATGACCATGATTACGGATTCACTGGC
CGTCGTTTTACAACGTCGTGACTGGGAAAACCCTGGCGTTACCCAACTTAATCGCCTTGCAGCACATCCCCCT
TTCGCCAGCTGGCGTAATAGCGAAGAGGCCCGCACCGATCGCCCTTCCCAACAGTTGCGCAGCCTGAATGGCG
AATGGCGCTTTGCCTGGTTTCCGGCACCAGAAGCGGTGCCGGAAAGCTGGCTGGAGTGCGATCTTCCTGAGGC
CGATACTGTCGTCGTCCCCTCAAACTGGCAGATGCACGGTTACGATGCGCCCATCTACACCAACGTAACCTAT
CCCATTACGGTCAATCCGCCGTTTGTTCCCACGGAGAATCCGACGGGTTGTTACTCGCTCACATTTAATGTTG
ATGAAAGCTGGCTACAGGAAGGCCAGACGCGAATTATTTTTGATGGCGTTAACTCGGCGTTTCATCTGTGGTG
CAACGGGCGCTGGGTCGGTTACGGCCAGGACAGTCGTTTGCCGTCTGAATTTGACCTGAGCGCATTTTTACGC
GCCGGAGAAAACCGCCTCGCGGTGATGGTGCTGCGTTGGAGTGACGGCAGTTATCTGGAAGATCAGGATATGT
GGCGGATGAGCGGCATTTTCCGTGACGTCTCGTTGCTGCATAAACCGACTACACAAATCAGCGATTTCCATGT
TGCCACTCGCTTTAATGATGATTTCAGCCGCGCTGTACTGGAGGCTGAAGTTCAGATGTGCGGCGAGTTGCGT
GACTACCTACGGGTAACAGTTTCTTTATGGCAGGGTGAAACGCAGGTCGCCAGCGGCACCGCGCCTTTCGGCG
GTGAAATTATCGATGAGCGTGGTGGTTATGCCGATCGCGTCACACTACGTCTGAACGTCGAAAACCCGAAACT
GTGGAGCGCCGAAATCCCGAATCTCTATCGTGCGGTGGTTGAACTGCACACCGCCGACGGCACGCTGATTGAA
GCAGAAGCCTGCGATGTCGGTTTCCGCGAGGTGCGGATTGAAAATGGTCTGCTGCTGCTGAACGGCAAGCCGT
TGCTGATTCGAGGCGTTAACCGTCACGAGCATCATCCTCTGCATGGTCAGGTCATGGATGAGCAGACGATGGT
GCAGGATATCCTGCTGATGAAGCAGAACAACTTTAACGCCGTGCGCTGTTCGCATTATCCGAACCATCCGCTG
TGGTACACGCTGTGCGACCGCTACGGCCTGTATGTGGTGGATGAAGCCAATATTGAAACCCACGGCATGGTGC
CAATGAATCGTCTGACCGATGATCCGCGCTGGCTACCGGCGATGAGCGAACGCGTAACGCGAATGGTGCAGCG
CGATCGTAATCACCCGAGTGTGATCATCTGGTCGCTGGGGAATGAATCAGGCCACGGCGCTAATCACGACGCG
CTGTATCGCTGGATCAAATCTGTCGATCCTTCCCGCCCGGTGCAGTATGAAGGCGGCGGAGCCGACACCACGG
CCACCGATATTATTTGCCCGATGTACGCGCGCGTGGATGAAGACCAGCCCTTCCCGGCTGTGCCGAAATGGTC
CATCAAAAAATGGCTTTCGCTACCTGGAGAGACGCGCCCGCTGATCCTTTGCGAATACGCCCACGCGATGGGT
AACAGTCTTGGCGGTTTCGCTAAATACTGGCAGGCGTTTCGTCAGTATCCCCGTTTACAGGGCGGCTTCGTCT
GGGACTGGGTGGATCAGTCGCTGATTAAATATGATGAAAACGGCAACCCGTGGTCGGCTTACGGCGGTGATTT
TGGCGATACGCCGAACGATCGCCAGTTCTGTATGAACGGTCTGGTCTTTGCCGACCGCACGCCGCATCCAGCG
CTGACGGAAGCAAAACACCAGCAGCAGTTTTTCCAGTTCCGTTTATCCGGGCAAACCATCGAAGTGACCAGCG
AATACCTGTTCCGTCATAGCGATAACGAGCTCCTGCACTGGATGGTGGCGCTGGATGGTAAGCCGCTGGCAAG
CGGTGAAGTGCCTCTGGATGTCGCTCCACAAGGTAAACAGTTGATTGAACTGCCTGAACTACCGCAGCCGGAG
AGCGCCGGGCAACTCTGGCTCACAGTACGCGTAGTGCAACCGAACGCGACCGCATGGTCAGAAGCCGGGCACA
TCAGCGCCTGGCAGCAGTGGCGTCTGGCGGAAAACCTCAGTGTGACGCTCCCCGCCGCGTCCCACGCCATCCC
GCATCTGACCACCAGCGAAATGGATTTTTGCATCGAGCTGGGTAATAAGCGTTGGCAATTTAACCGCCAGTCA
GGCTTTCTTTCACAGATGTGGATTGGCGATAAAAAACAACTGCTGACGCCGCTGCGCGATCAGTTCACCCGTG
CACCGCTGGATAACGACATTGGCGTAAGTGAAGCGACCCGCATTGACCCTAACGCCTGGGTCGAACGCTGGAA
GGCGGCGGGCCATTACCAGGCCGAAGCAGCGTTGTTGCAGTGCACGGCAGATACACTTGCTGATGCGGTGCTG
ATTACGACCGCTCACGCGTGGCAGCATCAGGGGAAAACCTTATTTATCAGCCGGAAAACCTACCGGATTGATG
GTAGTGGTCAAATGGCGATTACCGTTGATGTTGAAGTGGCGAGCGATACACCGCATCCGGCGCGGATTGGCCT
GAACTGCCAGCTGGCGCAGGTAGCAGAGCGGGTAAACTGGCTCGGATTAGGGCCGCAAGAAAACTATCCCGAC
CGCCTTACTGCCGCCTGTTTTGACCGCTGGGATCTGCCATTGTCAGACATGTATACCCCGTACGTCTTCCCGA

GCGAAAACGGTCTGCGCTGCGGGACGCGCGAATTGAATTATGGCCCACACCAGTGGCGCGGCGACTTCCAGTT
CAACATCAGCCGCTACAGTCAACAGCAACTGATGGAAACCAGCCATCGCCATCTGCTGCACGCGGAAGAAGGC
ACATGGCTGAATATCGACGGTTTCCATATGGGGATTGGTGGCGACGACTCCTGGAGCCCGTCAGTATCGGCGG
AATTCCAGCTGAGCGCCGGTCGCTACCATTACCAGTTGGTCTGGTGTCAAAAATAATAATAACCGGGCAGGCC
ATGTCTGCCCGTATTTCGCGTAAGGAAATCCATTATGTACTATTTAAAAAACACAAACTTTTGGATGTTCGGT
TTATTCTTTTTCTTTTACTTTTTTATCATGGGAGCCTACTTCCCGTTTTTCCCGATTTGGCTACATGACATCA
ACCATATCAGCAAAAGTGATACGGGTATTATTTTTGCCGCTATTTCTCTGTTCTCGCTATTATTCCAACCGCT
GTTTGGTCTGCTTTCTGACAAACTCGGGCTGCGCAAATACCTGCTGTGGATTATTACCGGCATGTTAGTGATG
TTTGCGCCGTTCTTTATTTTTATCTTCGGGCCACTGTTACAATACAACATTTTAGTAGGATCGATTGTTGGTG
GTATTTATCTAGGCTTTTGTTTTAACGCCGGTGCGCCAGCAGTAGAGGCATTTATTGAGAAAGTCAGCCGTCG
CAGTAATTTCGAATTTGGTCGCGCGCGGATGTTTGGCTGTGTTGGCTGGGCGCTGTGTGCCTCGATTGTCGGC
ATCATGTTCACCATCAATAATCAGTTTGTTTTCTGGCTGGGCTCTGGCTGTGCACTCATCCTCGCCGTTTTAC
TCTTTTTCGCCAAAACGGATGCGCCCTCTTCTGCCACGGTTGCCAATGCGGTAGGTGCCAACCATTCGGCATT
TAGCCTTAAGCTGGCACTGGAACTGTTCAGACAGCCAAAACTGTGGTTTTTGTCACTGTATGTTATTGGCGTT
TCCTGCACCTACGATGTTTTTGACCAACAGTTTGCTAATTTCTTTACTTCGTTCTTTGCTACCGGTGAACAGG
GTACGCGGGTATTTGGCTACGTAACGACAATGGGCGAATTACTTAACGCCTCGATTATGTTCTTTGCGCCACT
GATCATTAATCGCATCGGTGGGAAAAACGCCCTGCTGCTGGCTGGCACTATTATGTCTGTACGTATTATTGGC
TCATCGTTCGCCACCTCAGCGCTGGAAGTGGTTATTCTGAAAACGCTGCATATGTTTGAAGTACCGTTCCTGC
TGGTGGGCTGCTTTAAATATATTACCAGCCAGTTTGAAGTGCGTTTTTCAGCGACGATTTATCTGGTCTGTTT
CTGCTTCTTTAAGCAACTGGCGATGATTTTTATGTCTGTACTGGCGGGCAATATGTATGAAAGCATCGGTTTC
CAGGGCGCTTATCTGGTGCTGGGTCTGGTGGCGCTGGGCTTCACCTTAATTTCCGTGTTCACGCTTAGCGGCC
CCGGCCCGCTTTCCCTGCTGCGTCGTCAGGTGAATGAAGTCGCTTAAGCAATCAATGTCGGATGCGGCGCGAC
GCTTATCCGACCAACATATCATAACGGAGTGATCGCATTGAACATGCCAATGACCGAAAGAATAAGAGCAGGC
AAGCTATTTACCGATATGTGCGAAGGCTTACCGGAAAAAAGACTTCGTGGGAAAACGTTAATGTATGAGTTTA
ATCACTCGCATCCATCAGAAGTTGAAAAAAGAGAAAGCCTGATTAAAGAAATGTTTGCCACGGTAGGGGAAAA
CGCCTGGGTAGAACCGCCTGTCTATTTCTCTTACGGTTCCAACATCCATATAGGCCGCAATTTTTATGCAAAT
TTCAATTTAACCATTGTCGATGACTACACGGTAACAATCGGTGATAACGTACTGATTGCACCCAACGTTACTC
TTTCCGTTACGGGACACCCTGTACACCATGAATTGAGAAAAAACGGCGAGATGTACTCTTTTCCGATAACGAT
TGGCAATAACGTCTGGATCGGAAGTCATGTGGTTATTAATCCAGGCGTCACCATCGGGGATAATTCTGTTATT
GGCGCGGGTAGTATCGTCACAAAAGACATTCCACCAAACGTCGTGGCGGCTGGCGTTCCTTGTCGGGTTATTC
GCGAAATAAACGACCGGGATAAGCACTATTATTTCAAAGATTATAAAGTTGAATCGTCAGTTTAAATTATAAA
AATTGCCTGATACGCTGCGCTTATCAGGCCTACAAGTTCAGCGATCTACATTAGCCGCATCCGGCATGAACAA
AGCGCAGGAACAAGCGTCGCATCATGCCTCTTTGACCCACAGCTGCGGAAAACGTACTGGTGCAAAACGCAGG
GTTATGATCATCAGCCCAACGACGCACAGCGCATGAAATGCCCAGTCCATCAGGTAATTGCCGCTGATACTAC
GCAGCACGCCAGAAAACCACGGGGCAAGCCCGGCGATGATAAAACCGATTCCCTGCATAAACGCCACCAGCTT
GCCAGCAATAGCCGGTTGCACAGAGTGATCGAGCGCCAGCAGCAAACAGAGCGGAAACGCGCCGCCCAGACCT
AACCCACACACCATCGCCCACAATACCGGCAATTGCATCGGCAGCCAGATAAAGCCGCAGAACCCCACCAGTT
GTAACACCAGCGCCAGCATTAACAGTTTGCGCCGATCCTGATGGCGAGCCATAGCAGGCATCAGCAAAGCTCC
TGCGGCTTGCCCAAGCGTCATCAATGCCAGTAAGGAACCGCTGTACTGCGCGCTGGCACCAATCTCAATATAG
AAAGCGGGTAACCAGGCAATCAGGCTGGCGTAACCGCCGTTAATCAGACCGAAGTAAACACCCAGCGTCCACG
CGCGGGGAGTGAATACCACGCGAACCGGAGTGGTTGTTGTCTTGTGGGAAGAGGCGACCTCGCGGGCGCTTTG

CCACCACCAGGCAAAGAGCGCAACAACGGCAGGCAGCGCCACCAGGCGAGTGTTTGATACCAGGTTTCGCTAT
GTTGAACTAACCAGGGCGTTATGGCGGCACCAAGCCCACCGCCGCCCATCAGAGCCGCGGACCACAGCCCCAT
CACCAGTGGCGTGCGCTGCTGAAACCGCCGTTTAATCACCGAAGCATCACCGCCTGAATGATGCCGATCCCCA
CCCCACCAAGCAGTGCGCTGCTAAGCAGCAGCGCACTTTGCGGGTAAAGCTCACGCATCAATGCACCGACGGC
AATCAGCAACAGACTGATGGCGACACTGCGACGTTCGCTGACATGCTGATGAAGCCAGCTTCCGGCCAGCGCC
AGCCCGCCCATGGCCTGAGCGCCAGATATAGCGATAGGTATTGCGGCTGCCCAACACATATGGTTATCCTCCT
TTCGTGATTGTAAATAACTGAAATTGACCATCTCGTGTGTACTCTTCATGGAATACCGCACCGATAGTCTTGA
GGAAACGAATGTGGGACGTATTGCCTACCCATACGTAATTCCAAAGAGTATCATACTTCTCAAGCATCTTATC
GCGATACTCCATGATTAACTTACGGAACTTTCGCTTAGCCTTTCCACTAAGTCGCCACACTTGGTCGCTCGTA
ACGAACCAGCACTGGTCCCCGCAGTTACCACCGATAGCTAGAGGGAACCCATAGAGGCTCAACGTGACACACT
CGGAAGCATCAGGGAAACTCGGCTCAATACCAGCAGCCTTAGCTTCAAGAATGTCATGGTGAGCCGGAGTGAA
TACCTCAAAGTCTGTACTTTTAGTAGGTCTTATAGTCATCATAAGAAAACCCTCCCGTAGTCGTATTGTTCTC
CCTATAGTGAGTCGTATTAATTTCGAGCCACCACAGGGAGAATATTTAATTAAATACCGGAACTTCTCCGTAA
GTAGTTACCTTCCCAGCCACACCCAATGATGTTCAGAGGGGTAGTCTCATCTGACAAGATGGTCGACCGATGC
CCTTGAGAGCCTTCAACCCAGTCAGCTCCTTCCGGTGGGCGCGGGGCATGACTATCGTCGCCGCACTTATGAC
TGTCTTCTTTATCATGCAACTCGTAGGACAGGTGCCGGCAGCGCTCTGGGTCATTTTCGGCGAGGACCGCTTT
CGCTGGAGCGCGACGATGATCGGCCTGTCGCTTGCGGTATTCGGAATCTTGCACGCCCTCGCTCAAGCCTTCG
TCACTGGTCCCGCCACCAAACGTTTCGGCGAGAAGCAGGCCATTATCGCCGGCATGGCGGCCGACGCGCTGGG
CTACGTCTTGCTGGCGTTCGCGACGCGAGGCTGGATGGCCTTCCCCATTATGATTCTTCTCGCTTCCGGCGGC
ATCGGGATGCCCGCGTTGCAGGCCATGCTGTCCAGGCAGGTAGATGACGACCATCAGGGACAGCTTCAAGGAT
CGCTCGCGGCTCTTACCAGCCTAACTTCGATCACTGGACCGCTGATCGTCACGGCGATTTATGCCGCCTCGGC
GAGCACATGGAACGGGTTGGCATGGATTGTAGGCGCCGCCCTATACCTTGTCTGCCTCCCCGCGTTGCGTCGC
GGTGCATGGAGCCGGGCCACCTCGACCTGAATGGAAGCCGGCGGCACCTCGCTAACGGATTCACCACTCCAAG
AATTGGAGCCAATCAATTCTTGCGGAGAACTGTGAATGCGCAAACCAACCCTTGGCAGAACATATCCATCGCG
TCCGCCATCTCCAGCAGCCGCACGCGGCGCATCTCGGGCAGCGTTGGGTCCTGGCCACGGGTGCGCATGATCG
TGCTCCTGTCGTTGAGGACCCGGCTAGGCTGGCGGGGTTGCCTTACTGGTTAGCAGAATGAATCACCGATACG
CGAGCGAACGTGAAGCGACTGCTGCTGCAAAACGTCTGCGACCTGAGCAACAACATGAATGGTCTTCGGTTTC
CGTGTTTCGTAAAGTCTGGAAACGCGGAAGTCAGCGCCCTGCACCATTATGTTCCGGATCTGCATCGCAGGAT
GCTGCTGGCTACCCTGTGGAACACCTACATCTGTATTAACGAAGCGCTGGCATTGACCCTGAGTGATTTTTCT
CTGGTCCCGCCGCATCCATACCGCCAGTTGTTTACCCTCACAACGTTCCAGTAACCGGGCATGTTCATCATCA
GTAACCCGTATCGTGAGCATCCTCTCTCGTTTCATCGGTATCATTACCCCCATGAACAGAAATTCCCCCTTAC
ACGGAGGCATCAAGTGACCAAACAGGAAAAAACCGCCCTTAACATGGCCCGCTTTATCAGAAGCCAGACATTA
ACGCTTCTGGAGAAACTCAACGAGCTGGACGCGGATGAACAGGCAGACATCTGTGAATCGCTTCACGACCACG
CTGATGAGCTTTACCGCAGCTGCCTCGCGCGTTTCGGTGATGACGGTGAAAACCTCTGACACATGCAGCTCCC
GGAGACGGTCACAGCTTGTCTGTAAGCGGATGCCGGGAGCAGACAAGCCCGTCAGGGCGCGTCAGCGGGTGTT
GGCGGGTGTCGGGGCGCAGCCATGACCCAGTCACGTAGCGATAGCGGAGTGTATACTGGCTTAACTATGCGGC
ATCAGAGCAGATTGTACTGAGAGTGCACCATATGCGGTGTGAAATACCGCACAGATGCGTAAGGAGAAAATAC
CGCATCAGGCGCTCTTCCGCTTCCTCGCTCACTGACTCGCTGCGCTCGGTCGTTCGGCTGCGGCGAGCGGTAT
CAGCTCACTCAAAGGCGGTAATACGGTTATCCACAGAATCAGGGGATAACGCAGGAAAGAACATGTGAGCAAA
AGGCCAGCAAAAGGCCAGGAACCGTAAAAAGGCCGCGTTGCTGGCGTTTTTCCATAGGCTCCGCCCCCCTGAC
GAGCATCACAAAAATCGACGCTCAAGTCAGAGGTGGCGAAACCCGACAGGACTATAAAGATACCAGGCGTTTC

CCCCTGGAAGCTCCCTCGTGCGCTCTCCTGTTCCGACCCTGCCGCTTACCGGATACCTGTCCGCCTTTCTCCC
TTCGGGAAGCGTGGCGCTTTCTCAATGCTCACGCTGTAGGTATCTCAGTTCGGTGTAGGTCGTTCGCTCCAAG
CTGGGCTGTGTGCACGAACCCCCCGTTCAGCCCGACCGCTGCGCCTTATCCGGTAACTATCGTCTTGAGTCCA
ACCCGGTAAGACACGACTTATCGCCACTGGCAGCAGCCACTGGTAACAGGATTAGCAGAGCGAGGTATGTAGG
CGGTGCTACAGAGTTCTTGAAGTGGTGGCCTAACTACGGCTACACTAGAAGGACAGTATTTGGTATCTGCGCT
CTGCTGAAGCCAGTTACCTTCGGAAAAAGAGTTGGTAGCTCTTGATCCGGCAAACAAACCACCGCTGGTAGCG
GTGGTTTTTTTGTTTGCAAGCAGCAGATTACGCGCAGAAAAAAAGGATCTCAAGAAGATCCTTTGATCTTTTC
TACGGGGTCTGACGCTCAGTGGAACGAAAACTCACGTTAAGGGATTTTGGTCATGAGATTATCAAAAAGGATC
TTCACCTAGATCCTTTTAAATTAAAAATGAAGTTTTAAATCAATCTAAAGTATATATGAGTAAACTTGGTCTG
ACAGTTACCAATGCTTAATCAGTGAGGCACCTATCTCAGCGATCTGTCTATTTCGTTCATCCATAGTTGCCTG
ACTCCCCGTCGTGTAGATAACTACGATACGGGAGGGCTTACCATCTGGCCCCAGTGCTGCAATGATACCGCGA
GACCCACGCTCACCGGCTCCAGATTTATCAGCAATAAACCAGCCAGCCGGAAGGGCCGAGCGCAGAAGTGGTC
CTGCAACTTTATCCGCCTCCATCCAGTCTATTAATTGTTGCCGGGAAGCTAGAGTAAGTAGTTCGCCAGTTAA
TAGTTTGCGCAACGTTGTTGCCATTGCTGCAGGCATCGTGGTGTCACGCTCGTCGTTTGGTATGGCTTCATTC
AGCTCCGGTTCCCAACGATCAAGGCGAGTTACATGATCCCCCATGTTGTGCAAAAAAGCGGTTAGCTCCTTCG
GTCCTCCGATCGTTGTCAGAAGTAAGTTGGCCGCAGTGTTATCACTCATGGTTATGGCAGCACTGCATAATTC
TCTTACTGTCATGCCATCCGTAAGATGCTTTTCTGTGACTGGTGAGTACTCAACCAAGTCATTCTGAGAATAG
TGTATGCGGCGACCGAGTTGCTCTTGCCCGGCGTCAACACGGGATAATACCGCGCCACATAGCAGAACTTTAA
AAGTGCTCATCATTGGAAAACGTTCTTCGGGGCGAAAACTCTCAAGGATCTTACCGCTGTTGAGATCCAGTTC
GATGTAACCCACTCGTGCACCCAACTGATCTTCAGCATCTTTTACTTTCACCAGCGTTTCTGGGTGAGCAAAA
ACAGGAAGGCAAAATGCCGCAAAAAAGGGAATAAGGGCGACACGGAAATGTTGAATACTCATACTCTTCCTTT
TTCAATATTATTGAAGCATTTATCAGGGTTATTGTCTCATGAGCGGATACATATTTGAATGTATTTAGAAAAA
TAAACAAATAGGGGTTCCGCGCACATTTCCCCGAAAAGTGCCACCTGACGTCTAAGAAACCATTATTATCATG
ACATTAACCTATAAAAATAGGCGTATCACGAGGCCCTTTCGTCTTCAAGAATTGATCCGCTGTAATCCGGGCA
GCGCAACGGAACATTCATCAGTGTAAAAATGGAATCAATAAAGCCCTGCGCAGCGCGCAGGGTCAGCCTGAAT
ACGCGTTTAATGACCAGCACAGTCGTGATGGCAAGGTCAGAATAGCGCTGAGGTCTGCCTCGTGAAGAAGGTG
TTGCTGACTCATACCAGGCCTGAATCGCCCCATCATCCAGCCAGAAAGTGAGGGAGCCACGGTTGATGAGAGC
TTTGTTGTAGGTGGACCAGTTGGTGATTTTGAACTTTTGCTTTGCCACGGAACGGTCTGCGTTGTCGGGAAGA
TGCGTGATCTGATCCTTCAACTCAGCAAAAGTTCGATTTATTCAACAAAGCCACGTTGTGTCTCAAAATCTCT
GATGTTACATTGCACAAGATAAAAATATATCATCATGAACAATAAAACTGTCTGCTTACATAAACAGTAATAC
AAGGGGTGTTATGAGCCATATTCAACGGGAAACGTCTTGCTCGAGGCCGCGATTAAATTCCAACATGGATGCT
GATTTATATGGGTATAAATGGGCTCGCGATAATGTCGGGCAATCAGGTGCGACAATCTATCGATTGTATGGGA
AGCCCGATGCGCCAGAGTTGTTTCTGAAACATGGCAAAGGTAGCGTTGCCAATGATGTTACAGATGAGATGGT
CAGACTAAACTGGCTGACGGAATTTATGCCTCTTCCGACCATCAAGCATTTTATCCGTACTCCTGATGATGCA
TGGTTACTCACCACTGCGATCCCCGGGAAAACAGCATTCCAGGTATTAGAAGAATATCCTGATTCAGGTGAAA
ATATTGTTGATGCGCTGGCAGTGTTCCTGCGCCGGTTGCATTCGATTCCTGTTTGTAATTGTCCTTTTAACAG
CGATCGCGTATTTCGTCTCGCTCAGGCGCAATCACGAATGAATAACGGTTTGGTTGATGCGAGTGATTTTGAT
GACGAGCGTAATGGCTGGCCTGTTGAACAAGTCTGGAAAGAAATGCATAAGCTTTTGCCATTCTCACCGGATT
CAGTCGTCACTCATGGTGATTTCTCACTTGATAACCTTATTTTTGACGAGGGGAAATTAATAGGTTGTATTGA
TGTTGGACGAGTCGGAATCGCAGACCGATACCAGGATCTTGCCATCCTATGGAACTGCCTCGGTGAGTTTTCT
CCTTCATTACAGAAACGGCTTTTTCAAAAATATGGTATTGATAATCCTGATATGAATAAATTGCAGTTTCATT

TGATGCTCGATGAGTTTTTCTAATCAGAATTGGTTAATTGGTTGTAACACTGGCAGAGCATTACGCTGACTTG
ACGGGACGGCGGCTTTGTTGAATAAATCGAACTTTTGCTGAGTTGAAGGATCAGATCACGCATCTTCCCGACA
ACGCAGACCGTTCCGTGGCAAAGCAAAAGTTCAAAATCACCAACTGGTCCACCTACAACAAAGCTCTCATCAA
CCGTGGCTCCCTCACTTTCTGGCTGGATGATGGGGCGATTCAGGCCTGGTATGAGTCAGCAACACCTTCTTCA
CGAGGCAGACCTCAGCGCTATTCTGACCTTGCCATCACGACTGTGCTGGTCATTAAACGCGTATTCAGGCTGA
CCCTGCGCGCTGCGCAGGGCTTTATTGATTCCATTTTTACACTGATGAATGTTCCGTTGCGCTGCCCGGATTA
CAGCGGATCAATTCCCAATTCCAGGCATCAAATAAAACGAAAGGCTCAGTCGAAAGACTGGGCCTTTCGTTTT
ATCTGTTGTTTGTCGGTGAACGCTCTCCTGAGTAGGACAAATCCGCCGGGAGCGGATTTGAACGTTGCGAAGC
AACGGCCCGGAGGGTGGCGGGCAGGACGCCCGCCATAAACTGCCAGGAATTAATTCCAGGCATCAAATAAAAC
GAAAGGCTCAGTCGAAAGACTGGGCCTTTCGTTTTATCTGTTGTTTGTCGGTGAACGCTCTCCTGAGTAGGAC
AAATCCGCCGGGAGCGGATTTGAACGTTGCGAAGCAACGGCCCGGAGGGTGGCGGGCAGGACGCCCGCCATAA
ACTGCCAGGAATTAATTCCAGGCATCAAATAAAACGAAAGGCTCAGTCGAAAGACTGGGCCTTTCGTTTTATC
TGTTGTTTGTCGGTGAACGCTCTCCTGAGTAGGACAAATCCGCCGGGAGCGGATTTGAACGTTGCGAAGCAAC
GGCCCGGAGGGTGGCGGGCAGGACGCCCGCCATAAACTGCCAGGAATTAATTCCAGGCATCAAATAAAACGAA
AGGCTCAGTCGAAAGACTGGGCCTTTCGTTTTATCTGTTGTTTGTCGGTGAACGCTCTCCTGAGTAGGACAAA
TCCGCCGGGAGCGGATTTGAACGTTGCGAAGCAACGGCCCGGAGGGTGGCGGGCAGGACGCCCGCCATAAACT
GCCAGGAA

**Abbreviations**

| | | |
|---|---|---|
| 3’-dATP | – | 3'-Deoxyadenosine-5'-Triphosphate |
| AFM | – | Atomic force microscopy |
| B-ME | – | Betamercaptoethanol |
| BSA | – | Bovine serum albumin |
| CCD | – | Charge-coupled device |
| CFU | – | Colony-forming unit |
| CMOS | – | Complementary metal–oxide–semiconductor |
| COC | – | Cyclic olefin copolymer |
| CV | – | Coefficient of variance |
| dATP | – | Deoxyadenosine triphosphate |
| dNTP | – | Deoxyribonucleotide |
| dUTP | – | Deoxyuridine triphosphate |
| ddTTP | – | 2',3'-Dideoxythymidine-5'-Triphosphate |
| dsDNA | – | Double-stranded DNA |
| DMSO | – | Dimethyl sulfoxide |
| DNA | – | Deoxyribonucleic acid |
| DTT | – | Dithiothreitol |
| EB | – | Elution buffer |
| *E. coli* | – | *Escherichia coli* |
| EDTA | – | Ethylenediaminetetraacetic acid |
| ELWD | – | Extra-long working distance |
| FPLC | – | Fast phase liquid chromatography |
| FWHM | – | Full width half maximum |
| GUI | – | Graphical user interface |
| HEPES | – | 4-(2-hydroxyethyl)-1-piperazineethanesulfonic acid |
| HMT | – | Horizontal magnetic tweezers |
| LB | – | Lysogeny broth |
| LED | – | Light emitting diode |
| MS | – | Microspheres |
| NA | – | Numerical aperture |
| NEB | – | New England Biolabs |
| NHS | – | *N*-Hydroxysuccinimide |
| NMR | – | Nuclear magnetic resonance |

| | | |
|---|---|---|
| OD | – | Optical density |
| $OD_{600}$ | – | Optical density at 600 nm |
| PAG-MS | – | Protein A/G functionalised microspheres |
| PAG-AD-MS | – | Anti-digoxigenin and protein A/G functionalised microspheres |
| PBS | – | Phosphate Buffered Saline |
| PCR | – | Polymerase chain reaction |
| PDB | – | Protein Data Bank |
| PDMS | – | Polydimethylsiloxane |
| PMSF | – | Phenylmethanesulfonylfluoride |
| RIE | – | Reactive ion etching |
| RNA | – | Ribonucleic acid |
| RNAP | – | RNA polymerase |
| rNTP | – | Ribonucleotide |
| ROI | – | Region of interest |
| ROS | – | Reactive oxygen species |
| SDS | – | Sodium dodecyl sulfate |
| SDS PAGE | – | SDS polyacrylamide gel electrophoresis |
| SE | – | Standard error |
| SEM | – | Scanning electron microscope |
| STM | – | Scanning tunnelling microscope |
| TCEP | – | Tris(2-carboxyethyl)phosphine |
| TdT | – | Terminal transferase |
| TE | – | Tris-EDTA buffer |
| TEM | – | Transmission electron microscope |
| TEMED | – | Tetramethylethylenediamine |
| TFS | – | TransFluoSpheres |
| TIRF | – | Total internal reflection fluorescence |
| USAF | – | United States Air Force |
| UV | – | Ultra-violet radiation |
| WLC | – | Worm-like chain model |
| ZOI | – | Zone of interaction |

## References


1. L. F. Liu and J. C. Wang, *PNAS*, 1987, **84**, 7024–7.

2. D. M. Lilley, D. Chen, and R. P. Bowater, *Q. Rev. Biophys.*, 1996, **29**, 203–25.

3. J. C. Wang and A. S. Lynch, *Curr. Opin. Genet. Dev.*, 1993, **3**, 764–768.

4. Y. P. Tsao, H. Y. Wu, and L. F. Liu, *Cell*, 1989, **56**, 111–8.

5. Y. Harada, O. Ohara, A. Takatsuki, H. Itoh, N. Shimamoto, and K. Kinosita, *Nature*, 2001, **409**, 113–5.

6. J. K. Lodge, T. Kazic, and D. E. Berg, *J. Bacteriol.*, 1989, **171**, 2181–7.

7. J. E. Krebs and M. Dunaway, *Mol. Cell. Biol.*, 1996, **16**, 5821–9.

8. P. Nelson, *PNAS*, 1999, **96**, 14342–7.

9. M. Gellert, *Annu. Rev. Biochem.*, 1981, **50**, 879–910.

10. C. Levinthal and H. R. Crane, *PNAS*, 1956, **42**, 436–8.

11. H. K. Das, A. Goldstein, and L. I. Lowney, *J. Mol. Biol.*, 1967, **24**, 231–45.

12. B. ten Heggeler-Bordier, W. Wahli, M. Adrian, a Stasiak, and J. Dubochet, *EMBO J.*, 1992, **11**, 667–72.

13. R. Samul and F. Leng, *J. Mol. Biol.*, 2007, **374**, 925–35.

14. M. Drolet, X. Bi, and L. F. Liu, *J. Biol. Chem.*, 1994, **269**, 2068–74.

15. O. L. Miller and B. R. Beatty, *Science*, 1969, **164**, 955–7.

16. B. A. Hamkalo and O. L. Miller, *Annu. Rev. Biochem.*, 1973, **42**, 379–96.

17. G. P. Dimri and H. K. Das, *MGG*, 1988, **212**, 360–363.

18. H. Burns and S. Minchin, *Nucleic Acids Res.*, 1994, **22**, 3840–5.

19. J. D. Parvin and P. a Sharp, *Cell*, 1993, **73**, 533–40.

20. V. Epshtein and E. Nudler, *Science*, 2003, **300**, 801–5.

21. V. Epshtein, F. Toulme, A. R. Rahmouni, S. Borukhov, and E. Nudler, *EMBO J.*, 2003, **22**, 4719–4727.

22. R. Ferrari, C. Rivetti, and G. Dieci, *Biochem. Biophys. Res. Commun.*, 2004, **315**, 376–80.

23. D. L. Nelson and M. M. Cox, *Lehninger Principles of Biochemistry*, W.H. Freeman and Company, New York, 5th Ed., 2008.

24. R. Menzel and M. Gellert, *Cell*, 1983, **34**, 105–13.

25. T. R. Strick, J. F. Allemand, D. Bensimon, A. Bensimon, and V. Croquette, *Science*, 1996, **271**, 1835–7.

26. G. M. Skinner, C. G. Baumann, D. M. Quinn, J. E. Molloy, and J. G. Hoggett, *J. Biol. Chem.*, 2004, **279**, 3239–44.

27. J. H. Kim and R. G. Larson, *Nucleic Acids Res.*, 2007, **35**, 3848–58.

28. Y. Harada, T. Funatsu, K. Murakami, Y. Nonoyama, A. Ishihama, and T. Yanagida, *Biophys. J.*, 1999, **76**, 709–15.

29. Y. Tsuda, H. Yasutake, A. Ishijima, and T. Yanagida, *PNAS*, 1996, **93**, 12937–42.

30. T. R. Strick, J. F. Allemand, D. Bensimon, and V. Croquette, *Biophys. J.*, 1998, **74**, 2016–28.

31. J. H. White, *Am. J. Math.*, 1969, **91**, 693.

32. M. C. Schultz, S. J. Brill, Q. Ju, R. Sternglanz, and R. H. Reeder, *Genes Dev.*, 1992, **6**, 1332–1341.

33. G. M. T. Cheetham and T. A. Steitz, *Science*, 1999, **286**, 2305–9.

34. I. Kuzmine, P. A. Gottlieb, and C. T. Martin, *J. Biol. Chem.*, 2003, **278**, 2819–23.

35. A. J. Carpousis and J. D. Gralla, *Biochemistry*, 1980, **19**, 3245–53.

36. R. A. Ikeda and C. C. Richardson, *PNAS*, 1986, **83**, 3614–8.

37. C. T. Martin, D. K. Muller, and J. E. Coleman, *Biochemistry*, 1988, **27**, 3966–74.

38. G. M. T. Cheetham, D. Jeruzalmi, and T. A. Steitz, *Nature*, 1999, **399**, 80–83.

39. A. N. Kapanidis, E. Margeat, S. O. Ho, E. Kortkhonjia, S. Weiss, and R. H. Ebright, *Science*, 2006, **314**, 1144–7.

40. A. N. Kapanidis, E. Margeat, S. O. Ho, E. Kortkhonjia, S. Weiss, and R. H. Ebright, *Science*, 2006, **314**, 1144–7.

41. G. M. Skinner, B. S. Kalafut, and K. Visscher, *Biophys. J.*, 2011, **100**, 1034–41.

42. W. R. McClure, *Annu. Rev. Biochem.*, 1985, **54**, 171–204.

43. R. A. Ikeda, *J. Biol. Chem.*, 1992, **267**, 11322–11328.

44. Y. W. Yin and T. A. Steitz, *Science*, 2002, **298**, 1387–95.

45. T. H. Tahirov, D. Temiakov, M. Anikin, V. Patlan, W. T. McAllister, D. G. Vassylyev, and S. Yokoyama, *Nature*, 2002, **420**, 43–50.

46. T. A. Steitz, *EMBO J.*, 2006, **25**, 3458–3468.

47. J. Huang and R. Sousa, *J. Mol. Biol.*, 2000, **303**, 347–58.

48. D. Temiakov, P. E. Mentesana, K. Ma, A. Mustaev, S. Borukhov, and W. T. Mcallister, *PNAS*, 2000, **97**, 14109–14.

49. C. Liu and C. T. Martin, *J. Mol. Biol.*, 2001, **308**, 465–75.

50. R. Guajardo and R. Sousa, *J. Mol. Biol.*, 1997, **265**, 8–19.

51. P. Thomen, P. J. Lopez, and F. Heslot, *Phys. Rev. Lett.*, 2005, **94**, 128102–1 – 128102–4.

52. D. L. Lyakhov, B. He, X. Zhang, F. W. Studier, J. J. Dunn, and W. T. McAllister, *J. Mol. Biol.*, 1998, **280**, 201–213.

53. J. J. Dunn, F. W. Studier, and M. Gottesman, *J. Mol. Biol.*, 1983, **166**, 477–535.

54. L. E. Macdonald, R. K. Durbin, J. J. Dunn, and W. T. McAllister, *J. Mol. Biol.*, 1994, **238**, 145–58.

55. B. He, A. Kukarin, D. Temiakov, S. T. Chin-Bow, D. L. Lyakhov, M. Rong, R. K. Durbin, and W. T. Mcallister, *J. Biol. Chem.*, 1998, **273**, 18802–18811.

56. D. A. Mead, E. Szczesna-Skorupa, and B. Kemper, *Protein Eng.*, 1986, **1**, 67–74.

57. K. Ma, D. Temiakov, M. Anikin, and W. T. McAllister, *PNAS*, 2005, **102**, 17612–17617.

58. B. Ladoux and P. S. Doyle, *Eur. Lett.*, 2000, **52**, 511–517.

59. M. Reuter, F. Parry, D. T. F. Dryden, and G. W. Blakely, *Nucleic Acids Res.*, 2010, **38**, 3721–31.

60. T. Fazio, M.-L. Visnapuu, S. Wind, and E. C. Greene, *Langmuir*, 2008, **24**, 10524–31.

61. D. C. Duffy, J. C. McDonald, O. J. A. Schueller, and G. M. Whitesides, *Anal. Chem.*, 1998, **70**, 4974–4984.

62. A. Ashkin, *Phys. Rev. Lett.*, 1970, **24**, 156–159.

63. J. R. Moffitt, Y. R. Chemla, S. B. Smith, and C. Bustamante, *Annu. Rev. Biochem.*, 2008, **77**, 205–28.

64. C. G. Baumann and S. J. Cross, *Methods Mol. Biol.*, 2011, **778**, 175–91.

65. K. C. Neuman and A. Nagy, *Nat. Methods*, 2008, **5**, 491–505.

66. K. C. Neuman and S. M. Block, *Rev. Sci. Instrum.*, 2004, **75**, 2787–809.

67. D. G. Grier, *Nature*, 2003, **424**, 810–6.

68. M. E. J. Friese, T. A. Nieminen, N. R. Heckenberg, and H. Rubinsztein-Dunlop, *Nature*, 2003, **395**, 4.

69. A. La Porta and M. Wang, *Phys. Rev. Lett.*, 2004, **92**, 190801.

70. Y. Seol and K. C. Neuman, *Methods Mol. Biol.*, 2011, **778**, 229–41.

71. C. Gosse and V. Croquette, *Biophys. J.*, 2002, **82**, 3314–29.

72. J. Lipfert, J. W. J. Kerssemakers, T. Jager, and N. H. Dekker, *Nat. Methods*, 2010, **7**, 977–80.

73. K. C. Neuman, T. Lionnet, and J.-F. Allemand, *Annu. Rev. Mater. Res.*, 2007, **37**, 33–67.

74. C. Danilowicz, V. W. Coljee, C. Bouzigues, D. K. Lubensky, D. R. Nelson, and M. Prentiss, *PNAS*, 2003, **100**, 1694–9.

75. F. W. Schwarz, J. Tóth, K. van Aelst, G. Cui, S. Clausing, M. D. Szczelkun, and R. Seidel, *Science*, 2013, **340**, 353–6.

76. J. S. Graham, R. C. Johnson, and J. F. Marko, *Nucleic Acids Res.*, 2011, **39**, 2249–59.

77. M. T. J. van Loenhout, M. V de Grunt, and C. Dekker, *Science*, 2012, **338**, 94–7.

78. X. Zhang, H. Chen, H. Fu, P. S. Doyle, and J. Yan, *PNAS*, 2012, **109**, 8103–8.

79. H. Fu, H. Chen, X. Zhang, Y. Qu, J. F. Marko, and J. Yan, *Nucleic Acids Res.*, 2011, **39**, 3473–81.

80. X. Zhang, H. Chen, S. Le, I. Rouzina, P. S. Doyle, and J. Yan, *PNAS*, 2013, **110**, 3865–70.

81. C. Haber and D. Wirtz, *Rev. Sci. Instrum.*, 2000, **71**, 4561.

82. C.-H. Chiou, Y.-Y. Huang, M.-H. Chiang, H.-H. Lee, and G.-B. Lee, *Nanotechnology*, 2006, **17**, 1217–1224.

83. R. E. J. Farrell, *RNA Methodologies: A Laboratory Guide for Isolation and Characterization*, Elsevier Science, 1993.

84. C. A. Schneider, W. S. Rasband, and K. W. Eliceiri, *Nat. Methods*, 2012, **9**, 671–675.

85. A. S. Callaway, R. Abranches, J. Scroggs, G. C. Allen, and W. F. Thompson, *Plant Mol. Biol. Report.*, 2012, **20**, 265–277.

86. S. Houston, G. W. Blakely, A. McDowell, L. Martin, and S. Patrick, *Microbiology*, 2010, **156**, 2516–26.

87. K. Remaut, N. N. Sanders, F. Fayazpour, J. Demeester, and S. C. De Smedt, *J. Control. Release*, 2006, **115**, 335–43.

88. Y. Xu, K. D. Lunnen, and H. Kong, *PNAS*, 2001, **98**, 12990–5.

89. E. Goldstein and K. Drlica, *PNAS*, 1984, **81**, 4046–50.

90. J. D. Watson and F. H. C. Crick, *Nature*, 1953, **171**, 737–738.

91. C. Rivetti, M. Guthold, and C. Bustamante, *J. Mol. Biol.*, 1996, **264**, 919–32.

92. A. Sanchez-Sevilla, J. Thimonier, M. Marilley, J. Rocca-Serra, and J. Barbet, *Ultramicroscopy*, 2002, **92**, 151–8.

93. S. Mukherjee, L. G. Brieba, and R. Sousa, *Cell*, 2002, **110**, 81–91.

94. B. He, M. Rong, D. Lyakhov, H. Gartenstein, G. Diaz, R. Castagna, W. T. McAllister, and R. K. Durbin, *Protein Expr. Purif.*, 1997, **9**, 142–51.

95. G. A. F. Seber, *Nonlinear Regression*, Wiley, New York, 1989.

96. B. A. Moffatt, J. J. Dunn, and F. W. Studier, *J. Mol*, 1984, **173**, 265–9.

97. J. Grodberg and J. J. Dunn, *J. Bacteriol.*, 1988, **170**, 1245–53.

98. S. Schlehuber, G. Beste, and A. Skerra, *J. Mol. Biol.*, 2000, **297**, 1105–20.

99. J. Lipfert, X. Hao, and N. H. Dekker, *Biophys. J.*, 2009, **96**, 5040–9.

100. J. Sambrook, E. F. Fritsch, and T. Maniatis, *Molecular Cloning: A Laboratory Manual*, Cold Spring Harbor Laboratory Press, New York, Second., 1989.

101. M. A. Tycon, C. F. Dial, K. Faison, W. Melvin, and C. J. Fecko, *Anal. Biochem.*, 2012, **426**, 13–21.

102. B. Akerman and E. Tuite, *Nucleic Acids Res.*, 1996, **24**, 1080–90.

103. W. A. Lyon, M. M. Fang, W. E. Haskins, and S. Nie, *Anal. Chem.*, 1998, **70**, 1743–8.

104. C. Veigel, M. L. Bartoo, D. C. White, J. C. Sparrow, and J. E. Molloy, *Biophys. J.*, 1998, **75**, 1424–38.

105. S. Gurrieri, K. S. Wells, I. D. Johnson, and C. Bustamante, *Anal. Biochem.*, 1997, **249**, 44–53.

106. I. Amitani, B. Liu, C. C. Dombrowski, R. J. Baskin, and S. C. Kowalczykowski, *Methods Enzym.*, 2010, **472**, 261–91.

107. D. Axelrod, *J. Cell Biol.*, 1981, **89**, 141–5.

108. I. H. Malitson, *J. Opt. Soc. Am.*, 1965, **55**, 1205.

109. A. H. Harvey, J. S. Gallagher, and J. M. H. L. Sengers, *J. Phys. Chem. Ref. Data*, 1998, **27**, 761.

110. K. P. Birch and M. J. Downs, *Metrologia*, 1994, **31**, 315–316.

111. G. Binnig and C. F. Quate, *Phys. Rev. Lett.*, 1986, **56**, 930–933.

112. L. B. Oddershede, *Nat. Chem. Biol.*, 2012, **8**, 879–86.

113. S. Liu and Y. Wang, *Scanning*, 2010, **32**, 61–73.

114. S. Kasas, N. H. Thomson, B. L. Smith, P. K. Hansma, J. Miklossy, and H. G. Hansma, *Int. J. Imaging Syst. Technol.*, 1997, **8**, 151–161.

115. I. Y. Sokolov, G. S. Henderson, and F. J. Wicks, *Surf. Sci.*, 2000, **457**, 267–272.

116. D. Y. Abramovitch, S. B. Andersson, L. Y. Pao, and G. Schitter, *2007 Am. Control Conf.*, 2007, 3488–3502.

117. N. Jalili and K. Laxminarayana, *Mechatronics*, 2004, **14**, 907–945.

118. F. a Schabert and J. P. Rabe, *Biophys. J.*, 1996, **70**, 1514–20.

119. M. Stark, R. W. Stark, W. M. Heckl, and R. Guckenberger, *PNAS*, 2002, **99**, 8473–8.

120. Q. Zhong, D. Inniss, K. Kjoller, and V. B. Elings, *Surf. Sci.*, 1993, **290**, L688–L692.

121. M. Guthold, X. Zhu, C. Rivetti, G. Yang, N. H. Thomson, S. Kasas, H. G. Hansma, B. Smith, P. K. Hansma, and C. Bustamante, *Biophys. J.*, 1999, **77**, 2284–94.

122. H. Yamashita, A. Taoka, T. Uchihashi, T. Asano, T. Ando, and Y. Fukumori, *J. Mol. Biol.*, 2012.

123. T. Ando, T. Uchihashi, N. Kodera, D. Yamamoto, A. Miyagi, M. Taniguchi, and H. Yamashita, *Pflügers Arch.*, 2008, **456**, 211–25.

124. A. J. Katan and C. Dekker, *Cell*, 2011, **147**, 979–82.

125. T. Ando, N. Kodera, E. Takai, D. Maruyama, K. Saito, and A. Toda, *PNAS*, 2001, **98**, 12468–72.

126. J. Vesenka, M. Guthold, C. L. L. Tang, D. Keller, E. Delaine, and C. Bustamante, *Ultramicroscopy*, 1992, **42-44**, 1243–1249.

127. C. Bustamante, J. Vesenka, C. L. Tang, W. Rees, M. Guthold, and R. Keller, *Biochemistry*, 1992, **31**, 22–6.

128. W. A. Deer, R. A. Howie, and J. Zussman, *An Introduction to The Rock Forming Minerals*, Longman Scientific & Technical, New York, Second Edi., 1966.

129. R. Erlandsson, G. Hadziioannou, C. M. Mate, G. M. McClelland, and S. Chiang, *J. Chem. Phys.*, 1988, **89**, 5190.

130. F. Ostendorf, C. Schmitz, S. Hirth, A. Kühnle, J. J. Kolodziej, and M. Reichling, *Nanotechnology*, 2008, **19**, 305705.

131. D. Pastré, L. Hamon, F. Landousy, I. Sorel, M.-O. David, A. Zozime, E. Le Cam, and O. Piétrement, *Langmuir*, 2006, **22**, 6651–60.

132. N. Crampton, W. A. Bonass, J. Kirkham, C. Rivetti, and N. H. Thomson, *Nucleic Acids Res.*, 2006, **34**, 5416–25.

133. D. Pastré, O. Piétrement, S. Fusil, F. Landousy, J. Jeusset, M.-O. David, L. Hamon, E. Le Cam, and A. Zozime, *Biophys. J.*, 2003, **85**, 2507–18.

134. P. J. Flory, *Statistical Mechanics of Chain Molecules*, Interscience, New York, 1969.

135. C. Rivetti, M. Guthold, and C. Bustamante, *EMBO J.*, 1999, **18**, 4464–75.

136. P. Nelson, *Biological Physics: Energy, Information, Life*, W.H. Freeman and Company, New York, Third Edit., 2004.

137. O. Y. Limanskaya and A. P. Limanskii, *Mol. Biol. (Moscow, Russ. Fed., Engl. Ed.)*, 2008, **42**, 469–477.

138. R. T. Dame, C. Wyman, R. Wurm, R. Wagner, and N. Goosen, *J. Biol. Chem.*, 2002, **277**, 2146–50.

139. C. Rivetti, S. Codeluppi, G. Dieci, and C. Bustamante, *J. Mol. Biol.*, 2003, **326**, 1413–1426.

140. J. R. Levin, B. Krummel, and M. J. Chamberlin, *J. Mol. Biol.*, 1987, **196**, 85–100.

141. A. L. Chambers, A. J. Smith, and N. J. Savery, *Nucleic Acids Res.*, 2003, **31**, 6409–6418.

142. G. A. Diaz, M. Rong, W. T. McAllister, and R. K. Durbin, *Biochemistry*, 1996, **35**, 10837–43.

143. P. Gong and C. T. Martin, *J. Biol. Chem.*, 2006, **281**, 23533–44.

144. L. Hamon, D. Pastré, P. Dupaigne, C. Le Breton, E. Le Cam, and O. Piétrement, *Nucleic Acids Res.*, 2007, **35**, e58.

145. X. Zhang, X. Hou, C. Ji, M. Li, S. Dou, and P. Wang, *Chinese Sci. Bull.*, 2009, **54**, 2425–2433.

146. D. K. Chattoraj, L. C. Gosule, and J. A. Schellman, *J. Mol. Biol.*, 1978, **121**, 327–337.

147. R. W. Wilson and V. A. Bloomfield, *Biochemistry*, 1979, **18**, 2192–2196.

148. C. G. Baumann, S. B. Smith, V. A. Bloomfield, and C. Bustamante, *PNAS*, 1997, **94**, 6185–90.

149. C. Bustamante, J. F. Marko, E. D. Siggia, and S. Smith, *Science*, 1994, **265**, 1599–1600.

150. P. Cluzel, A. Lebrun, C. Heller, R. Lavery, J.-L. Viovy, D. Chatenay, and F. o. Caron, *Science*, 1996, **271**, 792–794.

151. S. B. Smith, Y. Cui, and C. Bustamante, *Science*, 1996, **271**, 795–9.

152. R. Hölzel, N. Calander, Z. Chiragwandi, M. Willander, and F. Bier, *Phys. Rev. Lett.*, 2005, **95**, 128102.

153. J. Lipfert, M. Wiggin, J. W. J. Kerssemakers, F. Pedaci, and N. H. Dekker, *Nat. Commun.*, 2011, **2**, 439.

154. H. D. Young and A. Freedman, Roger, *University Physics with Modern Physics*, Pearson Education, Inc., San Fransico, California, Eleventh E., 2004.

155. A. J. W. te Velthuis, J. W. J. Kerssemakers, J. Lipfert, and N. H. Dekker, *Biophys. J.*, 2010, **99**, 1292–1302.

156. D. L. Ermak and J. a. McCammon, *J. Chem. Phys.*, 1978, **69**, 1352.

157. Y. Deng, J. Bechhoefer, and N. R. Forde, *J. Opt. A*, 2007, **9**, S256–S263.

158. N. Pottier, *Nonequilibrium Statistical Physics: Linear Irreversible Processes*, Oxford University Press, Oxford, Illustrate., 2010.

159. B. M. Lansdorp and O. A. Saleh, *Rev. Sci. Instrum.*, 2012, **83**, 025115.

160. J. F. Beausang, C. Zurla, L. Finzi, L. Sullivan, and P. C. Nelson, *Am. J. Phys.*, 2007, **75**, 520.

161. M. K. Cheezum, W. F. Walker, and W. H. Guilford, *Biophys. J.*, 2001, **81**, 2378–88.

162. K. B. Towles, J. F. Beausang, H. G. Garcia, R. Phillips, S. Monte, and P. C. Nelson, *Phys. Biol.*, 2009, **6**, 025001.

163. P. M. Oliver, J. S. Park, and D. Vezenov, *Nanoscale*, 2011, **3**, 581–91.

164. H. Weichel, *Laser Beam Propagation in the Atmosphere*, SPIE Press, Illustrate., 1990.

165. H. Weichel, *Laser Beam Propagation in the Atmosphere*, SPIE Press, Illustrate., 1990.

166. J. Irudayaraj, *Biomedical Nanosensors*, CRC Press, Illustrate., 2011.

167. M. K. Bhalgat, R. P. Haugland, J. S. Pollack, and S. Swan, *J. Immunol. Methods*, 1998, **219**, 57–68.

168. S. Fedorov, *GetData*, 2008.

169. J. Gelles, B. J. Schnapp, and M. P. Sheetz, *Nature*, 1988, **331**, 450–3.

170. A. Kusumi, Y. Sako, and M. Yamamoto, *Biophys. J.*, 1993, **65**, 2021–40.

171. R. N. Ghosh and W. W. Webb, *Biophys. J.*, 1994, **66**, 1301–18.

172. G. M. Lee, A. Ishihara, and K. A. Jacobson, *PNAS*, 1991, **88**, 6274–8.

173. C. M. Anderson, G. N. Georgiou, I. E. Morrison, G. V Stevenson, and R. J. Cherry, *J. Cell Biol.*, 1992, **101 ( Pt 2**, 415–25.

174. G. J. Schütz, H. Schindler, and T. Schmidt, *Biophys. J.*, 1997, **73**, 1073–80.

175. N. Laurens, S. R. W. Bellamy, A. F. Harms, Y. S. Kovacheva, S. E. Halford, and G. J. L. Wuite, *Nucleic Acids Res.*, 2009, 1–11.

176. N. Pouget, C. Dennis, C. Turlan, M. Grigoriev, M. Chandler, and L. Salome, *Nucleic Acids Res.*, 2004, **32**, e73.

177. H. Ewers, A. E. Smith, I. F. Sbalzarini, H. Lilie, P. Koumoutsakos, and A. Helenius, *PNAS*, 2005, **102**, 15110–5.

178. F. Reif, *Fundamentals of Statistical and Thermal Physics*, McGraw-Hill Book Co., Singapore, Internatio., 1965.

179. H. F. Fan and H. W. Li, *Biophys. J.*, 2009, **96**, 1875–83.

180. S. K. Sia and L. J. Kricka, *Lab. Chip.*, 2008, **8**, 1982–3.

181. M. U. Kopp, *Science*, 1998, **280**, 1046–1048.

182. D. B. Weibel, W. R. Diluzio, and G. M. Whitesides, *Nat. Rev. Microbiol.*, 2007, **5**, 209–18.

183. X. Tan, M. Mizuuchi, and K. Mizuuchi, *PNAS*, 2007, **104**, 13925–9.

184. L. R. Brewer and P. R. Bianco, *Nat. Methods*, 2008, **5**, 517–25.

185. M. Reuter and D. T. F. Dryden, *Biochem. Biophys. Res. Commun.*, 2010, **403**, 225–9.

186. S. B. Smith, L. Finzi, and C. Bustamante, *Science*, 1992, **258**, 1122–6.

187. J. Shi, T. Yang, S. Kataoka, Y. Zhang, A. J. Diaz, and P. S. Cremer, *J. Am. Chem. Soc.*, 2007, **129**, 5954–61.

188. M. Vojtíšek, A. Iles, and N. Pamme, *Biosens. Bioelectron.*, 2010.

189. S. H. Kang, S. Jeong, D. Kim, Y. He, and E. S. Yeung, *Bull. Korean Chem. Soc.*, 2005, **26**, 315–318.

190. M. L. Bennink, O. D. Schärer, R. Kanaar, K. Sakata-Sogawa, J. M. Schins, J. S. Kanger, B. G. de Grooth, and J. Greve, *Cytometry*, 1999, **36**, 200–8.

191. F. Merenda, J. Rohner, J. Fournier, and R.-P. Salathé, *Opt. Express*, 2007, **15**, 6075.

192. M.-L. Visnapuu, D. Duzdevich, and E. C. Greene, *Using Total Internal Reflection Fluorescence Microscopy, DNA Curtains, and Quantum Dots to Investigate Protein-DNA Interactions at the Single-molecule Level*, 2007.

193. T. McCreedy, *Anal. Chim. Acta*, 2001, **427**, 39–43.

194. M. Stjernström and J. Roeraade, *J. Micromech. Microeng.*, 1998, **8**, 33–38.

195. B. H. Timmer, M. van Delft, W. Koelmans, W. Olthuis, and A. van den Berg, *IEEE Sens. J.*, 2006, **6**, 829–835.

196. G. Mehta, J. Lee, W. Cha, Y.-C. Tung, J. J. Linderman, and S. Takayama, *Anal. Chem.*, 2009, **81**, 3714–22.

197. J. Steigert, S. Haeberle, T. Brenner, C. Müller, C. P. Steinert, P. Koltay, N. Gottschlich, H. Reinecke, J. Rühe, R. Zengerle, and J. Ducrée, *J. Micromech. Microeng.*, 2007, **17**, 333–341.

198. J. Cheng and N. Giordano, *Phys. Rev. E Stat., Nonlinear, Soft Matter Phys.*, 2002, **65**, 031206.

199. S. G. Moorjani, L. Jia, T. N. Jackson, and W. O. Hancock, *Nano Lett.*, 2003, **3**, 633–637.

200. Y. Jia, J. Jiang, X. Ma, Y. Li, H. Huang, K. Cai, S. Cai, and Y. Wu, *Chinese Sci. Bull.*, 2008, **53**, 3928–3936.

201. L. Lei, H. Li, J. Shi, and Y. Chen, *Rev. Sci. Instrum.*, 2010, **81**, 023103.

202. K. Stephan, P. Pittet, L. Renaud, P. Kleimann, P. Morin, N. Ouaini, and R. Ferrigno, *J. Micromech. Microeng.*, 2007, **17**, N69–N74.

203. T. Yang, S. Jung, H. Mao, and P. S. Cremer, *Anal. Chem.*, 2001, **73**, 165–169.

204. J. C. McDonald, D. C. Duffy, J. R. Anderson, D. T. Chiu, H. Wu, O. J. Schueller, and G. M. Whitesides, *Electrophoresis*, 2000, **21**, 27–40.

205. P. Honarmandi, H. Lee, M. J. Lang, and R. D. Kamm, *Lab Chip*, 2011, **11**, 684–94.

206. P. Nath, D. Fung, Y. A. Kunde, A. Zeytun, B. Branch, and G. Goddard, *Lab Chip*, 2010, **10**, 2286–91.

207. B. Wang, J. Ho, J. Fei, R. L. Gonzalez, and Q. Lin, *Lab Chip*, 2011, **11**, 274–81.

208. J. Atencia, G. a Cooksey, and L. E. Locascio, *Lab Chip*, 2012, **12**, 309–16.

209. P. Abgrall, C. Lattes, V. Conédéra, X. Dollat, S. Colin, and A. M. Gué, *J. Micromech. Microeng.*, 2006, **16**, 113–121.

210. A. Taberham, M. Kraft, M. Mowlem, and H. Morgan, *J. Micromech. Microeng.*, 2008, **18**, 064011.

211. Y.-C. Tsai, H.-P. Jen, K.-W. Lin, and Y.-Z. Hsieh, *J. Chromatogr., A*, 2006, **1111**, 267–71.

212. P. Vulto, N. Glade, L. Altomare, J. Bablet, L. Del Tin, G. Medoro, I. Chartier, N. Manaresi, M. Tartagni, and R. Guerrieri, *Lab Chip*, 2005, **5**, 158–62.

213. D. Duval, A. B. González-Guerrero, S. Dante, J. Osmond, R. Monge, L. J. Fernández, K. E. Zinoviev, C. Domínguez, and L. M. Lechuga, *Lab Chip*, 2012, 1987–1994.

214. F. Larramendy, L. Mazenq, P. Temple-Boyer, and L. Nicu, *Lab Chip*, 2012, **12**, 387–90.

215. S. Cosson, S. A. Kobel, M. P. Lutolf, and B. S. Cosson, *Adv. Funct. Mater.*, 2009, **19**, 3411–3419.

216. D. Di Carlo, C. Ionescu-Zanetti, Y. Zhang, P. Hung, and L. P. Lee, *Lab Chip*, 2005, **5**, 171–8.

217. L. Kim, M. D. Vahey, H.-Y. Lee, and J. Voldman, *Lab Chip*, 2006, **6**, 394–406.

218. S. Kobel, A. Valero, J. Latt, P. Renaud, and M. Lutolf, *Lab Chip*, 2010, 10–12.

219. H. Wu, A. Wheeler, and R. N. Zare, *PNAS*, 2004, **101**, 12809–13.

220. B. Bilenberg, T. Nielsen, B. Clausen, and A. Kristensen, *J. Micromech. Microeng.*, 2004, **14**, 814–818.

221. N. Demierre, T. Braschler, P. Linderholm, U. Seger, H. van Lintel, and P. Renaud, *Lab Chip*, 2007, **7**, 355–65.

222. R. Hill, J. Millman, and O. D. Velev, *Pharm. Eng.*, 2004, 24, 1–7.

223. Y. Hiratsuka, T. Tada, K. Oiwa, T. Kanayama, and T. Q. Uyeda, *Biophys. J.*, 2001, **81**, 1555–61.

224. J. C. Ribeiro, G. Minas, P. Turmezei, R. F. Wolffenbuttel, and J. H. Correia, *Sens. Actuators, A*, 2005, **123-124**, 77–81.

225. F. E. H. Tay, J. A. van Kan, F. Watt, and W. O. Choong, *J. Micromech. Microeng.*, 2001, **11**, 27–32.

226. R. Tornay, T. Braschler, N. Demierre, B. Steitz, A. Finka, H. Hofmann, J. a Hubbell, and P. Renaud, *Lab Chip*, 2008, **8**, 267–73.

227. M. S. Munson, J. M. Spotts, A. Niemistö, J. Selinummi, J. G. Kralj, M. L. Salit, and A. Ozinsky, *Lab Chip*, 2010, **10**, 2402–10.

228. T. Braschler, L. Metref, R. Zvitov-Marabi, H. van Lintel, N. Demierre, J. Theytaz, and P. Renaud, *Lab Chip*, 2007, **7**, 420–2.

229. I. Fatt, *Trans. AIME*, 1956, **207**, 164–181.

230. C. Fütterer, N. Minc, V. Bormuth, J.-H. Codarbox, P. Laval, J. Rossier, and J.-L. Viovy, *Lab Chip*, 2004, **4**, 351–6.

231. J. Krüger, K. Singh, A. O'Neill, C. Jackson, A. Morrison, and P. O'Brien, *J. Micromech. Microeng.*, 2002, **12**, 486–494.

232. N. Bao, Q. Zhang, J. Xu, and H. Chen, *J. Chromatogr., A*, 2005, **1089**, 270–275.

233. T. T. Perkins, D. E. Smith, R. G. Larson, and S. Chu, *Science*, 1995, **268**, 83–7.

234. R. Dylla-Spears, J. E. Townsend, L. Jen-Jacobson, L. L. Sohn, and S. J. Muller, *Lab Chip*, 2010.

235. D. Freifelder and B. Trumbo, *Biopolymers*, 1969, **7**, 681–693.

236. C. Flors, C. N. J. Ravarani, and D. T. F. Dryden, *Chemphyschem*, 2009, **10**, 2201–4.

237. A. Kishino and T. Yanagida, *Nature*, 1988, **334**, 74–6.

238. S. W. Englander, D. B. Calhoun, and J. J. Englander, *Anal. Biochem.*, 1987, **161**, 300–6.

239. C. Kanony, B. Akerman, and E. Tuite, *J. Am. Chem. Soc.*, 2001, **123**, 7985–95.

240. A. Ujvári and C. T. Martin, *Biochemistry*, 1996, **35**, 14574–82.

241. I. J. Finkelstein, M.-L. Visnapuu, and E. C. Greene, *Nature*, 2010, **468**, 983–7.

242. P. L. O. György A. Marko-Varga, *Emerging Technologies in Protein and Genomic Material Analysis*, Elsevier, 2003.

243. S. Y. Tetin, K. M. Swift, and E. D. Matayoshi, *Anal. Biochem.*, 2002, **307**, 84–91.

244. E. a Burks, G. Chen, G. Georgiou, and B. L. Iverson, *PNAS*, 1997, **94**, 412–7.

245. G. Papadakos, J. A. Wojdyla, and C. Kleanthous, in *Q. Rev. Biophys.*, 2012, vol. 45, pp. 57–103.

246. E. Cascales, S. K. Buchanan, D. Duché, C. Kleanthous, R. Lloubès, K. Postle, M. Riley, S. Slatin, and D. Cavard, *Microbiol. Mol. Biol. Rev.*, 2007, **71**, 158–229.

247. R. Lloubès, E. Cascales, A. Walburger, E. Bouveret, C. Lazdunski, A. Bernadac, and L. Journet, *Res. Microbiol.*, 2001, **152**, 523–9.

248. M. Vankemmelbeke, Y. Zhang, G. R. Moore, C. Kleanthous, C. N. Penfold, and R. James, *J. Biol. Chem.*, 2009, **284**, 18932–41.

249. S. F. Sabet and C. A. Schnaitman, *J. Biol. Chem.*, 1973, **248**, 1797–806.

250. D. R. Di Masi, J. C. White, C. a Schnaitman, and C. Bradbeer, *J. Bacteriol.*, 1973, **115**, 506–13.

251. W. A. Cramer, F. S. Cohen, A. R. Merrill, and H. Y. Song, *Mol. Microbiol.*, 1990, **4**, 519–26.

252. C. J. Lazdunski, *Mol. Microbiol.*, 1995, **16**, 1059–66.

253. P. Elkins, A. Bunker, W. a Cramer, and C. V Stauffacher, *Structure*, 1997, **5**, 443–458.

254. K. Schaller and M. Nomura, *PNAS*, 1976, **73**, 3989–93.

255. R. James, C. Kleanthous, and G. R. Moore, *Microbiology*, 1996, **142 ( Pt 7**, 1569–80.

256. R. James, C. N. Penfold, G. R. Moore, and C. Kleanthous, *Biochimie*, 2002, **84**, 381–9.

257. R. Wallis, G. R. Moore, R. James, and C. Kleanthous, *Biochemistry*, 1995, **34**, 13743–13750.

258. K. Jakes, N. D. Zinder, and T. Boon, *J. Biol. Chem.*, 1974, **249**, 438–44.

259. J. Sidikaro and M. Nomura, *J. Biol. Chem.*, 1974, **249**, 445–53.

260. C. Kleanthous and D. Walker, *Trends Biochem. Sci.*, 2001, **26**, 624–31.

261. P. C. Cooper and R. James, *J. Gen. Microbiol.*, 1984, **130**, 209–15.

262. S. J. Singer and G. L. Nicolson, *Science*, 1972, **175**, 720–31.

263. K. Ritchie and J. Spector, *Biopolymers*, 2007, **87**, 95–101.

264. S. R. Loftus, D. Walker, M. J. Maté, D. a Bonsor, R. James, G. R. Moore, and C. Kleanthous, *PNAS*, 2006, **103**, 12353–8.

265. D. Duché, A. Frenkian, V. Prima, and R. Lloubès, *J. Bacteriol.*, 2006, **188**, 8593–600.

266. J. Spector, S. Zakharov, Y. Lill, O. Sharma, W. a Cramer, and K. Ritchie, *Biophys. J.*, 2010, **99**, 3880–6.

267. N. Metropolis, A. W. Rosenbluth, M. N. Rosenbluth, A. H. Teller, and E. Teller, *J. Chem. Phys.*, 1953, **21**, 1087.

268. M. C. Leake, J. H. Chandler, G. H. Wadhams, F. Bai, R. M. Berry, and J. P. Armitage, *Nature*, 2006, **443**, 355–8.

269. J. Deich, E. M. Judd, H. H. McAdams, and W. E. Moerner, *PNAS*, 2004, **101**, 15921–6.

270. M. J. Saxton, *Biophys. J.*, 1994, **66**, 394–401.

271. D. V Nicolau, J. F. Hancock, and K. Burrage, *Biophys. J.*, 2007, **92**, 1975–87.

272. A. V Weigel, S. Ragi, M. Reid, E. K. Chong, M. Tamkun, and D. Krapf, *Phys. Rev. E Stat., Nonlinear, Soft Matter Phys.*, 2012, **85**, 041924.

273. L. Niu and J. Yu, *Biophys. J.*, 2008, **95**, 2009–16.

274. T. Fujiwara, K. Ritchie, H. Murakoshi, K. Jacobson, and A. Kusumi, *J. Cell Biol.*, 2002, **157**, 1071–81.

275. Y. Wang, *Biochem. Biophys. Res. Commun.*, 2002, **292**, 396–401.

276. A. Lin, R. Kopelman, and P. Argyrakis, *Phys. Rev. E*, 1996, **53**, 1502–1509.

277. H. Berry, *Biophys. J.*, 2002, **83**, 1891–1901.

278. V. Cherezov, E. Yamashita, W. Liu, M. Zhalnina, W. a Cramer, and M. Caffrey, *J. Mol. Biol.*, 2006, **364**, 716–34.

279. T. Cierpicki, B. Liang, L. K. Tamm, and J. H. Bushweller, *J. Am. Chem. Soc.*, 2006, **128**, 6947–51.

280. E. Yamashita, M. V Zhalnina, S. D. Zakharov, O. Sharma, and W. a Cramer, *EMBO J.*, 2008, **27**, 2171–80.

281. R. Koebnik, K. P. Locher, and P. Van Gelder, *Mol. Microbiol.*, 2000, **37**, 239–53.

282. R. N. Reusch, *FEBS J.*, 2012, **279**, 894–909.

283. B. Lugtenberg and L. Van Alphen, *Biochim. Biophys. Acta*, 1983, **737**, 51–115.

284. H. Nikaido, M. Vaara, and Nikaido, in *Escherichia Coli and Salmonella Typhimurium*, ed. F. C. Neidhardt, American Society for Microbiology, Washington, D.C., First., 1987, pp. 7–22.

285. G. L. Ryan and A. D. Rutenberg, *J. Bacteriol.*, 2007, **189**, 4749–4755.

286. K. Lipkow, S. S. Andrews, and D. Bray, *J. Bacteriol.*, 2005, **187**, 45–53.

287. R. D. Finn, E. V Orlova, B. Gowen, M. Buck, and M. van Heel, *EMBO J.*, 2000, **19**, 6833–44.

288. H. P. Erickson, *Biol. Proced. Online*, 2009, **11**, 32–51.

289. S. R. Oh, *J. Micromech. Microeng.*, 2008, **18**, 115025.

290. G. Bjørnsen, L. Henriksen, J. H. Ulvensøen, and J. Roots, *Microelectron. Eng.*, 2010, **87**, 67–71.

291. A. Grosse, M. Grewe, and H. Fouckhardt, *J. Micromech. Microeng.*, 2001, **11**, 257–262.

292. S. Song, A. K. Singh, T. J. Shepodd, and B. J. Kirby, *Anal. Chem.*, 2004, **76**, 2367–73.

293. I. Steingoetter and H. Fouckhardt, *J. Micromech. Microeng.*, 2005, **15**, 2130–2135.

294. H. Zhu, M. Holl, T. Ray, S. Bhushan, and D. R. Meldrum, *J. Micromech. Microeng.*, 2009, **19**, 065013.